

KfK 5261
Dezember 1994

Dry Core BWR Test CORA-33: Test Results

S. Hagen, P. Hofmann, V. Noack, G. Schanz,
G. Schumacher, L. Sepold

Hauptabteilung Ingenieurtechnik
Institut für Materialforschung
Institut für Neutronenphysik und Reaktortechnik
Projekt Nukleare Sicherheitsforschung

Kernforschungszentrum Karlsruhe

Kernforschungszentrum Karlsruhe
Hauptabteilung Ingenieurtechnik
Institut für Materialforschung
Institut für Neutronenphysik und Reaktortechnik
Projekt Nukleare Sicherheitsforschung

KfK 5261

Dry Core BWR Test
CORA-33: Test Results

S. Hagen, P. Hofmann, V. Noack, G. Schanz, G. Schumacher, L. Sepold

Kernforschungszentrum Karlsruhe GmbH, Karlsruhe

Als Manuskript gedruckt
Für diesen Bericht behalten wir uns alle Rechte vor

Kernforschungszentrum Karlsruhe GmbH
Postfach 3640, 76021 Karlsruhe

ISSN 0303-4003

Dry Core BWR Test CORA-33: Test Results

Abstract

The experimental program of the out-of-pile facility CORA is part of the international Severe Fuel Damage (SFD) research . It was set up to provide information on the failure mechanisms of Light Water Reactor (LWR) fuel elements in the temperature range from 1200°C to 2400°C.

Test CORA-33 was designed to address the BWR "dry" core severe accident scenario . The BWR "dry" accident conditions would develop, if after a Short-Term Station Blackout (STSB) according to the Emergency Procedure Guidelines the vessel is depressurized, to give a preliminary steam cooling. The characteristics of this sequence are loss of off-site power, failure of station diesels and of steam driven turbine injection systems → no injection; vessel depressurized; boil off with flashing during depressurization and steam starved core degradation.

Precalculation at ORNL showed, that these conditions could be simulated with a BWR bundle heated at about 0.3 K/s and without additional steam input. The evaporation from the quench cylinder simulated the steam starved "dry" conditions.

Review of CORA-33 indicates that the test objective were achieved: Core degradation occurred at a core heat up rate (characterized by the absence of temperature escalation due to oxidation) and a test section axial temperature at incipient structural melting, that are prototypic of "dry" core conditions. The flat axial temperature profile resulted, by B₄C/SS/Zry interaction, in complete dissolution of absorber blade and channel box walls with a strong attack on the Zircaloy cladding of the fuel rods over most of the length of the bundle. The molten material was relocated into the lower part of the bundle, with the maximum blockage at about 100 mm elevation. Relocated material was found as low as the -70 mm elevation.

Regarding the uncertainty of draining into the lower core and core plate region of a BWR under dry core conditions, these results show that there is a tendency for refreezing of the molten material to take place in the lower part of the bundle. A fraction will however also fall below the core plate.

CORA-33, SWR-Experiment unter Dampfmangel: Versuchsergebnisse

Zusammenfassung:

Die Experimente in der Out-of-pile Anlage CORA sind ein Teil des internationalen Forschungsprogramms zu sog. Schweren Kernschäden (Severe Fuel Damage). Mit ihnen sollten Informationen über die Schadensmechanismen in Leichtwasserreaktoren im Temperaturbereich von 1200°C bis 2400°C gewonnen werden. Der Versuch CORA-33 untersucht das Verhalten eines Siedewasserreaktor-Brennelements beim Unfall unter Dampfmangelbedingungen (BWR dry core accident scenario).

Diese Bedingungen würden entstehen, wenn nach einem totalen Netzausfall mit Ausfall der dampfgetriebenen Turbinen (STSB) der Druckbehälter druckentlastet wird, um eine zeitweilige Dampfkühlung zu erreichen. Das Verhalten dieser Unfallsequenz ist durch folgende Schritte gekennzeichnet: 1. Der totale Ausfall aller Einspeisesysteme; 2. Der Druckbehälter wird druckentlastet; 3. Das verdampfende Wasser kühlte vorübergehend den Kern bis zum Absinken des Wasserspiegels unter die untere Kernplatte; 4. Kernversagen unter Dampfmangelbedingungen.

Vorausrechnungen am ORNL haben gezeigt, daß diese Bedingungen für ein Bündel erreicht werden können, das mit 0,3 K/s aufgeheizt wird ohne daß zusätzlich Dampf eingespeist wird. Das vom Quenchzylinder verdampfende Wasser simuliert den Dampfmangel.

Die Ergebnisse des Versuchs zeigen, daß die Zielsetzungen von CORA-33 erreicht wurden: Die Schadensentwicklung geschieht bei der gewünschten Aufheizrate, die durch das Fehlen der Temperatureskalation charakterisiert ist. Die axiale Temperaturverteilung bei Schmelzbeginn ist typisch für Bedingungen unter Dampfmangel. Das flache axiale Temperaturprofil führt durch die B₄C/Edelstahl/Zry-Wechselwirkung zu einer kompletten Auflösung des Absorberkastens und der Kanalwände. Es entwickelt sich ein starker Angriff auf die Zry-Hülle der Brennstabsimulatoren über einen großen Bereich des Bündels. Die Schmelze erstarrt im unteren Bereich des Bündels, mit einer maximalen Blockade bei ca. 100 mm. Erstarnte Schmelze wurde bis zu -70 mm gefunden.

In Bezug auf das Verlagerungsverhalten der in SWR unter Dampfmangel entstehenden Schmelze zeigt dieser Versuch, daß eine starke Tendenz zum Erstarren im unteren Bereich des Bündels vorhanden ist. Ein Teil der Schmelze fließt aber auch in den Bereich unterhalb der unteren Kernplatte.

Contents

ABSTRACT	1
Zusammenfassung	II
1. Introduction	1
2. Description of the CORA test facility	2
3.1 Initial and boundary conditions	6
3.2 Test conduct	7
4. Temperature measurements	8
5. Failure of fuel rods and absorber rods	10
6. Hydrogen generation	11
7.1 Posttest appearance of the bundle	13
7.2 Blockage formation and mass distribution	15
8. Summary and discussion of major results	17
9. Pre-transient data	18
10. References	18
11. Acknowledgements	19
12. List of tables	20
13. Tables	21
14. List of figures	33
15. Figures	41
16. Appendix A: Pre-transient data	151
17. Appendix B: Complete set of cross sections	167

1. Introduction

The TMI-2 accident has demonstrated that a severe fuel damage transient will not necessarily escalate to an uncontrolled core melt down accident if the design basis accident limits are exceeded. Therefore, comprehensive research programs have been initiated in various countries to investigate the relevant fuel rod bundle damage mechanisms that occur in an uncovered core, after an increase of temperature.

In the Federal Republic of Germany at the Kernforschungszentrum Karlsruhe (KfK) the Severe Fuel Damage (SFD) Program is now coordinated by the Project Nuclear Safety Research (PSF) as successor of Project Nuclear Safety (PNS) and LWR Safety Project Group (PRS). As part of this program, out-of-pile experiments (the CORA-Program) are being conducted at the Hauptabteilung Ingenieur-technik (HIT). These experiments have been designed to provide information on the behavior of Light Water Reactor (LWR) fuel elements under severe fuel damage (SFD) conditions, up to meltdown. The results of the out-of-pile experiments will also be used for the assessment of the SFD computer codes.

Within the framework of international cooperation the out-of-pile experiments are contributing confirmatory and complementary information to the results obtained from the limited number of in-pile tests. The investigation of the basic phenomena of the damage process is supported by separate-effect tests.

The most important aspects concerning fuel rod failure and subsequent core degradation are the chemical interactions amongst the fuel element components in competition with the oxidation of the cladding in steam, which causes also the temperature escalation.

Melt formation starts around 1200°C by chemical interactions of the Inconel spacer grids and absorber materials (Ag, In, Cd for PWRs and B₄C/stainless steel for BWRs) with the Zircaloy cladding. The dissolution of the UO₂ pellets by liquid Zircaloy starts far below the UO₂ melting point.

Melt formation, relocation, blockage formation and finally fragmentation of fuel elements during reflooding characterize the degraded core and the potential of long term coolability. Furthermore the influence of internal pressure of the fuel rods (ballooning and bursting) and external pressure of the system (solid contact between pellets and cladding) on the bundle meltdown behavior is investigated.

Further on, the investigation of the influence of pre-oxidation, initial heat-up rate, steam availability, water level in the bundle and bundle size is included in the program. The damage behavior of VVER fuel elements is the subject of the last two CORA tests.

The tests performed in the CORA-facility are listed in the test matrix (Table 1). The original test matrix was directed towards the behavior of PWR fuel elements only. In 1988 discussion showed that in most countries using nuclear energy, information on the behavior of BWRs in severe accident conditions was needed. In consequence, five planned PWR experiments were replaced by BWR tests in the revised test matrix. Also the original sequence of tests was changed, as one can see from the test numbers.

In this report test CORA-33 will be discussed. It was designed to address the BWR accident scenario which occurs under "dry" core severe accident conditions.

Probabilistic risk assessment studies have shown that BWR postulated accident sequence scenarios leading to core damage always involve a means for failure of function of the vessel injection systems. The station blackout accident sequence has consistently been identified as the leading contributor to the calculated core damage frequency, as the majority of the reactor vessel injection systems are dependent upon the availability of alternative electrical power.

If the loss of all AC power is combined with the failure of station diesels or gas turbines the scenario is termed a Short-Term Station Blackout (STS). In the STS scenario, partial uncovering of the core will occur. However it is assumed that the operators can follow the Emergency Procedure Guidelines, according to which the "steam cooling" manoeuvre should be initiated. The purpose of this manoeuvre is to delay fuel heatup by cooling the uncovered upper regions of the core by a rapid flow of steam, induced by depressurisation.

Since the source of the steam is the remaining inventory of water in the reactor vessel, the steam cooling manoeuvre provides only a temporary delay (20 to 30 minutes) in core heatup and concludes with a vessel water level below the core plate. The characteristics of this sequence are: no injection, vessel depressurized, boil off with flashing during depressurisation and steam starved core degradation. This sequence is therefore termed a "dry" core degradation scenario because core degradation occurs with a stagnant, steam starved core atmosphere.

2. Description of the CORA test facility

The CORA out-of-pile facility is designed to investigate the behavior of LWR fuel elements under severe fuel damage accident conditions. In the experiments the decay heat is simulated by electrical heating. Great emphasis is placed on the fact that the test bundles contain the original materials used in light-water reactor fuel elements to investigate the different material interactions.

Pellets, cladding, grid spacers, absorber rods and channel box walls are typical of those of the investigated LWRs with respect to their compositions and radial dimensions. In test CORA-33 the following BWR components are used: Original UO₂-pellets, Zry 4-cladding, Zry-spacers, Zry-channel box walls and B₄C absorber inside stainless steel tubes surrounded by the stainless steel of the blade.

Figure 1 gives a simplified flow diagram of the facility. The geometrical arrangement of the different CORA components is given in Figure 2. The central part of the facility is the fuel rod bundle. The bundle is enclosed in a Zry shroud with ZrO₂ fibre insulation. A high temperature radiation shield surrounds the bundle and shroud assembly, leaving an annular space for introduction of the quench cylinder. The bundle is connected to the power supply system at the upper and lower ends.

Below the bundle is the quench unit with a water-filled quench cylinder, which can be raised around the bundle at a controlled speed. The cylinder is guided by three rods, which also connect the electric power to the bundle lower end.

The bundle upper end is fixed in the bundle head plate. The plate is connected by a funnel shaped tube to the surge condenser. The surge condenser is double-walled, leaving access to the bundle end fittings above the bundle head funnel.

The steam is produced in the steam generator, superheated and guided to the lower end of the bundle. The steam not consumed within the bundle is condensed in two parallel condensers and the hydrogen produced is fed into the off-gas system after dilution by air to a low H₂ concentration.

Bundle design:

The bundle and its surroundings are shown in Figure 3 + 4. The bundle arrangement is given in Figure 5a and the bundle components in Figure 5b. Characteristic data of the bundle are presented in Tables 2, 3 and 4. The bundle consists of 12 heated rods, 6 unheated rods, two channel box walls and the absorber blade, representing part of a BWR absorber fuel element arrangement.

The heated fuel rod simulator is sheathed with standard Zry4 cladding tube, containing UO₂ annular pellets with a central heater. The heater consists of a 1024 mm long tungsten rod (6 mm diameter), the upper electrode (300 mm molybdenum; 689-770 mm copper) and the lower electrode (300 mm molybdenum; 183-219 mm copper). The electrodes have a diameter of 9 mm. The electrodes are flame-sprayed with 0.2 mm thick layer of ZrO₂. Large flexible copper cables provide the connection to the electrical system. The resistance of the flexible cables to the points of voltage measurement for the determination of the power was less than 1 m Ω per rod (recommended value: 0.5 mΩ).

The resistivities R of tungsten, molybdenum and copper are given respectively in the following 3 lines:

$$R_W = -2.61 \cdot 10^{-2} + 2.63 \cdot 10^{-4} T_W + 2.20 \cdot 10^{-8} T_W^2$$

$$R_{Mo} = 2.249 \cdot 10^{-2} + 5.36 \cdot 10^{-5} T_{Mo} + 1.38 \cdot 10^{-7} T_{Mo}^2 - 2.22 \cdot 10^{-11} T_{Mo}^3$$

$$R_{Cu} = -7.89 \cdot 10^{-3} + 9.90 \cdot 10^{-5} T_{Cu} - 5.49 \cdot 10^{-8} T_{Cu}^2 + 3.16 \cdot 10^{-11} T_{Cu}^3$$

The unheated fuel rod simulators consist of solid UO₂-pellets and Zry cladding. The unheated rods extend to -200 mm elevation, i.e. to 20 mm above the initial water-level of the quench cylinder (-220 mm). Zry-4 spacers are used at three elevations (-33 mm, 578 mm 1167 mm) to maintain the positions of the rods. The fuel rod simulators are screwed into the bundle head plate sealing it hermetically. The bundle head plate thus gives the fixed elevation for the axial thermal movement of the rods. The channel box walls are made of 1.2 mm thick Zry-4. The absorber blade contains stainless steel and B₄C and is made from original LWR-components.

For upper end bundle cooling the heated rods (the copper electrode inside the ZrNb cladding) and the connectors for the pressure capillaries and the thermocouples of the unheated rods are surrounded by water. The water is cooled by a heat exchanger. Argon is blown against the lower surface of the plate to protect the sealing in the bundle head plate.

At the lower end the heated fuel rod simulators are cooled by the water of the quench cylinder. The initial water level is at the -220 mm elevation. The unheated rods are in contact with the water of the quench cylinder only by the thermocouple connections. The gross volume of water inside the quench cylinder (230 mm ID) is about 70 l.

The bundle is surrounded by a Zry-44 shroud of 1.2 mm thickness. The shroud conducts the steam through the bundle. The steam enters at an orientation of 180° into the lower end (0 mm elevation). To minimize the heat losses from the shroud, it is surrounded by a 19 mm (0.75 inch) thick insulating layer of ZrO₂ fibre. On account of the low heat conductivity and heat capacity of the ZrO₂ fibre the shroud temperature can follow the bundle temperature closely. The shroud participates in the interaction with steam. The resulting oxidation energy contributes substantially to bundle heat-up.

The connection between steam inlet at 0 mm elevation and shroud is made by a stainless steel steam distribution tube. This tube extends down into the water of the quench cylinder thus forming a lower closure. The time history of the water level in the quench cylinder shows that there is no net condensation of steam in the quench cylinder.

At an elevation of 40 mm the steam distribution tube joins into the shroud. From here the shroud extends in vertical direction for 1195 mm and the insulation for 1070 mm. At 8 elevations (190-890 mm) windows of 30x30 mm in the shroud and shroud insulation allow bundle inspection by a video-system (Figure 5c).

The annuli between the shroud and the high-temperature shield on one hand and high temperature shield and pressure containment on the other hand are closed at the upper end by fibre ceramic layers of 38 mm thickness.

High temperature shield:

To keep the heat losses as low as possible, the bundle is surrounded by an additional high temperature shield (HTS). The vertical and the horizontal cross-sections of the high temperature shield are given in Figures 3 and 4. The high temperature shield consists mainly of ceramic fibre plates. The inner layer of plates consists of ZrO_2 , and the outer layer of Al_2O_3 . The fibre ceramics are excellent insulators and have a low density which results in a low heat capacity. The thermal shock behaviour of the fibre ceramics is also excellent.

The mechanical strength of the high temperature shield is ensured by external walls of stainless steel (0.9 mm). The fibre ceramic plates are attached to the stainless steel cover by ceramic nails. The inner ZrO_2 layer is 38 mm thick, and the outer Al_2O_3 layer is 76 mm thick, they are separated by a gap of 23 mm. The distance from the inner insulation surface to the centre of the bundle is 153 mm.

The high temperature shield is located within the pressure tube. In the pressure tube a large number of flanges allow access to the bundle. Through these holes and their extensions in the temperature shield, the bundle can be inspected during the test with the help of the videoscope systems.

Heating system:

In CORA-33 12 rods out of 18 are heated. The rods can be individually connected to three power systems available. In this test the intended power input was the same for all rods. Since the voltages and currents of the individual rods are measured, the power input for each rod can be determined. The power input is controlled by a computer. The time dependent power history is programmed before the test. The power is controlled by measurement of the currents of the groups, and by setting the voltage necessary to obtain the desired power.

3.1 Initial and boundary conditions

To characterize the initial and boundary conditions for the CORA-33 dry core experiment, a study of the typical dominant BWR accident sequence occurring under dry core conditions was completed at ORNL. Due to the availability of detailed data on the relative power distribution, the Susquehanna plant was used as the model BWR facility. The core power distribution is similar to that of Browns Ferry, which had been used as the model plant in previous ORNL severe accident analyses, and is considered representative of the distributions produced by the U.S. BWR core fuel loading arrangements. The accident scenario studied is the Short-Term Station Blackout (STS) sequence with automatic depressurization system (ADS) actuation per operator adherence to the EPG guidelines. This sequence involves dry core degradation.

The primary variables from the ORNL Station Blackout study that have been used to formulate the desired experimental boundary conditions for CORA-33 are:

- (1) the core heatup rate (0.3-0.5 K/s),
- (2) the core axial temperature profile at incipient control blade liquefaction, and
- (3) the water evaporation rate from the vessel lower plenum (the only steam source to the lower core region).

The primary CORA experimental variables that can be manipulated to achieve the desired dry core degradation conditions are:

- (1) the test section electrical power input and
- (2) the composition and flow rate of the gas stream entering the test section.

From the of the CORA-31 BWR test, it was known that a core heatup of 0.3-0.5 K/s would be achieved using the CORA-31 electrical power input. Subsequent BWR/CORA simulations indicated that the predicted test section heatup rate and evaporation rates from the CORA quench tank were consistent with the STS accident sequence.

Since representation of steam-starved conditions in the core region was a primary purpose of this test, it would have been preferable to have had no additional gas flow entering the test section. However, the experimental bundle is warmed initially by argon, which is electrically heated prior to entering the test section. To avoid damage to the heater, gas flow through the device must be maintained. In the BWR experiments conducted in CORA, the argon flow through the steam heater and test section is maintained at ~8 g/s for the preheat, transient, and cooldown phases of the experiment and ~2 g/s of water is vaporized and superheated along with the argon during the transient phase. Toward the

purpose of CORA-33, no water was added, and after preheating the bundle with argon at 8 g/s, the argon flow was reduced to the minimum (3 g/s) recommended by the heater manufacturer for the transient phase of the experiment.

3.2 Test conduct

In the CORA experiments the following phases for the test sequence are generally distinguished (Figure 7):

1. 0-3000 s: pre-heating
2. 3000-8300 s: transient
3. > 8300 s: cooldown.

To keep the videoscope windows clear a flow of 1.7 g/s argon is directed to the front of the windows. For the protection of the bundle head plate, 4.3 g/s of argon are flooding the area below the plate. The 6 g/s flow from videoscopes and bundle head plate does not move through the bundle and is marked with the label "videoscopes" in the second graph of Figure 7. The pressure in the system is controlled to 0.22 MPa.

During the preheat phase there is a flow of 8 g/s preheated argon through the bundle and a low constant electric power input of about 0.52 kW. In consequence the temperature in the insulation reaches a level which is high enough to avoid steam condensation.

During the transient phase the initial temperature increase of about 0.3 K/s is produced by raising the electric power input from 4.5 to 22.3 kW (Figure 7). As discussed in the last section there was no extra steam input, also the argon flow was reduced to 3 g/s to reach the steam starved conditions for the "dry" scenario.

The test was terminated by turning off the electric power at 8300 s (slow cooldown by heat losses). At the same time the argon flow was restored to 8 g/s for cooling of the steam superheater.

The boundary conditions during the test are given in detail in Figures 8 to 23. Figure 10 shows the total electric power input, which was produced by the voltage inputs to the three groups of rods (Figure 11) and the resulting total current (Figure 14). The electric power input is controlled by measurement of the voltages of the rod groups and the currents of the individual rods. Then the computer sets the voltages to give the power required.

In Figure 11 the regular increase of the voltage is disturbed at about 5500 s. The irregularities are produced by melt formation allowing flow of current in neighbouring rods as well. This effect can be seen more pronounced in Figure 17, showing the currents of the single rods. Consequently the resistance of the bundle (Figure 15) is reduced instead of increasing with the temperature (of the tungsten heater rods).

Figures 16, 18, 19, 20 show the resistances of the rod groups and of the single rods. The tendency is the same for all measurements as for the total resistance. The sharp spikes at 8300 s during power shutdown are artificial due to measurement of voltage and current at not exactly the same times.

The evaporation rate of water (Figure 21b) giving the only steam source in this test is determined by measuring the change of the water level. Measurement of pressure difference was used to determine the height of the water column. The increase of the steam production starts with the melt relocation.

In Figures 21a the water temperatures in the quench cylinder at -250 mm and -300 mm (initial water level at -220 mm) are indicated. Again one can see the increase in temperature rise at about 5500 s, correlated with the beginning of melt production and relocation. Also the temperatures measured at -50 mm elevation (Figure 22) show the change in increase at around 5500 s.

For azimuthal angles of 15° and 195° the temperatures are measured on the steam distribution tube and for angles of 165° and 345° at 15 mm inside the tube.

The temperature of the incoming argon at the steam inlet is measured with two thermocouples (Figure 23). The resulting measurements are practically the same. The decrease of the temperature at 2700 s is caused by the decrease of the argon flow from 8 g/s to 3 g/s, which leads to a greater loss of temperature of the gas as it passes along the connecting tube from the superheater to the entrance to the bundle.

4. Temperature measurements

The temperatures in the bundle were measured by high-temperature thermocouples of WRe5/WRe26 wires and HfO₂ insulating material. The sheath was made of tantalum and Zircaloy. Thermocouples with "Ker" in the name were additionally shielded with a ZrO₂ sheath. The measurements in the high temperature shield were performed with NiCrNi-thermocouples sheathed with stainless steel. Also the compensation cables were sheathed with stainless steel. The positions of the thermocouples in the bundle are given in Table 5 and those in the high temperature shield in Figure 49a and 49b.

The temperature measurements of the bundle are presented as functions of time in the following way: on one hand, the temperatures of the components (heated rods, unheated rods, channel box walls, absorber blade, etc.; Figures 24-36) are given, on the other hand - for comparison reasons - the temperature measurements for different components are grouped by axial elevations (Figures 37-44).

The temperature measurements of the high temperature shield are given in Figures 50 -63.

Temperature of the components

The comparison of temperatures measured on the components of the bundle (Figures 37-44) show that there is no large gradient inside the bundle in the radial direction. The measurements at the same elevation have therefore been combined to give one representative temperature for the bundle at that elevation. Due to failure of some thermocouples after 5500 s these "estimated" temperatures are more reliable before 5500 s. The results of this combination of measurements is given in Figure 45 as "estimated" temperatures of the bundle as functions of time for different elevations. In Figure 46 these values are rearranged as axial temperature distributions for different times in the test sequence.

CORA-33 was the first test without additional steam input into the bundle. The temperature histories for different elevations (Figure 45) are therefore best discussed in comparison with test CORA-31 (Figure 47), which had the same electrical input, but an additional 2 g/s steam input, and 8 g/s argon flow instead of 3 g/s (Figure 48). No significant temperature escalation is found in test CORA-33. The temperature transient is mainly determined by the electric power input and the heat losses. After an initial increase at about 0,3°C/s up to 4500 s after 5500 s at about 1500 °C the temperature increase is remarkably reduced. The still increasing linear power input mainly compensates for the increasing heat losses. The much stronger temperature increases after 5500 s at the 50 mm and 150 mm elevations are caused by relocation of molten material.

For CORA-31 the additional steam input (2 g/s) to the bundle produces the temperature escalation found in all the other CORA tests. After 4700 s, when a temperature of 1100°C is reached, the exothermal Zr/steam reaction accelerates the temperature increase. Correlated to the temperature increase is the increase of the H₂ production rate, as can be seen in Figure 47. Also the temperature increase in the lower part of bundle CORA-31 is much faster. If the temperature at the lower elevation rises above 1000°C, the influence of the exothermal

reaction enhances the temperature rise. On the other hand, the stronger convective cooling of steam and additional argon reduce the temperature for ≤ 550 mm elevations, when the contribution of the exothermal reaction is decreasing due to the influence of the growing protective oxide layer.

Temperatures of the High Temperature Shield (HTS)

To reduce the radial heat losses, the insulated bundle is surrounded by the additional fibre insulation of the high temperature shield. HTS results of the measurement of the temperatures at the different locations are given in Figures 49-63. The positions of thermocouples on the inner surface (153 mm radius), inside the insulation and on the outer surface (293 mm radius) are shown in Figures 49a and 49b.

The maximum temperature of the inner surface of the HTS (Figure 50) increases from about 300°C at -50 mm elevation to about 1200°C at 1150 mm. At 950 mm a maximum temperature of 1150°C was reached compared with about 1200°C at the outside of the bundle insulation at the same elevation, giving a temperature decrease of 50°C over the gap between bundle and HTS. The azimuthal variation of the temperature at the inner surface (Figures 51-53) is less than 50°C. The steep temperature decrease within the insulation is shown in Figures 60-62. On the outside the temperature decreases to below 150°C at the upper end and to below 100°C at the lower end.

5. Failure of fuel rods and absorber rods

On three unheated and two heated rods the internal pressure was measured, as shown in Figures 67 + 68. The sudden release of the pressure difference of about 3 bar between internal and system-pressure indicates the failure of the fuel rod simulators. The rods failed in sequence: 4.2, 6.4, 3.5 4.6, 7.1 (compare Figure 5a) i.e. the innermost registered rods failed first followed the heated rod 7.1, which lies at the outermost edge of the bundle. The failure times are: 4845 s, 4850 s, 4880 s, 4980 s and 5165 s. Using the measured temperatures on the unheated rod 2.4 and the heated rod 5.3 (Figure 69), temperatures at time of failure of between 1220 °C and 1415 °C are obtained. The higher values are somewhat doubtful, as the temperature is measured on inner rods and the failing rod was positioned on the outside of the bundle.

The rods failed due to strain, a mechanism favoured by the relative lack of cladding oxidation compared with the normal CORA tests. This is the result of the about 3 bar pressure differential between the inside and outside of the rods.

Calculations of the failure time with the ORNL experiment-specific CORA models /2/ give failure times between 4940 and 5012 s, close to the measured values. On the other hand the temperature of the absorber at 4845 s - the time of the first failure - is only less than 1100°C, which shows that attack on the fuel rod cladding by the absorber was not possible at that time.

Information on the failure of the absorber blade can be derived from the irregularities in the absorber blade temperatures.

In Figure 71 deviations from a smooth temperature reading is visible at 350 mm at about 4950 s. The thermocouples for the measurement in the absorber blade are positioned inside the blade between the ss tubes filled with the B₄C-powder. The irregular increase is interpreted as the influence of melt within the blade coming from higher elevations. The temperature at 4950 s and 350 mm is about 1000°C compared with 1150°C in the upper part between 550 mm and 850 mm. The melt has developed by interaction of B₄C and stainless steel and at this time the inner stainless steel tubes must have been dissolved.

The sudden increase in the temperature measured with thermocouples at the outside of the absorber blade (Figure 28), show that at about 5100 s the melt must have dissolved the blade wall and reached the channel between blade and channel box wall. The sudden increase at about 5150 s at the outside of the channel box wall (Figure 27) points out that at this time the melt must have dissolved already the channel box wall, and is now interacting with the Zircaloy of the fuel rod simulators.

Information on melt movement within the bundle can also be gained by the irregularities in the measured currents of the single rods. If relocating melt with a metallic character forms bridges between a heated rod and surrounding unheated rods, the current flow in this rod is suddenly increased. This sudden increase in the current of the single rods can be seen in Figure 17. Sudden increases of the current of individual rods start at the following times: 7.5, 5550 s; 1.5, 5630 s; 5.7, 5650 s; 1.3, 5870 s; 7.3, 5910 s; 3.1 6020 s; 5.3, 6200 s; 3.7, 6280 s; 3.5, 6430 s; 7.1, 7600 s. These irregularities in the single rod currents show that major melt movement within the bundle must start at least as early as at 5550 s, and has reached the outermost end of the bundle at 7600 s.

6. Hydrogen Generation

The hydrogen produced during the test by the steam/zirconium reaction is measured with mass spectrometer systems installed at two positions, i.e. above the test section, and in the mixing chamber after the gas has passed the condenser (see Figure 1). The gas at the test section outlet can contain a high

steam partial pressure and has therefore to be diluted by helium before it enters the analyzer through the capillary tube. For this purpose a dilution chamber with flow meters is installed.

A schematic diagram of the probes, gas lines, and gas analysis system is provided in Figure 6b. The off-gas mixture which contains hydrogen among other gases is transported to the spectrometer via capillary tubes. It is analyzed by quadrupole mass spectrometers of the type Leibold PQ 100. The ion currents representing the concentration of the respective gases are determined. The production rate of a gas component is calculated with the ratio of the partial pressure of the particular gas to that of argon (carrier gas) and multiplied by the argon flow rate through the test bundle. The hydrogen generation rate is evaluated as follows:

$$R_m = 2 \cdot p_H F_{Ar} / (22.4 \cdot p_{Ar}) [\text{g/s}]$$

with

R_m = mass production rate of hydrogen [g/s]

p_H = partial pressure of hydrogen

p_{Ar} = partial pressure of argon

F_{Ar} = volumetric argon flow through mixing chamber [l/s].

Based on a calibration test with bundle CORA-7, in which a mixture of argon and 30% hydrogen was radially injected into the test section, the delay time of monitoring the gas was estimated to be 80 s. This time was taken into account for the measured hydrogen production in all CORA experiments. The same calibration test, however, showed lower increases in the rate of hydrogen production than would be expected from the injected gas flow. For this reason the measured data were corrected based on the actual gas concentration, i.e. on the gas input during the calibration test. A transfer function was determined and applied to the measured data. The result is a corrected curve that better represents the H₂ production rate in the test section.

The hydrogen production rate during test CORA-33 is given in Figure 64a, whereas the corrected data are based on the transfer function of the CORA-7 calibration test. On account of the small hydrogen production rates and the absence of temperature escalation there is nearly no difference between the measured and the corrected values. The steam source was the evaporation of water from the quench cylinder. About 1400 g of water evaporated between 3000 s and 10000 s in the test. The rate of evaporation was obtained from the water level measured in the quench cylinder and is shown in Figure 21b. The maximum value of about 0.55 g/s was obtained at the end of the test.

The total hydrogen measured amounts to 84 g. This corresponds to 756 g steam consumed, about half of the water evaporated from the quench cylinder. If on the other hand one assumes that an uniform oxidation took place between 250 mm and 1250 mm the 84 g H₂ correspond to 24% oxidation of the Zircaloy between these elevations.

In the exothermic Zircaloy/steam reaction the formation of hydrogen is correlated with the production of energy. Using the corrected values of measured hydrogen, in Figure 64b, the resulting chemical power is shown. In Figure 66 the chemical power is compared with the electric power input. Due to the chosen highly steam starved conditions, this is the smallest contribution from all the CORA tests performed.

The total amount of hydrogen produced was 84 g. This corresponds to an oxidation energy of 12.8 MJ. The total electric input amounted to 75.6 MJ. These values show that in this test the exothermic energy was only 17% of the electric input, compared with nearly 100% in test CORA-29 for instance.

For comparison also the hydrogen values and the chemical power of test CORA-31 are given in Figures 65 and 66. As discussed in section 3 the peak at about 6000 s is correlated with the temperature escalation in test CORA-31.

7.1 Posttest Appearance of the bundle

The posttest appearance of test bundle CORA-33 is shown in Figures 82-109. Fig. 82 shows the bundle with insulation at different orientations. This demonstrates the state of the bundle still in its test position. Only the surrounding high temperature shield was moved down. The piece of insulation missing at 360° between about 100 and 300 mm was broken away after the test.

The state of the inner side of the insulation material (ZrO₂ fibre) is shown in Figures 83-91. The attack of melt on the fibre material which reduces the thickness can be clearly seen. On the 120° side this interaction is effective down to about 300 mm. The depth of attack can be recognized from the detailed representation in Figures 84-91.

The appearance of the bundle after removal of the insulation and partial removal of the shroud is shown in Figure 92 and in detail in Figures 93-109. The damage to the bundle and shroud down to about 100 mm corresponds to the flat axial temperature profile as given in Figure 46.

The damage in the bundle can best be discussed by including the information from cross sections of the bundle. To enable cutting of the cross sections a Lucite box was placed around the bundle for encapsulation with epoxy resin. The lower

end of this box was closed by a paraffin layer which was produced by refreezing paraffin floating on the water of the quench cylinder. As epoxy, Mutapox 0273 with the hardener LC (Bakelite GmbH, Iserlohn) was used. The bundle was filled starting from the bottom through the steam inlet. This epoxy was chosen, as its reaction time was slow enough for the shrinkage effect to be negligible. The hardening time was one week. A saw with 2.3 mm thick diamond blade of 500 mm OD (mean diamond grain size 138 µm) was used to cut the bundle at 3200 rpm.

An overview of horizontal cross sections is shown in [Figures 110 and 112](#). Vertical cross sections for the region from -100 to +200 are given in [Figure 111](#). The whole set of horizontal cross sections is presented in Appendix B.

From the posttest photography and the cross sections the following information can be obtained:

- In accordance with the flat temperature profile the attack on the bundle can be seen over the whole length: At the lower end the highest cross section with all intact components is found at 17 mm ([Figure B14](#)). There may be also at this elevation a slight attack in the area where the fuel rods are surrounded by relocated refrozen melt. At 69 mm ([Figure B13](#)) the damage can clearly be recognized. The damage is visible up to the highest cross section, at 1160 mm ([Figure B1](#)). The posttest photographs ([Figure 92](#)) have the same appearance.
- The absorber blade is destroyed between 50 mm and 1160 mm ([Figure 113 + B1](#)): At 17 mm elevation the absorber blade and the stainless steel tubes are intact. The missing B₄C powder at this elevation points to no interaction between B₄C and ss-tubes. At 69 mm the blade has disappeared. The vertical cross sections ([Figure 111](#)) show that the blade is destroyed above 50 mm. The empty absorber tubes at this elevation in contrast to the sintered structure at 121 mm suggest, that internal interaction starts at between 69 and 121 mm. The absorber blade is missing up to 1160 mm and the absorber rods can be found at 1145 and 1160 in a sintered structure only, showing that the B₄C/ss reaction has started.
- Between 350 mm and 1050 mm the main fraction of absorber is missing. Possible consequences on the criticality of a reflooded reactor must be taken into account.
- The Zircaloy channel box wall has survived at the lower end only on the 30° side below 69 mm ([Figure B30](#)). On the upper end it is destroyed at least up to 1160 mm ([Figure B1](#)).
- The major part of the Zircaloy cladding has melted between the 150 mm and 1050 mm elevations. Some flowering of oxidized cladding (much less than in

the steam rich tests) can be observed on the outer side of the bundle in the 345° direction.

- Partial dissolution of UO₂ can be seen mainly on the pellets of the heated rods above 350 mm.
- A partial flow blockage has formed between -20 and 150 mm elevation. In the absorber blade region the melt has relocated down to -70 mm (Figures 110-112, B12-B16).

7.2 Blockage formation and mass distribution

The relocation of molten material is also determined by measurement of the axial distribution of the blocked area and bundle mass. These measurements were performed in connection with the epoxying process. As can be seen in Figure 73 the resin is paired into the Lucite mould from the bottom end. By weighing the resin left in the feed tank after each step, i.e. when the resin level has raised by 1 cm in the bundle, the difference of mass allows the void volume of the bundle to be calculated as a function of the axial height. The filling process is slow enough so that the reading on the scale can be taken every cm.

The error of this measured mass distribution amounts to about 15%; 10% with respect to the measurement of 1 cm increments of the epoxy level and 5% due to the error in mass measurement. The error, however, is alternating, i.e. epoxy not measured in one step is certainly included in the next reading at the scale. A filtering method using a Fourier transformation, with the higher frequencies cut off by a low pass filter, was performed to deal with these errors.

The data of the mass of resin as a function of elevation (g/cm) in Figure 74 demonstrate the scatter. The smoothed solid-line curve in Figure 74 was obtained from the data (crosses) by filtering. The axial distribution in Figure 74 is the distribution of the epoxy bundle fill, i.e. a complement to blockage in the bundle.

Using the measured mass and density of epoxy and the cross sectional area inside the Lucite mould the structural area of the final state of the bundle state can be evaluated. Referred to the area inside the shroud, it is given in Figure 76 as "blocked area inside the shroud".

Blocked area = (cross section mould interior -cross section epoxy-cross section of shroud remnants) related to cross section of shroud interior.

As part of the shroud was removed together with the fibre insulation after the test, the remnants of the shroud which were present during the filling process

were eliminated in the evaluation by measuring their contribution to the cross section separately, i.e. Figure 76 represents only bundle material.

To determine the axial mass distribution, the epoxy filled bundle was cut into horizontal slices and these bundle segments were weighed. The distribution is shown in Figure 75. Knowing the axial epoxy distribution, the contribution of the resin is subtracted from the measured weight, to give the mass distribution of the bundle. Also this distribution is corrected for the share contributed by the shroud. The result is given in Figure 77. These data represent the mass of the rods and spacers. In Figure 77 the measured curve is compared with the mass distribution of the intact bundle.

Specific mass = mass of weighed samples -epoxy mass -mass of shroud remnants related to the respective axial segment.

If one compares the uncertainty of the axial mass distribution with the axial volume distribution, one can state that the method based on the weighed samples is the more accurate one. The uncertainty of the measurement of the filled-in epoxy mass includes the same absolute error, however, the relative error is only one fifth, because the epoxy resin is related to a 5 cm block compared with the reference of 1 cm in the volume method. Because of the lower density of the epoxy resin in comparison with the density of the structural material, the relative error is further reduced. On the other hand in the mass distribution the resolution is reduced.

The axial distribution of blocked area (Figure 76) and of mass in the bundle (Figure 77) are very similar and in agreement with the results from the cross sections. A relatively uniform removal of material from the upper part of the bundle between 400 and 1100 mm elevation to the lower end is observed. The blockage formed has its maximum at about 100 mm.

In Figures 78 and 79 the axial volume distribution and axial mass distribution are compared with the axial temperature distributions at different times in the test. It is recognized that the relatively uniform removal of material is in accordance with the flat axial profile, and the elevation of the blockage is correlated to the elevation of the steep axial temperature gradient. As seen in many tests, the relocation of the molten material is determined by the axial temperature distribution.

This correlation between temperature distribution and material removal and melt relocation is evident from the corresponding graphs for test CORA-31 which are shown in Figures 80 + 81 for comparison.

8. Summary and discussion of major results

CORA-33 is the first BWR experiment conducted in the CORA facility without direct steam feed to the test section. This is in line with the basic purpose of the experiment, which consists in observing the core degradation phenomena of prototypical BWR core structures subjected to dry core accident conditions.

- Since there was no direct steam feed to the bundle, no temperature escalation due to the Zircaloy/steam reaction occurred. The maximum temperature of about 1850 °C was reached at the end of the test, at 950 mm. A relatively flat temperature profile is found over a large part of bundle.
- The hydrogen production history is in agreement with the lack of a temperature escalation. The production rate which is low compared to the other CORA-experiments reaches a maximum of about 30 mg/s at the end of the test. The total hydrogen measured amounts to 84 g. This corresponds to 756 g of steam consumed, which is about half of the water evaporated from the quench cylinder. Under the assumption of an uniform oxidation between 250 mm to 1250 mm 84 g H₂ corresponds to 24% oxidation of the Zircaloy. On the other hand 84 g H₂ corresponds to an oxidation energy of 12.8 MJ, which is 17% of the electric input.
- The interaction of B₄C and stainless steel starts at about 850°C and at 4950 s the first melt movement inside the absorber blade is observed. At that time, the maximum temperature in the blade between 550 mm and 850 mm has reached a value of 1150 °C.
- Melt movement between blade and channel box wall can be recognized at about 5100 s, showing that at this time the B₄C/ss melt must have dissolved part of the blade wall.
- At about 5150 s the B₄C stainless steel melt has dissolved part of the Zry channel box wall and reached the bundle region.
- Large melt movement and relocation can be registered by measurement of the current change in single rods in the period 5550 s to 7600 s.
- At the end of the test the absorber blade is destroyed between 50 and 1160 mm. Between 350 and 1050 mm the main fraction of the absorber is missing.
- The channel box wall is dissolved over the same length.
- The major part of the Zircaloy cladding melted and relocated between the 150 and 1050 mm elevations.
- Only a limited amount of flowering of oxidized cladding (much less than in the steam rich test) can be observed.

- Partial dissolution of UO₂, mainly on the pellets of the heated rods, can be seen above 350 mm.
- A partial flow blockage has formed between -20 and 150 mm elevation.
- The relocation is mainly determined by the axial temperature distribution. On the other hand the axial temperature distribution is influenced by the melt relocation.
- For the draining behavior of melt formed in a BWR under steam-starved conditions the results of CORA-33 show a tendency of refreezing of the molten material in the lower part of the bundle. But a fraction will fall also below the core plate.
- The relocation of a large part of the absorber material into the lower part of the bundle, indicates that the reflooding water must have a sufficient concentration in boron, to avoid re-criticality.

9. Pre-transient data

To show enough detail, the results of measurement of temperature are given, in section 4, only after 3000 s, when the increase of electric power is starting. For the understanding of the thermo-hydraulic behavior of the facility in connection with code calculations, also the period before 3000 s may be of interest. The low electric power input between 0 and 3000 s is given in Figure A3. In the time before, the heating of the bundle results only from the flow of hot argon (Figure A1, bundle) coming from the steam superheater.

10. References

- /1/ L.J. Ott, "Posttest Analyses of the CORA-31 Slow Heatup BWR Experiment", letter report (ORNL/NRC/LTR-92/29).
- /2/ L.J. Ott, "Posttest Analysis of the CORA-33 Dry Core BWR Experiment", letter report (ORNL/NRC/LTR-93/21).
- /3/ R.O. Gauntt, K.O. Reil; "Results of the XR1-1 and XR1-2 Developmental Ex-Reactor Tests on Metallic Melt Relocation and Blockage Formation under BWR Dry Core Conditions", CSARP-Review Meeting, Bethesda, Maryland, May 2-6, 1994.
- /4/ S. Hagen, K. Hain, "Out-of-pile Bundle Experiments on Severe Fuel Damage (CORA-Program): Objectives, Test Matrix and Facility Description", KfK 3677 (1986).

- /5/ S. Hagen, P. Hofmann, G. Schanz, L. Sepold, "Interactions in Zry/UO₂ Fuel Rod Bundles with Inconel Spacers at Temperatures above 1200°C; (Post-test Results of Severe Fuel Damage Experiments CORA-2 and CORA-3)", KfK 4378, (1990).
- /6/ S. Hagen, V. Noack, L. Sepold, P. Hofmann, G. Schanz, G. Schumacher, "Results of SFD Experiments CORA-13 (OECD International Standard Problem 31)", KfK 5054 (1993).
- /7/ J. Burbach, "Ergebnisse von REM-Mikrobereichsanalysen des DWR-Bündelabschmelzexperiments CORA-13", KfK 5162 (1993).
- /8/ S. Hagen, P. Hofmann, V. Noack, G. Schanz, G. Schumacher, L. Sepold; "Behavior of a VVER Fuel Element Tested under Severe Accident Conditions in the CORA Facility (Test Results of Experiment CORA-W1)", KfK 5212 (1994).
- /9/ S. Hagen, P. Hofmann, V. Noack, G. Schanz, G. Schumacher, L. Sepold; "Behavior of a VVER-1000 Fuel Element with Boron /Steel Absorber Tested under Severe Fuel Damage Conditions in the CORA Facility (Results of Experiment CORA-W2)", KfK 5363 (1994).
- /10/ S. Hagen, P. Hofmann, V. Noack, G. Schanz, G. Schumacher, L. Sepold; "BWR Slow Heatup Test CORA-31, Test Results", KfK 5383 (1994).

11. Acknowledgements

Test CORA-33 was included into our program under the special request of the USNRC, as the Dry BWR core conditions are a risk-dominant set of accident scenarios, that had been neglected experimentally. Consequently this test was run in close cooperation with Oak Ridge National Laboratory. The authors would like to express their thanks to Dr. Larry Ott from ORNL, who has supported the planning, performance and evaluation of the test by his fruitful calculations with the ORNL BWR experiment-specific CORA models.

The authors wish to thank Dr. T. Haste, AEA Technology, for his thorough and critical review of this paper.

At the Kernforschungszentrum Karlsruhe support in many fields - needed for preparation, conduct, and evaluation of the experiment - is hereby gratefully acknowledged: The facility was designed by K. Hain and his team. The special bundle setup was arranged by Mr. H.Junker. The test rods were assembled by Mr.E. Mackert, the test bundles by Messrs. H. Gießmann and R. Röder. The

authors would like to thank Messrs. H.Benz, C. Grehl and H.J. Röhling for test preparation and conduct.

Mr.K.P. Wallenfels was responsible for arrangement of camera and video systems and for the preparation of temperature measurements. Messrs. R. Huber and H. Malauscheck prepared and conducted the on-line measurements of the off-gas composition.

The sectioning of the epoxied bundle and the preparation of the metallographic samples was performed by Mr. L. Anselment.

We would like finally to express our gratitude to Mrs. U. Ivanitsch for the careful typing of this report.

12. List of Tables

- Tab. 1: CORA test matrix
- Tab. 2: Design characteristics of bundle CORA-33
- Tab. 3: Total specific mass data of bundle CORA-33
- Tab. 4: Cross-sectional areas of bundle CORA-33
- Tab. 5: Positions of thermocouples
- Tab. 6: List of cross sections of test bundle CORA-33
- Tab. 7: Temperatures at 0 seconds of various components
- Tab. 8: Temperatures at 3000 seconds of various components
- Tab. 9: Distribution of void volumes in unheated and heated rods

Tables

Test CORA-33



Tab. 1: CORA test matrix

Test no.	Max. cladding temperatures	Absorber material	Other test conditions	Date of test
2	≈ 2000°C	-	UO ₂ refer., Inconel spacer	Aug. 6, 1987
3	≈ 2400°C	-	UO ₂ refer., high temperature	Dec. 3, 1987
5	≈ 2000°C	Ag, In, Cd	PWR-absorber	Febr. 26, 1988
12	≈ 2000°C	Ag, In, Cd	quenching	June 9, 1988
16	≈ 2000°C	B ₄ C	BWR-absorber	Nov. 24, 1988
15	≈ 2000°C	Ag, In, Cd	rods with internal pressure	March 2, 1989
17	≈ 2000°C	B ₄ C	quenching	June 29, 1989
9	≈ 2000°C	Ag, In, Cd	10 bar system pressure	Nov. 9, 1989
7	< 2000°C	Ag, In, Cd	<u>57</u> -rod bundle, slow cooling	Febr. 22, 1990
18	< 2000°C	B ₄ C	<u>59</u> -rod bundle, slow cooling	June 21, 1990
13	≈ 2200°C	Ag, In, Cd	OECD/ISP; quench initiation at higher temperature	Nov. 15, 1990
29*	≈ 2000°C	Ag, In, Cd	pre-oxidized,	April 11, 1991
31*	≈ 2000°C	B ₄ C	slow initial heat-up (≈ 0.3 K/s)	July 25, 1991
30*	≈ 2000°C	Ag, In, Cd	slow initial heat-up (≈ 0.2 K/s)	Oct. 30, 1991
28*	≈ 2000°C	B ₄ C	pre-oxidized	Febr. 25, 1992
10	≈ 2000°C	Ag, In, Cd	cold lower end 2 g/s steam flow rate	July 16, 1992
33	≈ 2000°C	B ₄ C	dry core conditions, no extra steam input	Oct. 1, 1992
W1	≈ 2000°C	-	WWER-test	Febr. 18, 1993
W2	≈ 2000°C	B ₄ C	WWER-test with absorber	April 21, 1993

Initial heat-up rate: ≈ 1.0 K/s; steam flow rate, PWR: 6 g/s, BWR: 2 g/s; quench rate (from the bottom) ≈ 1 cm/s

Table 2: Design characteristics of bundle CORA-33

Bundle type	BWR	
Bundle size	18 rods	
Number of heated rods	12	
Number of unheated rods	6	
Pitch	14.3 mm	
Rod outside diameter	10.75 mm	
Cladding material	Zircaloy-4	
Cladding thickness	0.725 mm	
Rod length	- heated rods elevation	1840 mm - 369 to 1471 mm
	- unheated rods elevation	1672 mm - 201 to 1471 mm
Heated pellet stack	0 to 1000 mm	
Heater material	tungsten (W)	
Heater	- length	1000 mm
	- diameter	6 mm
Fuel pellets	- heated rods	UO ₂ annular pellets
	- unheated rods	UO ₂ solid pellets
Pellet stack	- heated rods	0 to 1000 mm
	- unheated rods:	- 200 to 1300 mm
U-235 enrichment	0.2 %	
Pellet outer diameter (nominal)	9.1 mm	
Grid spacer	- material	Zircaloy -4
	- length	42 mm
	- location (upper end)	lower -33 mm center 578 mm top 1167 mm
Shroud	- material	Zircaloy -4
	- wall thickness	1.2 mm
	- outside dimensions	94.4 x 116 mm
	- elevation	40 - 1235 mm

Table 2 (continuation)

Shroud insulation	- material	ZrO ₂ -fibre
	- thickness of insulation	19 mm
	- elevation	40 mm to 1110 mm
Mo electrode	- length	300 mm (upper and lower ends, resp.)
	- diameter	8.6 mm
Cu electrode	- length	189 mm (lower end)
	- length	669 mm (upper end)
	- diameter	8.6 mm
Absorber rod	- number of rods	11
	- material	B ₄ C powder
	- cladding	stainless steel
	- cladding OD	5.8 mm
	- cladding ID	4.6 mm
	- length	1600 mm
Absorber blade	- absorber material	-270 mm to +1300 mm
	- material	stainless steel
	- inside dimensions	76 x 6 mm
Channel box wall	- wall thickness	1 mm
	- material	Zircaloy-4
	- inside dimensions	13 x 92 mm
Plenum Volume	- wall thickness	1.2 mm
	- heated rods	19.8 · 10 ⁻⁶ m ³
	- unheated rods	39.0 · 10 ⁻⁶ m ³

Table 3: Total specific mass data of bundle CORA-28

Specific mass [kg/m]	
Tungsten heater elements	6.55
UO ₂	8.65
Zircaloy in rods	2.70
Absorber, B ₄ C	0.311
Absorber rods , stainless steel	0.852
Absorber blade, stainless steel	1.293
Grid spacer	0.114
Zircaloy of channel box wall *	1.45
Zircaloy of shroud	2.90
Total Zircaloy	7.05

* two walls inside the bundle

Table 4: Areas of bundle CORA-28

Cross sectional areas [m ²]	
Tungsten	3.393·10 ⁻⁴
UO ₂	8.314·10 ⁻⁴
Zircaloy cladding	4.110·10 ⁻⁴
Absorber, B ₄ C	1.828·10 ⁻⁴
Absorber rods , Stainless steel	1.08·10 ⁻⁴
Absorber blade, Stainless steel	1.637·10 ⁻⁴
Zircaloy of channel box wall *	2.21·10 ⁻⁴
Zircaloy of shroud	4.41·10 ⁻⁴
Total area inside the shroud	7.42·10 ⁻³

* two walls inside the bundle

Table 5: Position of Thermocouples

Positions of thermocouples in unheated rods (CORA 33)		
Slot Number	Elevation [mm]	Rod Number
131	1350	6.2
101	1150	2.6
102	1050	6.4
103	950	4.2
104	850	4.6
105	750	2.4
221	550	2.4
222	450	2.6
223	350	4.2
231	250	6.4
232	150	4.6
233	50	6.2
Positions of thermocouples at unheated rods (CORA-33)		
Slot Number	Elevation [mm]	Rod Number
132	1511	2.4
133	1511	6.4
134	1471	2.4
135	1471	6.4
Positions of thermocouples at heated rods (CORA-33)		
Slot Number	Elevation [mm]	Rod Number
136	1511	3.5
137	1471	3.5
106	1150	1.7
107	950	3.5
108	750	5.3
224	550	5.3
225	350	3.5
226	150	1.7
234	50	7.1
Positions of thermocouples in absorber blade (CORA-33)		
Slot Number	Elevation [mm]	Direction of TE
109	1350	300°
110	1250	120°
111	1150	120°
112	1050	120°
113	950	300°
114	850	300°
115	750	120°
227	550	120°
Positions of thermocouples in absorber blade (CORA-33)		
Slot Number	Elevation [mm]	Direction of TE
228	450	120°
229	350	300°
230	250	300°
241	150	120°
235	50	120°
Positions of thermocouples at inside shroud (CORA-33)		
Slot Number	Elevation [mm]	Direction of TE
250	550	78°
251	450	250°
252	350	48°
253	150	190°
Positions of thermocouples shroud outer surface		
Slot Number	Elevation [mm]	Direction of TE
128	1150	75°
129	950	255°
130	750	255°
247	550	255°
248	350	255°
249	150	75°
264	50	75°
Positions of thermocouples at the Channel Box Wall		
Slot Number	Elevation [mm]	Direction of TE
118	1150	120°
119	950	300°
120	750	300°
242	550	120°
243	350	300°
244	150	300°
261	50	180°
Positions of thermocouples in ceramic tube(CORA-33)		
Slot Number	Elevation [mm]	Direction of TE
121	950	120°
122	950	340
123	750	300°
124	750	165°
Positions of thermocouples at the grid spacer (CORA-33)		
Slot Number	Elevation [mm]	Direction of TE
126	1146	10°
127	1146	190°
245	557	10°
246	557	190°
262	-54	10°
263	-54	190°
Positions of thermocouples steam distribution tube		
Slot Number	Elevation [mm]	Direction of TE
62	-300	180°
276	-250	300°
266	0	180°
267	0	180°
268	-50	15°
269	-50	195°
270	-50	165°
271	-50	345°

Table 6: List of cross sections for test bundle CORA-33

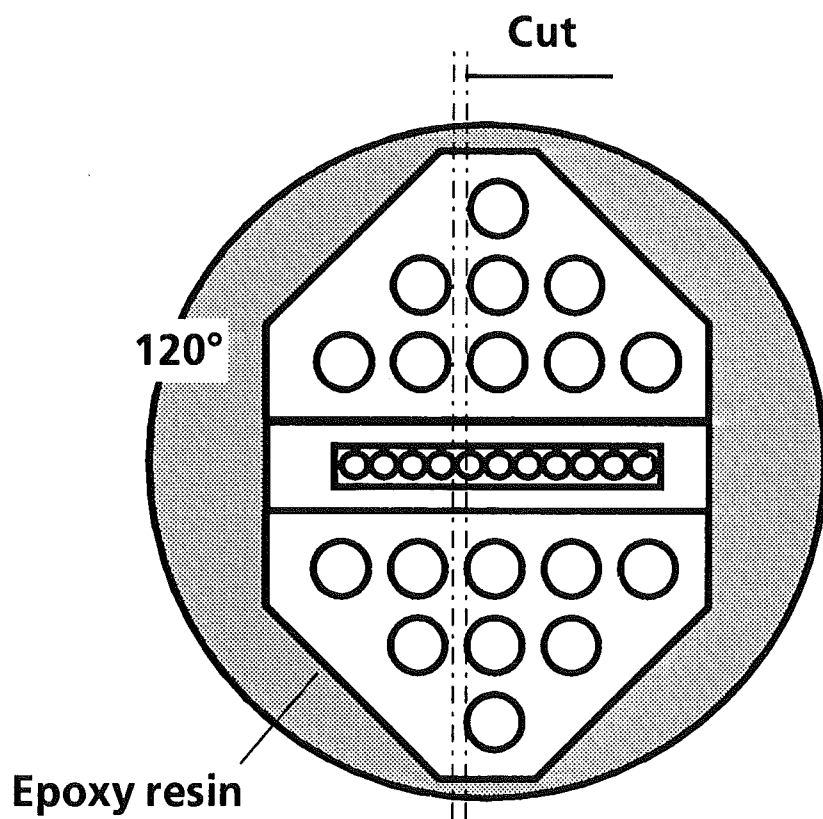
Sample	Sample length	Elevation bottom	Elevation top	Remarks
33-a	110 mm	-212 mm	-102 mm	Additional vertical cut
Cut	2 mm			
33-b	50 mm	-100 mm	-50 mm	Additional vertical cut
Cut	2 mm			Lower grid spacer
33-01	13 mm	-48 mm	-35 mm	Top polished
Cut	2 mm			
33-c	33 mm	-33 mm	0 mm	
Cut	2 mm			
33-x	15 mm	2 mm	17 mm	Top polished
Cut	2 mm			
33-d	50 mm	19 mm	69 mm	
Cut	2 mm			
33-e	50 mm	71 mm	121 mm	
Cut	2 mm			
33-02	13 mm	123 mm	136 mm	Bottom polished
Cut	2 mm			
33-f	50 mm	138 mm	188 mm	
Cut	2 mm			
33-g	50 mm	190 mm	240 mm	
Cut	2 mm			
33-03	13 mm	242 mm	255 mm	Top polished
Cut	2 mm			
33-h	50 mm	257 mm	307 mm	
Cut	2 mm			
33-i	50 mm	309 mm	359 mm	
Cut	2 mm			

Table 6: ctd

33-04	13 mm	361 mm	374 mm	Top polished
Cut	2 mm			
33-J	50 mm	376 mm	426 mm	
Cut	2 mm			
33-k	50 mm	428 mm	478 mm	
Cut	2 mm			
33-l	50 mm	480 mm	530 mm	
Cut	2 mm			Central grid spacer
33-05	13 mm	532 mm	545 mm	Top polished
Cut	2 mm			
33-m	50 mm	547 mm	597 mm	
Cut	2 mm			
33-n	50 mm	599 mm	649 mm	
Cut	2 mm			
33-o	50 mm	651 mm	701 mm	
Cut	2 mm			
33-p	50 mm	703 mm	753 mm	
Cut	2 mm			
33-06	13 mm	755 mm	768 mm	Top polished
Cut	2 mm			
33-q	50 mm	770 mm	820 mm	
Cut	2 mm			
33-r	50 mm	822 mm	872 mm	
Cut	2 mm			
33-s	50 mm	874 mm	924 mm	
Cut	2 mm			
33-t	50 mm	926 mm	976 mm	

Table 6: ctd

Cut	2 mm			
33-07	13 mm	978 mm	991 mm	Top polished
Cut	2 mm			
33-u	50 mm	993 mm	1043 mm	
Cut	2 mm			
33-v	100 mm	1045 mm	1145 mm	
Cut	2 mm			Upper grid spacer
33-08	13 mm	1147 mm	1160 mm	Top polished
Cut	2 mm			
33-w	xxx mm	1162 mm	xxxx mm	Upper remnant



Vertical cuts through sections CORA-33a and CORA-33b

Table 7: Temperatures [°C] in CORA-33 test at 0 second for various components

Elevation [mm]	Components						
	Heated rod	Unheated rod	Absorber blade	Channel box wall	Shroud	Shroud insulation	HTS 153 mm
1511	25	21					
1471	43	44					
1350		62	65				
1250			161				72
1150	248	271	241	253	191		92
1050		299	262				93
950	281	323	274	296	275	118	91
850		270	284				87
750	338	308	296	313	275	111	85
650						126	84
550	380	340	341	357	332	117	82
450		343	355			124	80
350	340	405	368	387	352	113	75
250		405	373				71
150	362	333	401	417	343	126	68
50	368	426	405	450	343	57	73
-50							62

Table 8: Temperatures [°C] in CORA-33 test at 3000 seconds for various components

Elevation [mm]	Components						
	Heated rod	Unheated rod	Absorber blade	Channel box wall	Shroud	Shroud insulation	HTS 153 mm
1511	26	20					
1471	47	42					
1350		69	61				
1250			167				80
1150	312	334	281	297	230		103
1050		357	317				100
950	374	381	330	348	322	133	96
850		341	337				94
750	396	380	347	360	312	119	92
650						138	89
550	439	401	388	384	366	122	88
450		396	393			134	84
350	403	433	401	412	354	120	79
250		399	399				74
150	396	369	420	424	353	130	73
50	385	421	412	428	330	56	76
-50							65

Table 9: Distribution of void volumes in unheated and heated rods

Void volume of one unheated rod

	Elevation [mm]	Volume [cm ³]	Relative volume [cm ³ /cm]
Dishing of uranium pellets; gap between pellet stack and cladding	-201 to 1315	4.083	0.027
Void volume above pellet stack	1315 to 1439	8.378	0.678
	1439 to 1456	0.711	0.419
	1456 to 1522	3.658	0.55
	1522 to 1531	0.387	0.43
	1531 to 1762	6.531	0.283
	1762 to 1764	0.084	0.419
System for pressure measurement		15.120	
Total void volume		38.952	

Void volume of one heated rod

	Elevation [mm]	Volume [cm ³]	Relative volume [cm ³ /cm]
Void volume below pellet stack	-369 to -334	0.826	0.236
	-334 to 0	1.391	0.0417
Gap between pellet stack and cladding and between pellet stack and heater	0 to 1024	2.311	0.023
void above pellet stack	1024 to 1875	3.545	0.0417
	1875 to 1911	0.852	0.24
System for pressure measurement		10.860	
Total void volume		19.785	

List of Figures

- Fig. 1 : SFD Test Facility, simplified flow diagram
- Fig. 2 : SFD Test Facility CORA; Main Components
- Fig. 3 : CORA Bundle Arrangment
- Fig. 4 : Horizontal cross section of the high temperature shield
- Fig. 5a : Bundle arrangement
- Fig. 5b : CORA bundle components
- Fig. 5c : Positions of view ports in the shroud
- Fig. 6a : Videoscope system for the CORA test bundle
- Fig. 6b : Hydrogen measurement
- Fig. 7 : System overpressure, argonflow and power
- Fig. 8 : Argonflow through bundle and videoscopes
- Fig. 9 : System overpressure
- Fig. 10 : Electric power input
- Fig. 11 : Voltage input for the 3 rod groups
- Fig. 12 : Comparison of chemical and electric power
- Fig. 13 : Energy input
- Fig. 14 : Total current
- Fig. 15 : Resistance of bundle (voltage group1/total current)
- Fig. 16 : Resistance of rod groups
- Fig. 17 : Variation of currents within the rod groups
- Fig. 18 : Resistance of single rods (group 1)
- Fig. 19 : Resistance of single rods: (group 2)
- Fig. 20 : Resistance of single rods: (group 3)

- Fig. 21a : Water temperature in the quench cylinder at -250 and -300 mm
- Fig. 21b : Evaporation rate of water from quench cylinder determined by measured water level change
- Fig. 22 : Temperatures at the steam distribution tube at -50mm elevation
- Fig. 23 : Temperatures at steam inlet
- Fig. 24 : Thermocouple locations within the bundle (CORA-33)
- Fig. 25 : Temperatures on heated rods
- Fig. 26 : Temperatures in unheated rods
- Fig. 27 : Temperatures on the channel box walls
- Fig. 28 : Temperatures in the absorberblade
- Fig. 28b : Temperatures at the absorberblade
- Fig. 29 : Temperatures measured with ceramic protected TCs
- Fig. 30 : Temperatures on the spacers
- Fig. 31 : Location of thermocouples at shroud and shroud insulation (CORA-33)
- Fig. 32 : Temperatures on the inner side of shroud
- Fig. 33 : Temperatures on the shroud
- Fig. 34 : Temperatures on shroud insulation
- Fig. 35 : Gastemperatures in the upper part of the bundle
- Fig. 36 : Temperatures at the bundle head plate
- Fig. 37 : Temperatures at fixed elevation (1511, 1491, 1471)
- Fig. 38 : Temperatures at fixed elevation (1400, 1350, 1250, 1150, 1146)
- Fig. 39 : Temperatures at fixed elevation (1050, 950)
- Fig. 40 : Temperatures at fixed elevation (850, 750)
- Fig. 41 : Temperatures at fixed elevation (650, 557, 550)

- Fig. 42 : Temperatures at fixed elevation (450, 350)
- Fig. 43 : Temperatures at fixed elevation (150, 50)
- Fig. 44 : Temperatures at fixed elevation (0, -50, -54)
- Fig. 45 : Best estimate bundle temperatures at different elevations
- Fig. 46 : Best estimate axial distribution of bundle temperatures
- Fig. 47 : Comparison of temperatures and hydrogen production for test CORA-33 and CORA-31
- Fig. 48 : Test conduct of CORA-31
System overpressure , argonflow, steam input and power
- Fig. 49a : Position of thermocouples in the high temperature shield (CORA-33)
- Fig. 49b : Locations of thermocouples in the high temperature shield (CORA-33)
- Fig. 50 : Temperatures of HTS, Temperature on inner surface, 153 mm radius (345°)
- Fig. 51 : Temperatures of HTS, Comparison on inner surface at 153 mm radius; 550mm elevation
- Fig. 52 : Temperatures of HTS, Comparison on inner surface at 153 mm radius; 950mm elevation
- Fig. 53 : Temperatures of HTS, Comparison on inner surface at 153 mm radius; 50 mm elevation
- Fig. 54 : Temperatures of HTS, Temperatures on inner surface; 153 mm radius (345°)
- Fig. 55 : Temperatures of HTS, Temperatures in HT-shield; 172 mm radius (345°)
- Fig. 56 : Temperatures of HTS, Temperatures in HT-shield; 192 mm radius (345 °)
- Fig. 57 : Temperatures of HTS, Temperatures in HT-shield; 255 mm radius (345°)
- Fig. 58 : Temperatures of HTS, Temperatures in HT-shield; 293 mm radius (345°)
- Fig. 59 : Temperatures of HTS, Temperatures in HT-shield; 380 mm radius

- Fig. 60 : Temperatures of HTS, Radial dependence at 950 mm elevation
- Fig. 61 : Temperatures of HTS, Radial dependence at 550 mm elevation
- Fig. 62 : Temperatures of HTS, Radial dependence at 50 mm elevation
- Fig. 63 : Axial temperature distribution of bundle, on shroudinsulation and on inner side of HTS
- Fig. 64a : Hydrogen production rate
- Fig. 64b : Chemical power due to corrected hydrogen measurement
- Fig. 65 : Comparison of hydrogen production for CORA-33 and CORA-31
- Fig. 66 : Comparison of electric and chemical power test CORA-33 and CORA-31
- Fig. 67 : Internal pressure of fuel rod simulators
- Fig. 68 : Determination of failure time by pressure loss measurement
- Fig. 69 : Temperatures at time of pressure loss
- Fig. 70 : Irregularities in the absorberblade temperatures used for estimation of absorber failure
- Fig. 71 : Irregularities in the absorberblade temperatures used for estimation of absorber failure
- Fig. 71a : Irregularities in the absorberblade temperatures used for estimation of absorber failure
- Fig. 71b : Irregularities in the absorberblade temperatures used for estimation of absorber failure
- Fig. 71c : Irregularities in the absorberblade temperatures (detection of further melt relocation)
- Fig. 71d : Irregularities in the absorberblade temperatures (detection of further melt relocation)
- Fig. 72 : Smooth temperature increase in unheated rods for comparison to irregularities in temperatures of the absorber blade (see Fig. 70, 71)
- Fig. 73 : Epoxying process of the tested bundle
- Fig. 74 : Axial distribution of epoxy bundle fill-up

- Fig. 75 : Axial distribution of bundle segments filled with epoxy
- Fig. 76 : Axial distribution of blocked area inside the shroud
- Fig. 77 : Axial mass distribution
- Fig. 78 : Axial volume distribution after the test and axial temperature distribution during the test
- Fig. 79 : Axial mass distribution after the test and axial temperature distribution during the test
- Fig. 80 : CORA-31:Axial volume distribution after the test and axial temperature distribution during the test
- Fig. 81 : Comparison of axial volume distribution for test CORA-33 and CORA-31
- Fig. 82 : Post test appearance of bundle CORA-33 with shroud insulation
- Fig. 83 : Inner side of shroud insulation after the test (Total view)
- Fig. 84 : Inner side of shroud insulation 30° und 120°; 1160-900 mm, partial view
- Fig. 85 : Inner side of shroud insulation 30° und 120°; 900-640 mm, partial view
- Fig. 86 : Inner side of shroud insulation 30° und 120°; 700-440mm, partial view
- Fig. 87 : Inner side of shroud insulation 30° und 120°; 400-140 mm, partial view
- Fig. 88 : Inner side of shroud insulation 210° und 300°; 1160-900 mm, partial view
- Fig. 89 : Inner side of shroud insulation 210° und 300°; 920-660 mm, partial view
- Fig. 90 : Inner side of shroud insulation 210° und 300°; 700-440 mm, partial view
- Fig. 91 : Inner side of shroud insulation 210° und 300°; 400-120 mm, partial view
- Fig. 92 : Post test view of bundle CORA-33 after partial removal of shroud (Total view)

- Fig. 93 : Post test view of bundle, 30° partial view, 1370-1110 mm
- Fig. 94 : Post test view of bundle, 30° partial view, 1120-860 mm
- Fig. 95 : Post test view of bundle, 30° partial view, 870-620 mm
- Fig. 96 : Post test view of bundle, 30° partial view, 620-370 mm
- Fig. 97 : Post test view of bundle, 30° partial view, 380-130 mm
- Fig. 98 : Post test view of bundle, 30° partial view, 210 to -40 mm
- Fig. 99 : Post test view of bundle, 120° partial view, 1360-1100 mm
- Fig. 100 : Post test view of bundle, 120° partial view, 1130-870 mm
- Fig. 101 : Post test view of bundle, 120° partial view, 930-670 mm
- Fig. 102 : Post test view of bundle, 120° partial view, 700-450 mm
- Fig. 103 : Post test view of bundle, 120° partial view, 470-210 mm
- Fig. 104 : Post test view of bundle, 210° partial view, 1370-1090mm
- Fig. 105 : Post test view of bundle, 210° partial view, 1150-870 mm
- Fig. 106 : Post test view of bundle, 210° partial view, 920-650 mm
- Fig. 107 : Post test view of bundle 210° partial view, 680-400 mm
- Fig. 108 : Post test view of bundle 210° partial view, 450-180 mm
- Fig. 109 : Post test view of bundle 210° partial view, 230 to -50 mm
- Fig. 110 : Horizontal cross sections of bundle CORA-33, top view
- Fig. 111 : Vertical cross sections of bundle CORA-33, -100 to 200 mm
- Fig. 112 : Horizontal cross sections of the absorber region of bundle CORA-33

Appendix A:

- Fig. A1 : Argon input prior to test CORA-33
- Fig. A2 : Temperature at the entrance of the bundle prior to test

- Fig. A3 : Power input during the pre-heat phase
- Fig. A4 : Resistance during the pre-heat phase
- Fig. A5 : Temperatures on heated rods; pre-heat phase
- Fig. A6 : Temperatures in unheated rods; pre-heat phase
- Fig. A7 : Temperatures on the channel box walls; pre-heat phase
- Fig. A8 : Temperatures in the absorberblade
- Fig. A9 : Temperatures measured with ceramic protected TCs;
pre-heat phase
- Fig. A10 : Temperatures at the spacer; pre-heat phase
- Fig. A11 : Temperatures on the inner side of shroud; pre-heat phase
- Fig. A12 : Temperatures on outer side of shroud; pre-heat phase
- Fig. A13 : Temperatures on shroud insulation; pre-heat phase
- Fig. A14 : Gas temperature in the upper part of the bundle; pre heat phase
- Fig. A15 : Temperature at the bundle head plate; pre heat phase
- Fig. A16 : Temperatures in the steam tube; pre-heat phase

Appendix B:

- Fig. B1 : Horizontal cross sections of bundle CORA-33;
1160, 1147, 1145 mm
- Fig. B2 : Horizontal cross sections of bundle CORA-33,
1045, 1043, 993, 991 mm
- Fig. B3 : Horizontal cross sections of bundle CORA-33,
978, 976, 926, 924 mm
- Fig. B4 : Horizontal cross sections of bundle CORA-33,
874, 872, 822, 820 mm
- Fig. B5 : Horizontal cross sections of bundle CORA-33,
770, 768, 755, 753 mm

Fig. B6 : Horizontal cross sections of bundle CORA-33,
703, 701, 651, 649 mm

Fig. B7 : Horizontal cross sections of bundle CORA-33,
599, 597, 547, 545 mm

Fig. B8 : Horizontal cross sections of bundle CORA-33,
532, 530, 480, 478 mm

Fig. B9 : Horizontal cross sections of bundle CORA-33,
428, 426, 376, 374 mm

Fig. B10 : Horizontal cross sections of bundle CORA-33,
361, 359, 309, 307 mm

Fig. B11 : Horizontal cross sections of bundle CORA-33,
257, 255, 242, 240 mm

Fig. B12 : Horizontal cross sections of bundle CORA-33,
190, 188, 138, 136 mm

Fig. B13 : Horizontal cross sections of bundle CORA-33; 123,
121, 71, 69 mm

Fig. B14 : Horizontal cross sections of bundle CORA-33; 19, 17, 2, 0 mm

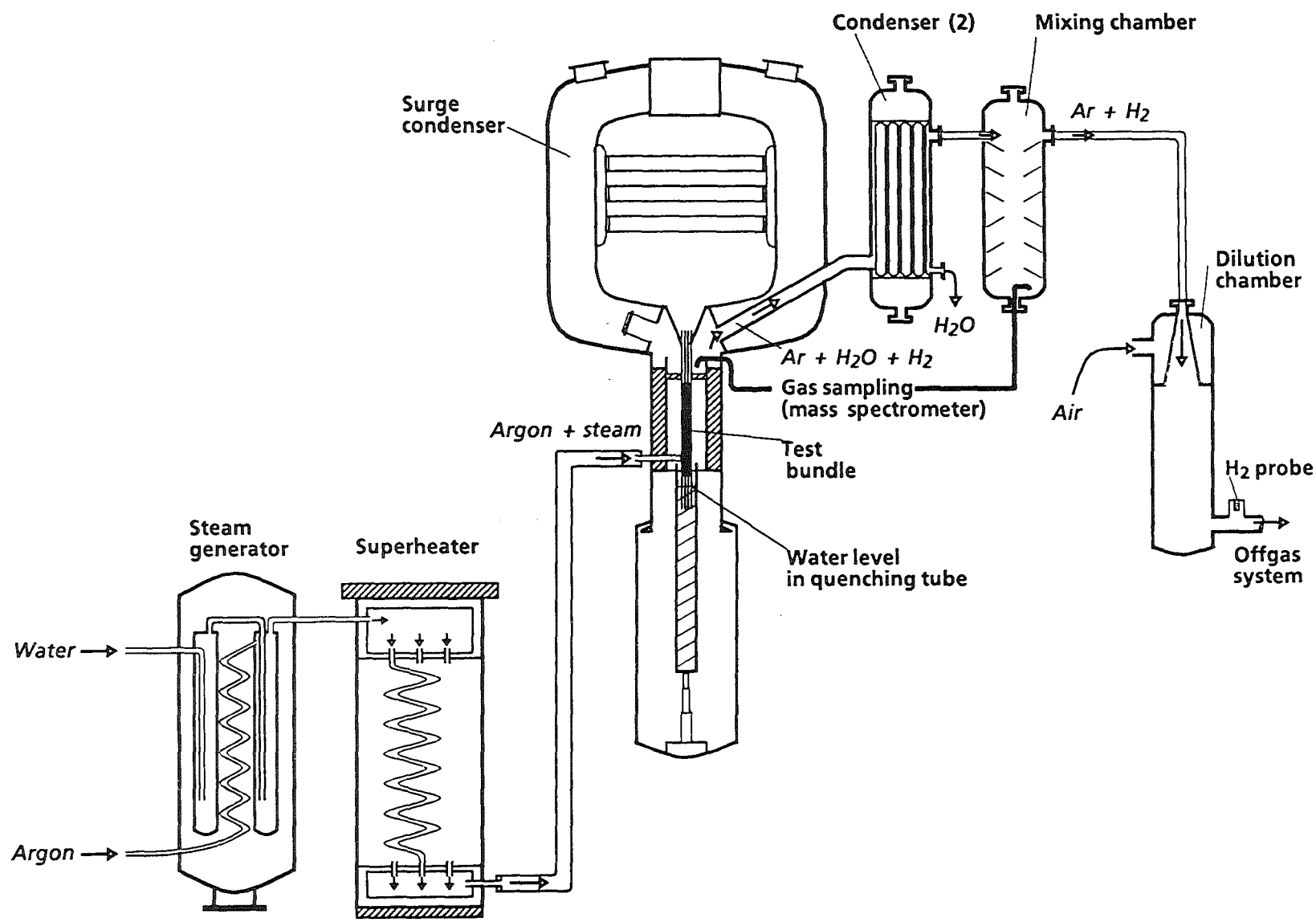
Fig. B15 : Horizontal cross sections of bundle CORA-33; -33, -35, -48,
50 mm

Fig. B16 : Horizontal cross sections of bundle CORA-33;
100, -102, -212 mm

Figures

Test CORA-33

Fig. 1: SFD Test Facility (Simplified flow diagram)



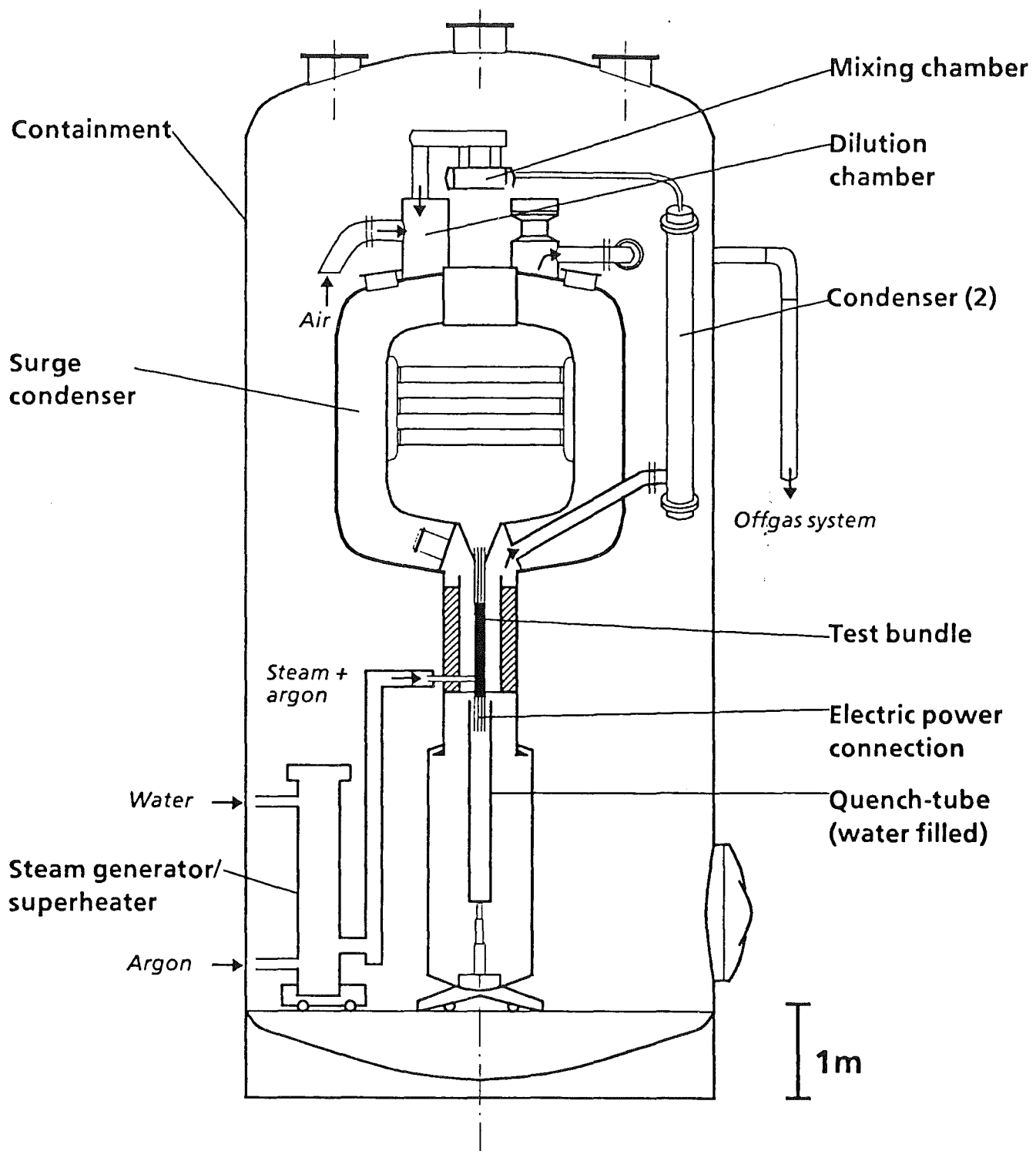


Fig. 2: SFD Test Facility CORA (Main components)

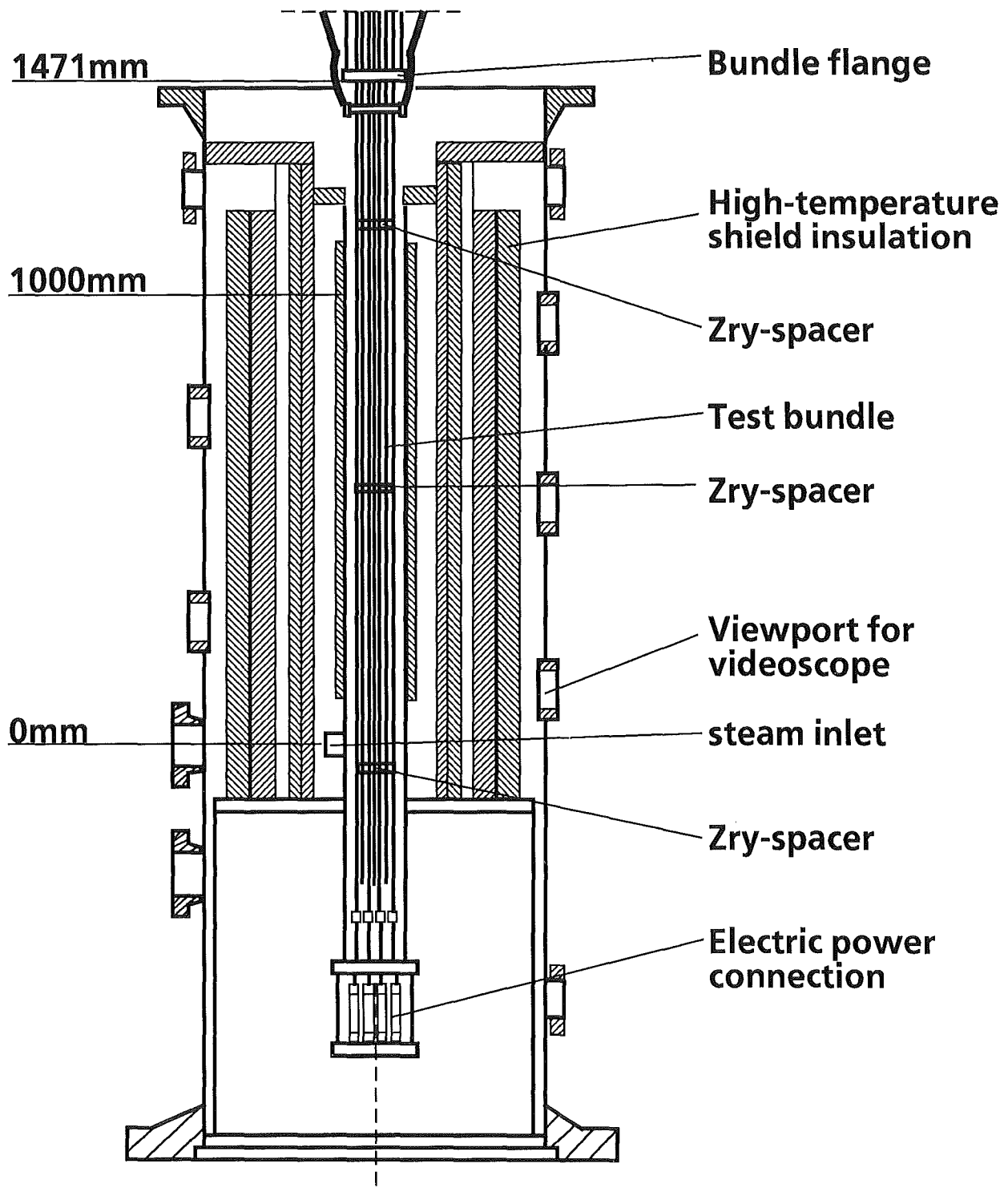


Fig. 3: CORA bundle arrangement

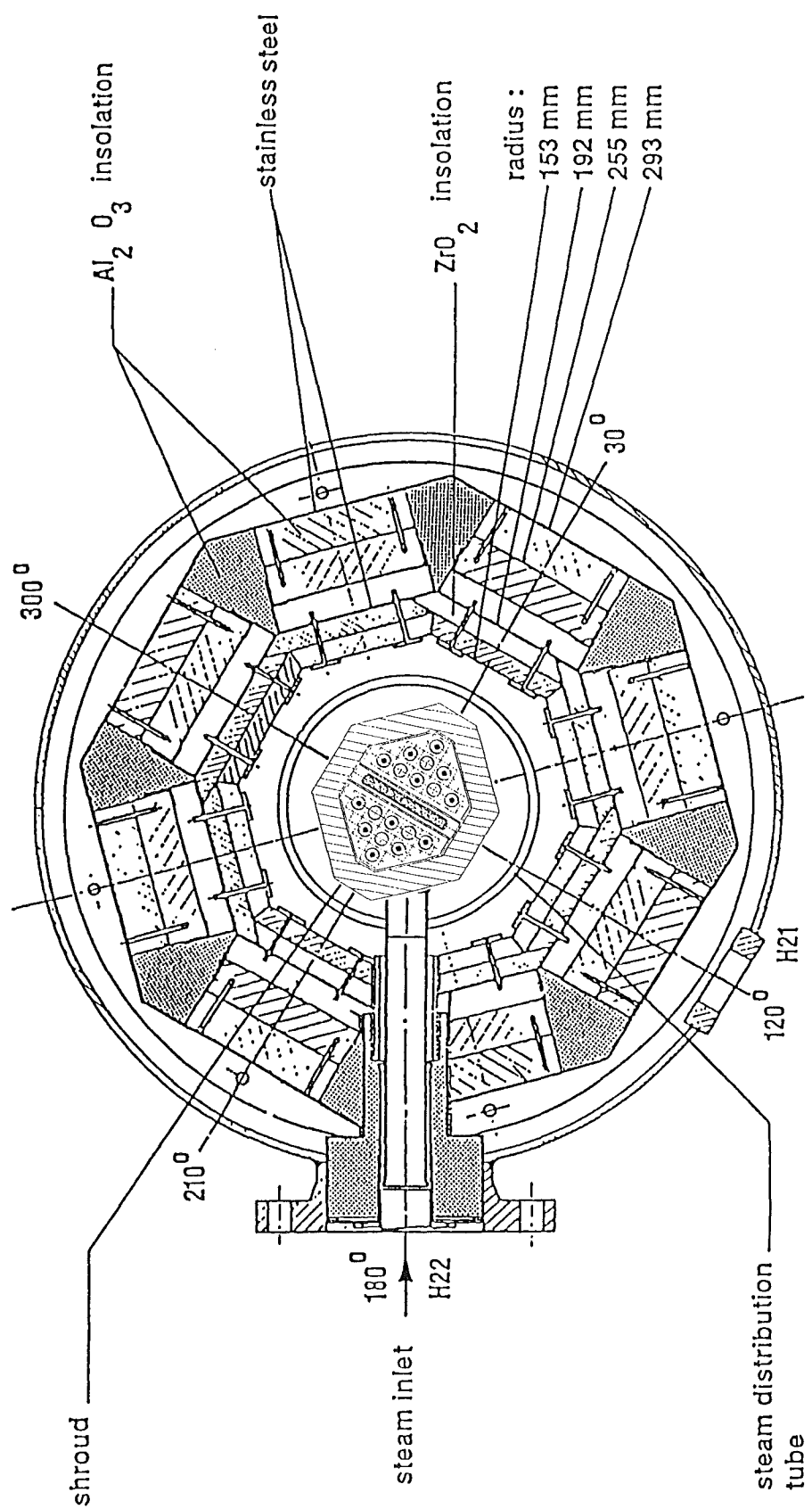


Fig. 4: Horizontal cross section
of the high temperature shield

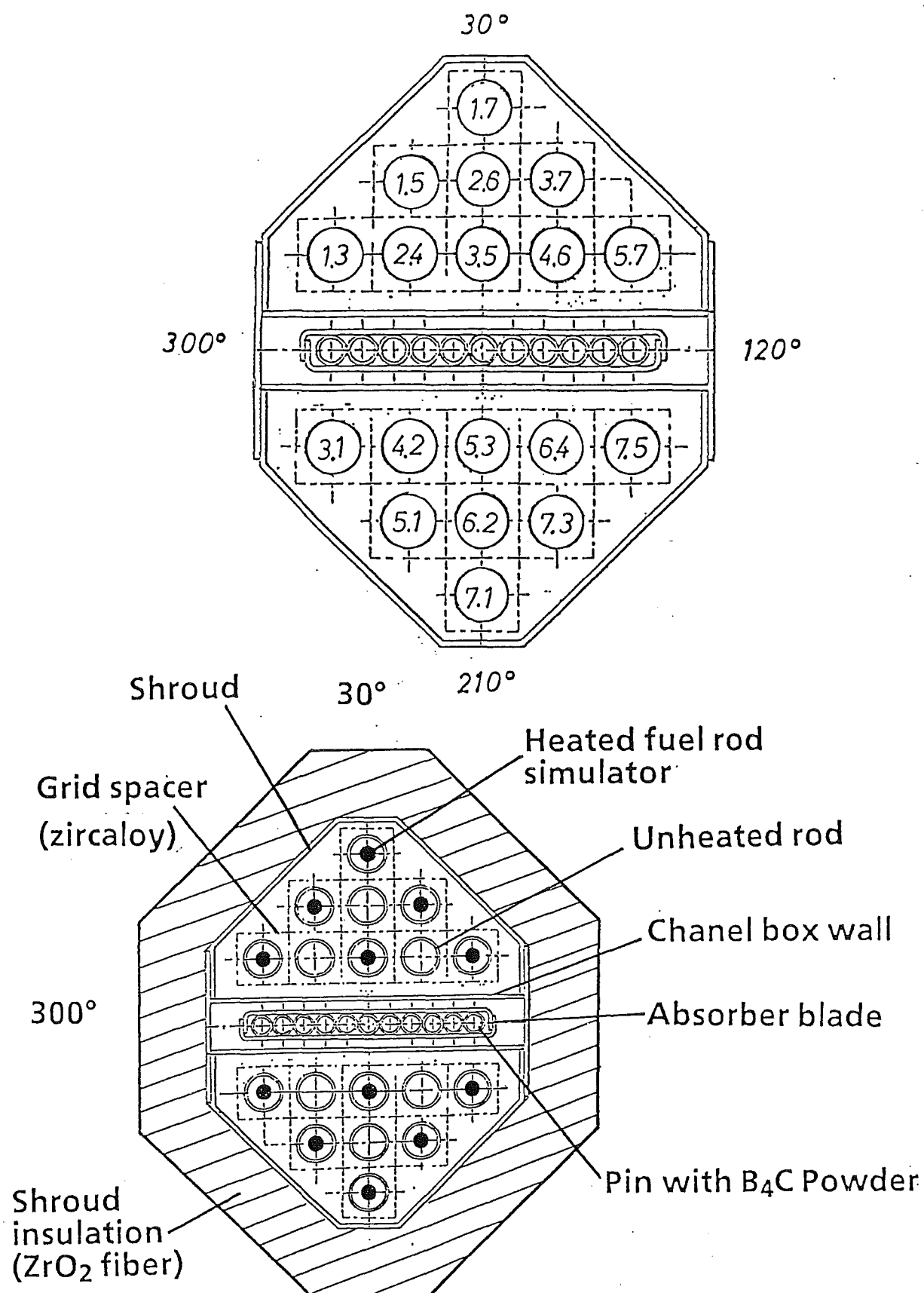


Fig. 5a: Bundle arrangement

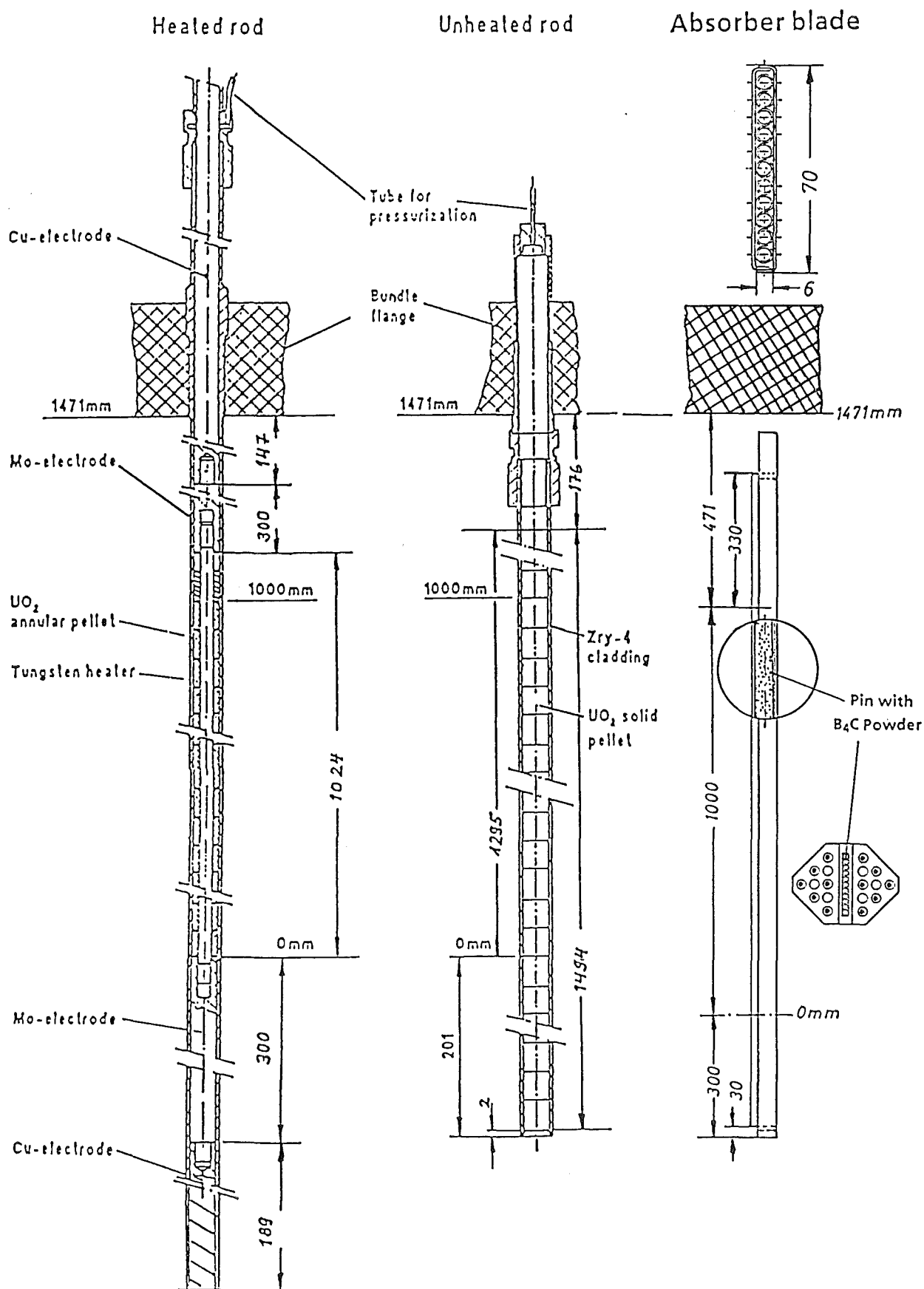


Fig. 5b: CORA bundle components



Fig. 5c: CORA-33: Positions of view ports in the shroud

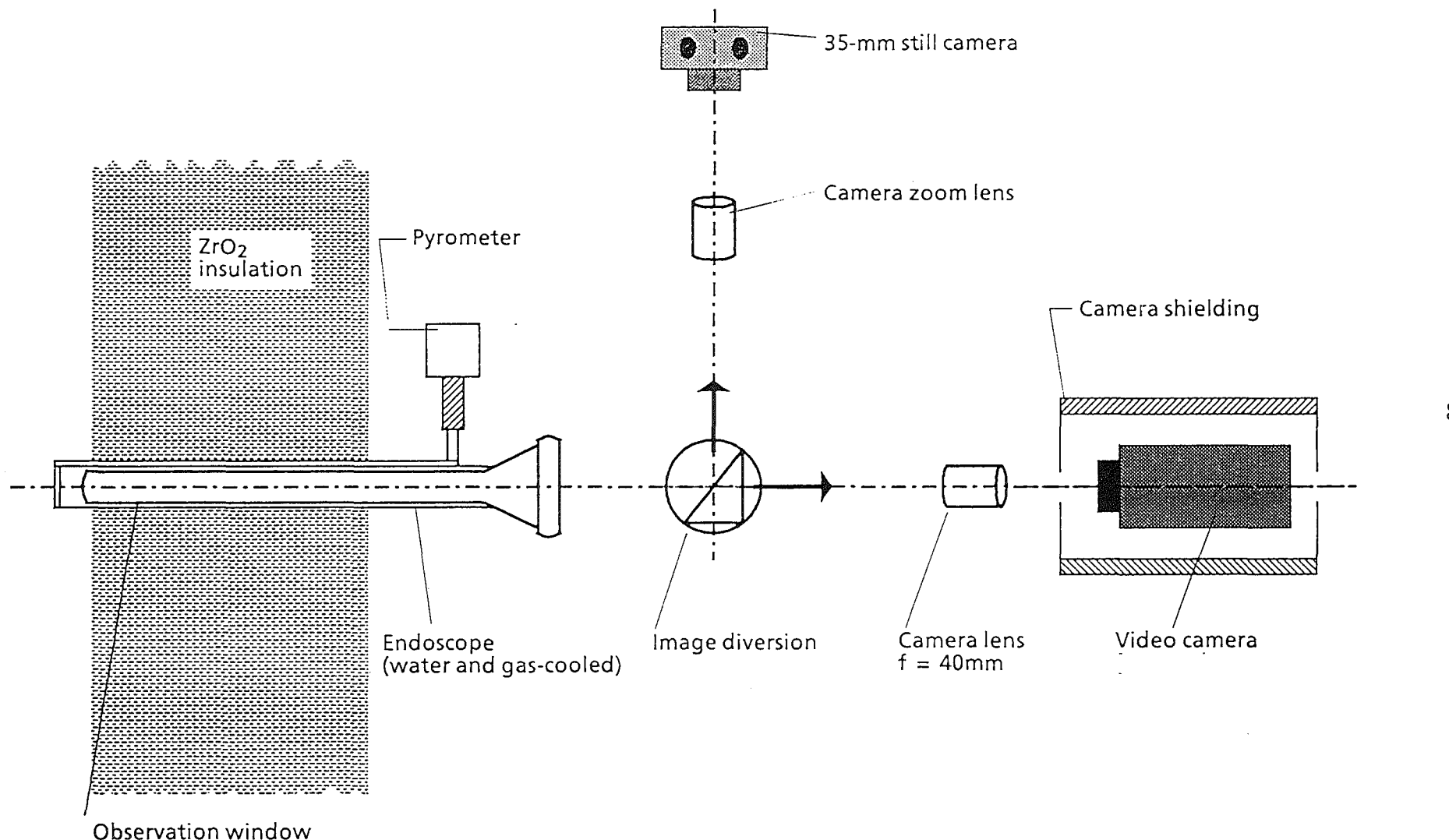
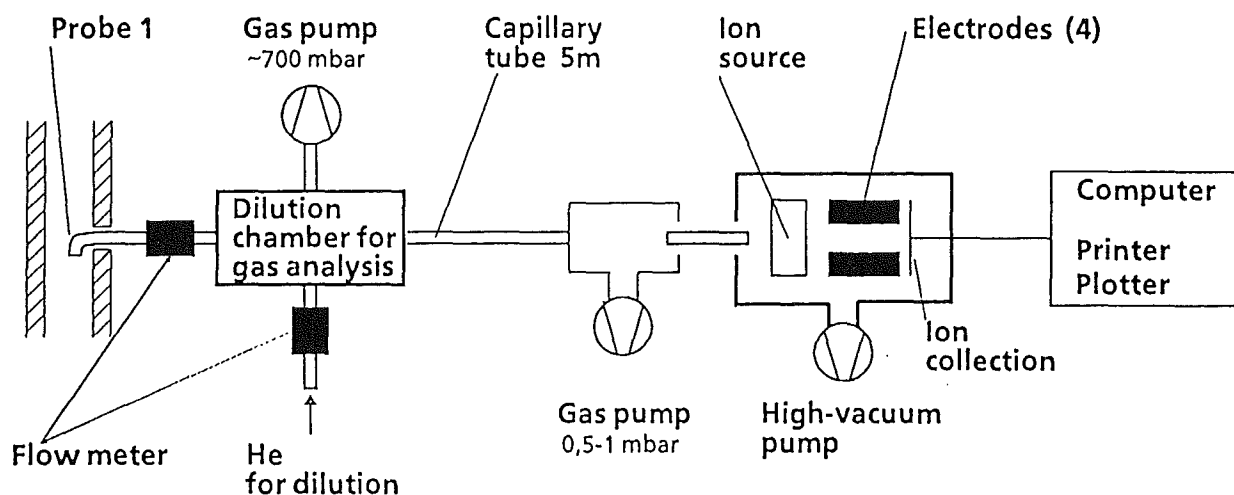
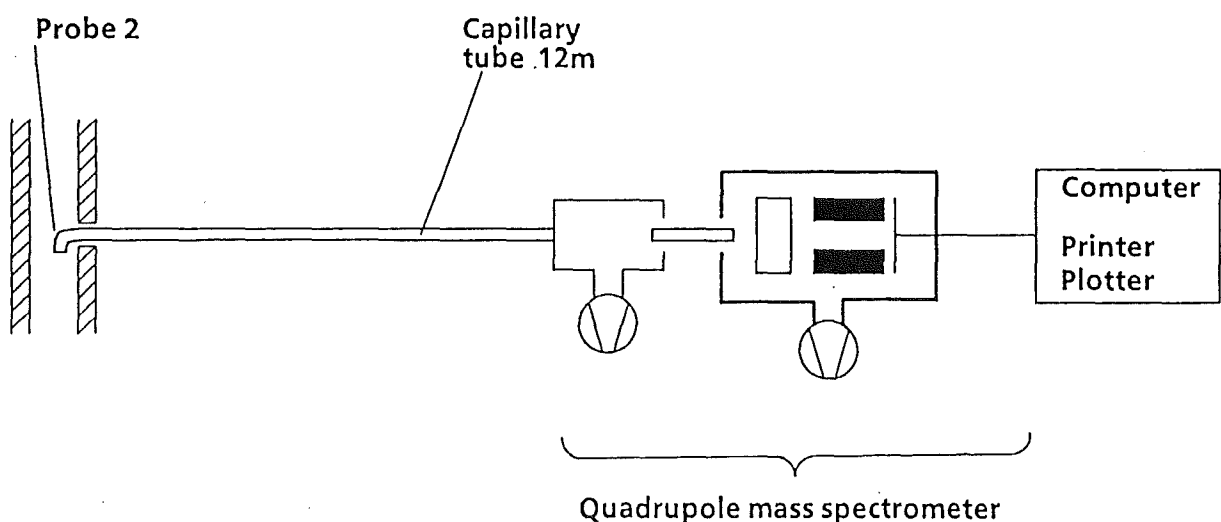


Fig. 6a: **Videoscope system for the CORA test bundle**

(a)



(b)

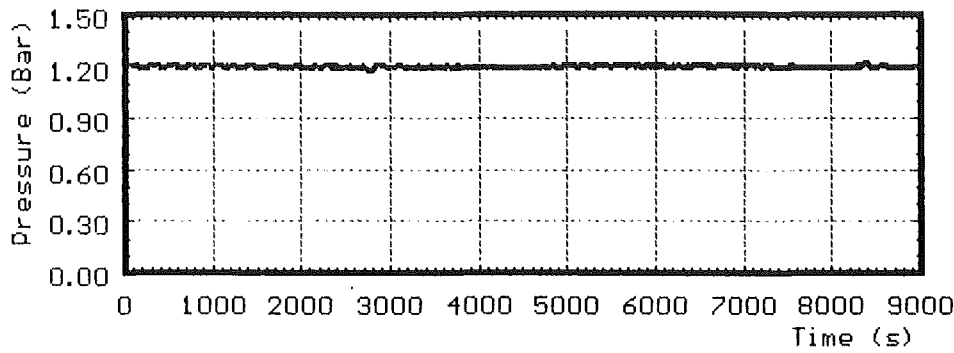


Location (a) : Outlet of test section

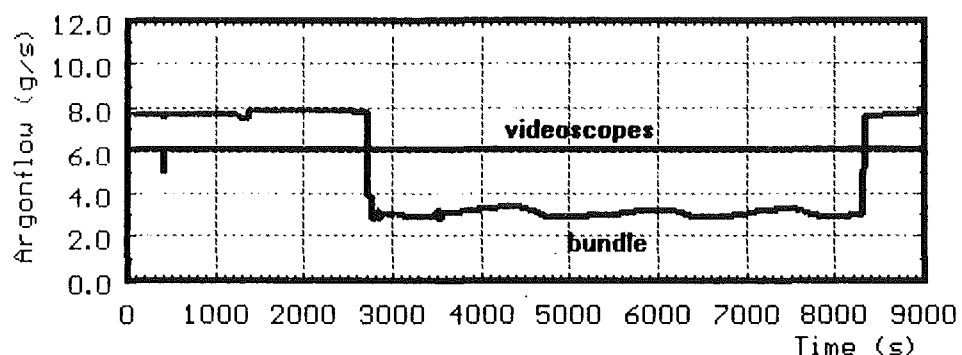
Location (b) : Mixing chamber

Fig. 6b: Hydrogen measurement

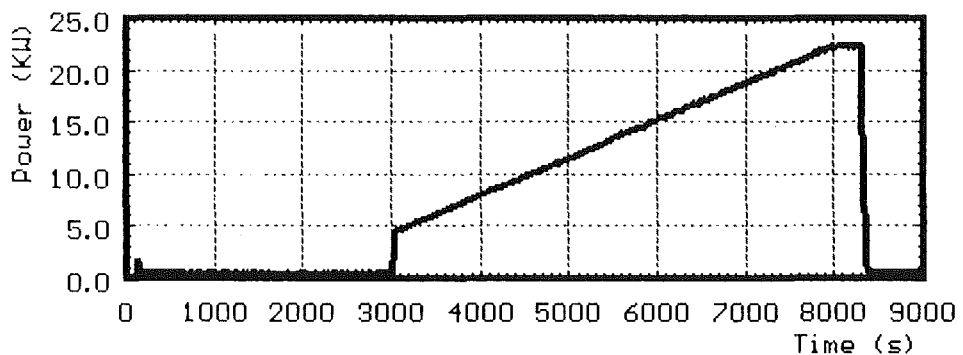
CORA - 33 :



system
overpressure



argonflow



power

No extra steam input

Fig. 7: System overpressure, Argonflow and power

CORA-33:

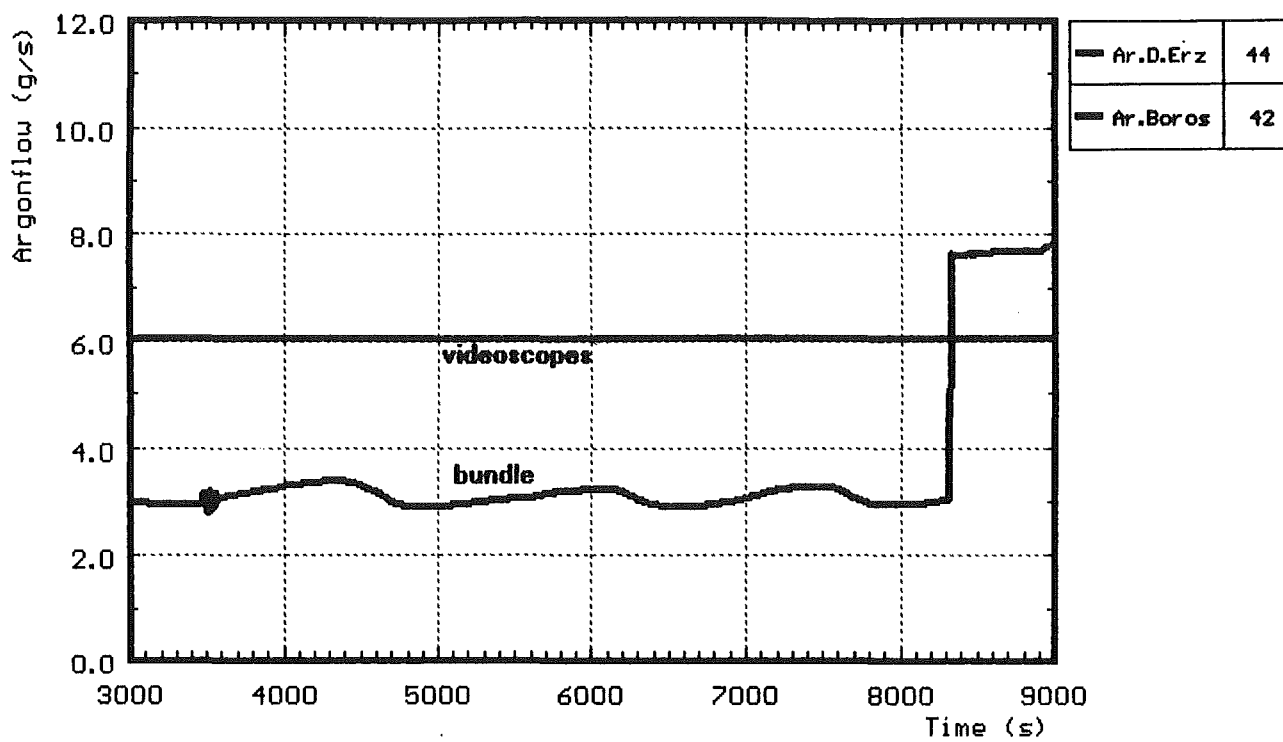


Fig. 8: Argon flow through bundle and videoscopes

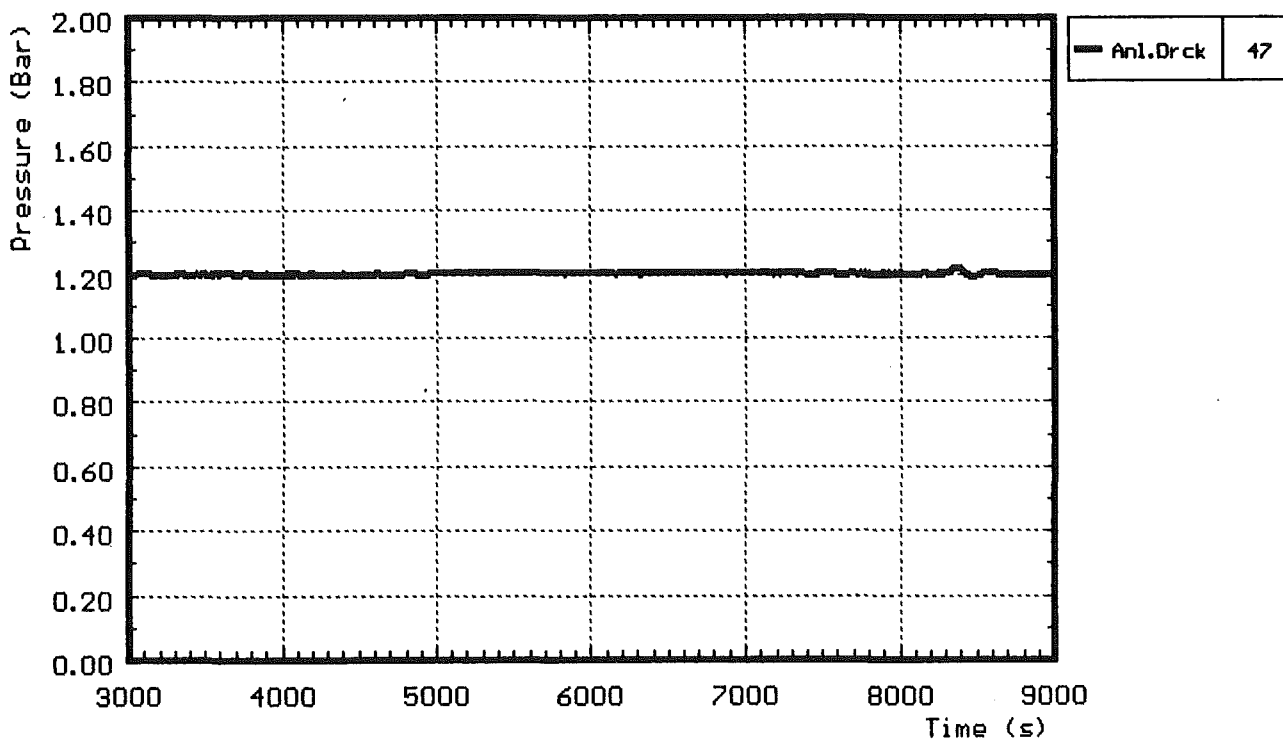


Fig. 9: System overpressure

CORA-33:

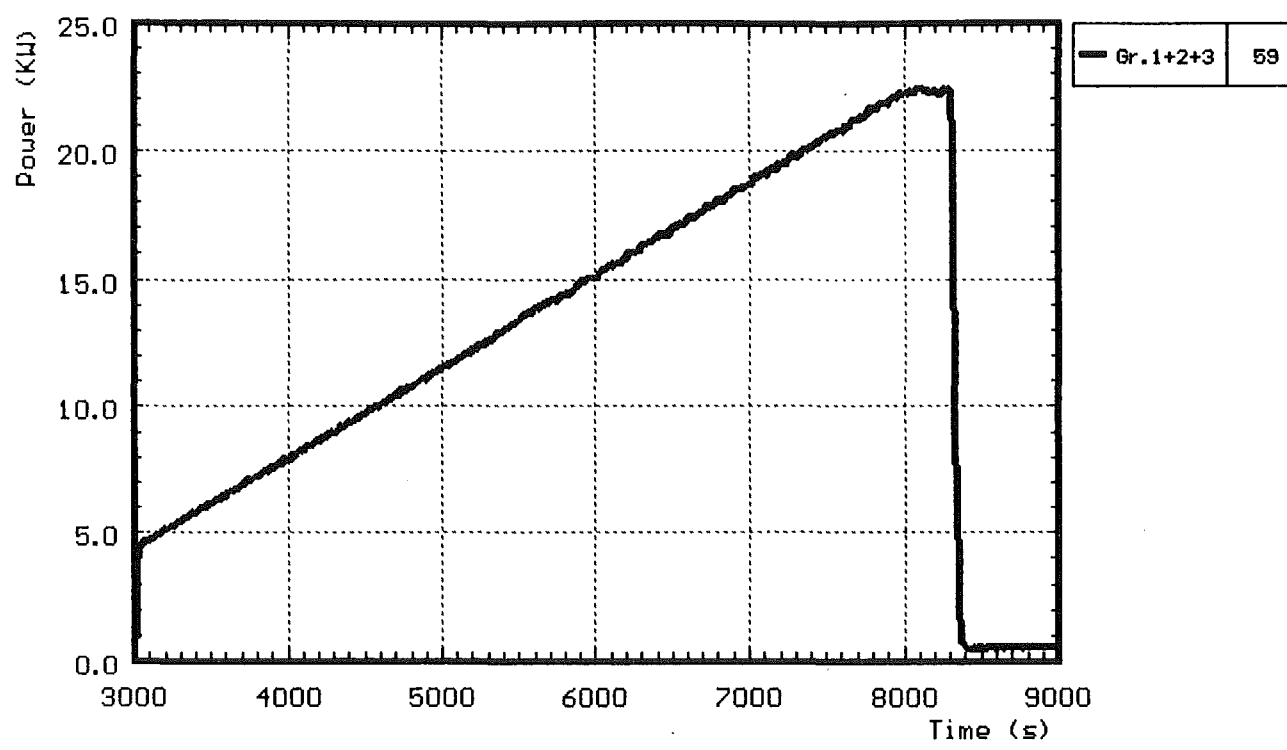


Fig. 10: Electric power input

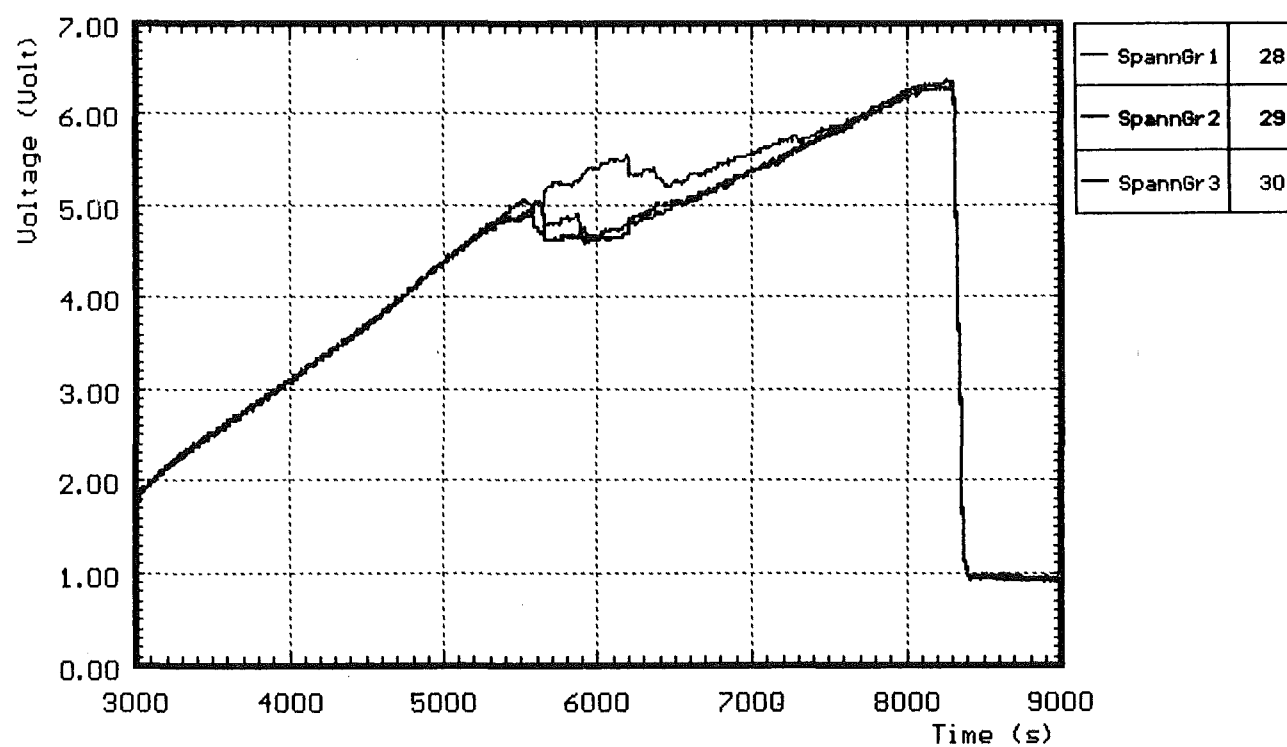


Fig. 11: Voltage input for the 3 rod groups

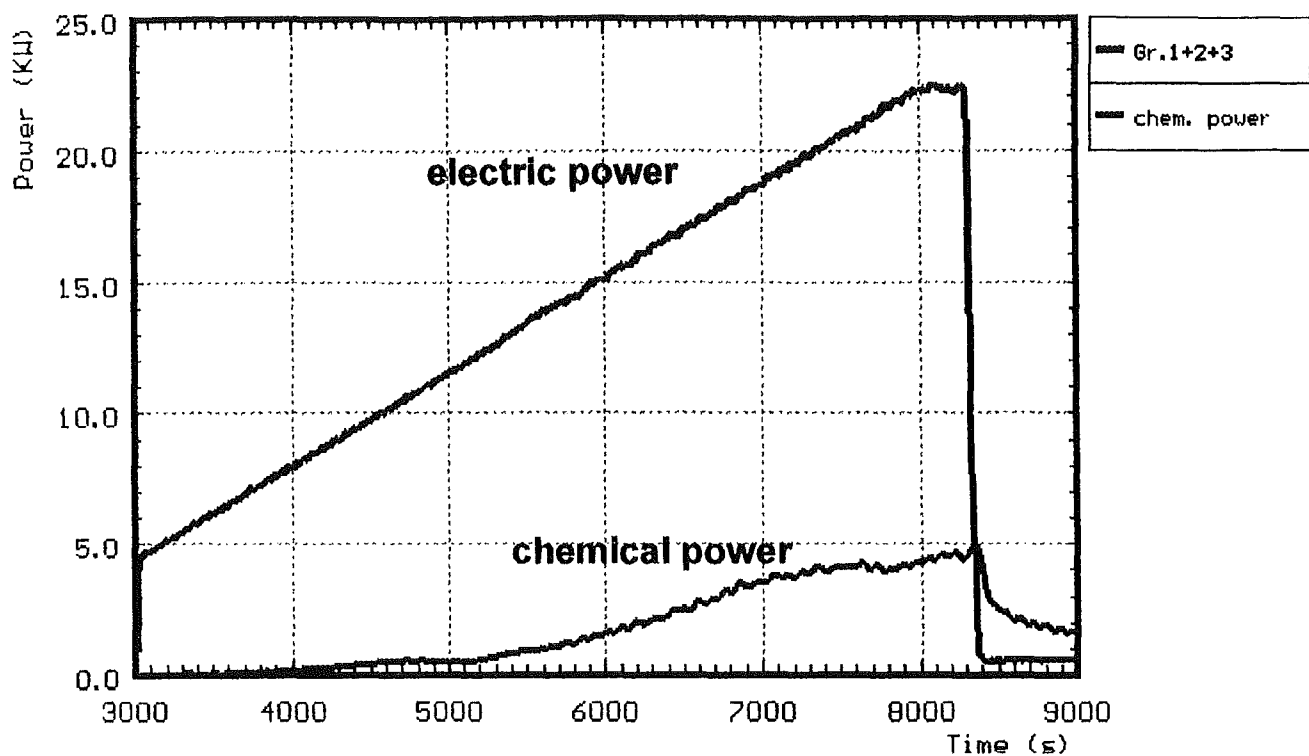


Fig. 12: Comparison of chemical and electric power

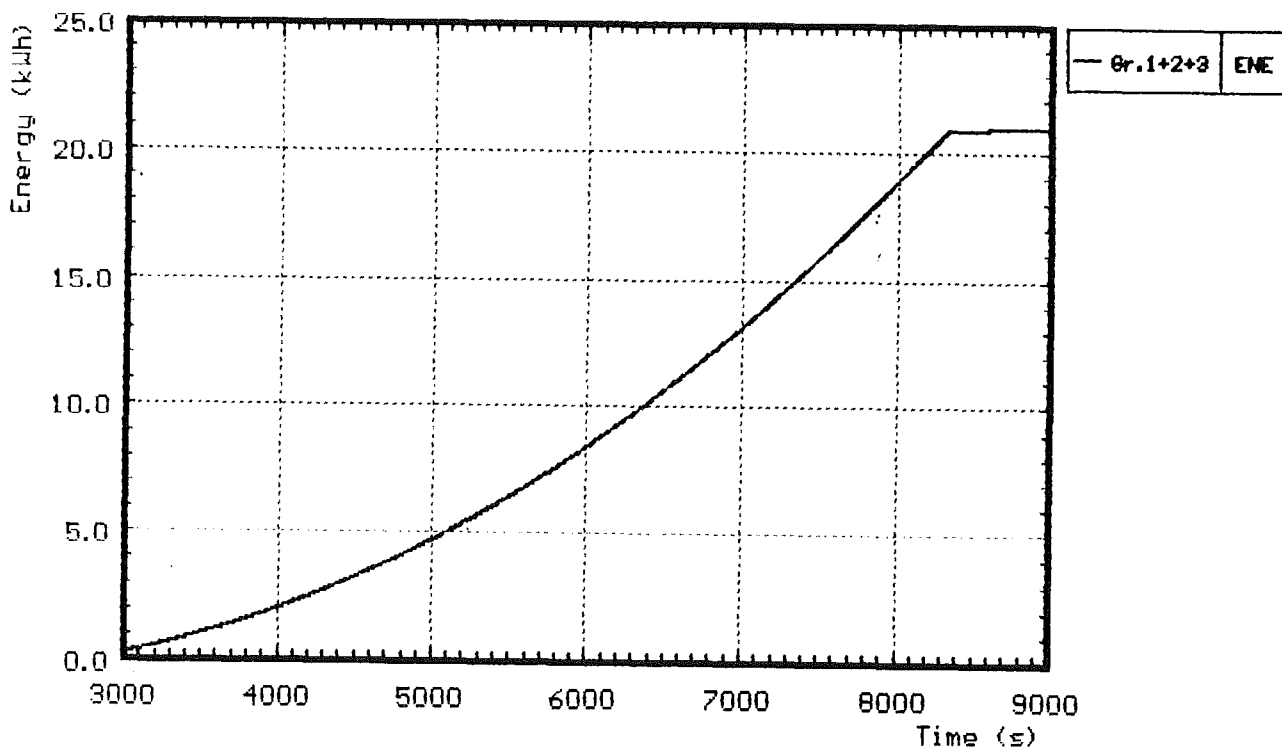


Fig. 13: Energy input

CORA-33:

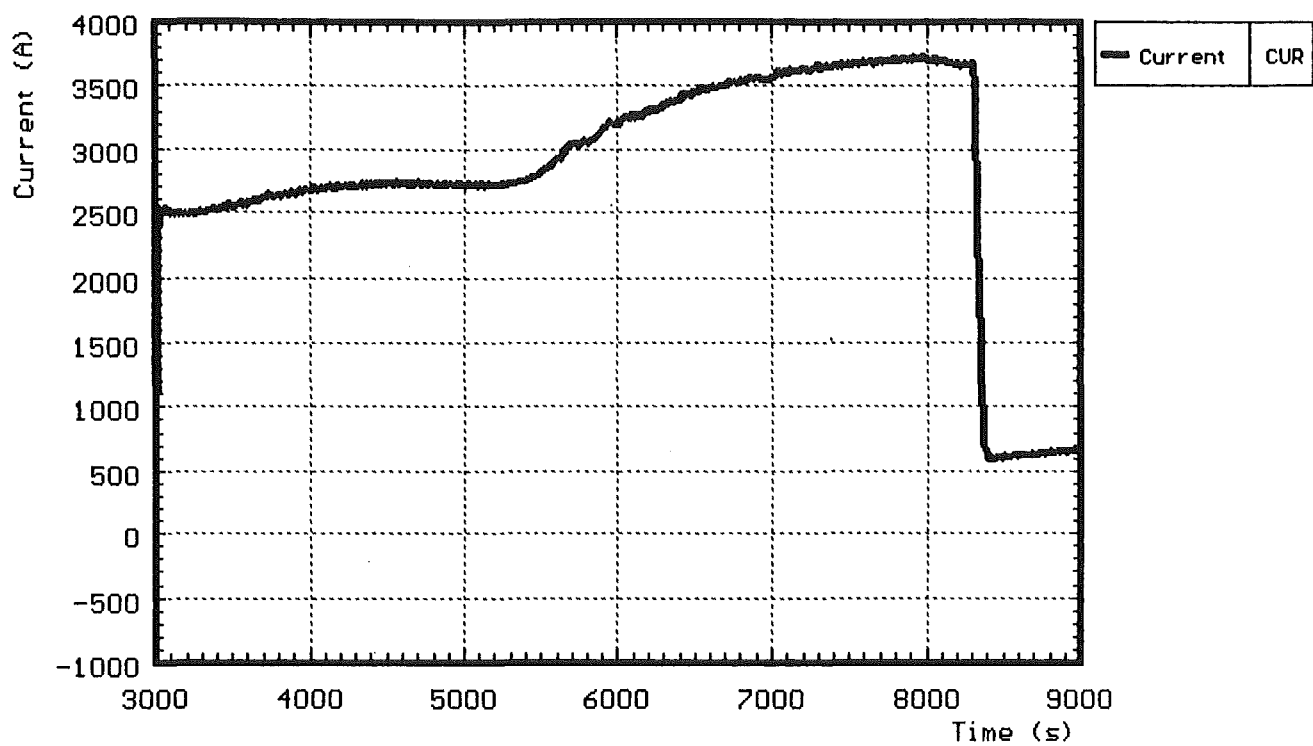
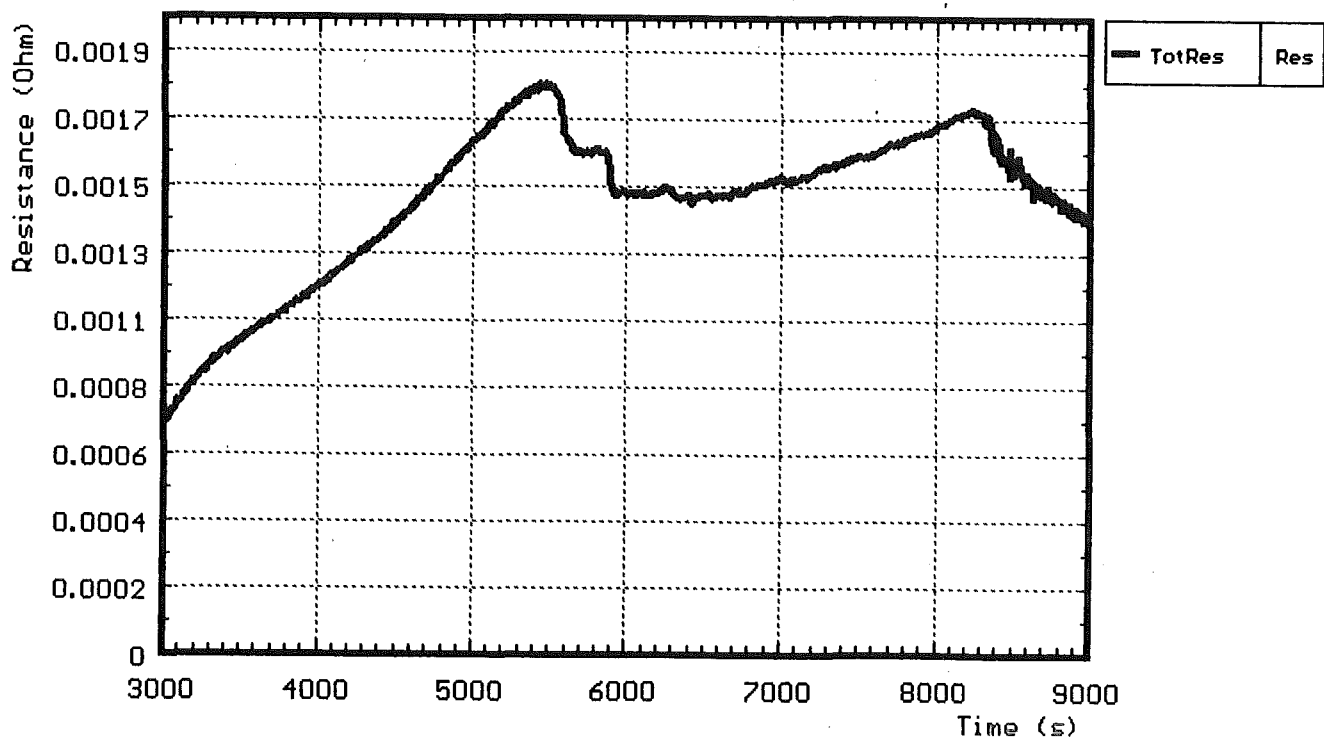


Fig. 14: Total Current



**Fig. 15: Resistance of bundle
(Voltage group 1 / total current)**

CORA-33: Resistance of rod groups

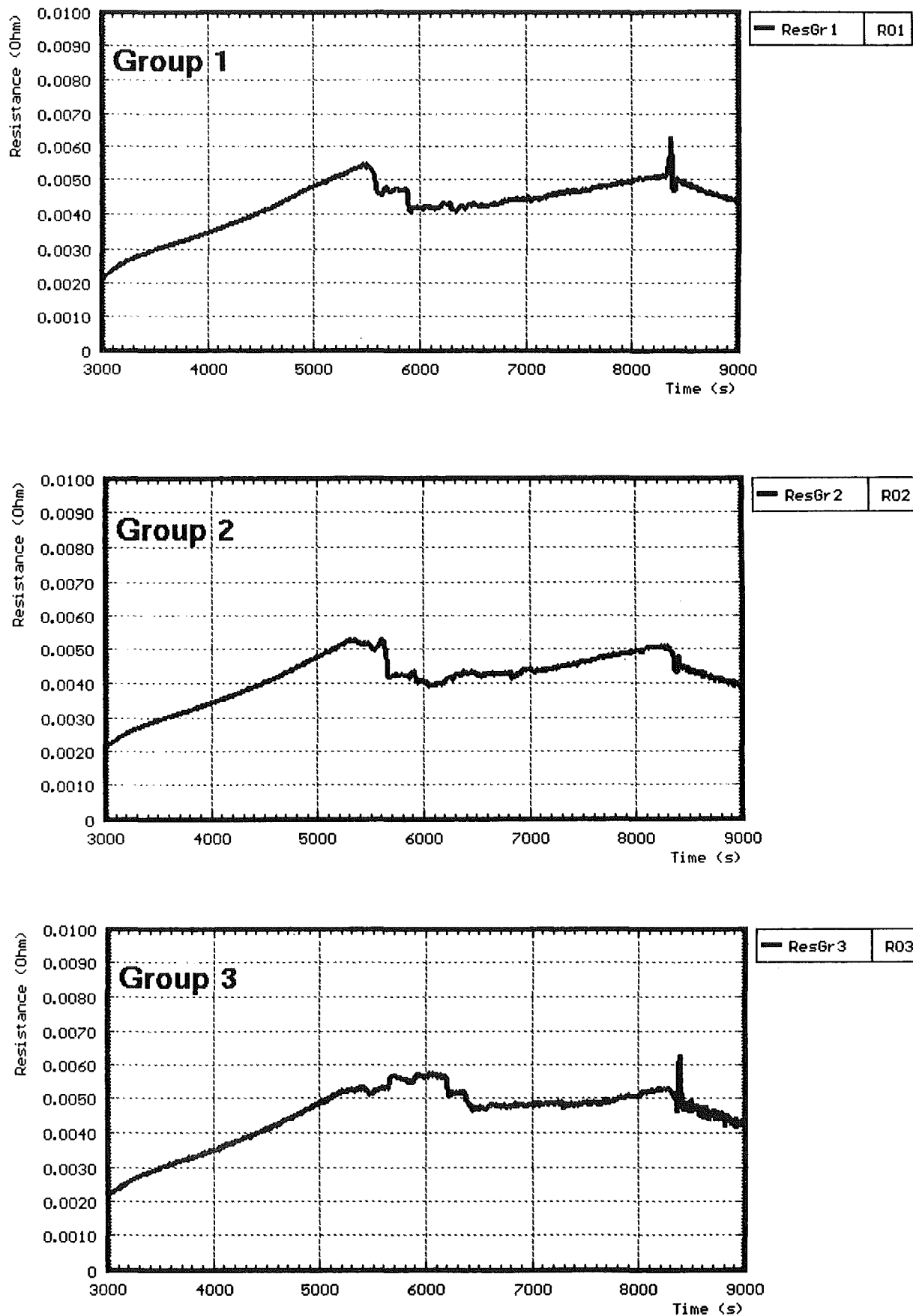


Fig. 16

CORA-33: Variation of currents within the rod groups

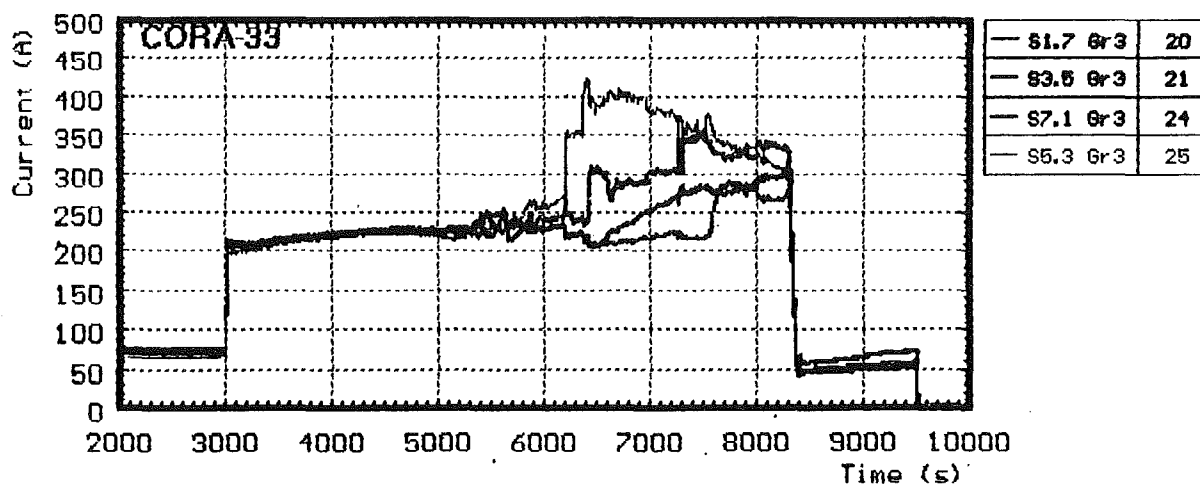
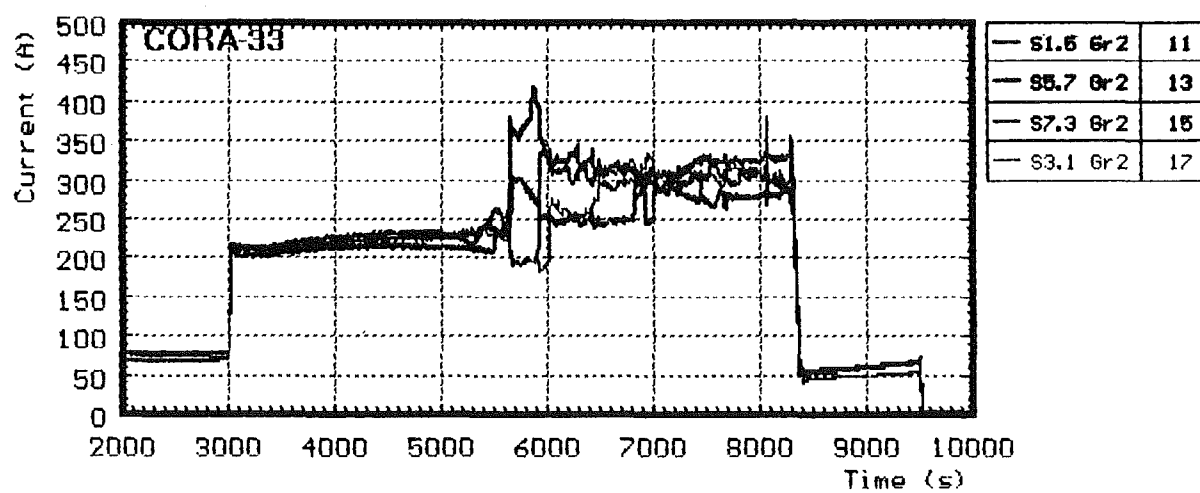
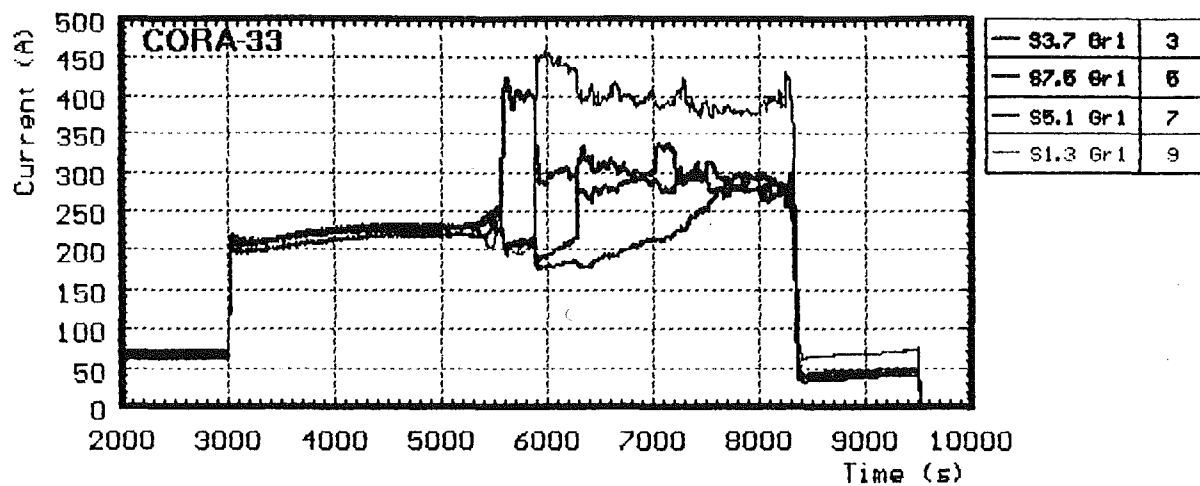


Fig. 17

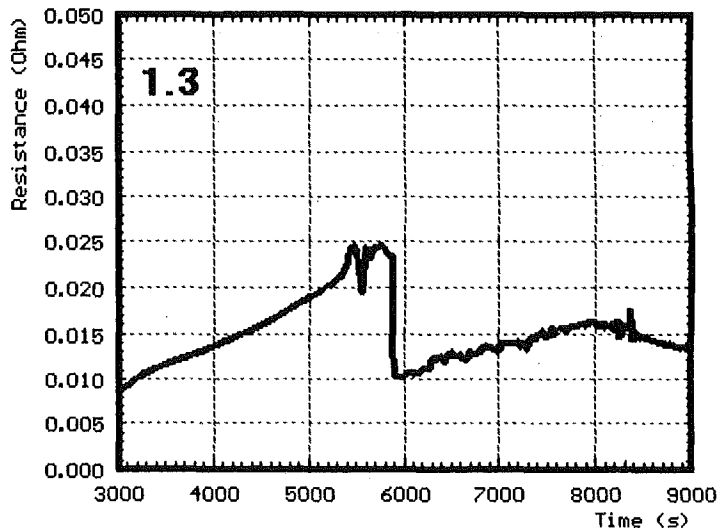
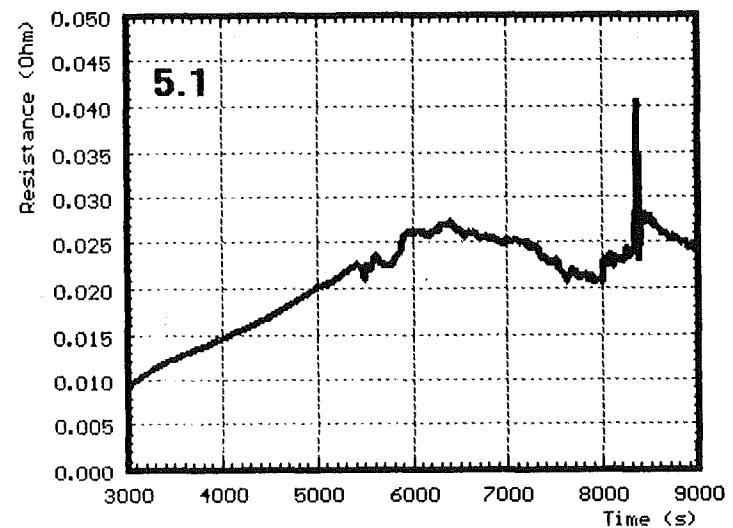
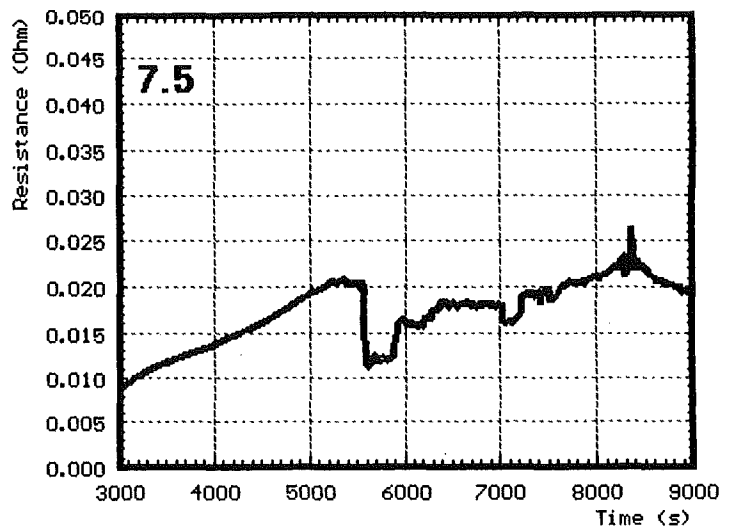
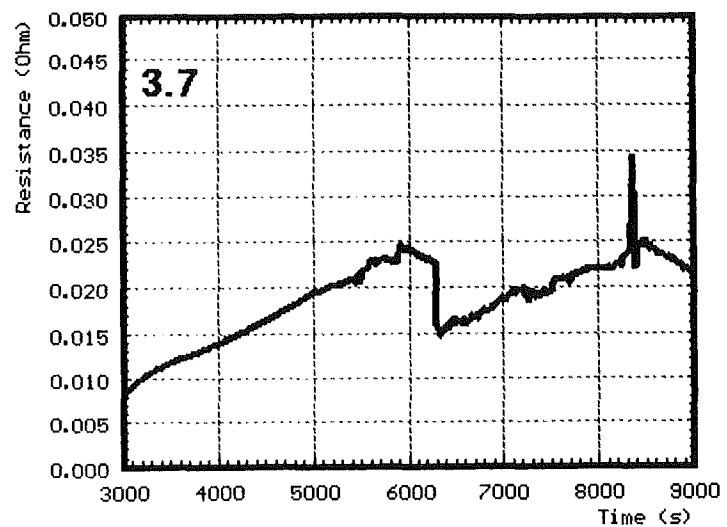


Fig. 18: Resistance of single rods: group 1

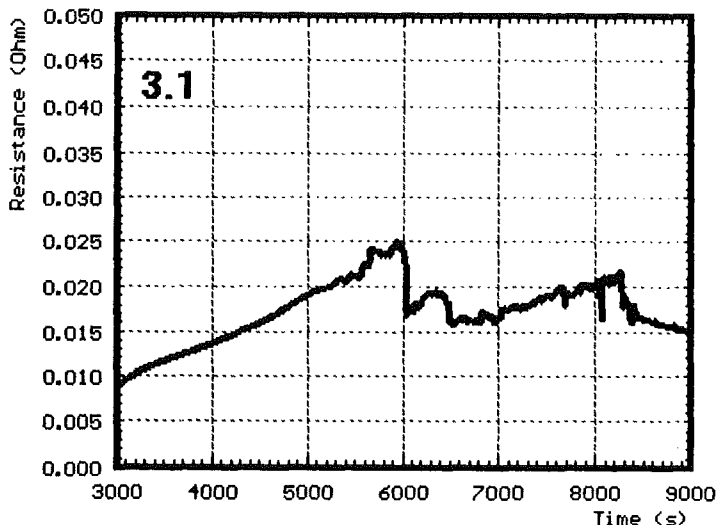
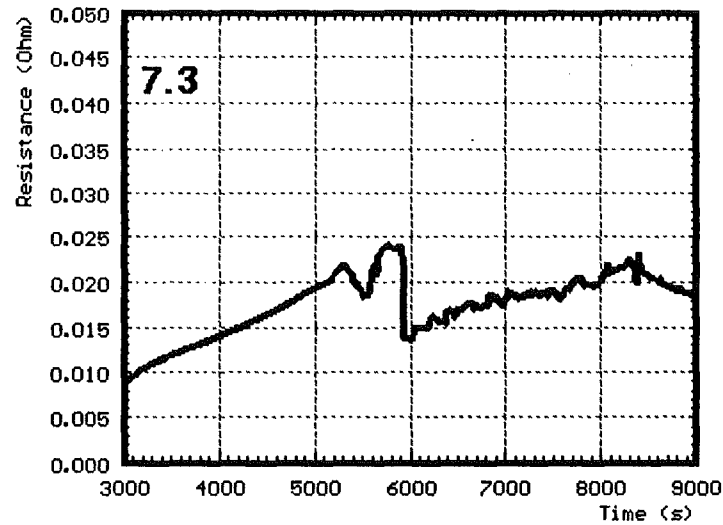
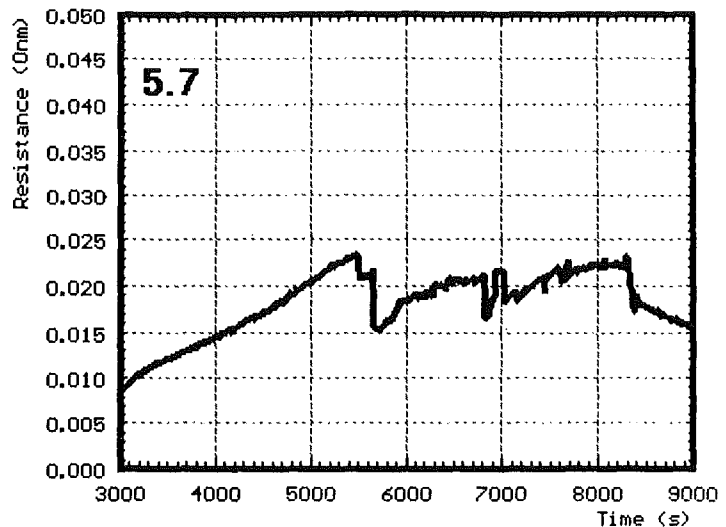
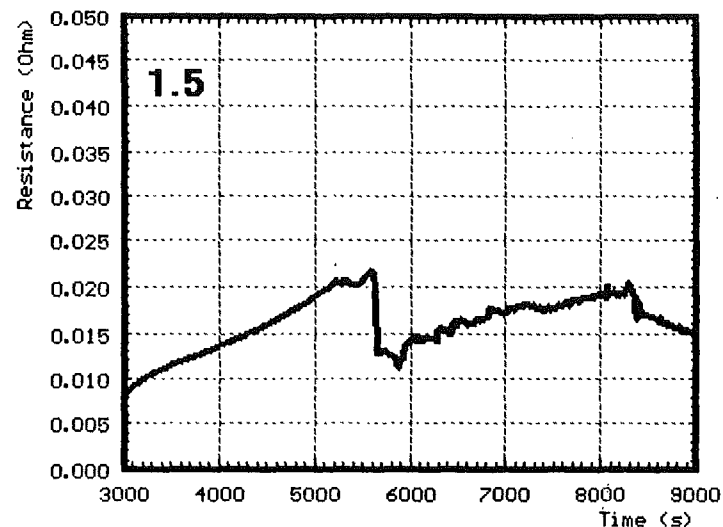


Fig. 19: Resistance of single rods: group 2

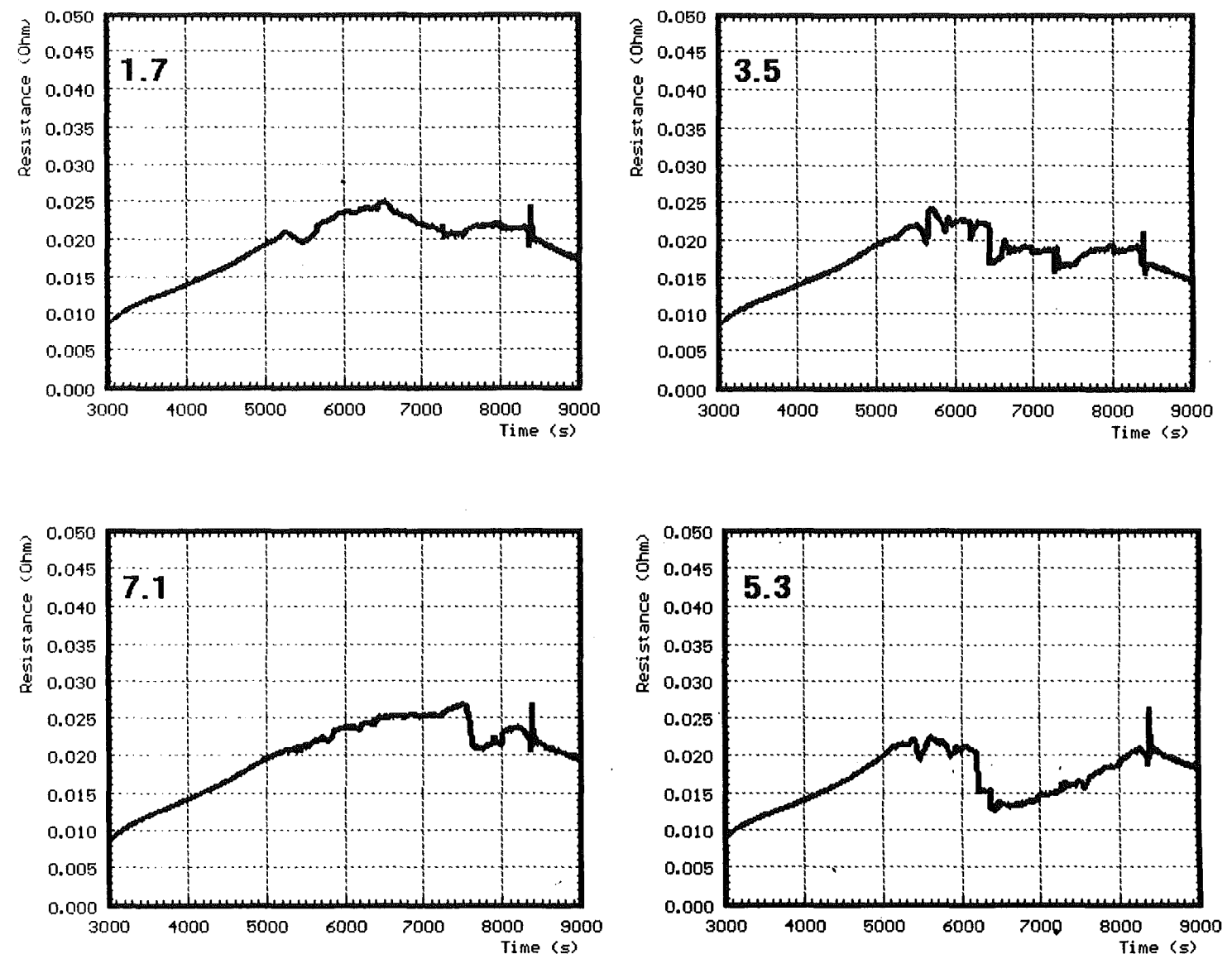


Fig. 20: Resistance of single rods: group 3

CORA-33: Water temperature in the quench cylinder at -250 and -300 mm

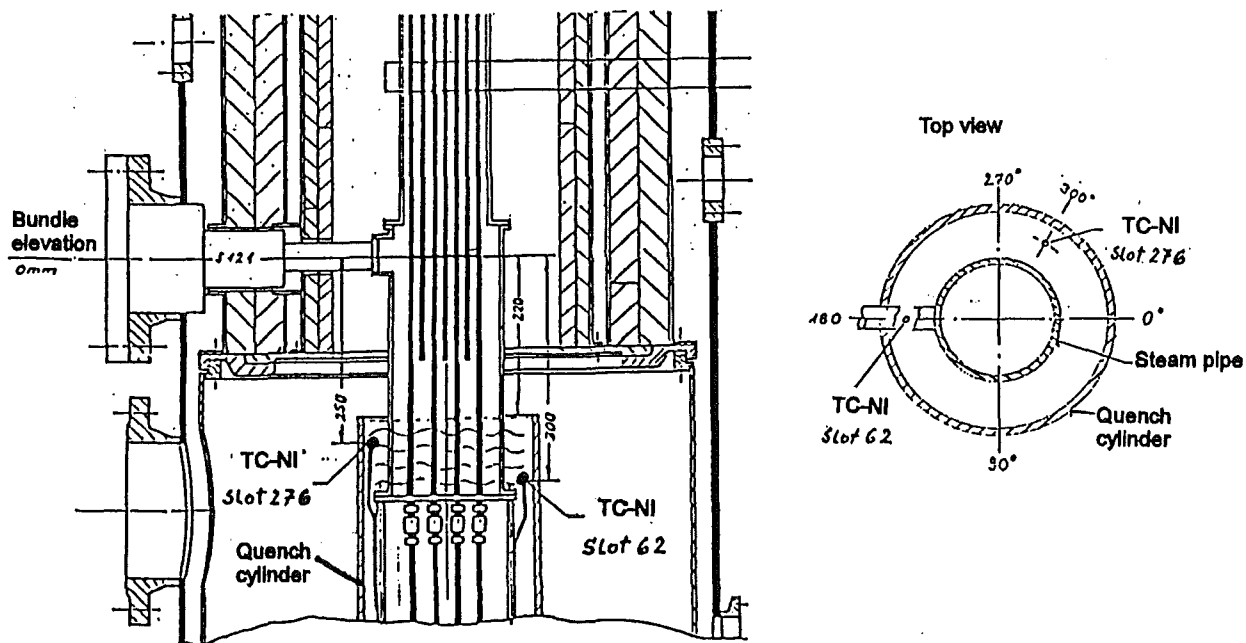
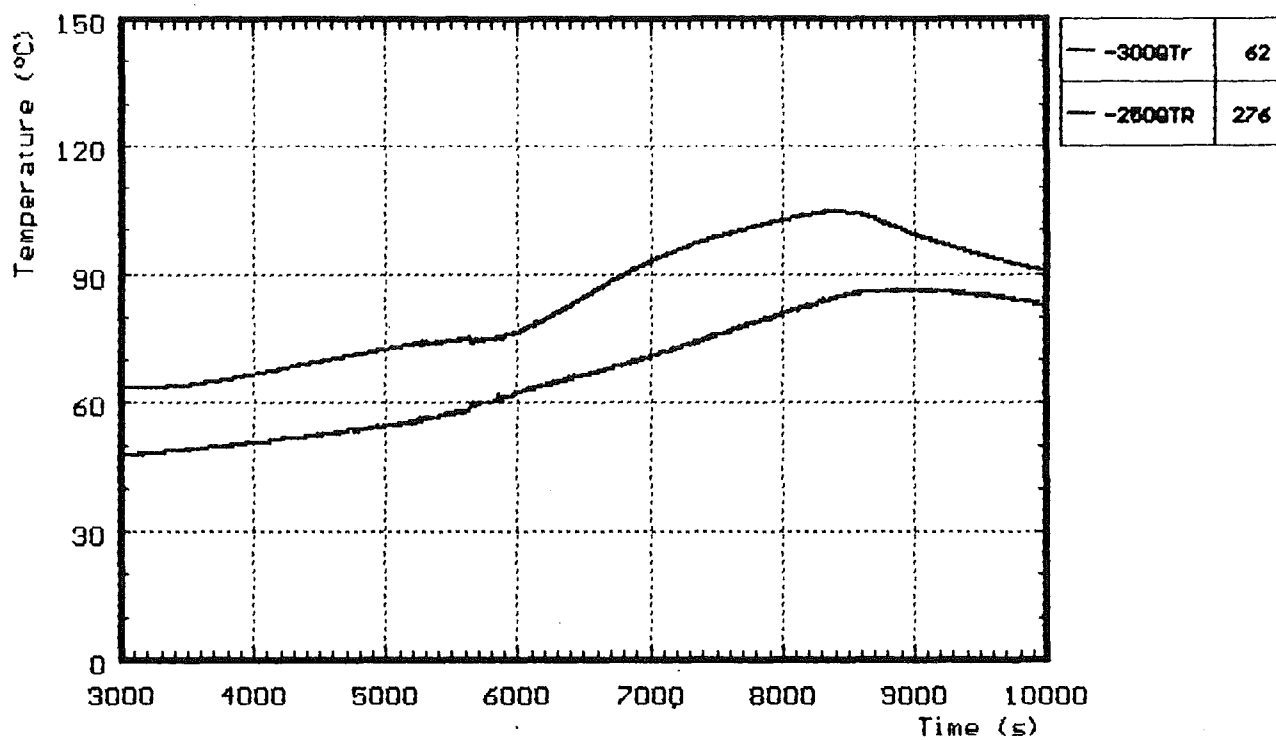


Fig. 21a

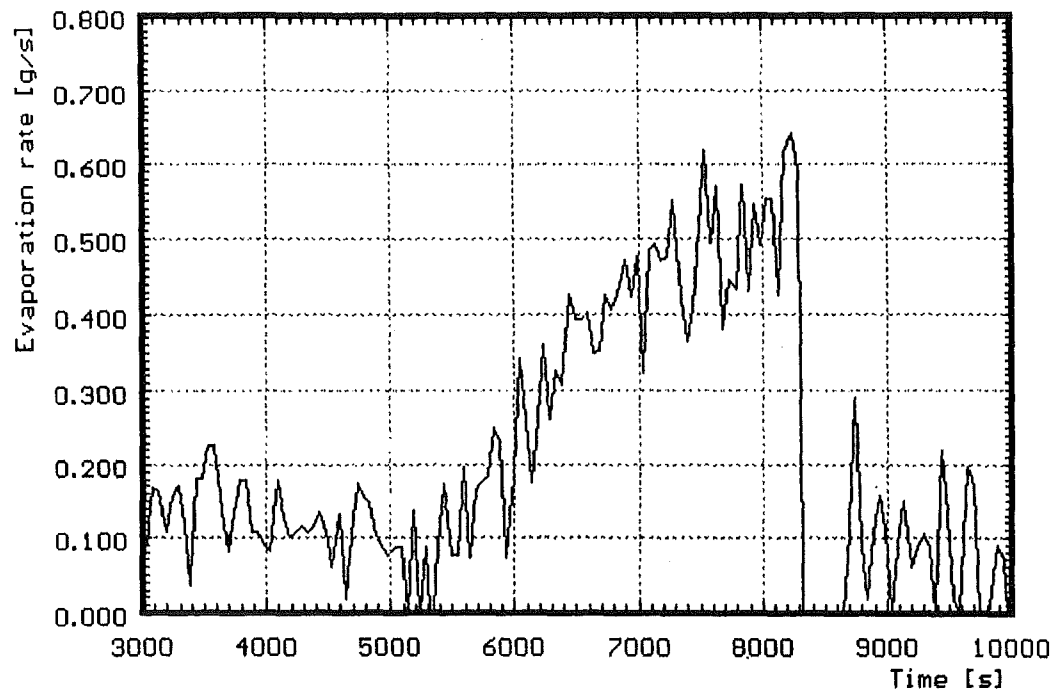


Fig. 21b: CORA-33; Evaporation rate of water from quench cylinder determined by measured water level change

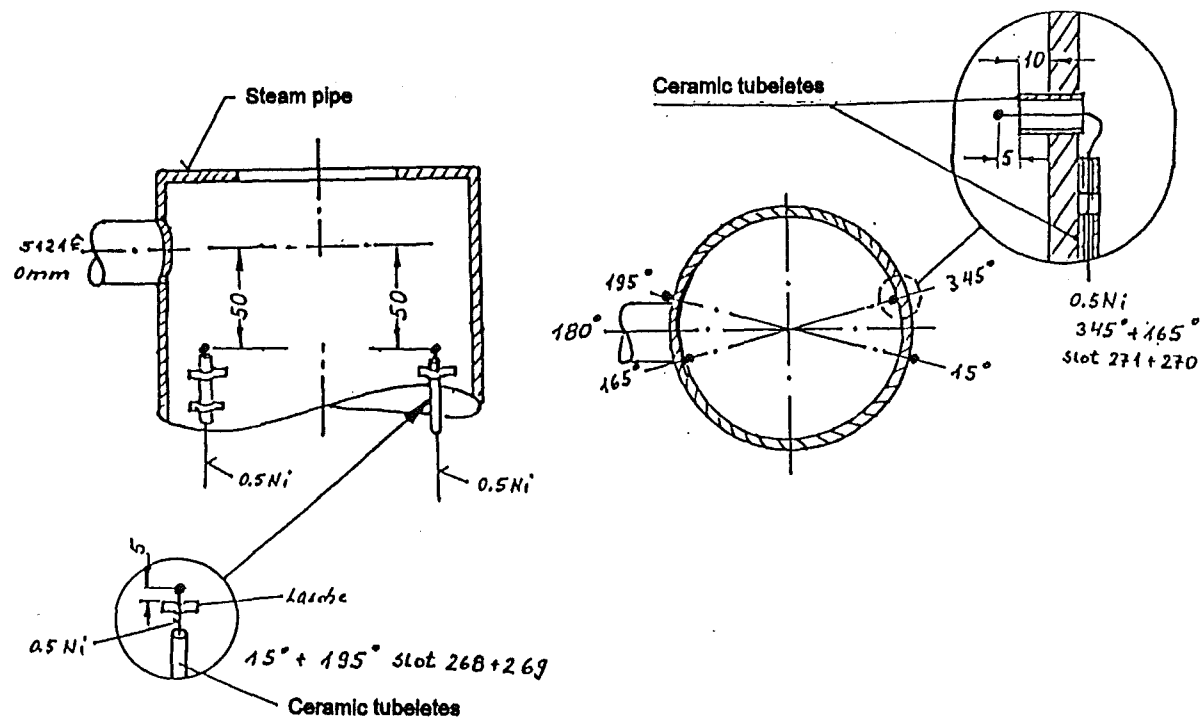
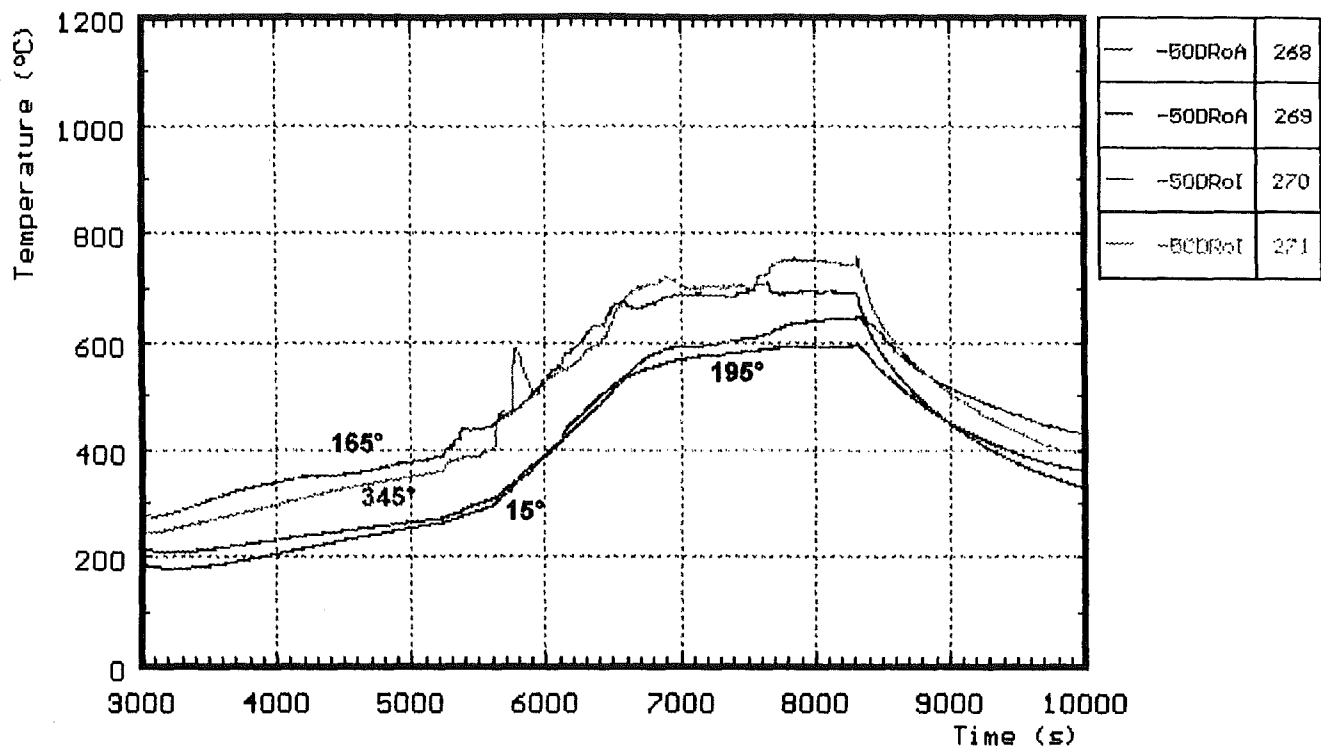


Fig. 22: CORA-33; Temperatures at the steam distribution tube at -50mm elevation

CORA-33:

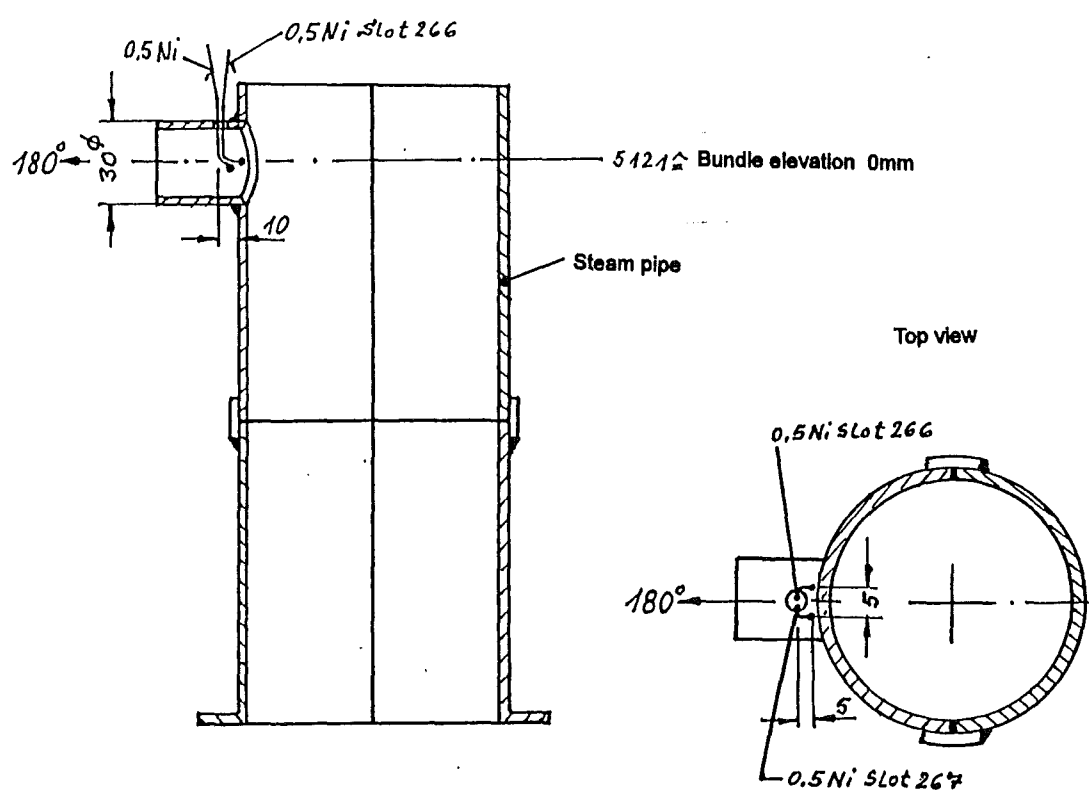
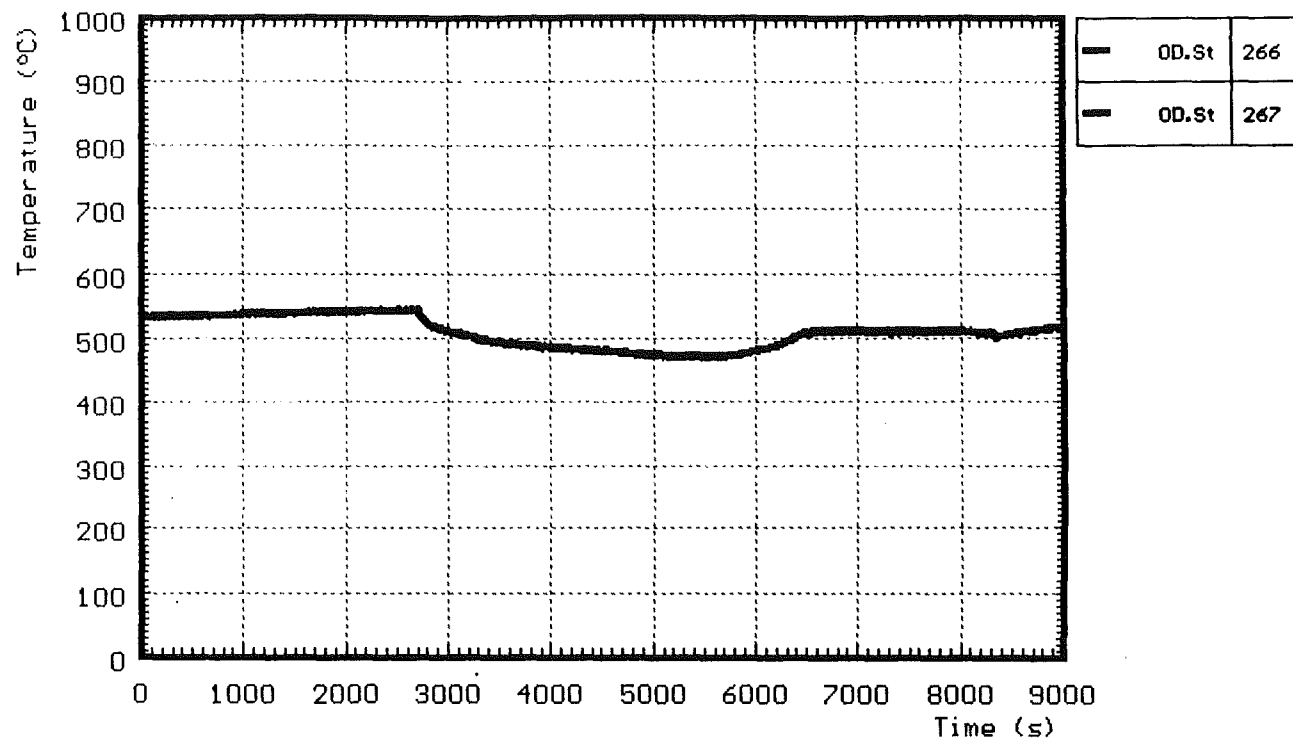
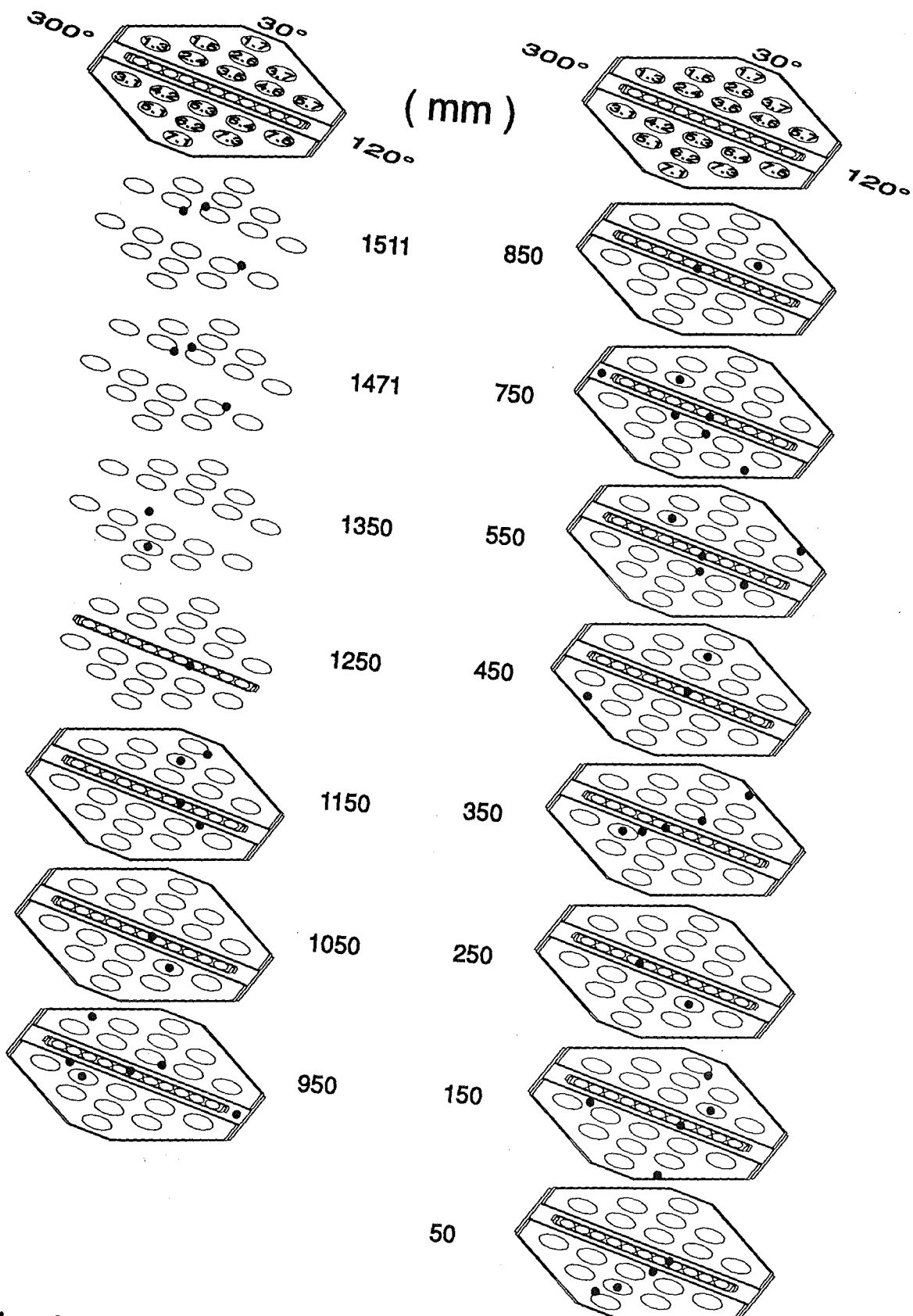


Fig. 23: Temperatures at steam inlet



**Fig. 24: Thermocouple locations within the bundle
(CORA-33)**

CORA-33: Temperatures on heated rods

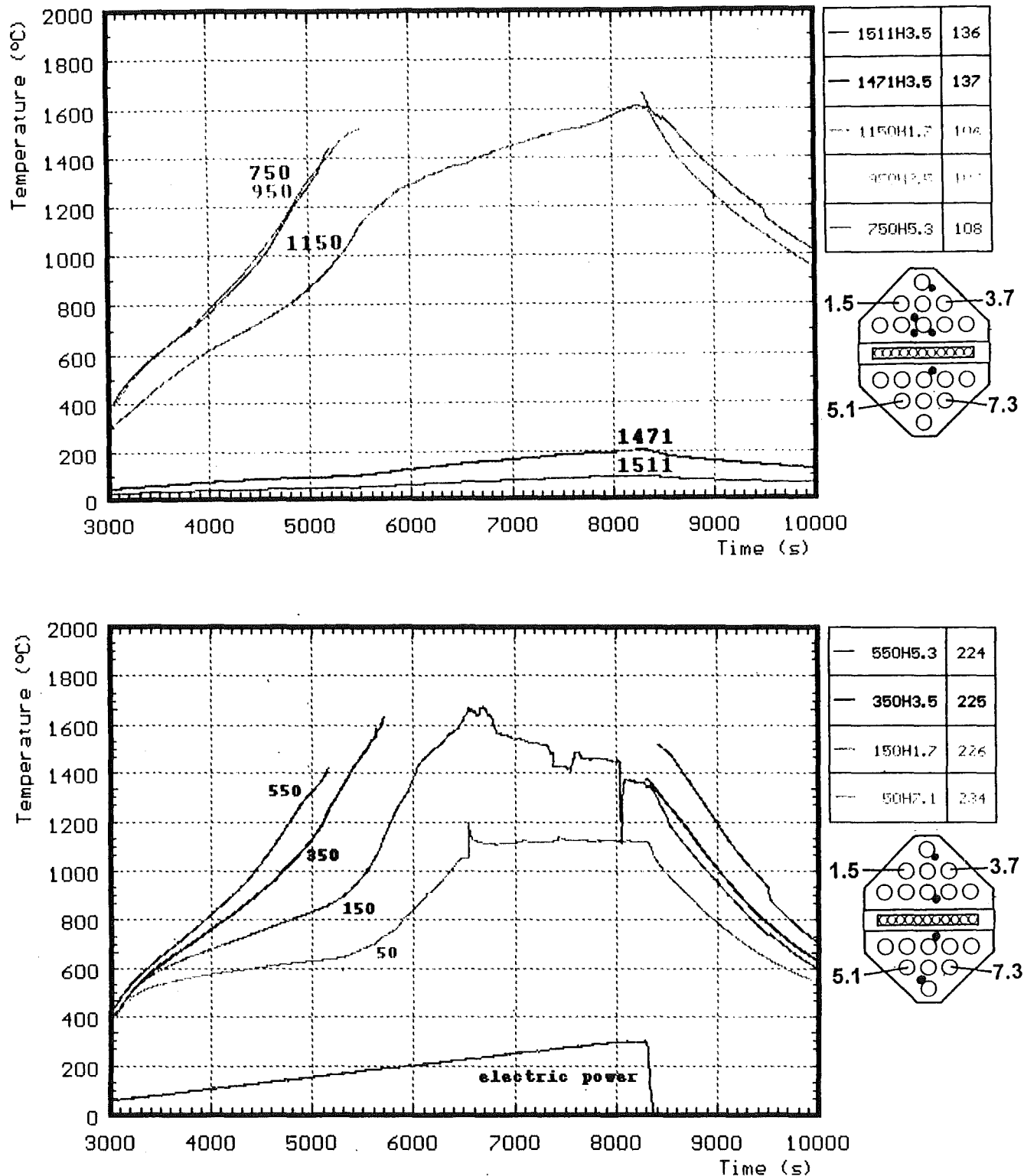


Fig. 25

CORA-33: Temperatures in unheated rods

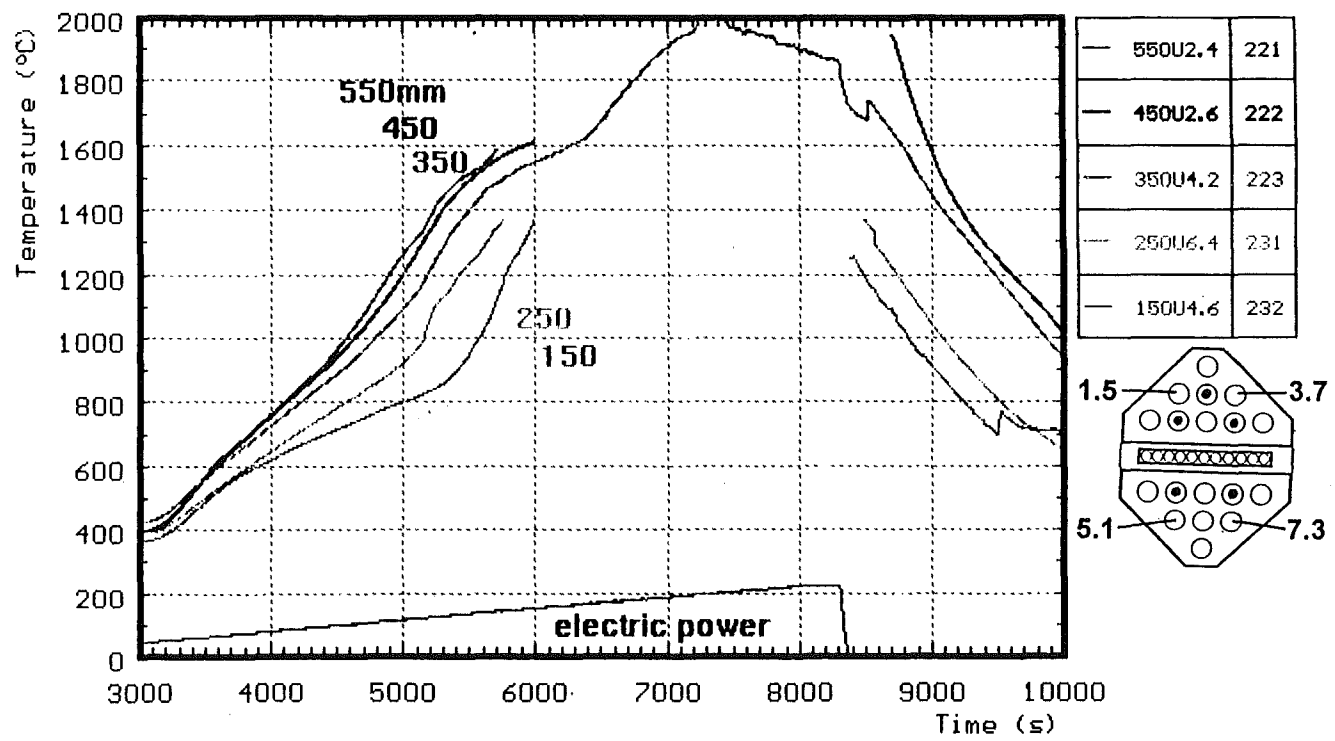
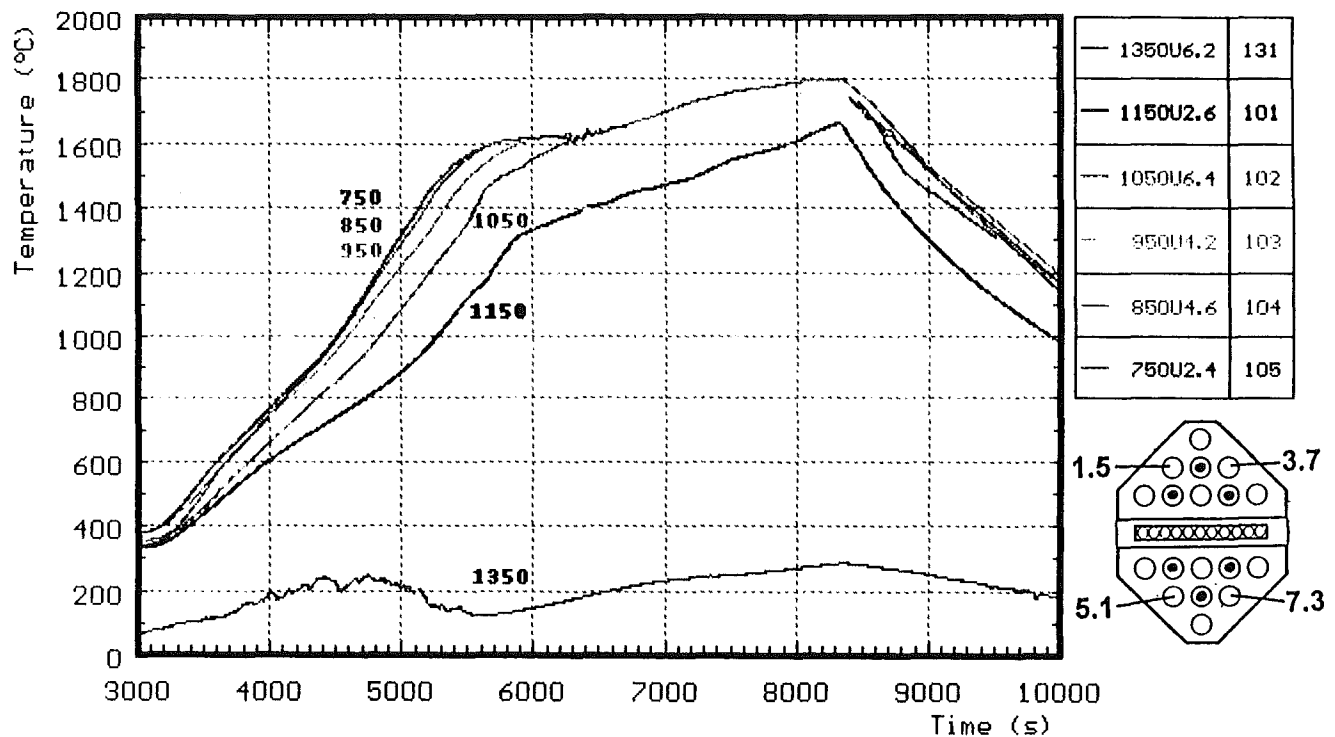


Fig. 26

CORA-33: Temperatures on the channel box walls

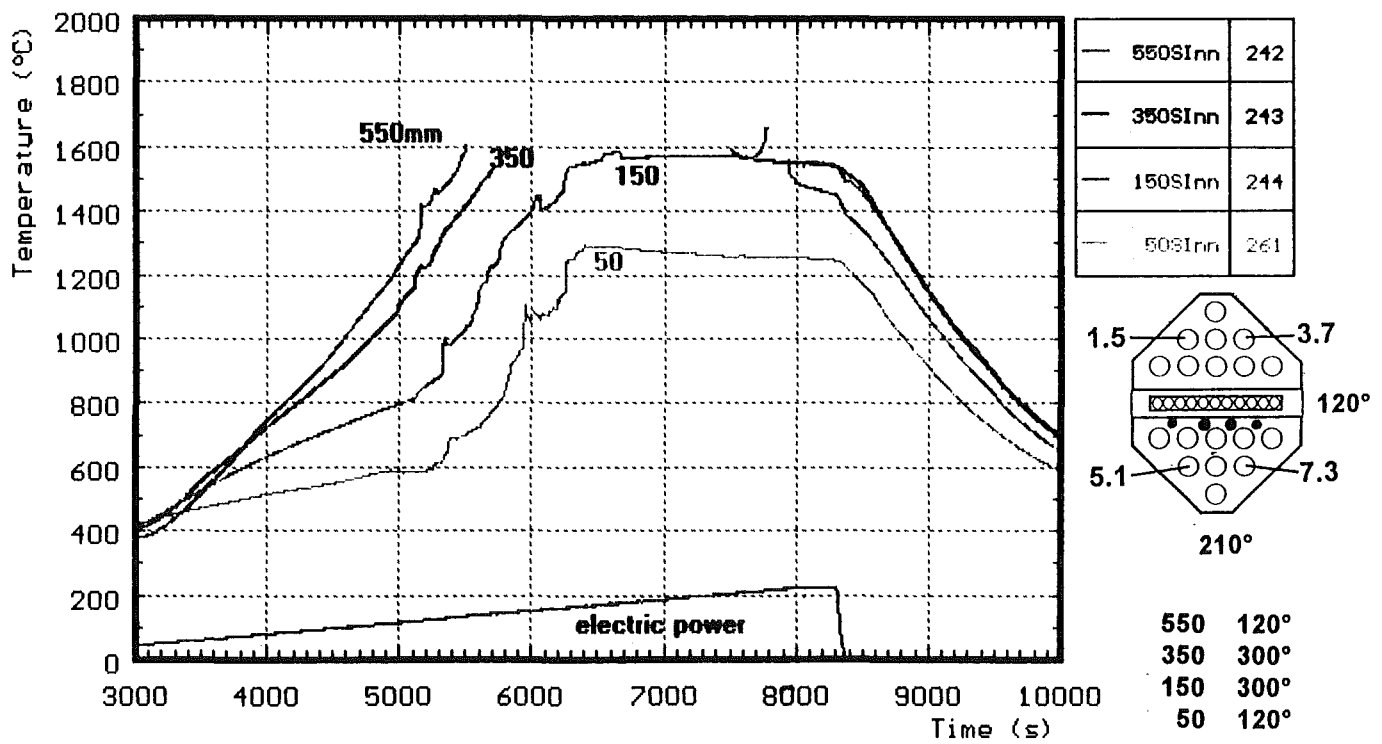
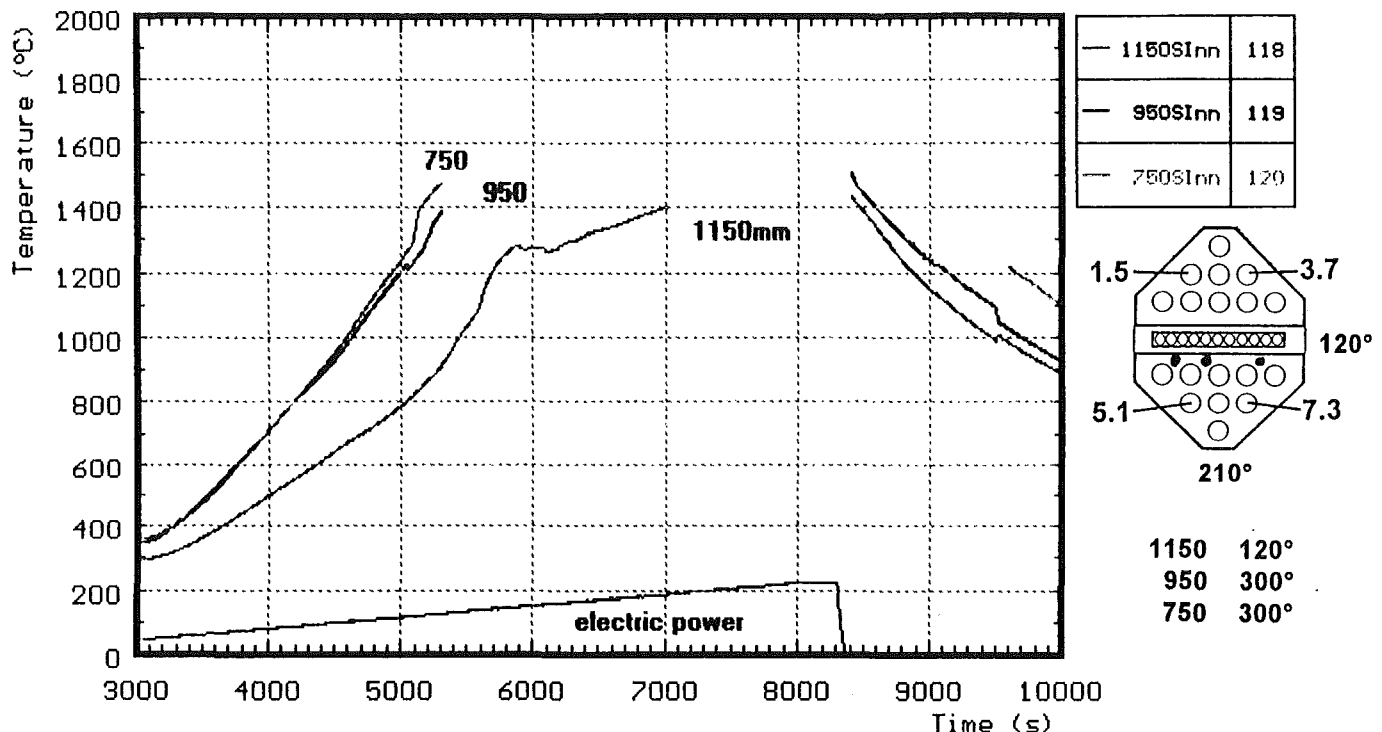


Fig. 27

CORA-33: Temperatures in the absorberblade

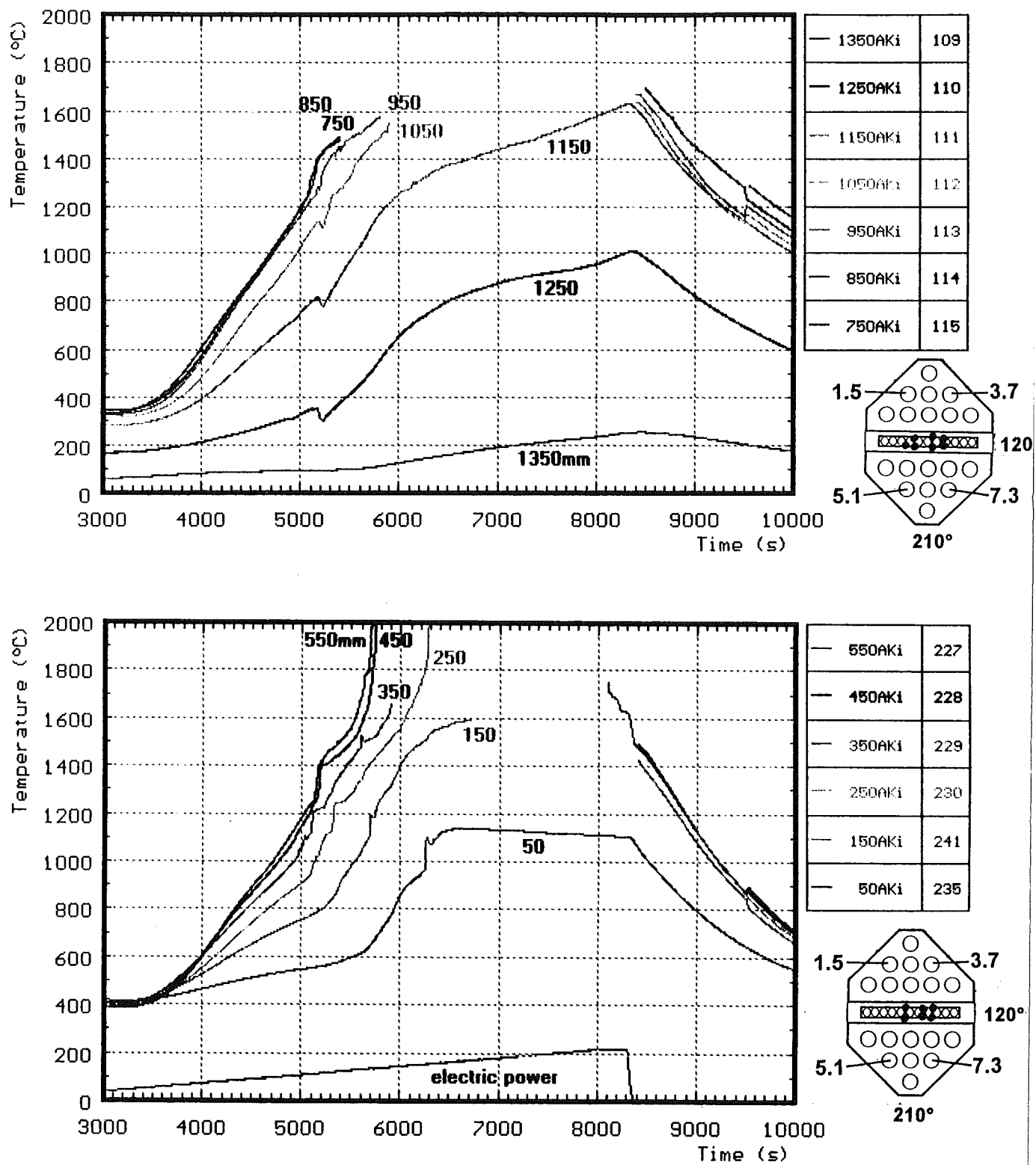


Fig. 28

CORA-33: Temperatures at the absorberblade

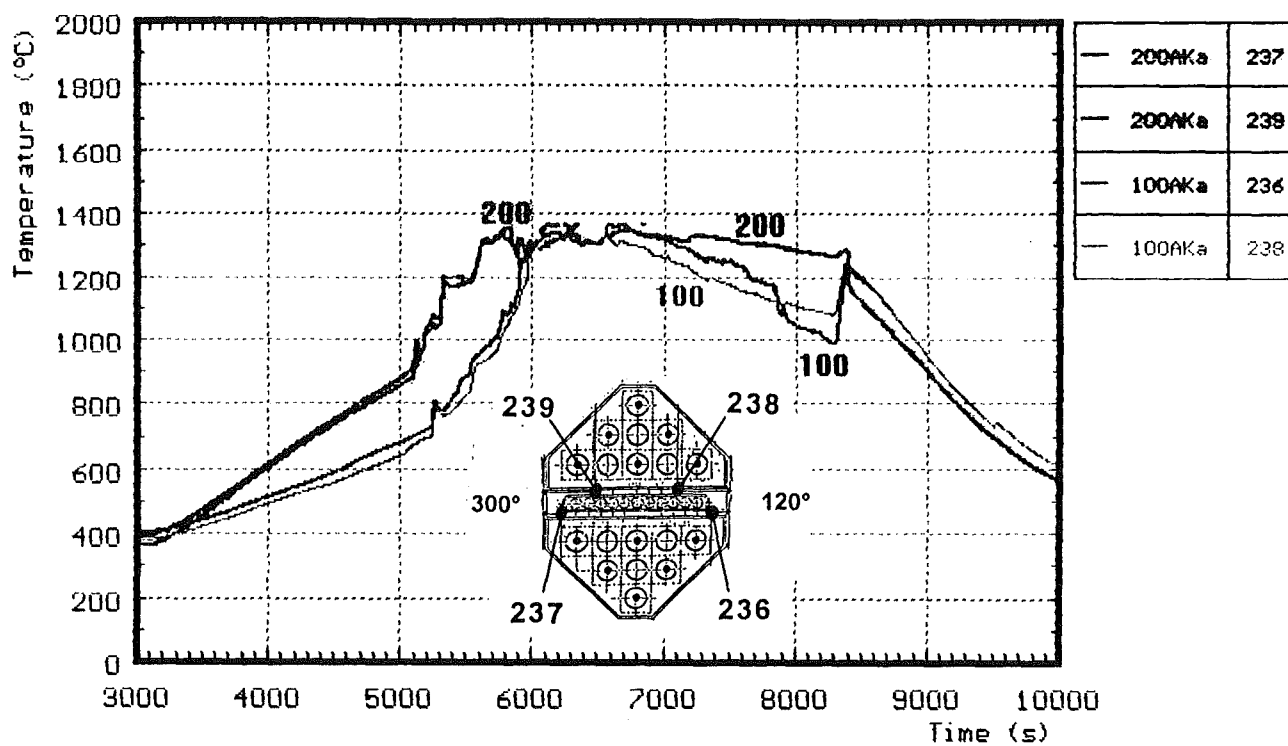


Fig. 28a

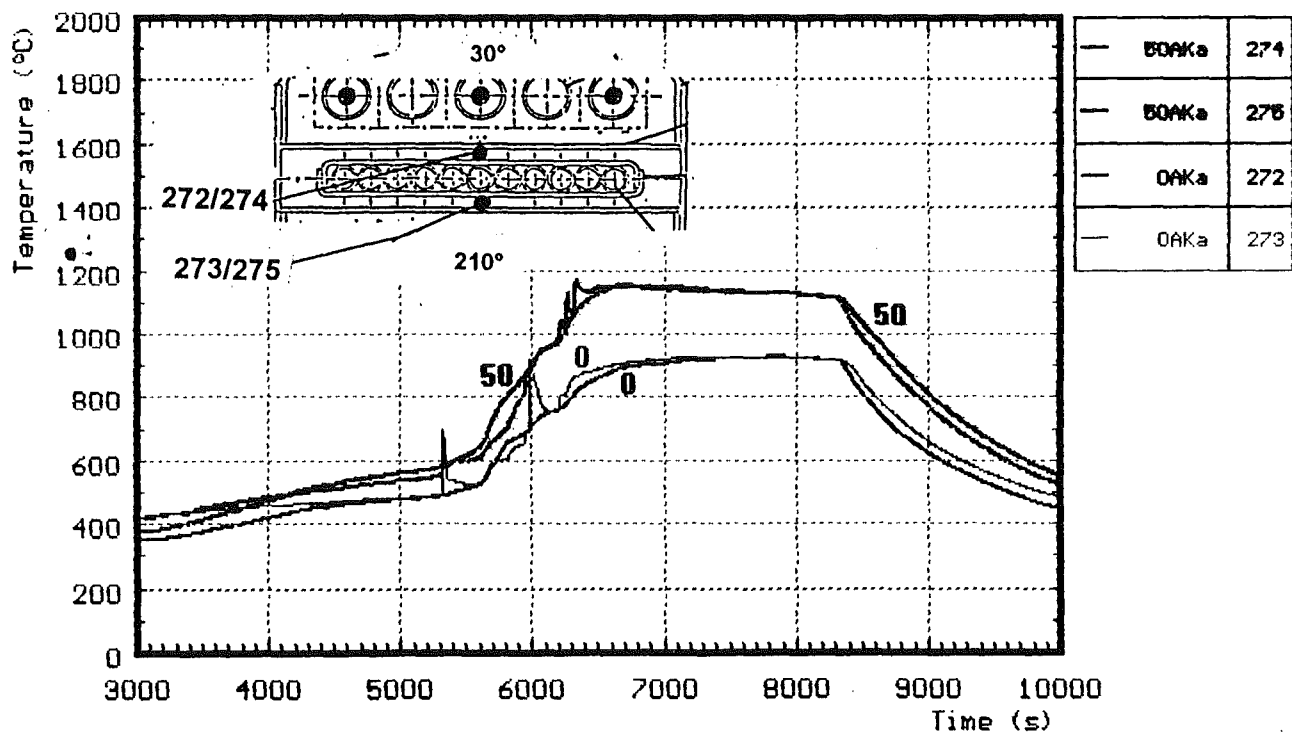


Fig. 28b

CORA-33: Temperatures measured with ceramic protected TCs

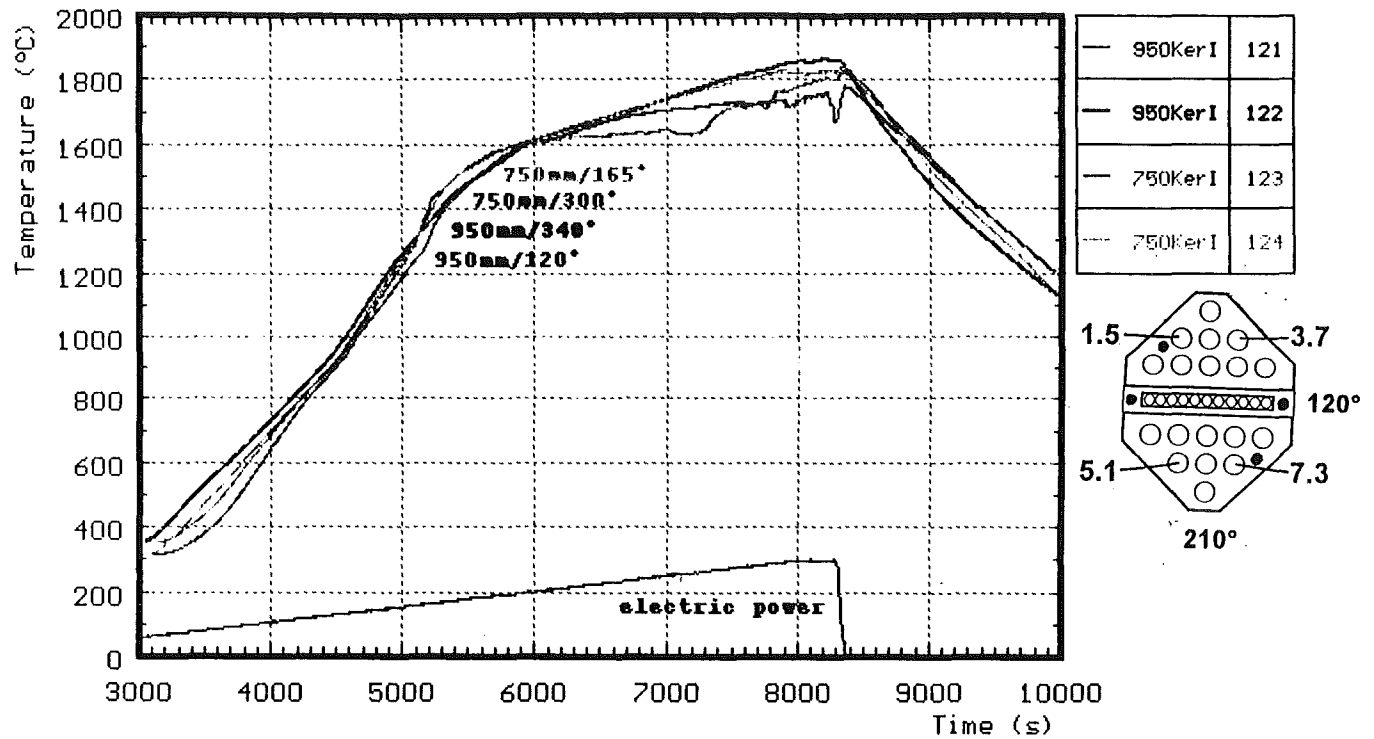


Fig. 29

CORA-33: Temperatures on the spacers

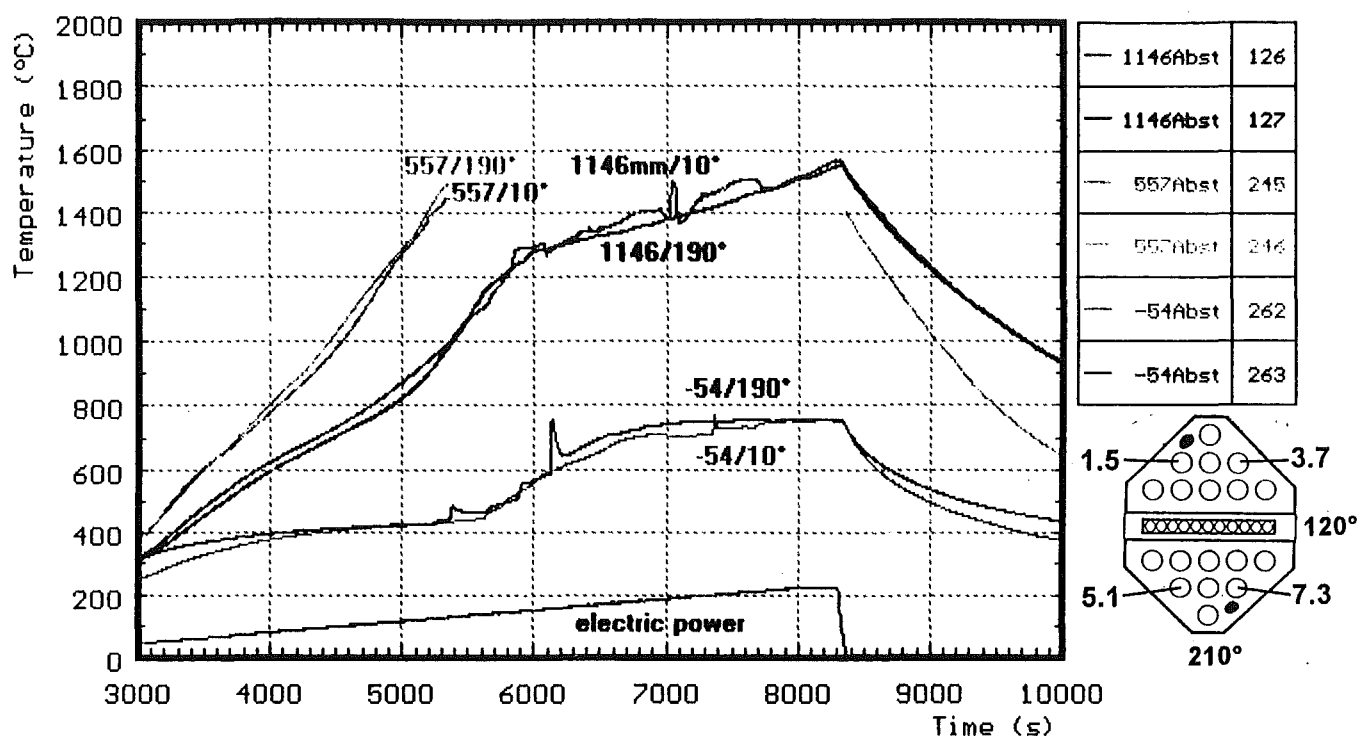


Fig. 30: Temperatures on the spacers

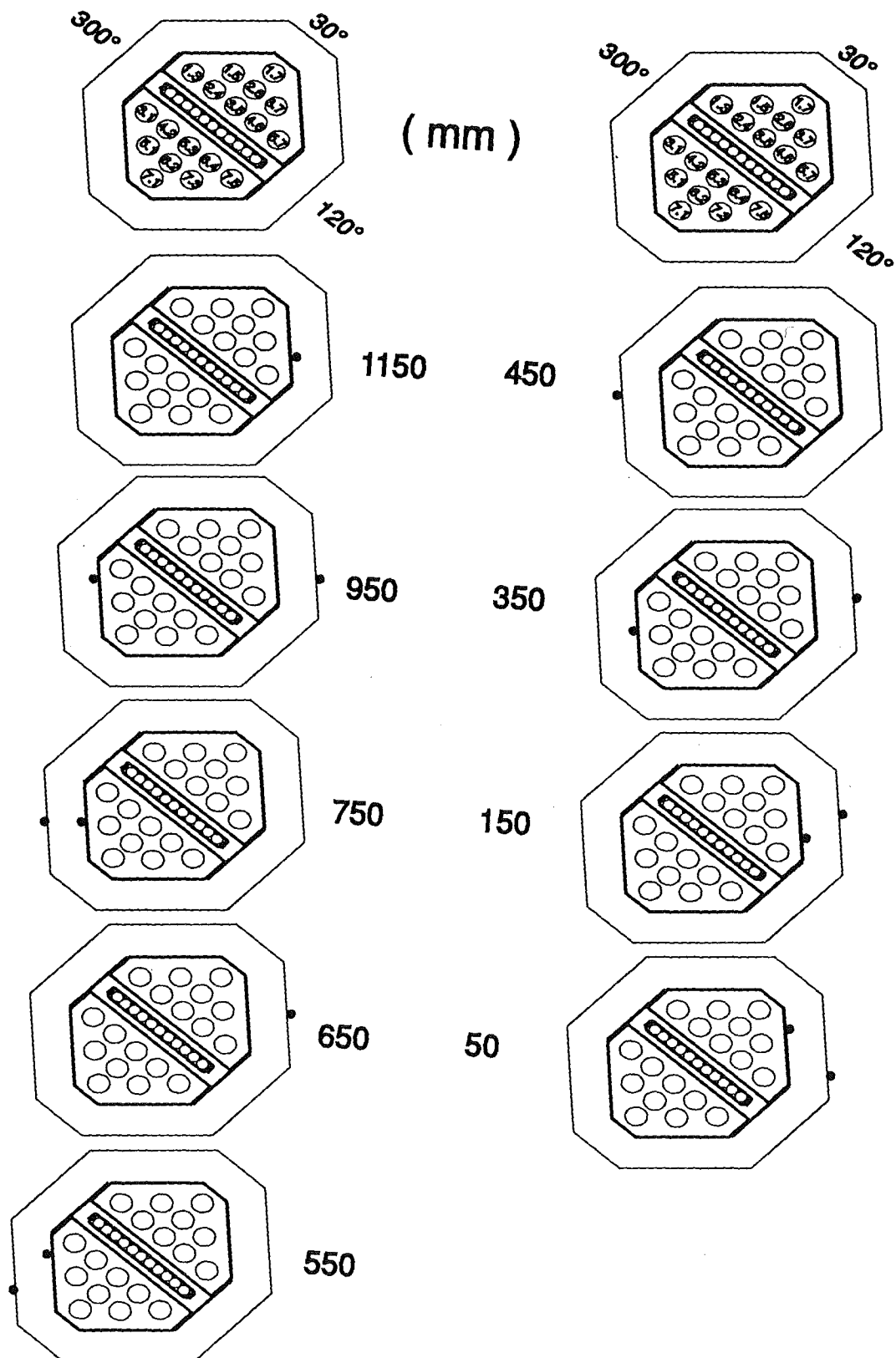


Fig. 31: Location of thermocouples at shroud and shroud insulation (CORA-33)

CORA-33: Temperatures on the inner side of shroud

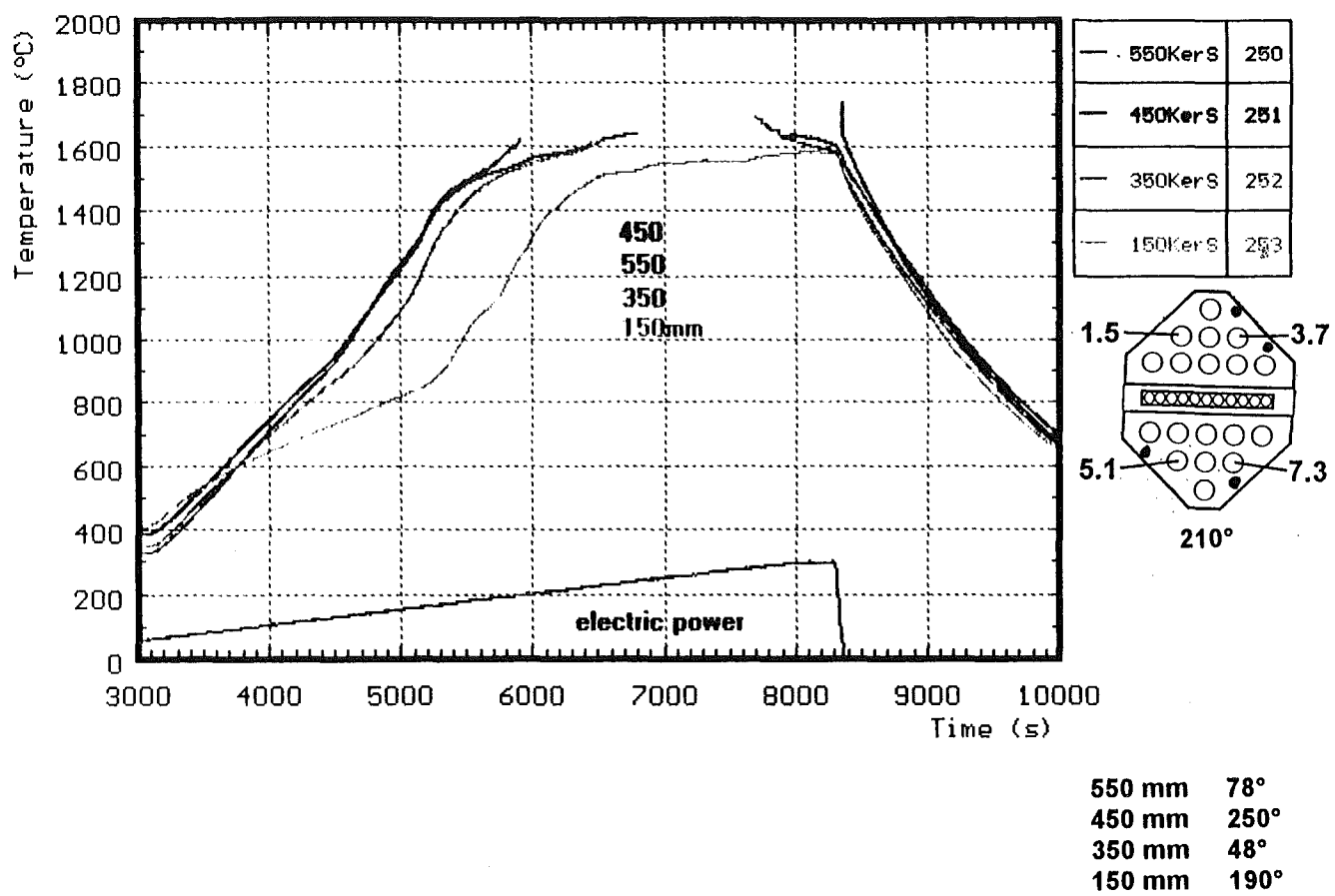


Fig. 32

CORA-33: Temperatures on the shroud

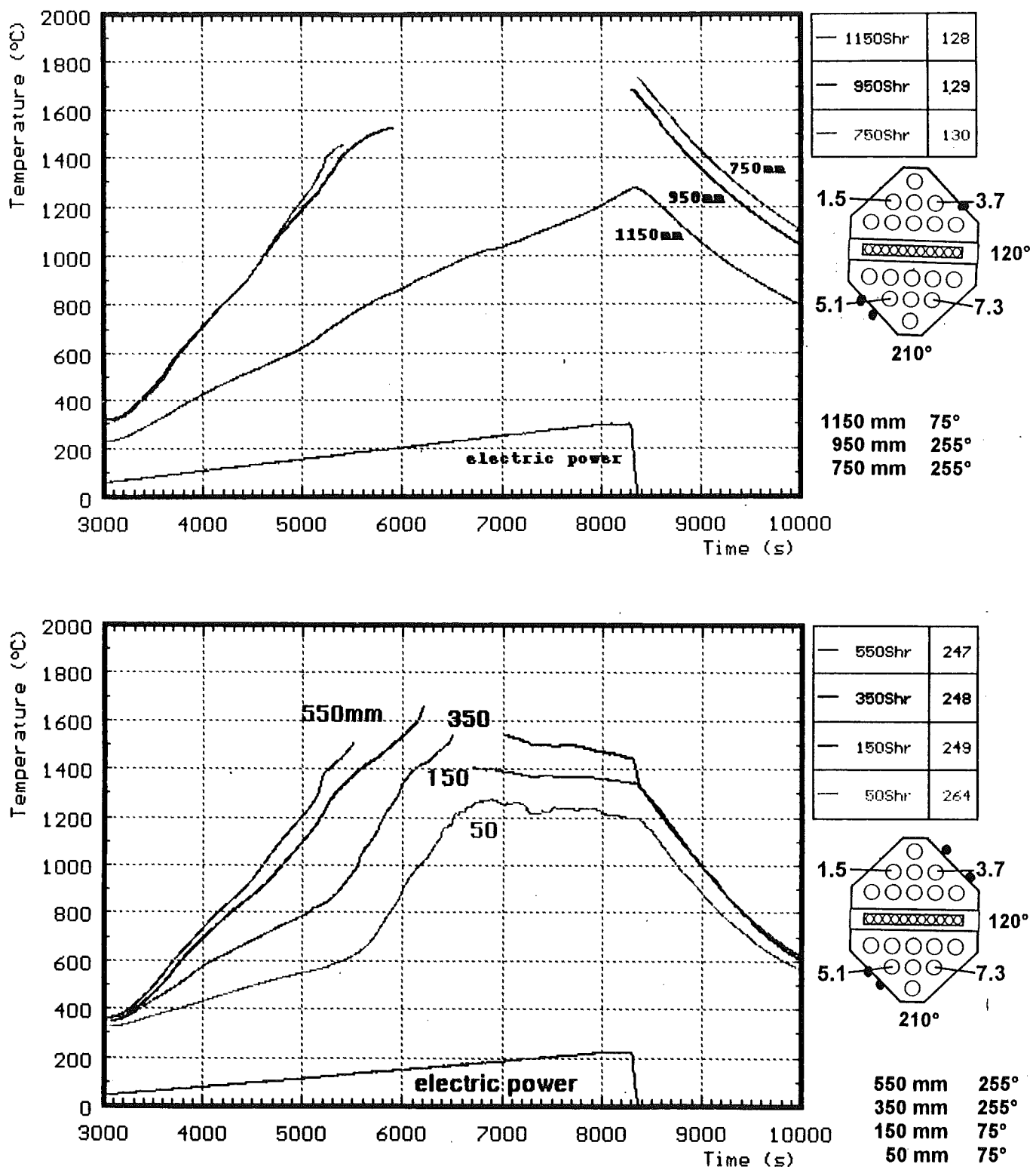


Fig. 33

CORA-33: Temperatures on the shroud insulation

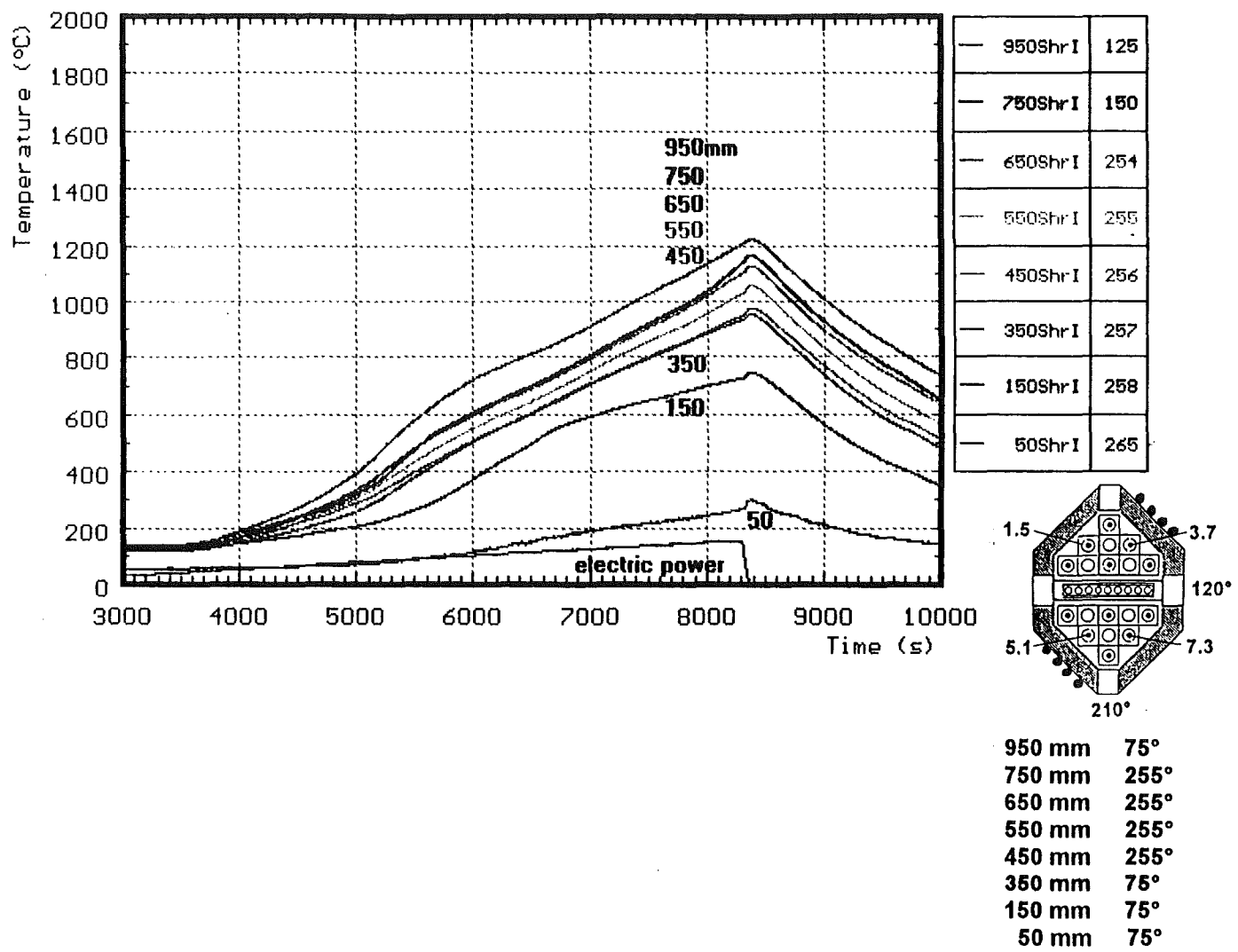


Fig. 34

CORA-33: Gastemperatures in the upper part of the bundle

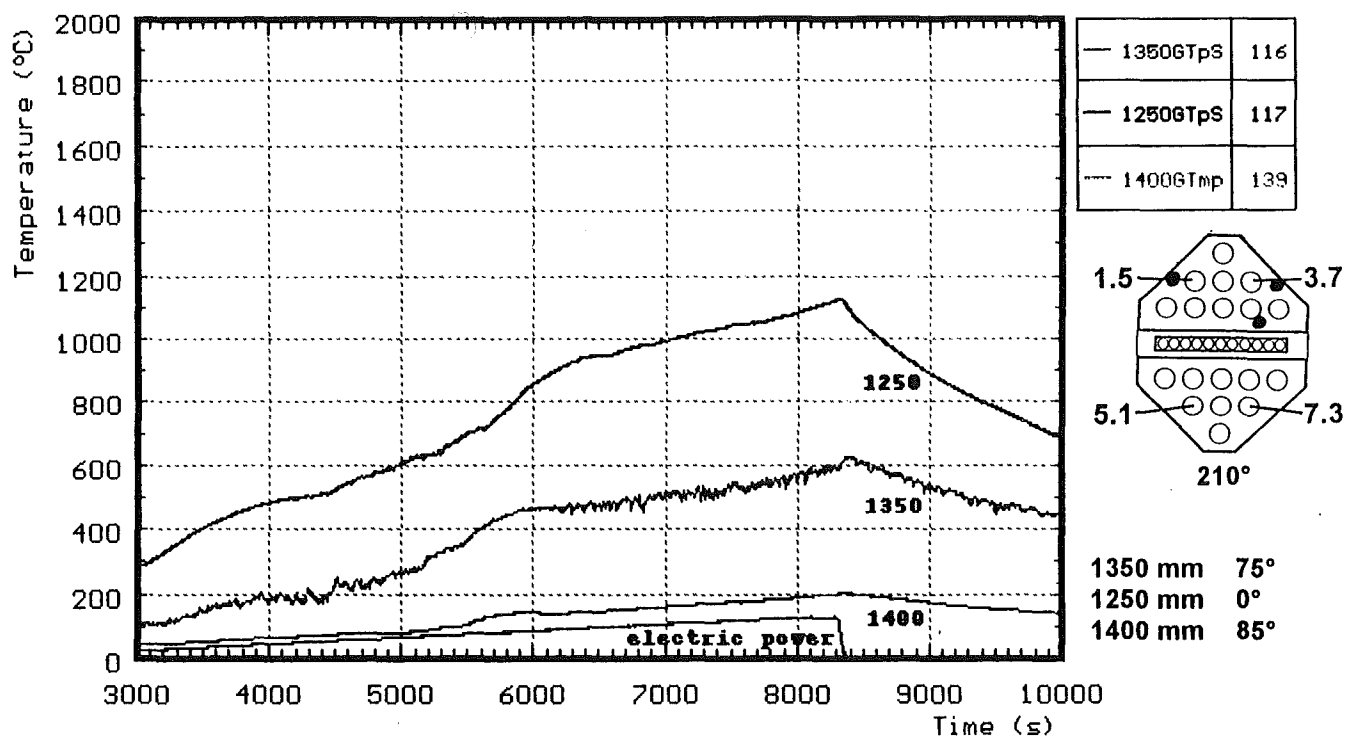


Fig. 35

CORA-33: Temperatures at the bundle head plate

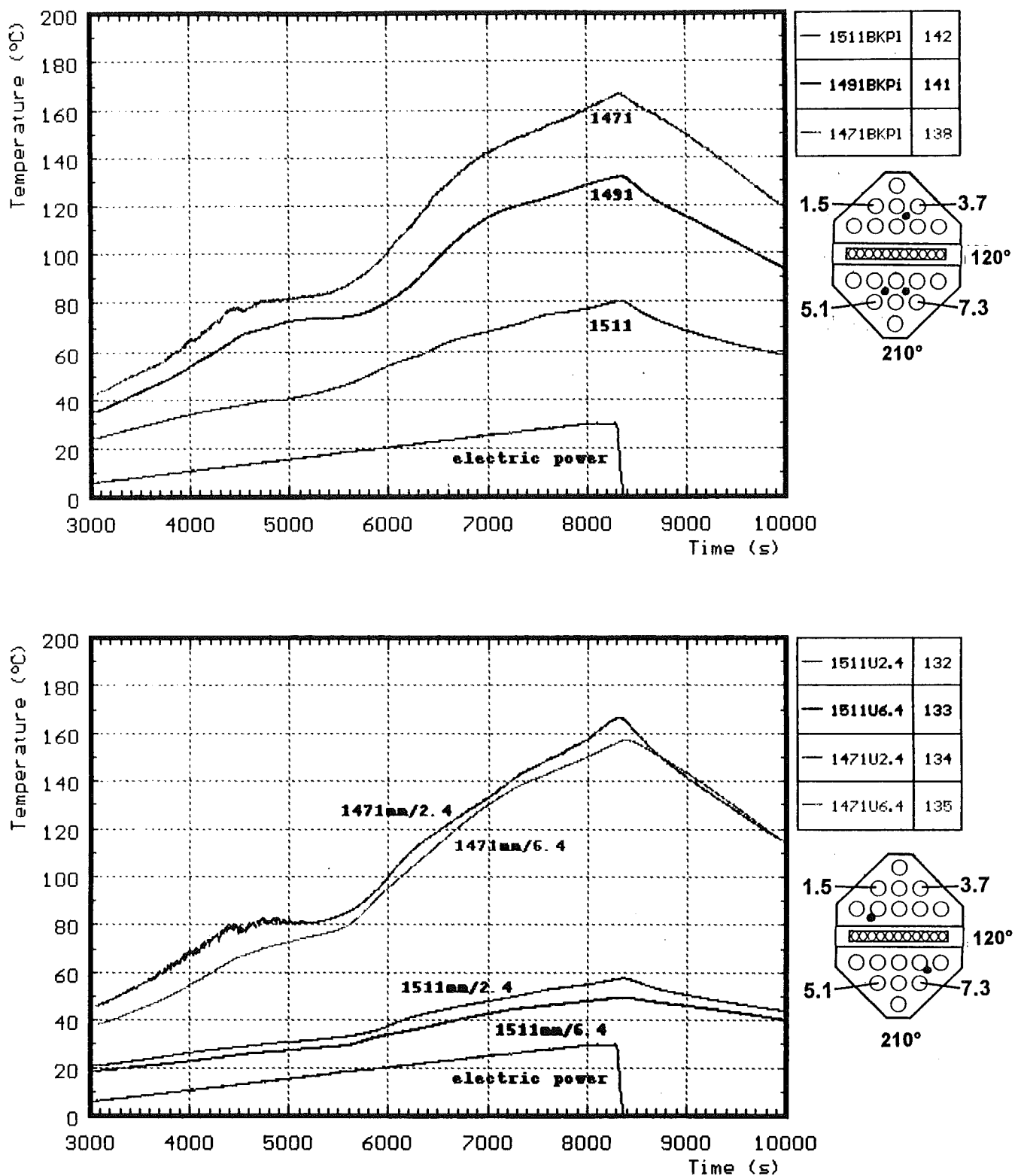
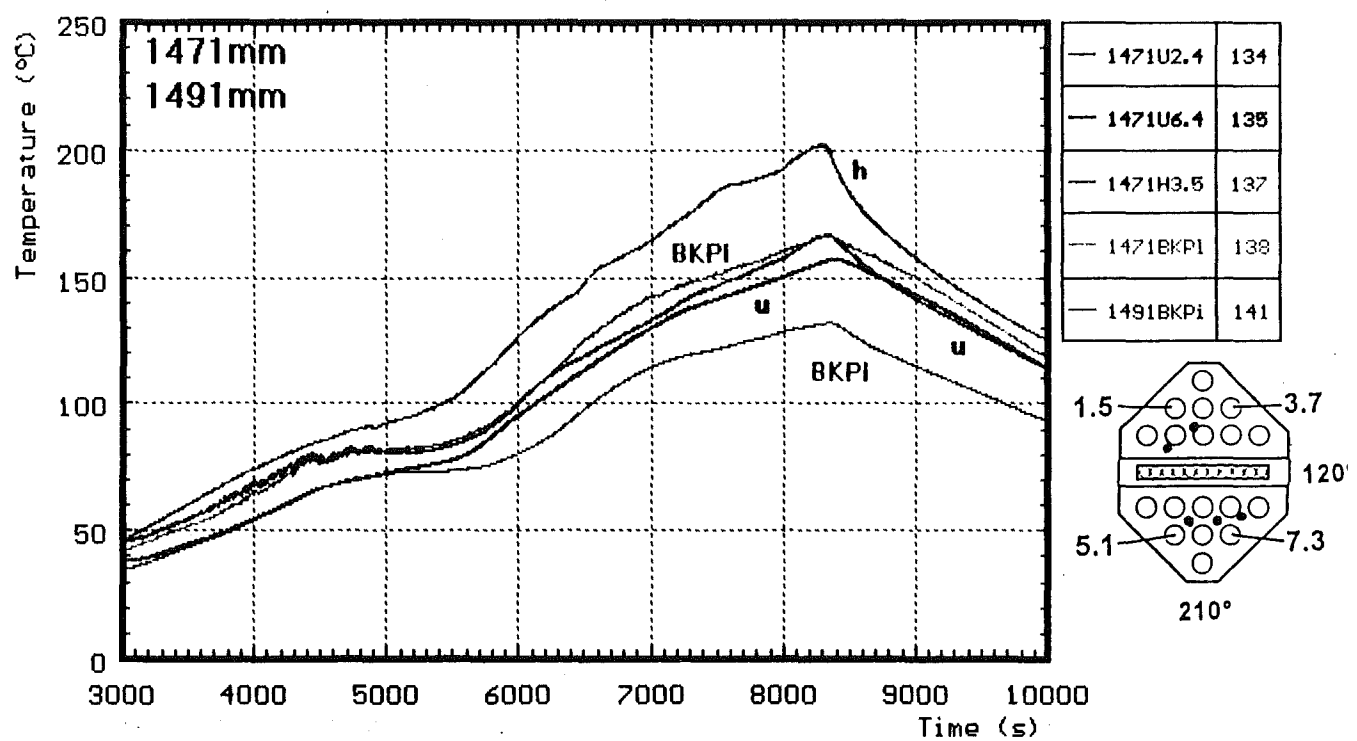
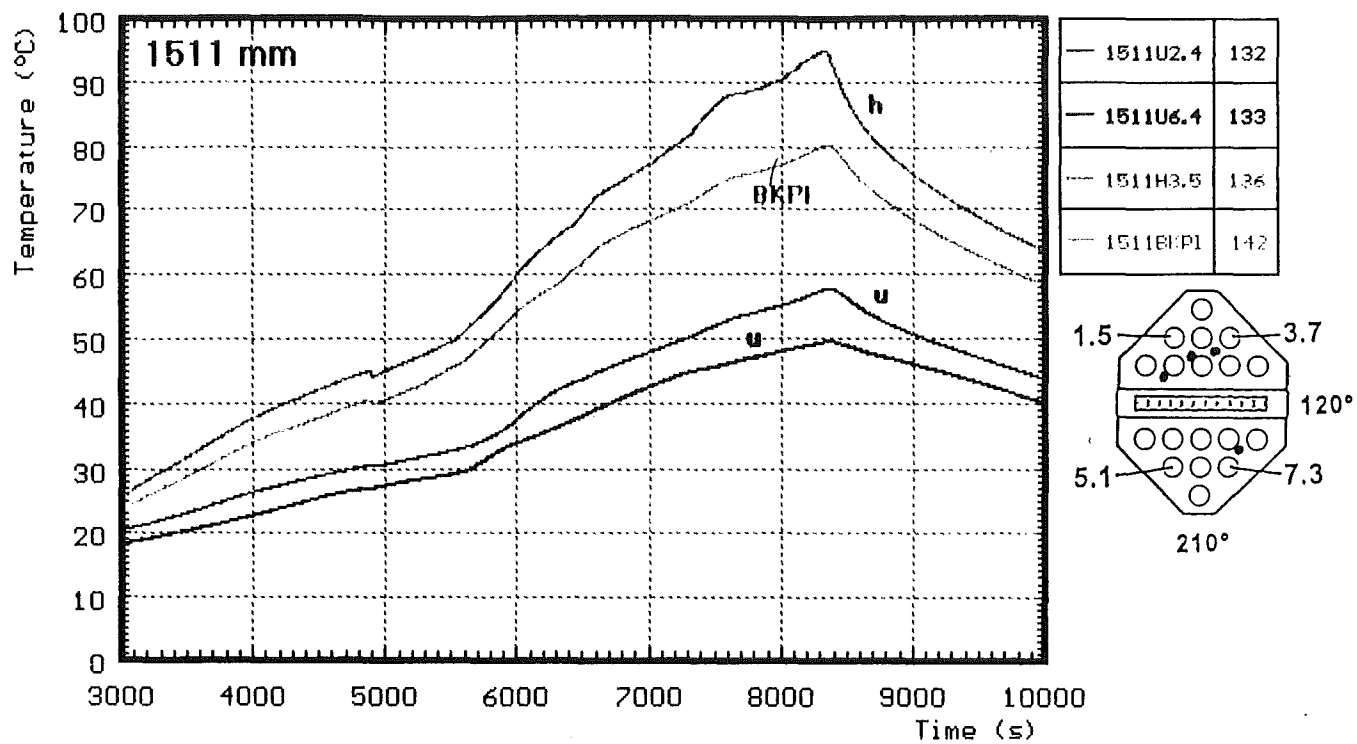


Fig. 36

CORA 33: Temperatures at fixed elevation



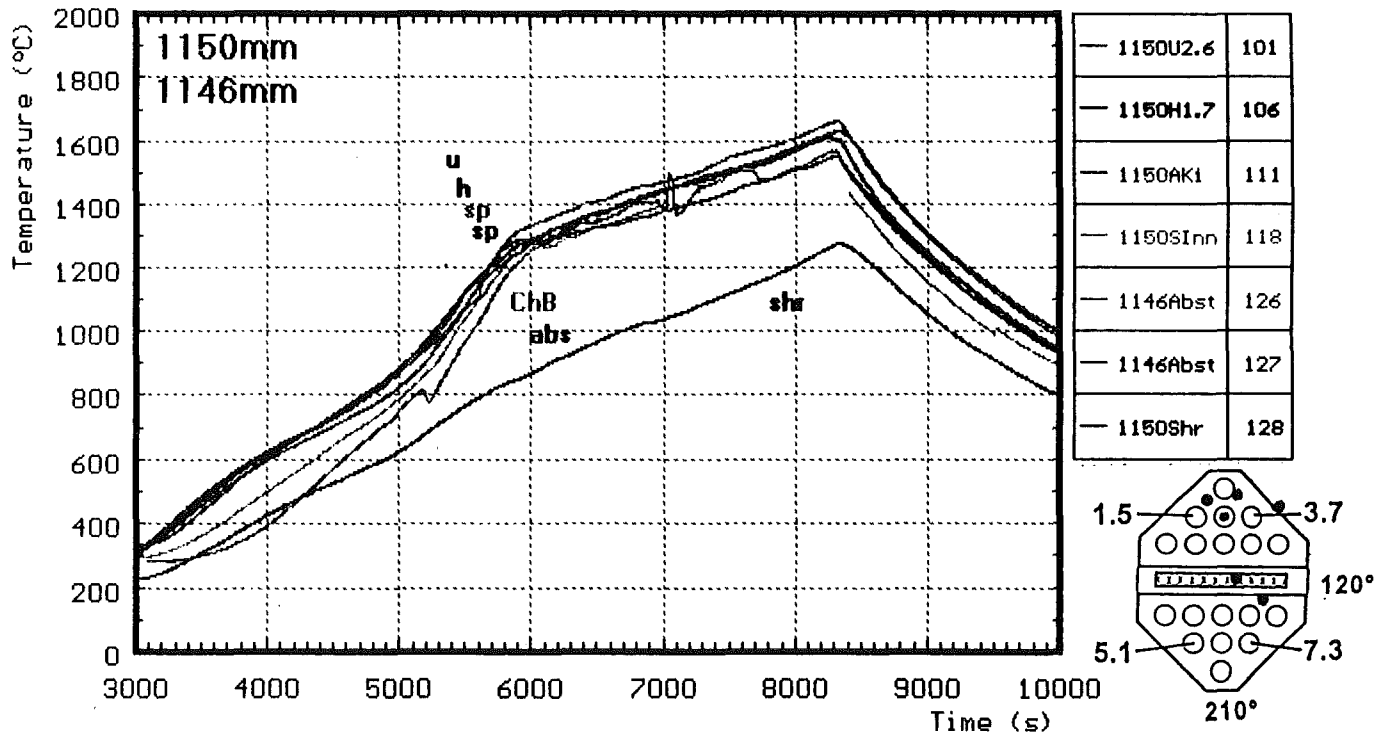
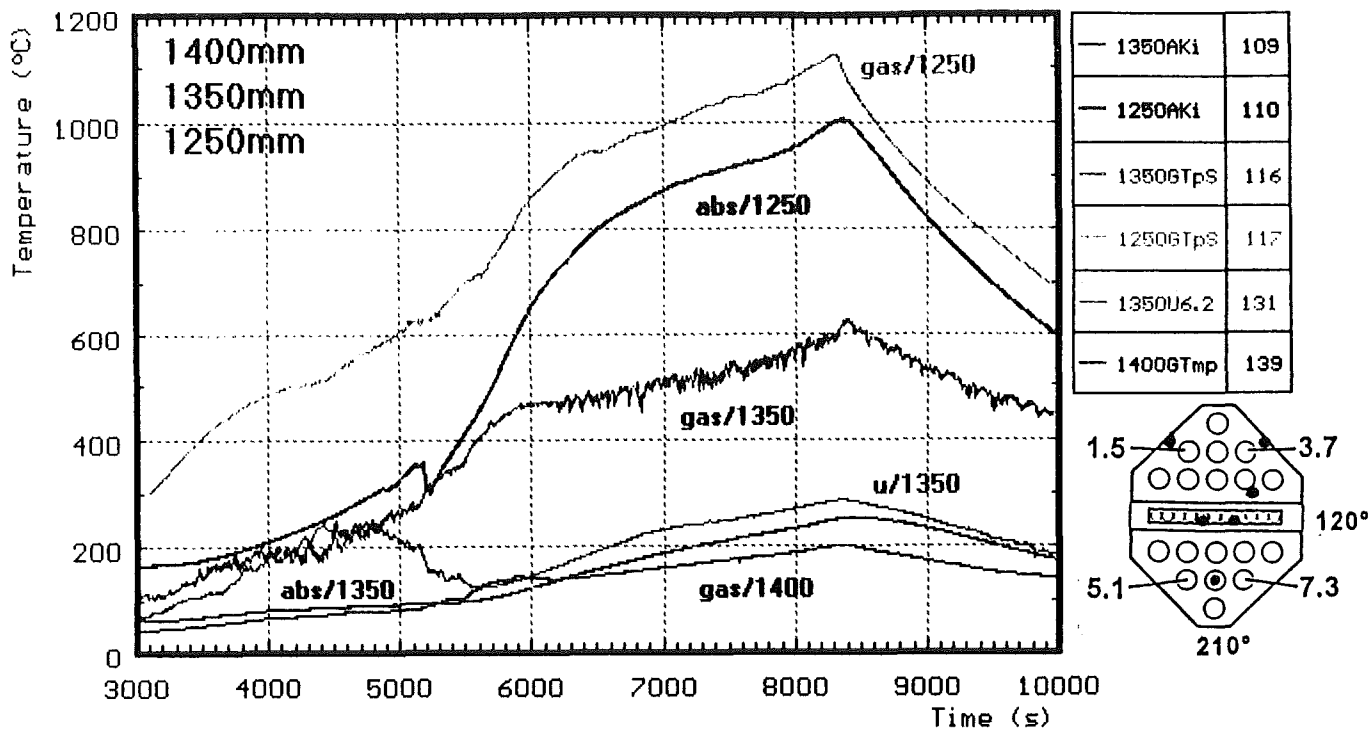
h : heated rods
 u : unheated rods

BKPI : bundle head plate
 gas : gas temperature

Fig. 37

CORA 33:

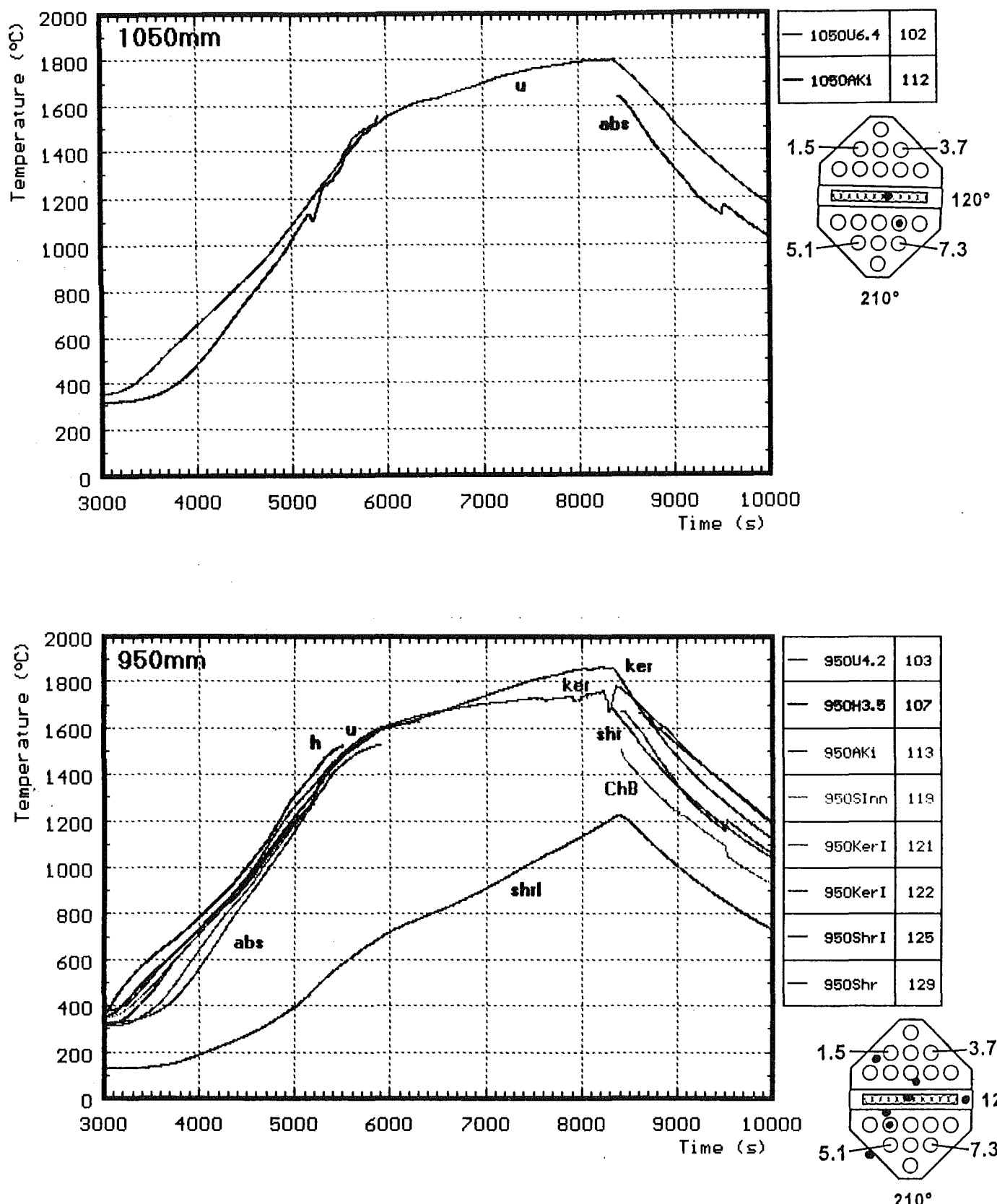
Temperatures at fixed elevation



h : heated rods
u : unheated rods
shr : on shroud
sp : spacer

abs : in absorberblade
ChB : channel box wall
gas : gas temperature

Fig. 38

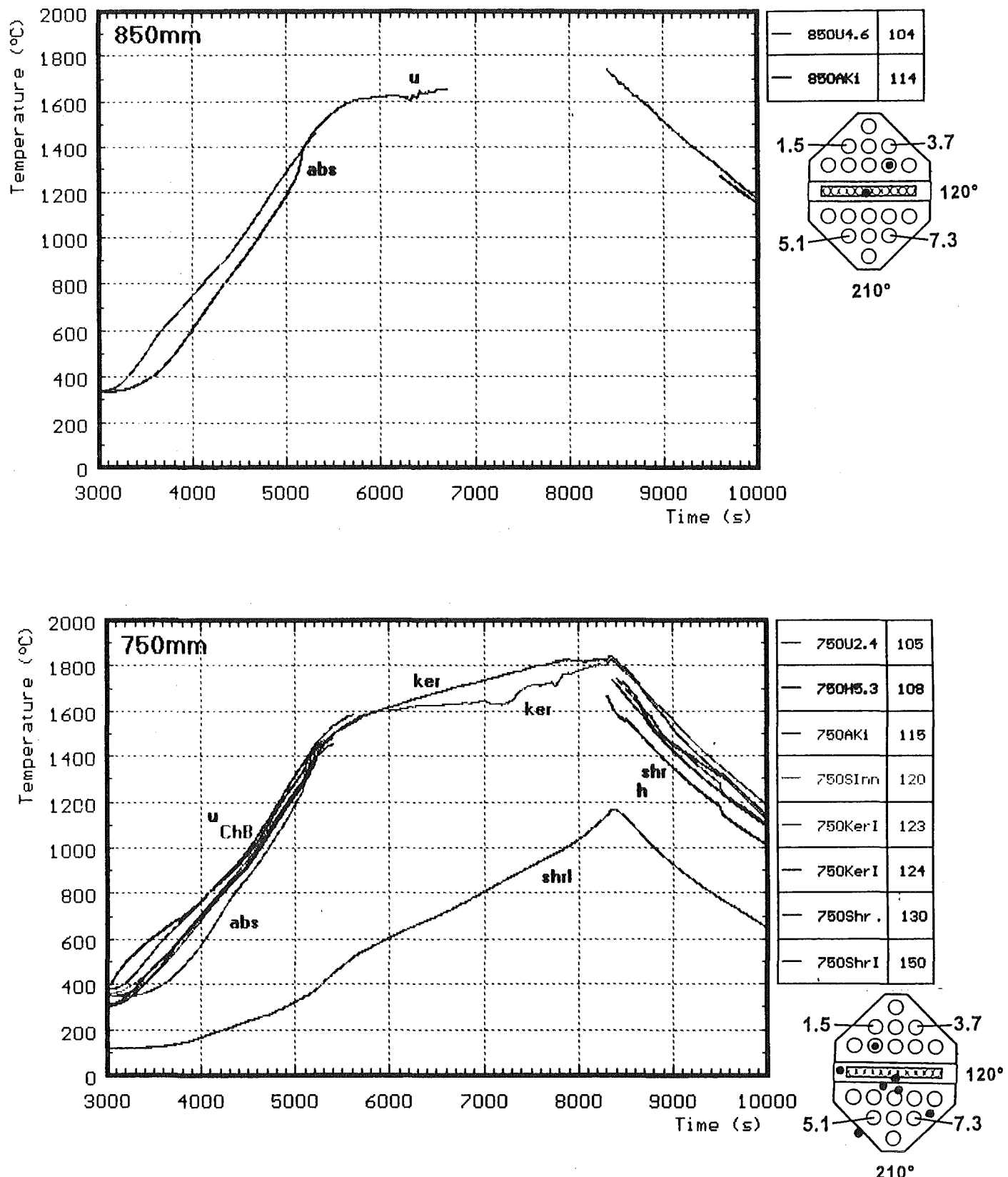
CORA 33:**Temperatures at fixed elevation**

h : heated rods
 u : unheated rods
 shr : on shroud
 shrI : shroud insolation

abs : in absorberblade
 ChB : channel box wall
 ker : ceramic protected termocouples

Fig. 39

CORA 33: Temperatures at fixed elevation

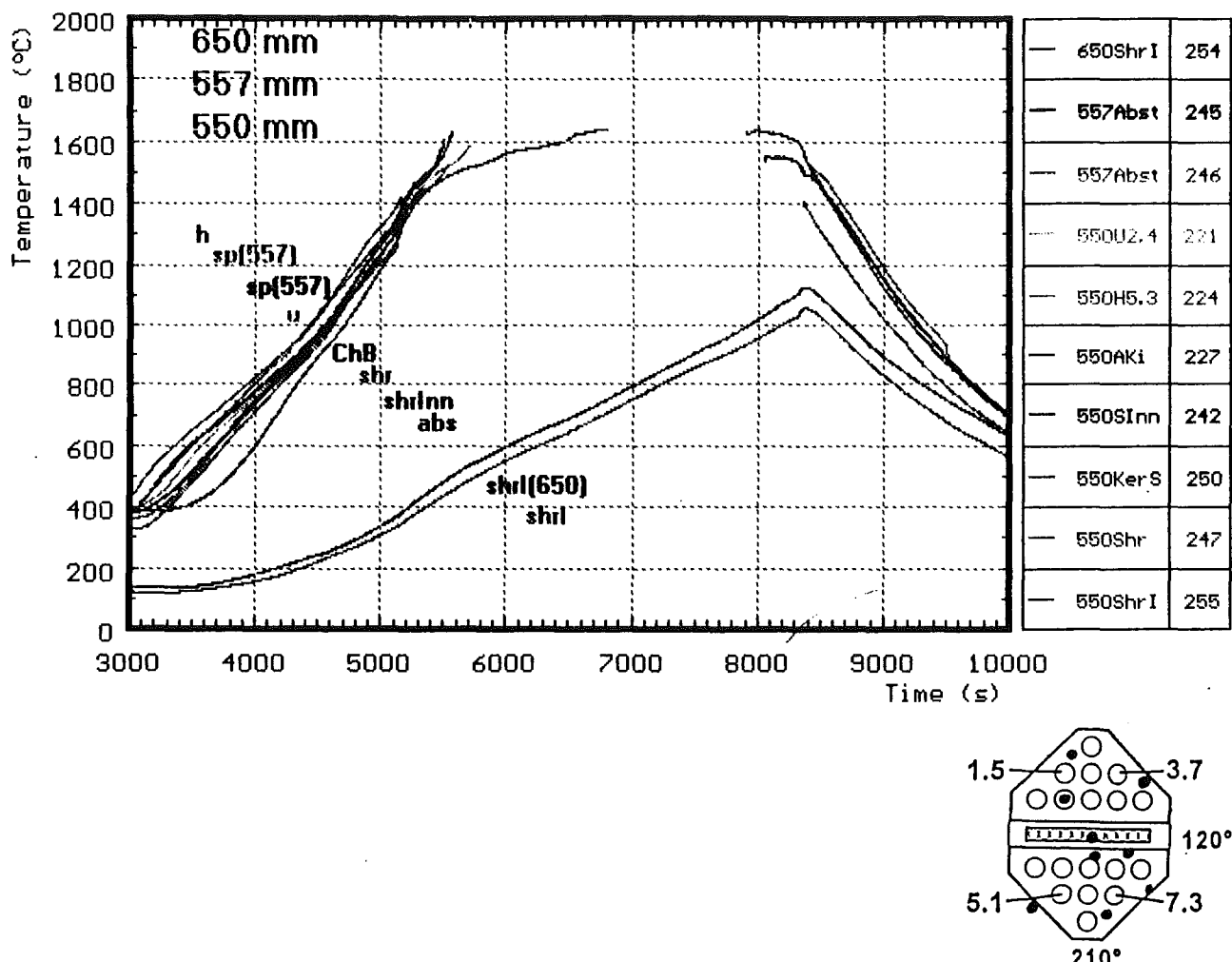


h : heated rods
u : unheated rods
shr : on shroud
shrl : shroud insolation

abs : in absorberblade
ChB : channel box wall
ker : ceramic protected termocouples

Fig. 40

CORA 33: Temperatures at fixed elevation

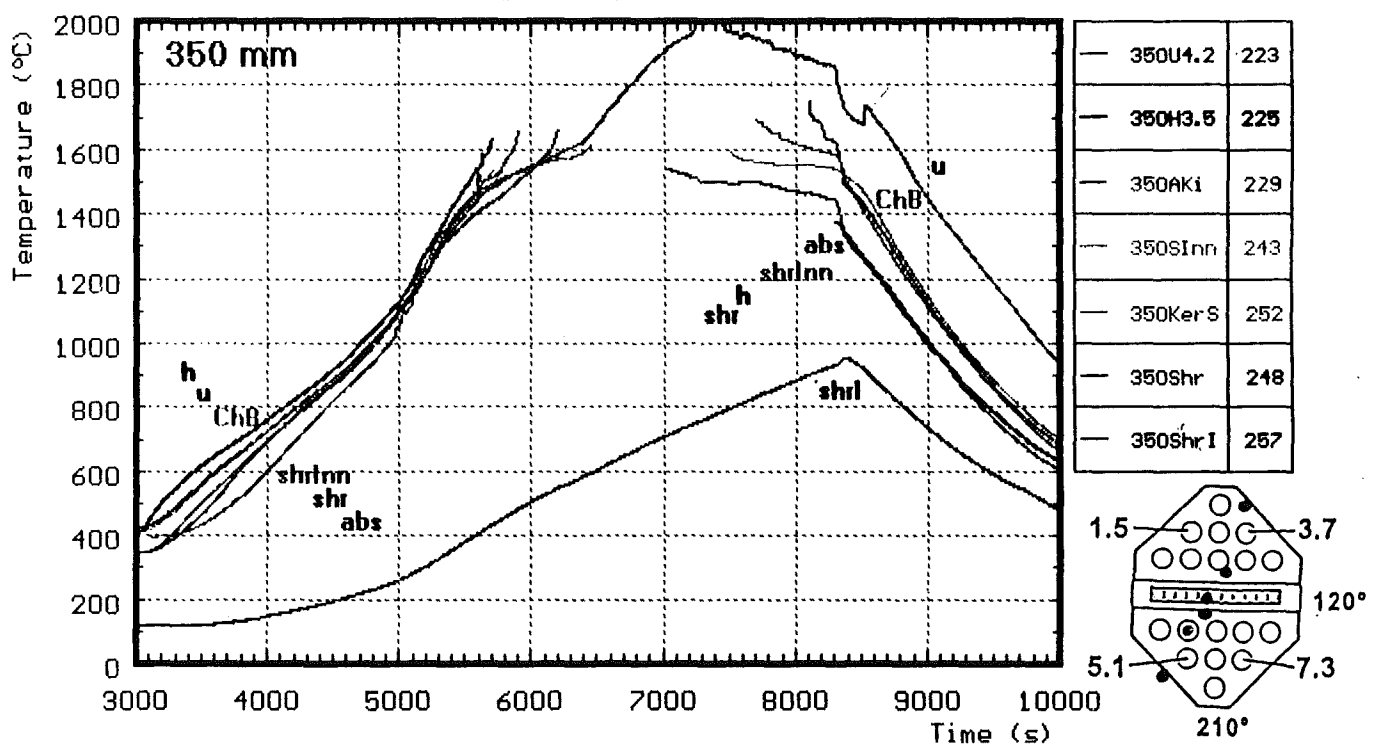
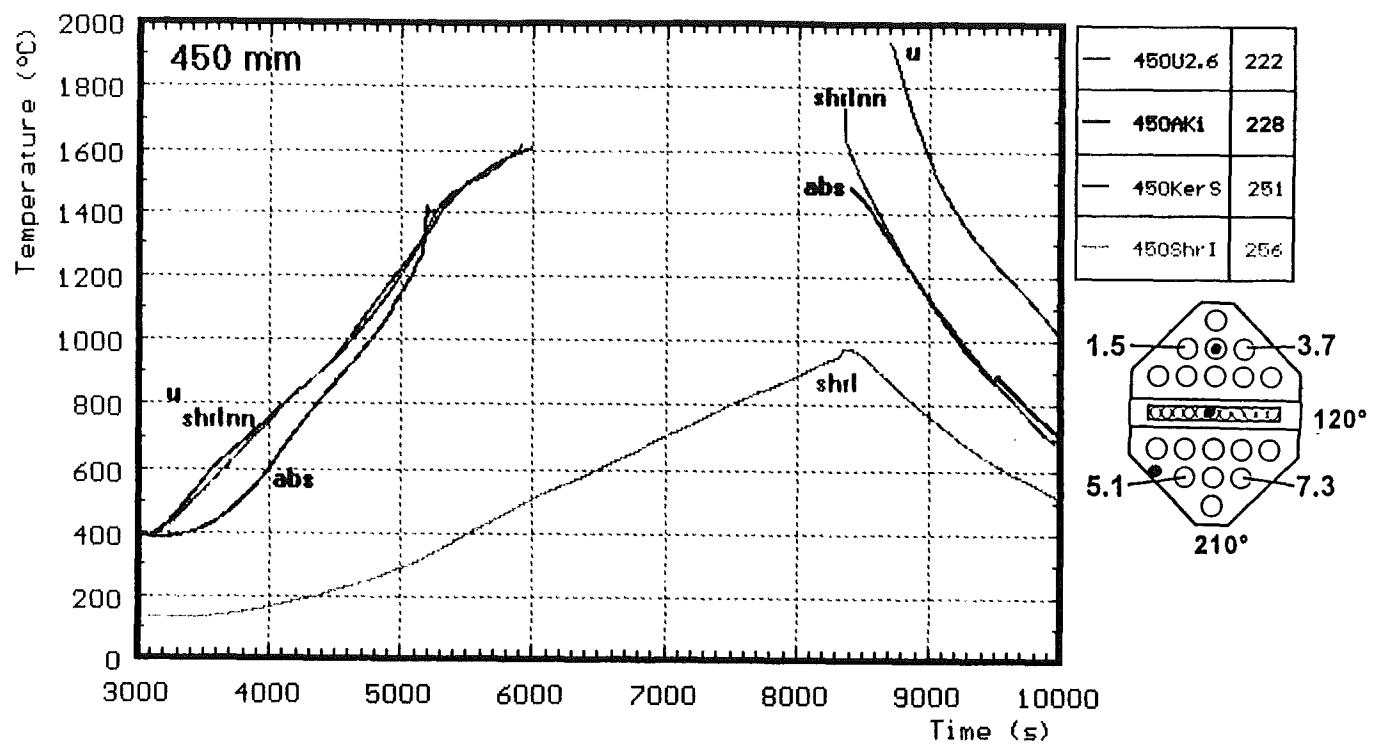


h : heated rods
u : unheated rods
abs : in absorberblade
ChB : channel box wall

shrlnn: inside shroud
shr : on shroud
shrl : shroud insulation
sp : spacer

Fig. 41

CORA 33: Temperatures at fixed elevation

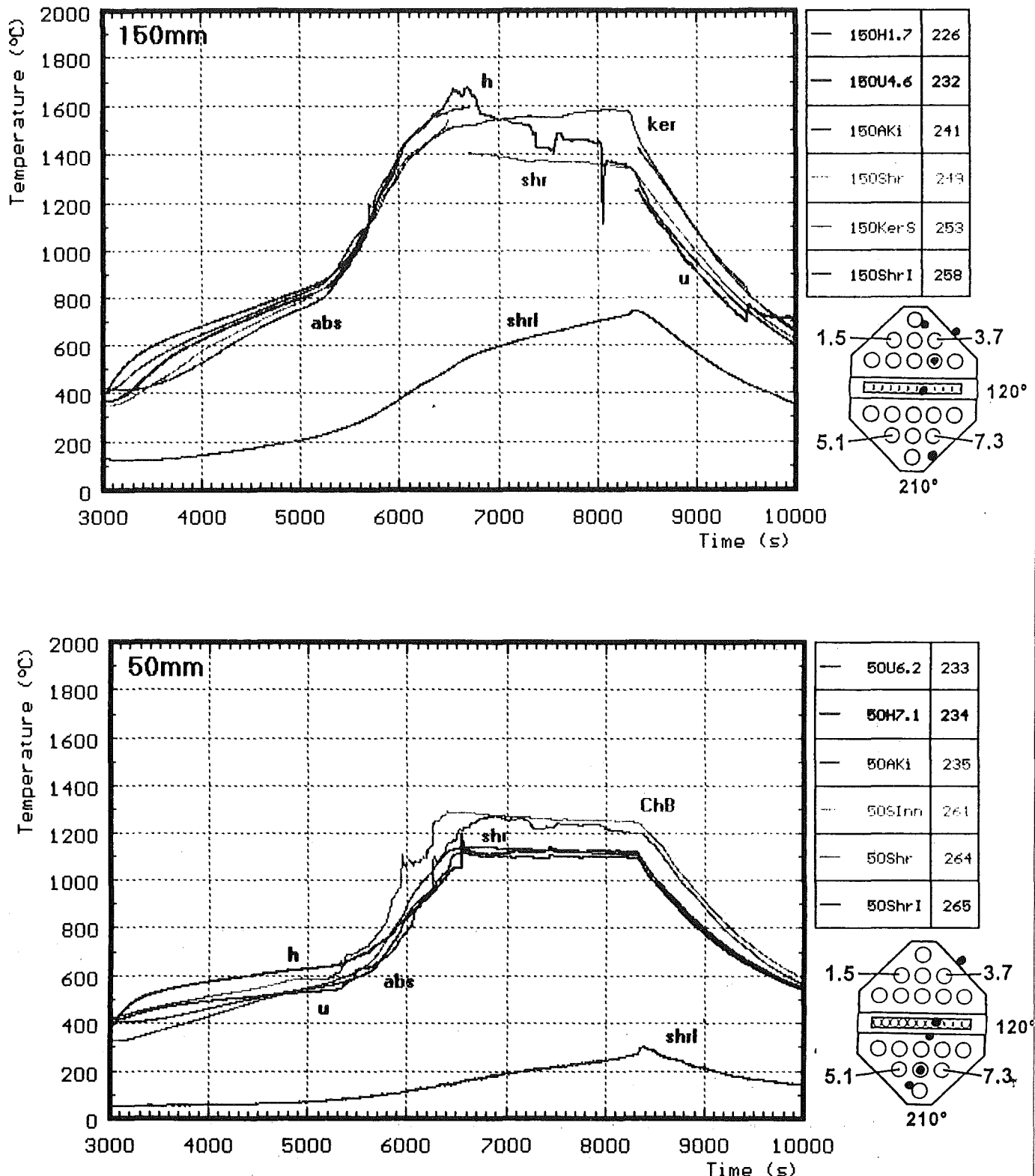


h : heated rods
 u : unheated rods
 abs : in absorberblade
 ChB : channel box wall

shrlnn: inside shroud
 shr : on shroud
 shrl : shroud insulation

Fig. 42

CORA 33: Temperatures at fixed elevation

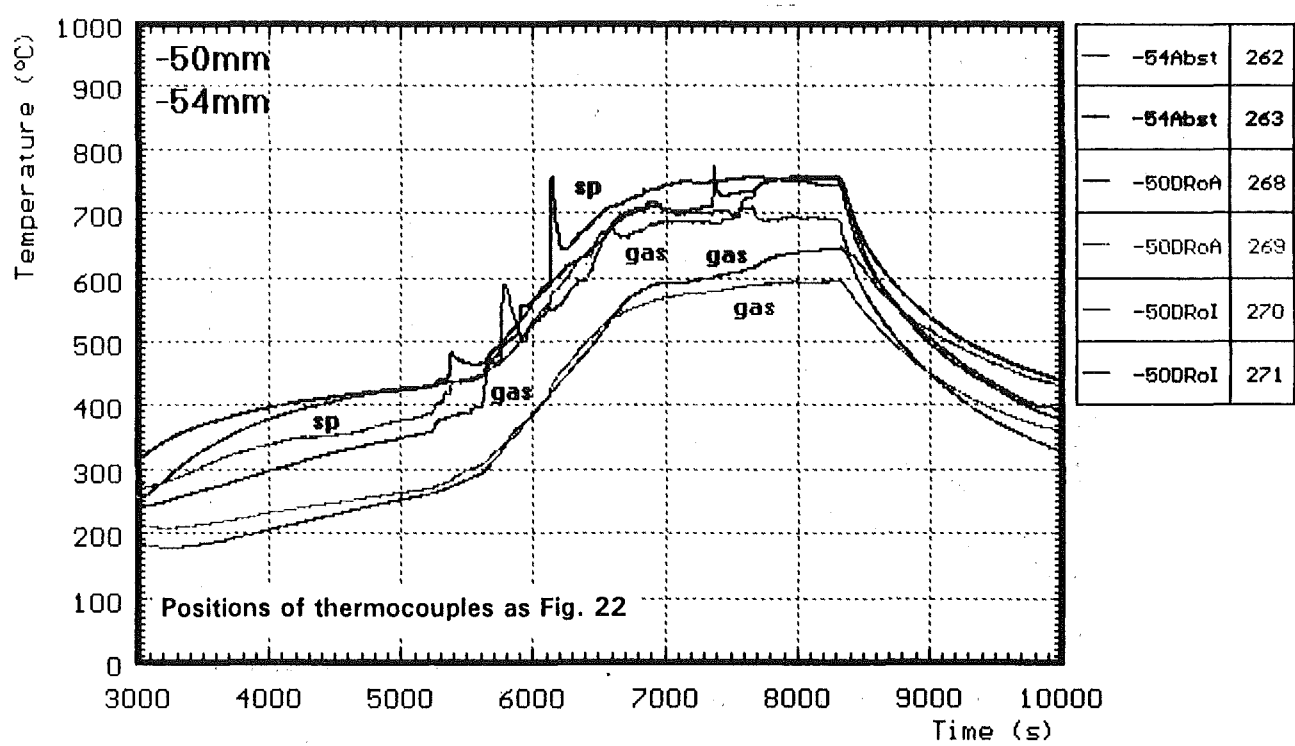
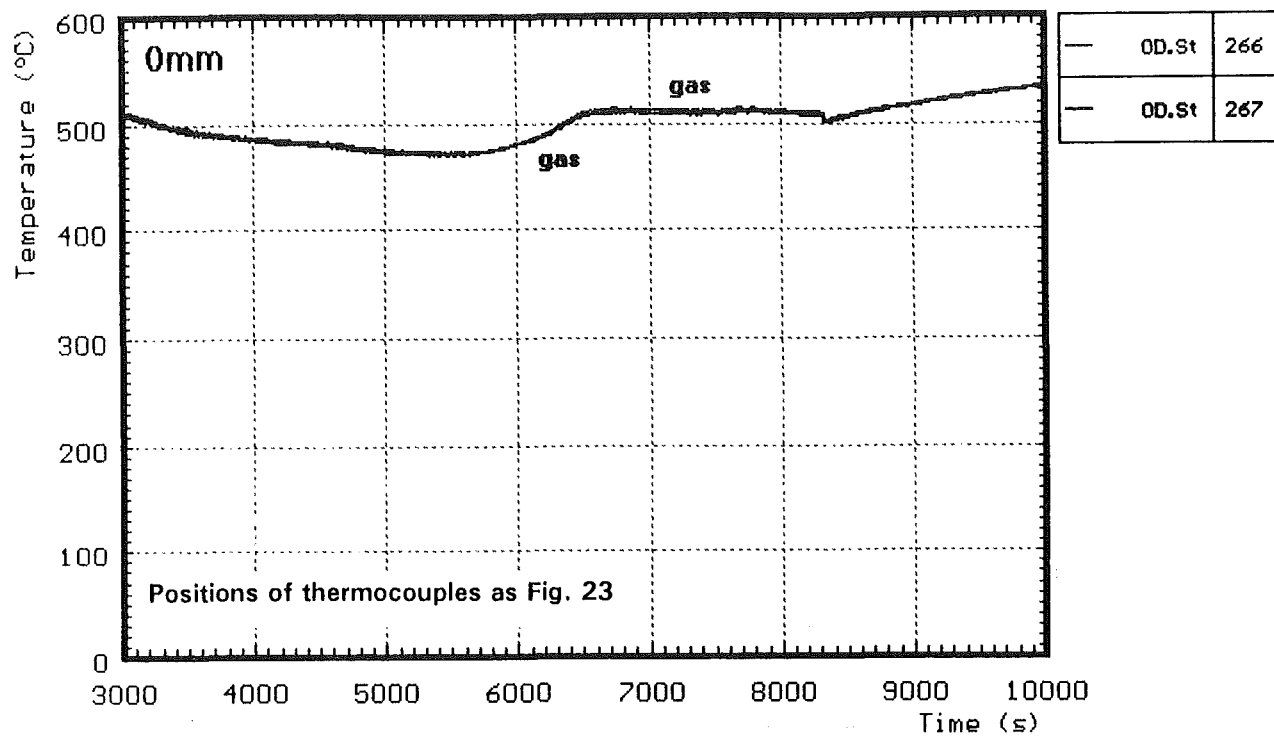


h : heated rods
 u : unheated rods
 shr : on shroud
 shrl : shroud insulation

abs : in absorberblade
 ChB : channel box wall
 ker : ceramic protected termocouples

Fig. 43

CORA 33: Temperatures at fixed elevation



sp : spacer

gas : gas temperature

Fig. 44

CORA-33: Best estimate bundle temperatures at different elevations

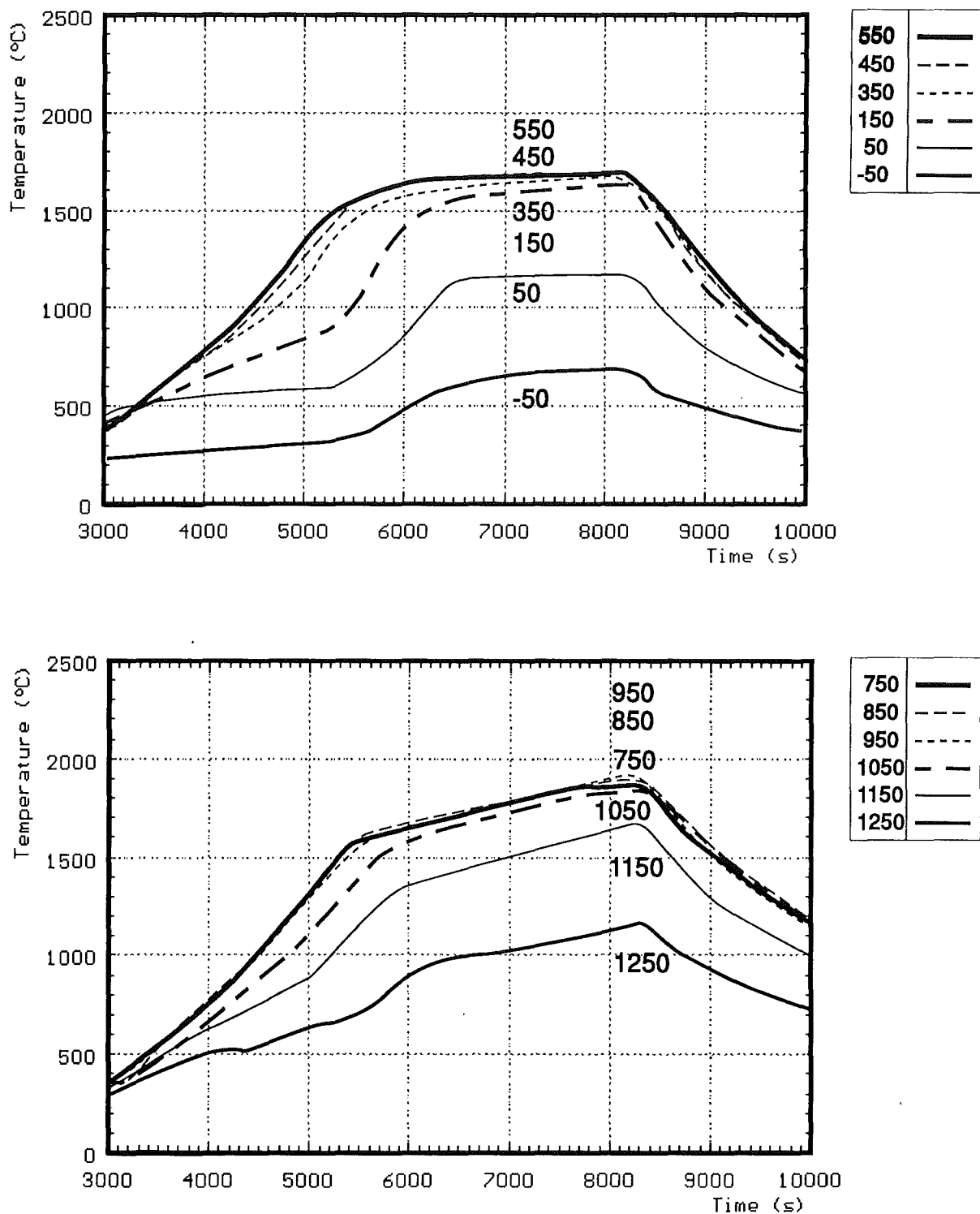


Fig. 45

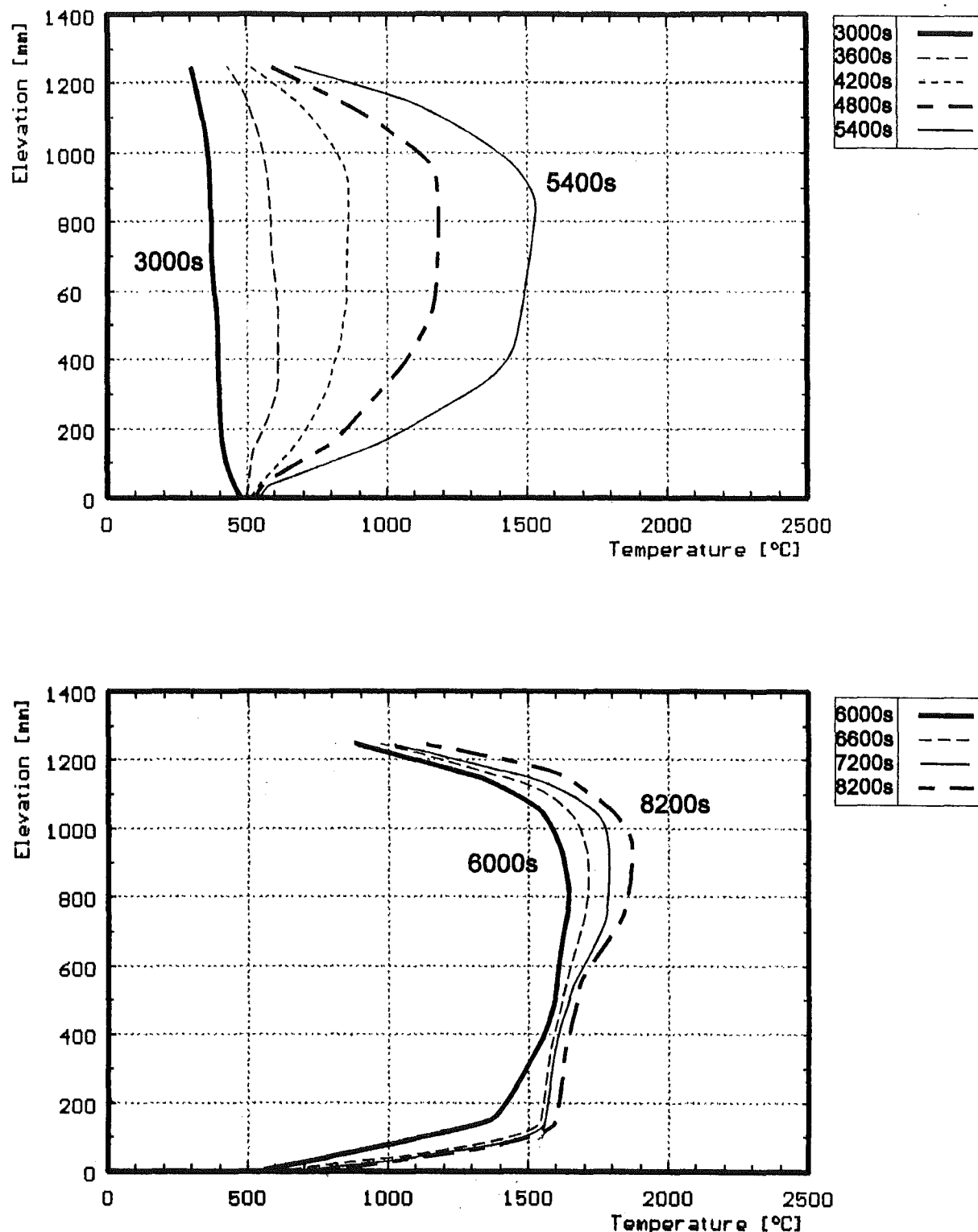
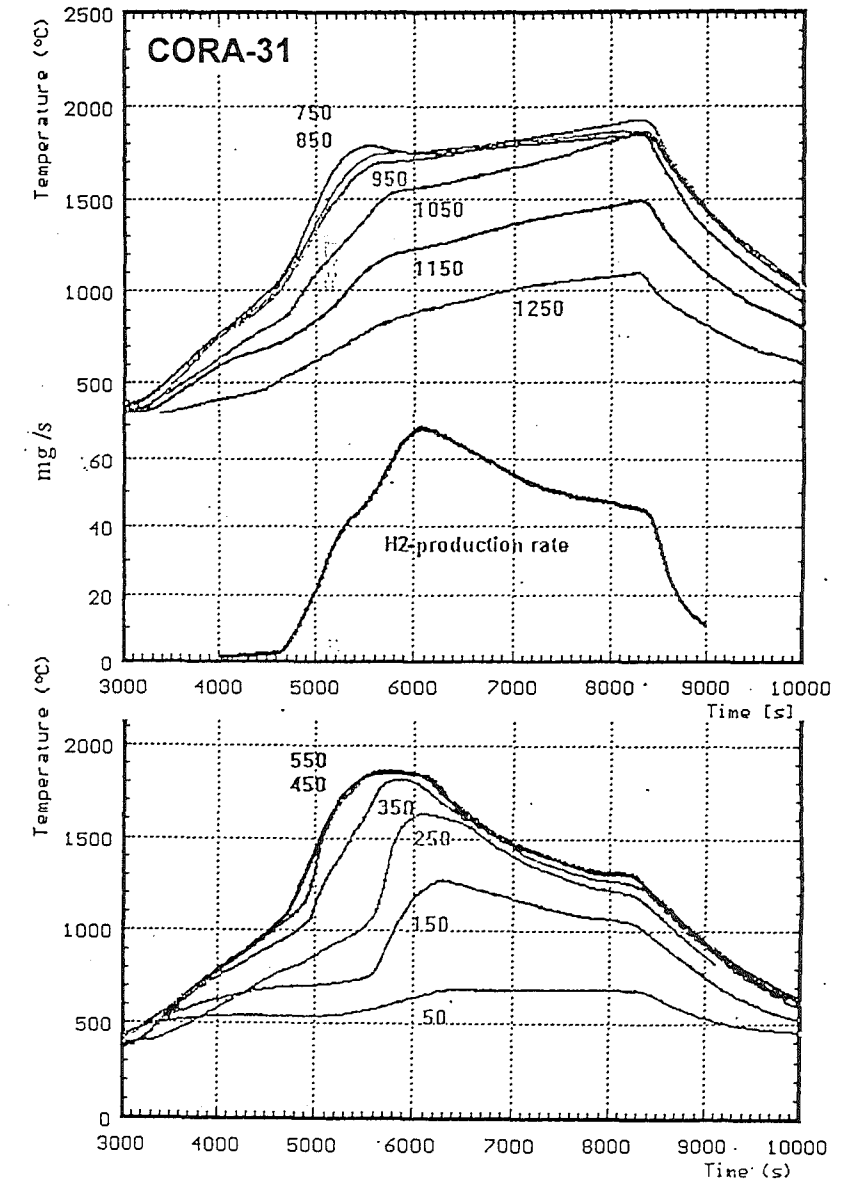
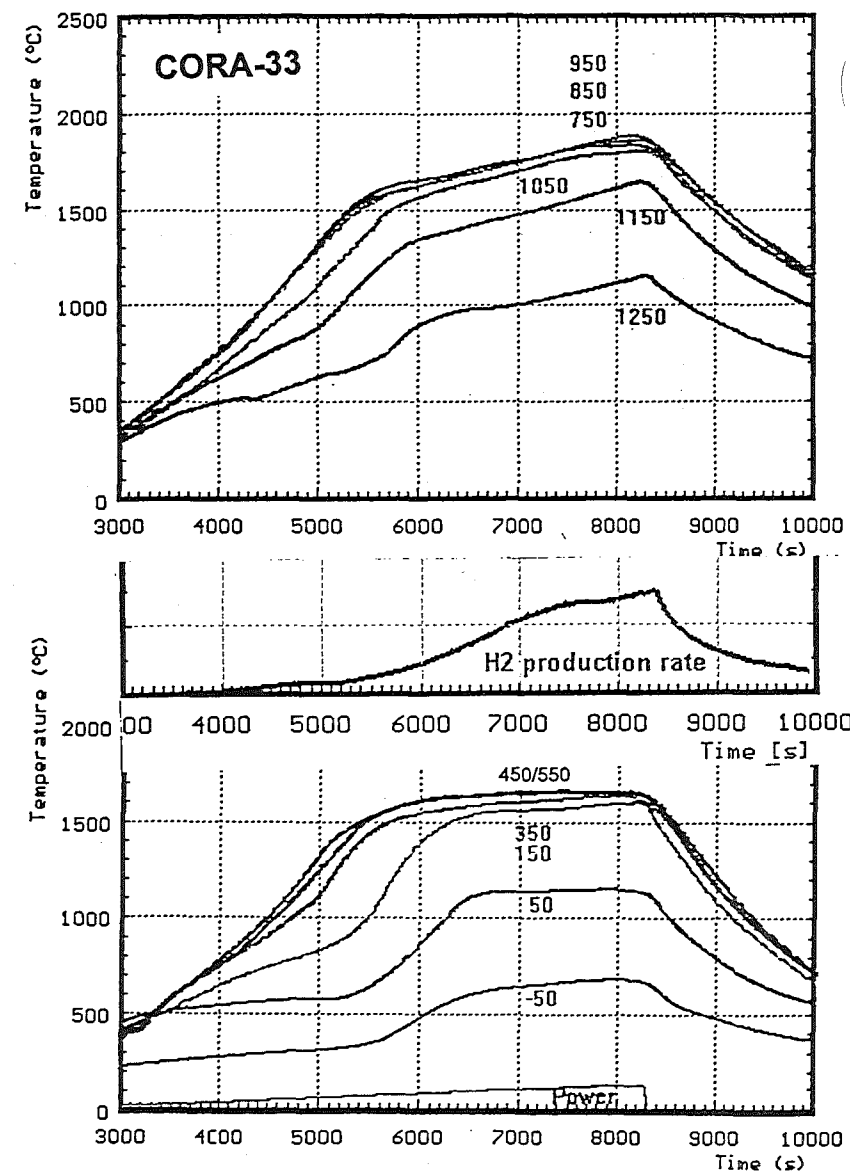


Fig. 46: CORA-33: Best estimate axial distribution of bundle temperatures

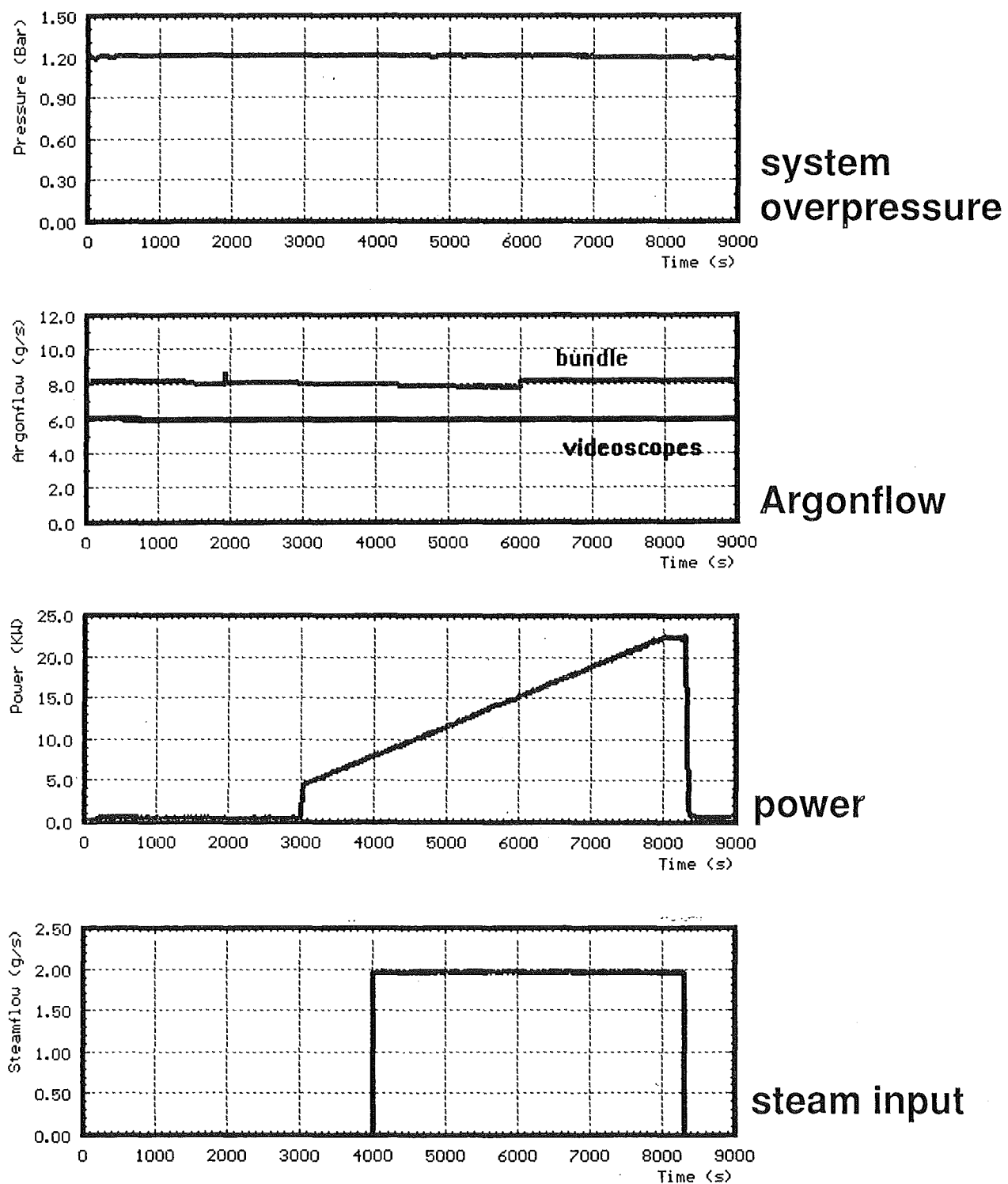
Fig. 46

Fig. 47



Comparison of temperatures with hydrogen production (CORA-33 / CORA-31).

CORA - 31 :



*Fig. 48: Test conduct of CORA-31
System overpressure, Argonflow, steam input and power*

Fig. 49a :

CORA-33

Position of thermocouples in the high-temperature shield

ANGLE \angle	30°	55°	75°	120°	145°	165°	210°	235°	255°	300°	345°				
RADIUS (mm)	153	153	153	153	153	153	153	153	153	153	153	172	192	255	293
1250											174 33Ni				
1150											175 56Ni				
1050											176 55Ni				
950		162 54Ni			166 53Ni			170 52Ni			177 51Ni	188 29Ni	191 30Ni	194 38Ni	197 39Ni
850											178 24Ni				
750											179 23Ni				
650											180 22Ni				
550	slot161 19Ni		163 18Ni	165 17Ni		167 16Ni	169 15Ni		171 14Ni	173 13Ni	181 12Ni	189 20Ni	192 21Ni	195 36Ni	198 37Ni
450											182 11Ni				
350											183 10Ni				
250											184 9Ni				
150											185 8Ni				
50			164 5Ni			168 4Ni			172 3Ni		186 2Ni	190 6Ni	193 7Ni	196 34Ni	199 35Ni
-50											187 1Ni				

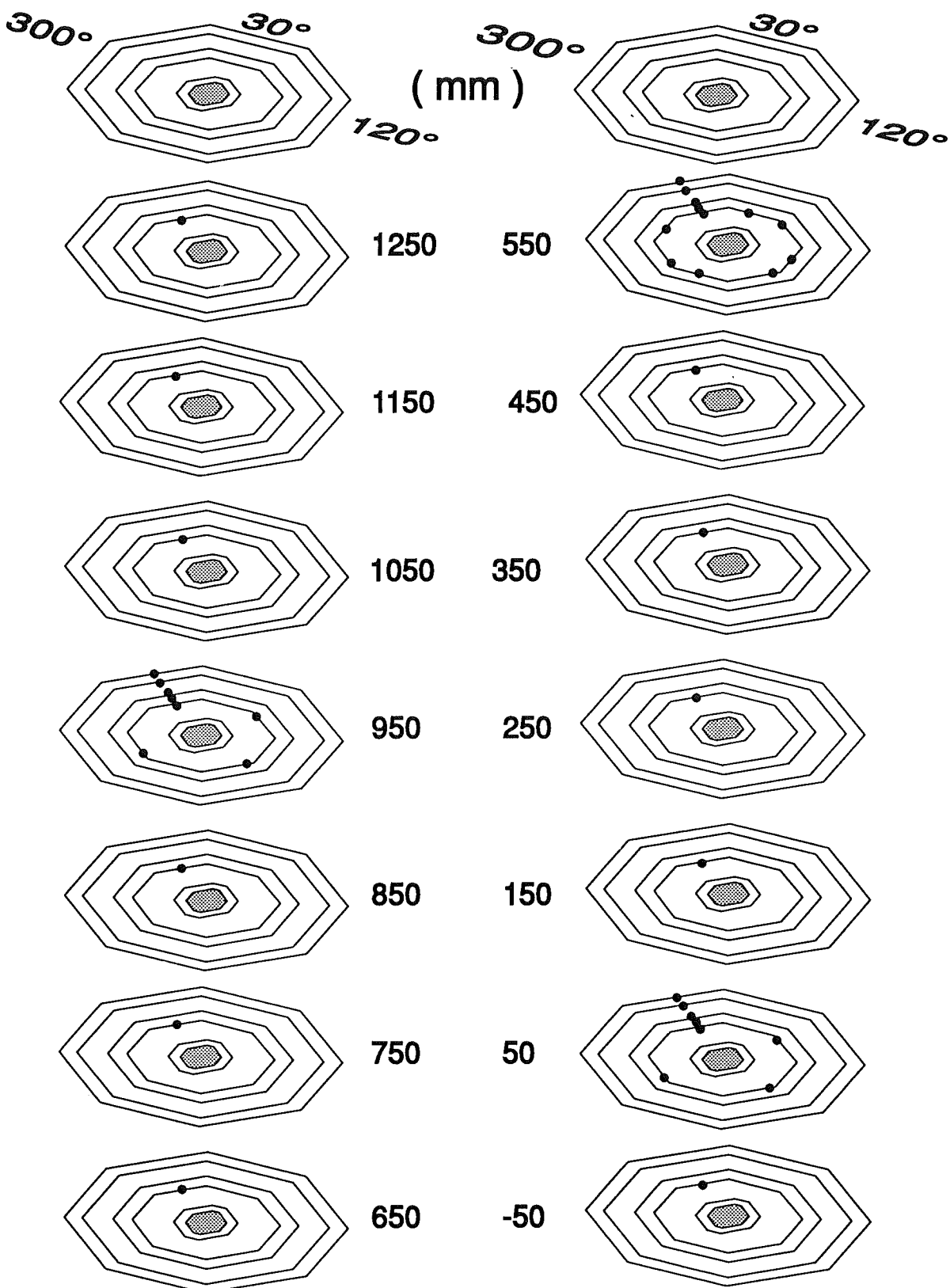


Fig. 49b: Locations of thermocouples in the high-temperature shield (CORA - 33)

CORA-33: Temperatures of HTS

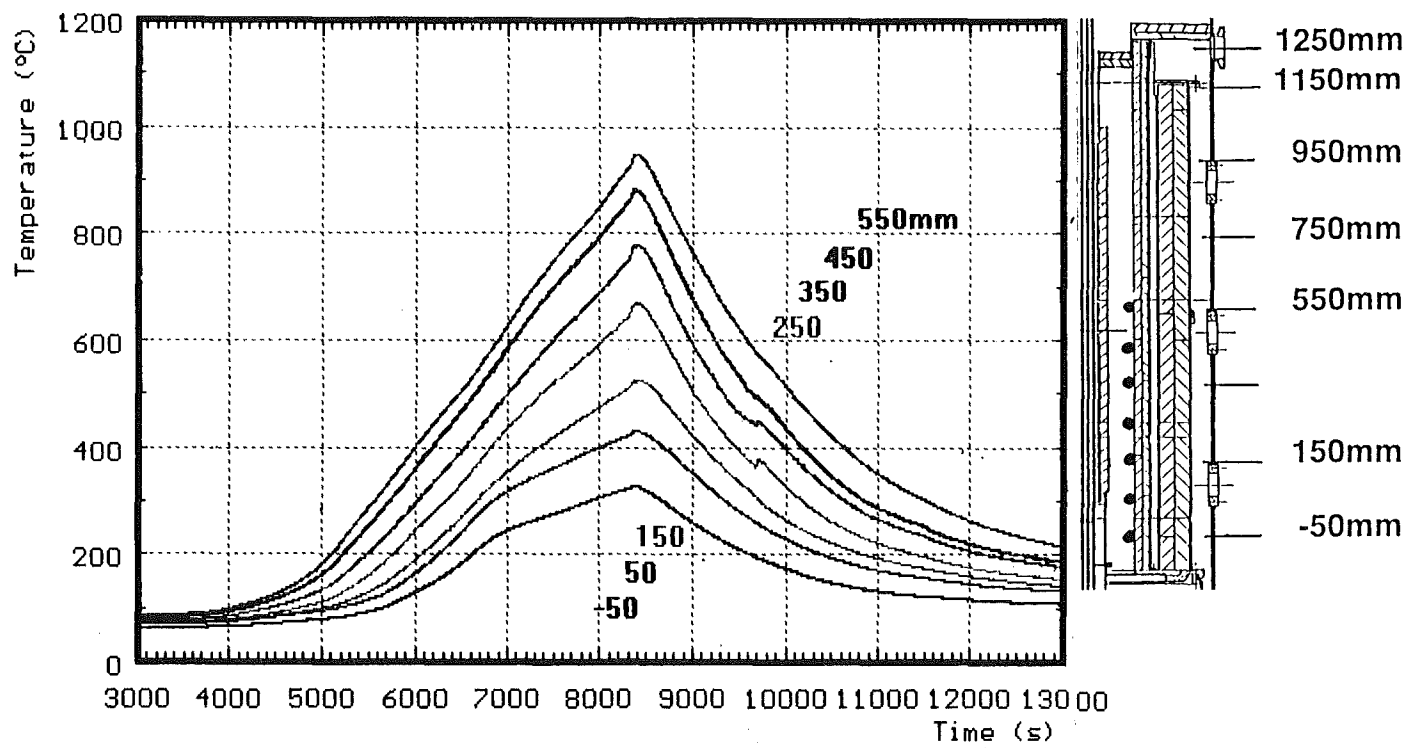
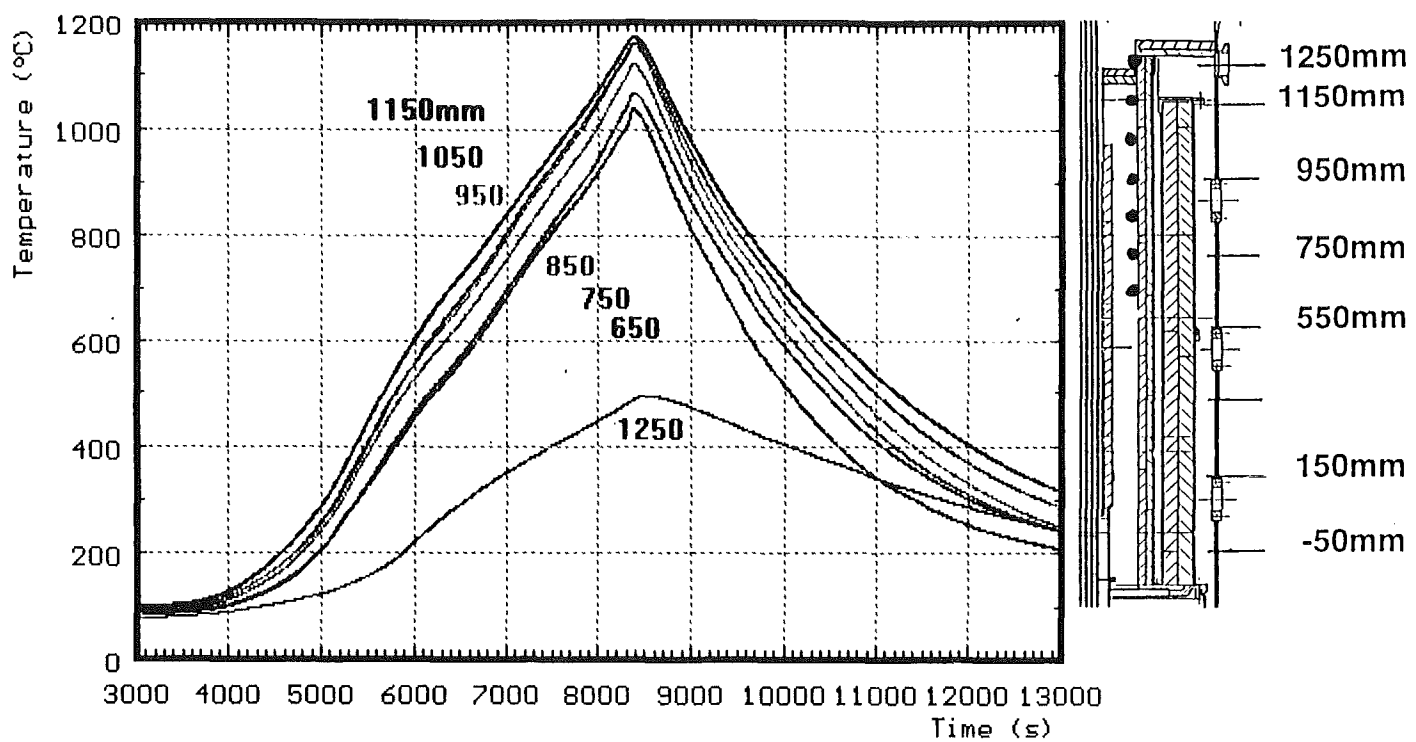


Fig. 50: Temperatures on inner surface at 153 mm radius;
(345°)

CORA-33: Temperatures of HTS

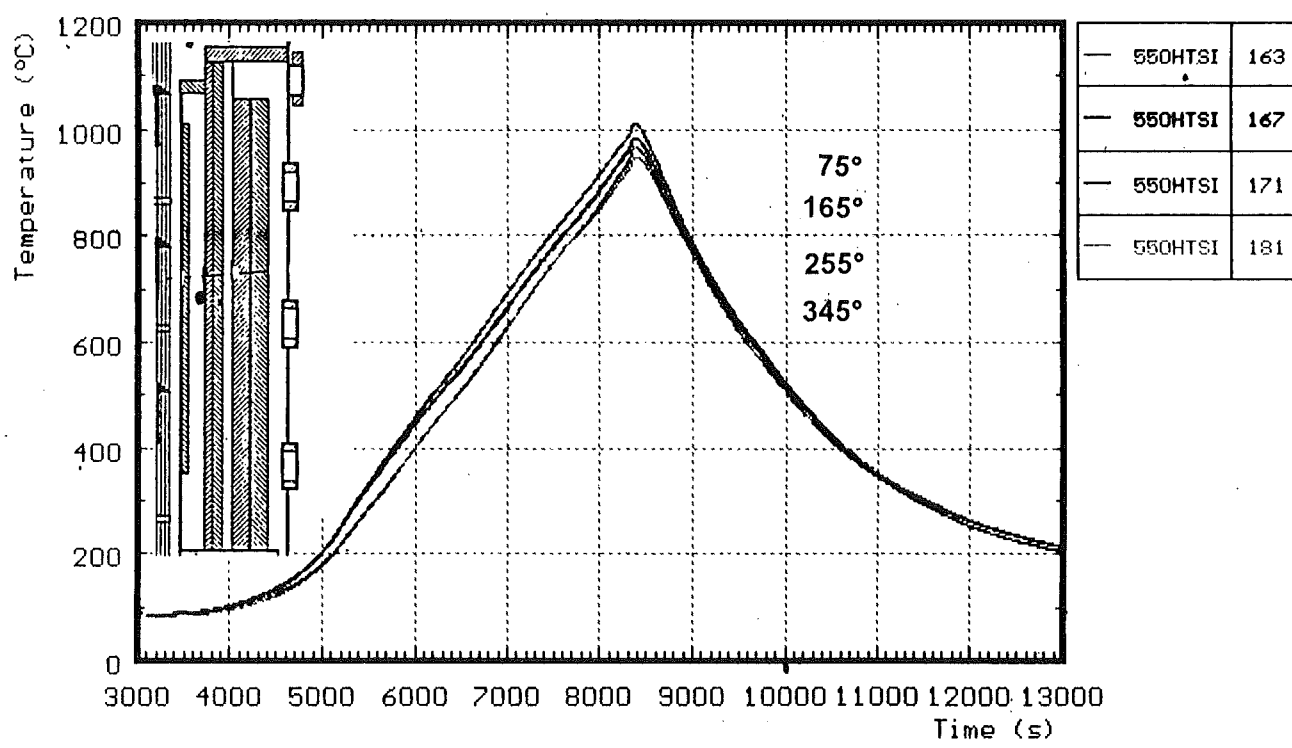
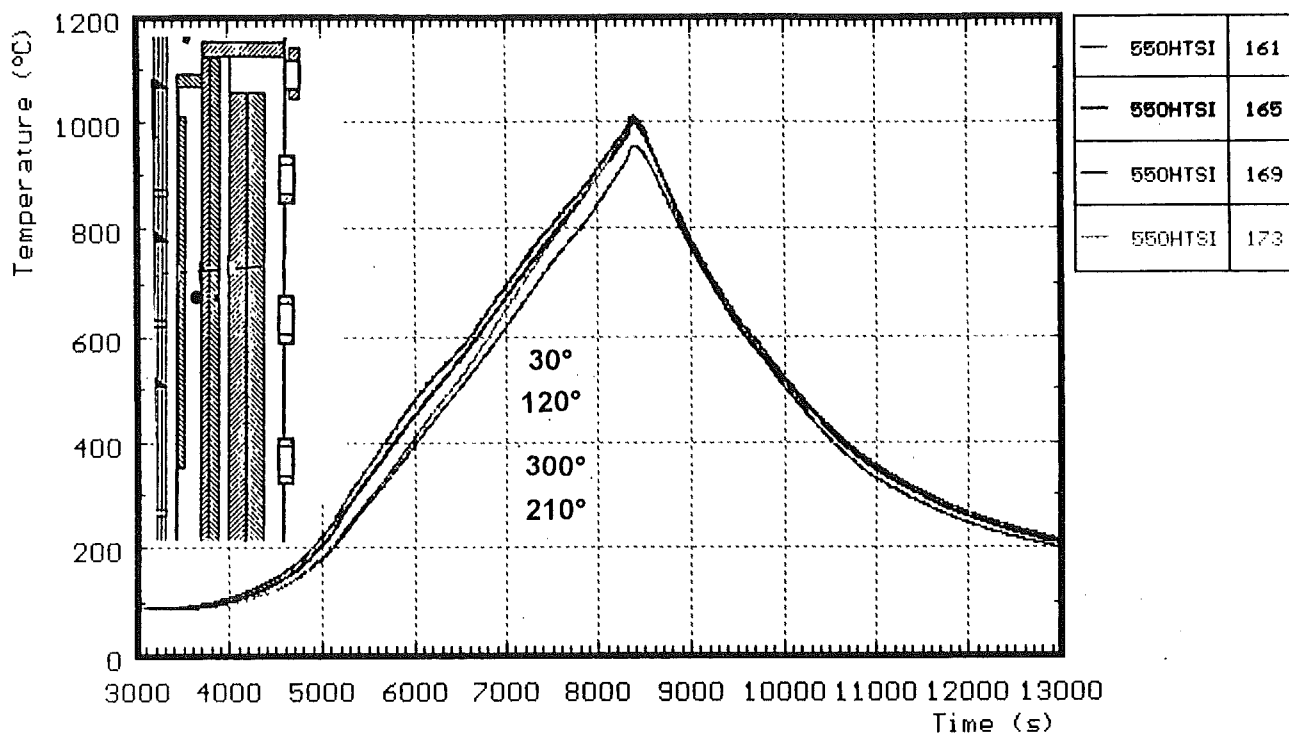


Fig. 51: Comparision on inner surface at 153 mm radius; 550 mm elevation

CORA-33:

Temperatures of HTS

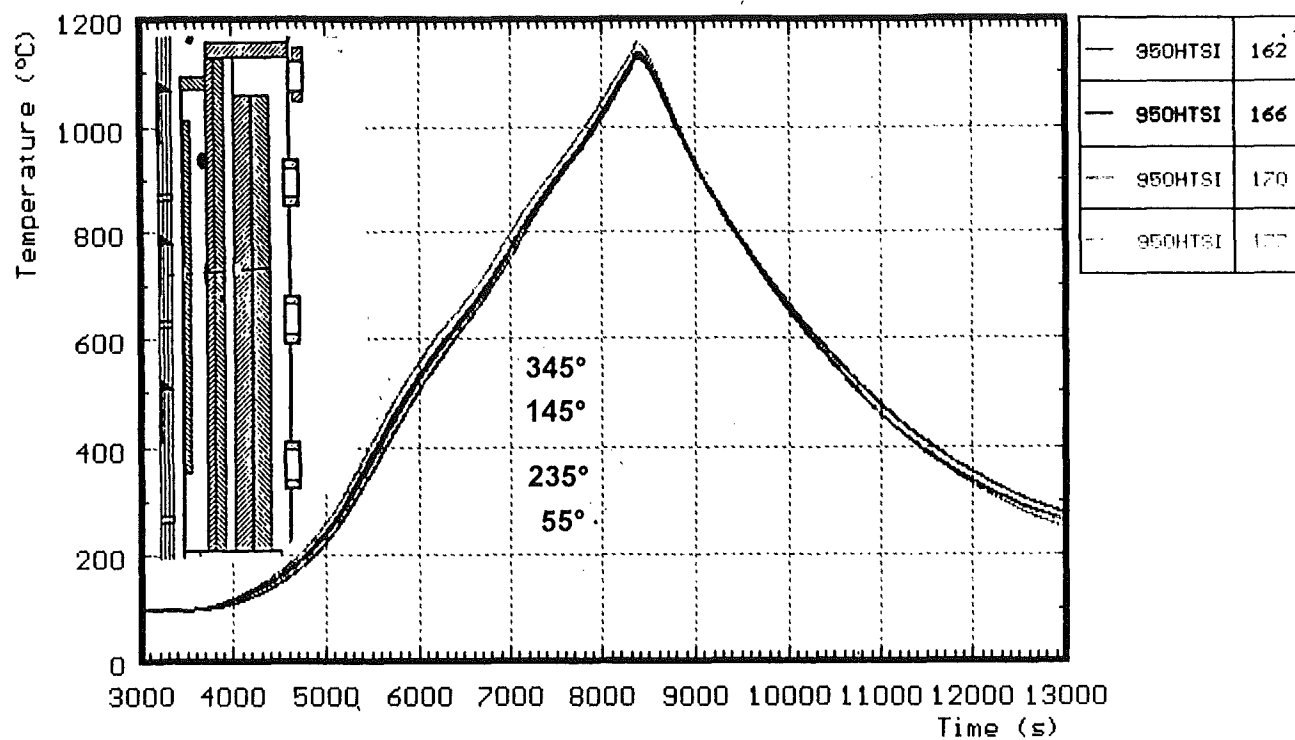


Fig. 52: Comparision on inner surface at 153 mm radius; 950 mm elevation

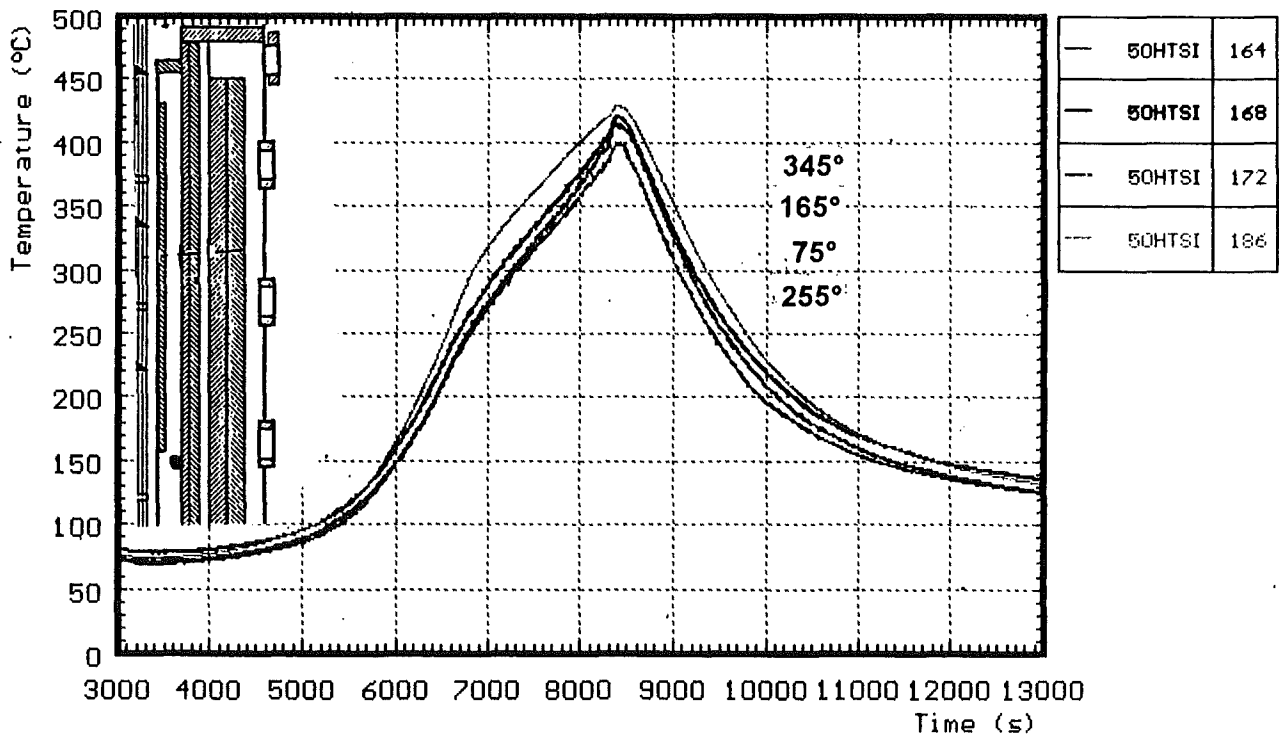


Fig. 53: Comparision on inner surface at 153 mm radius; 50 mm elevation

CORA-33:

Temperatures of HTS

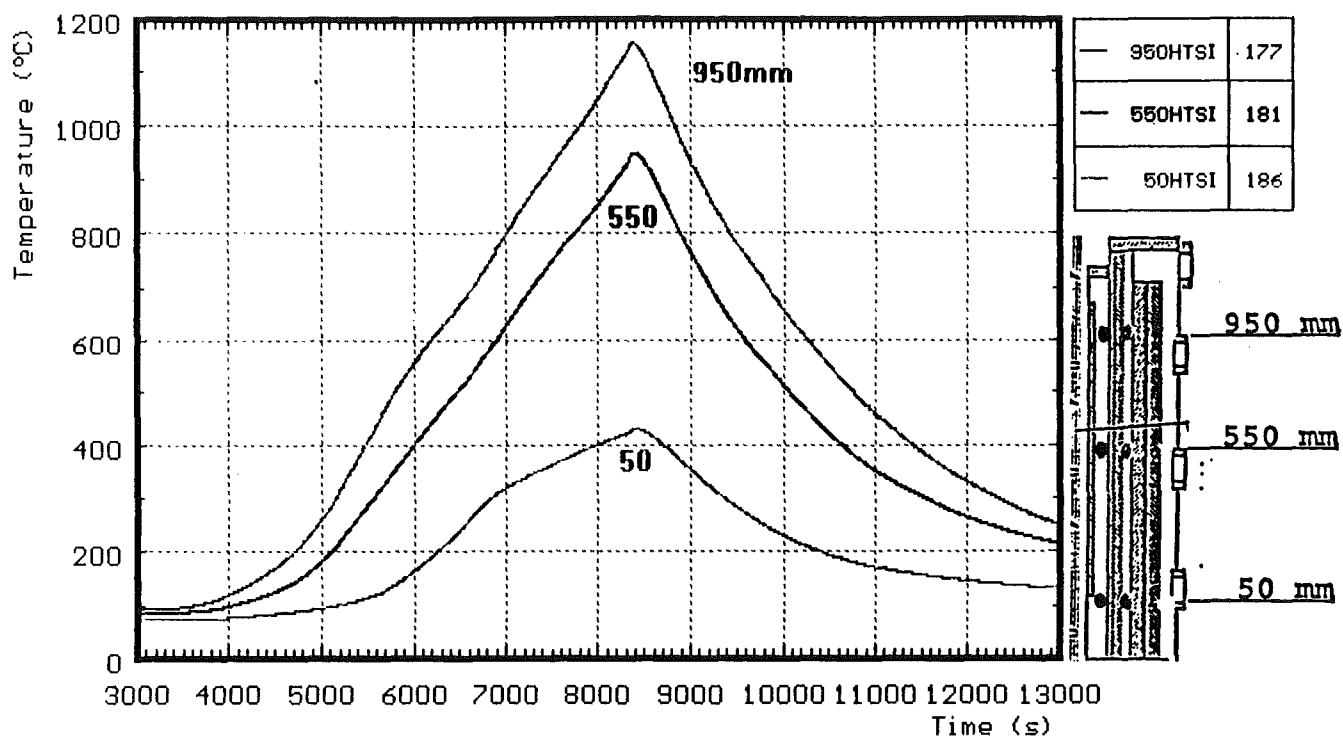


Fig. 54: Temperatures on inner surface; 153 mm radius (345°)

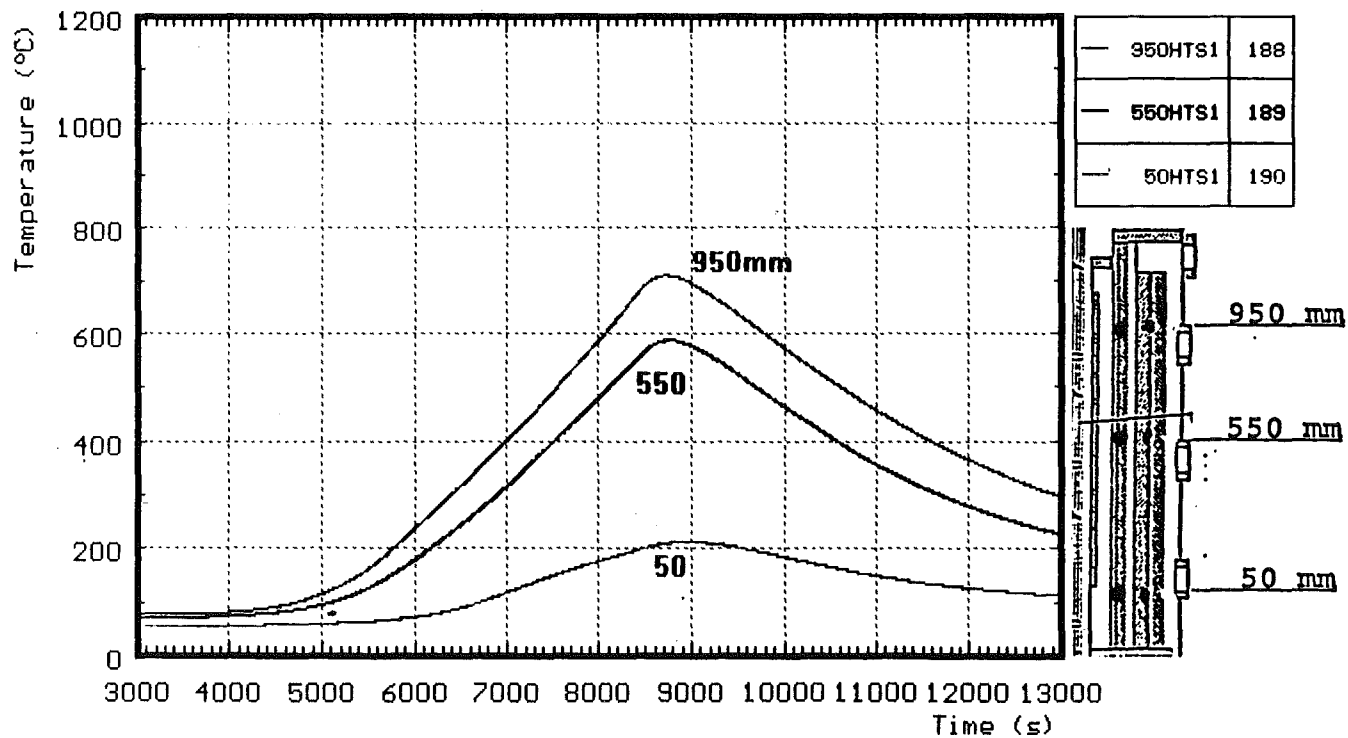


Fig. 55: Temperatures in HT-Shield; 172 mm radius (345°)

CORA-33:

Temperatures of HTS

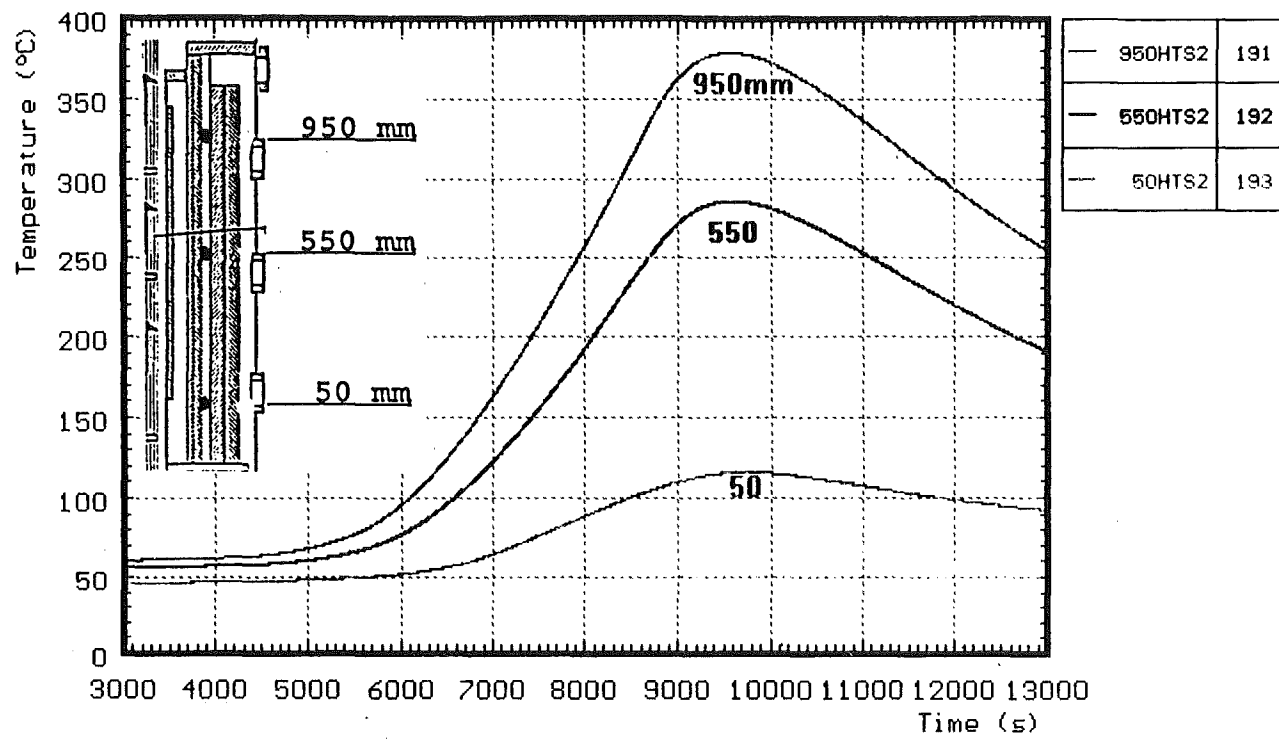


Fig. 56: Temperatures in HT-Shield; 192 mm radius (345°)

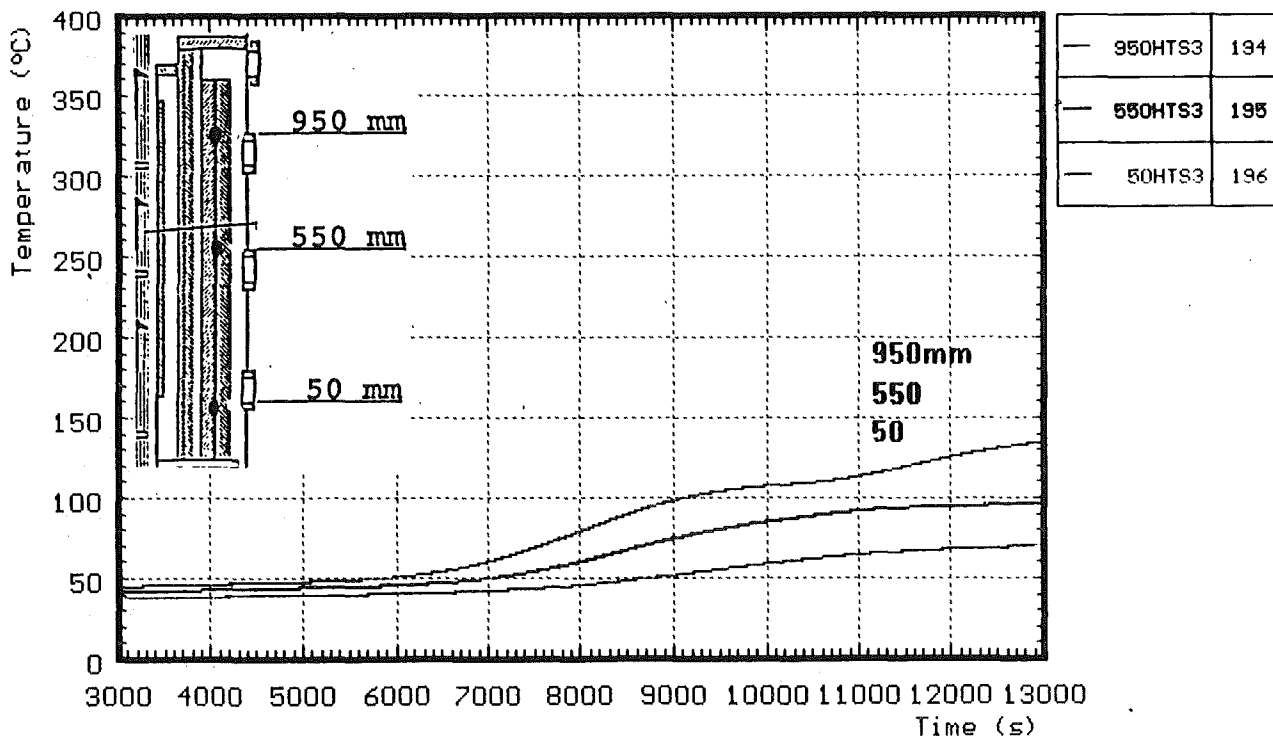


Fig. 57: Temperatures in HT-Shield; 255 mm radius (345°)

CORA-33:

Temperatures of HTS

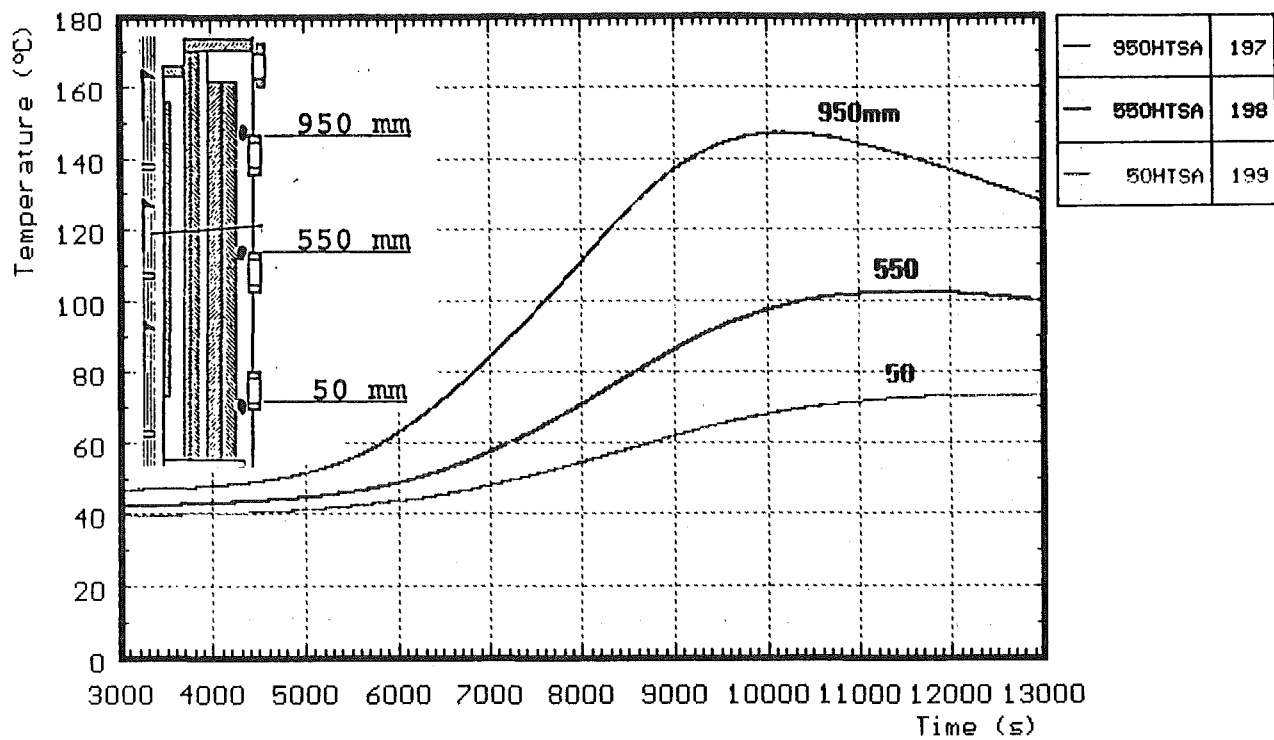


Fig. 58: Temperatures in HT-Shield; 293 mm radius (345°)

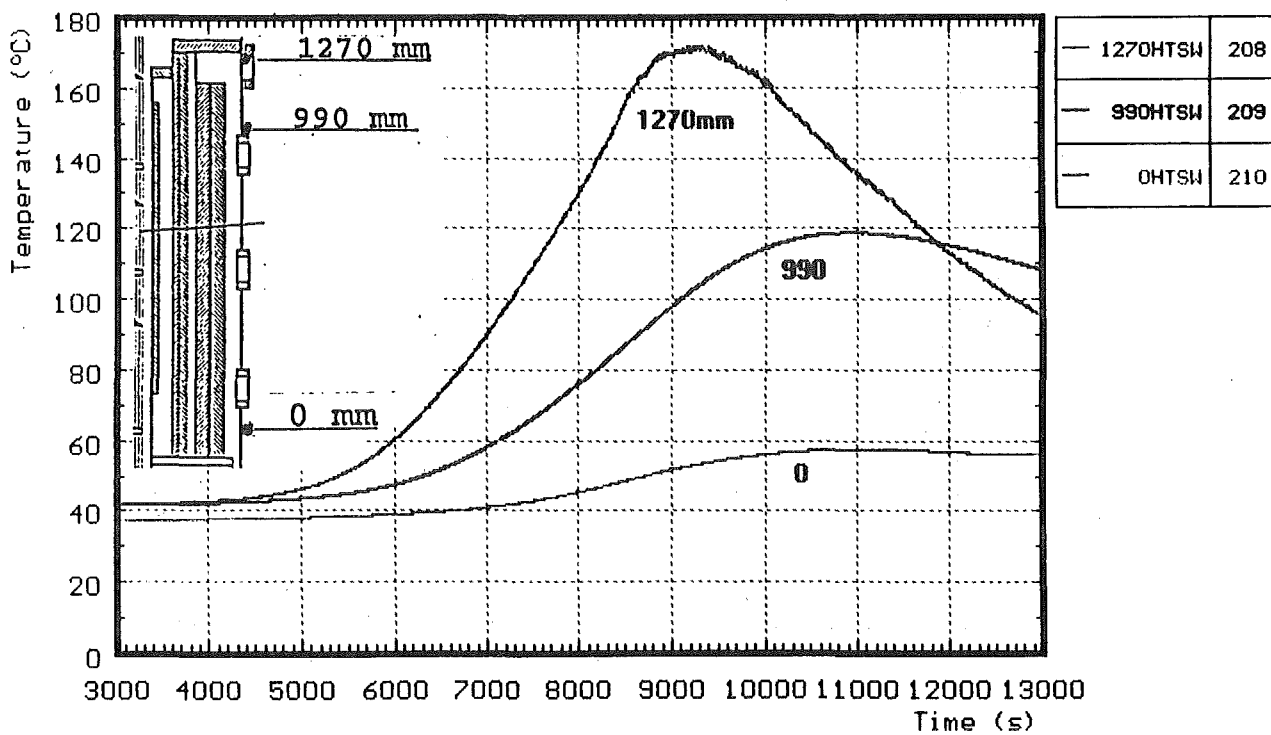


Fig. 59: Temperatures in HT-Shield; 380 mm radius

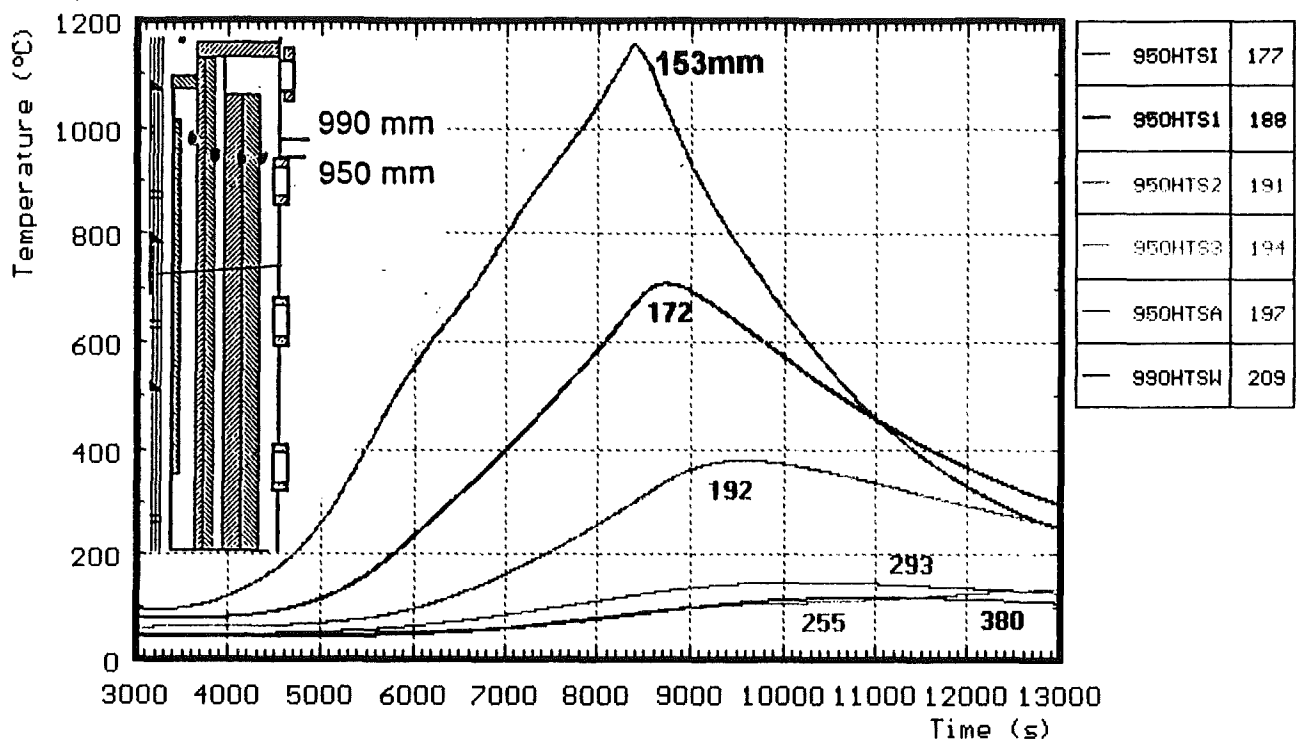
CORA-33:**Temperatures of HTS**

Fig. 60: Radial dependence at 950 mm elevation

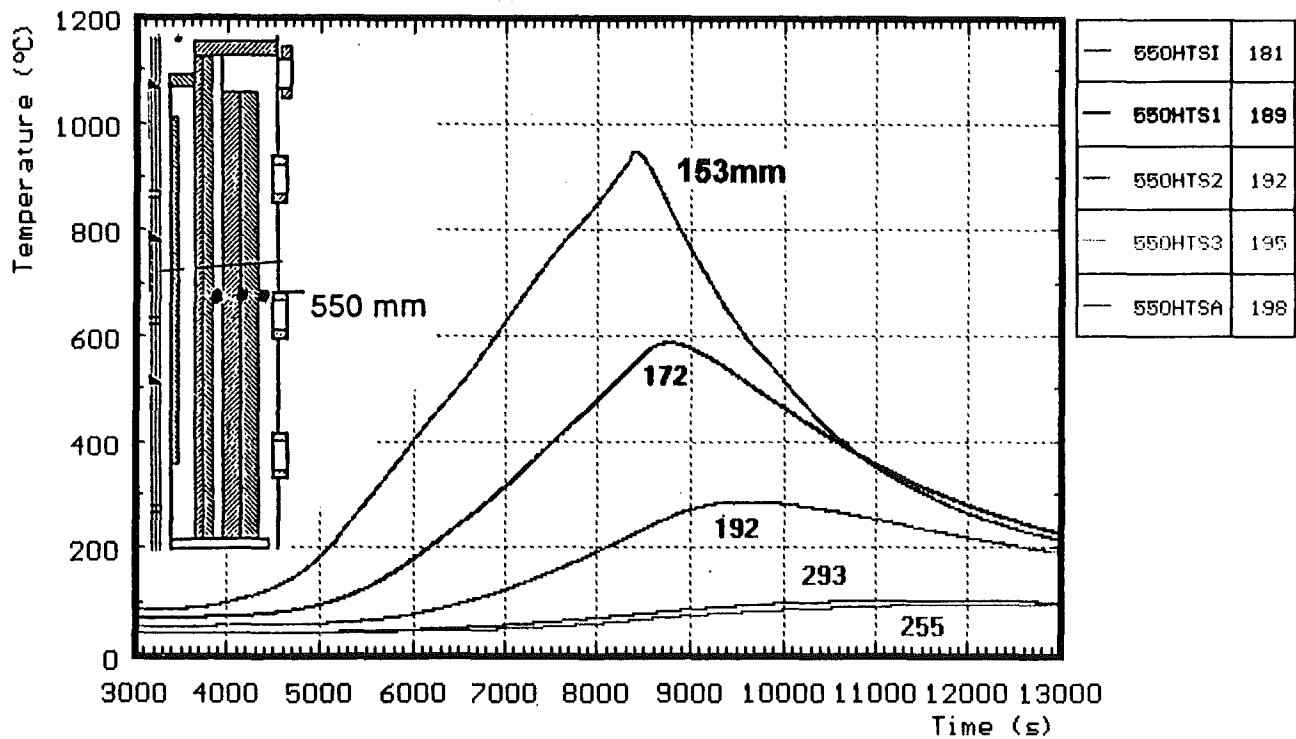


Fig. 61: Radial dependence at 550 mm elevation

CORA-33:

Temperatures of HTS

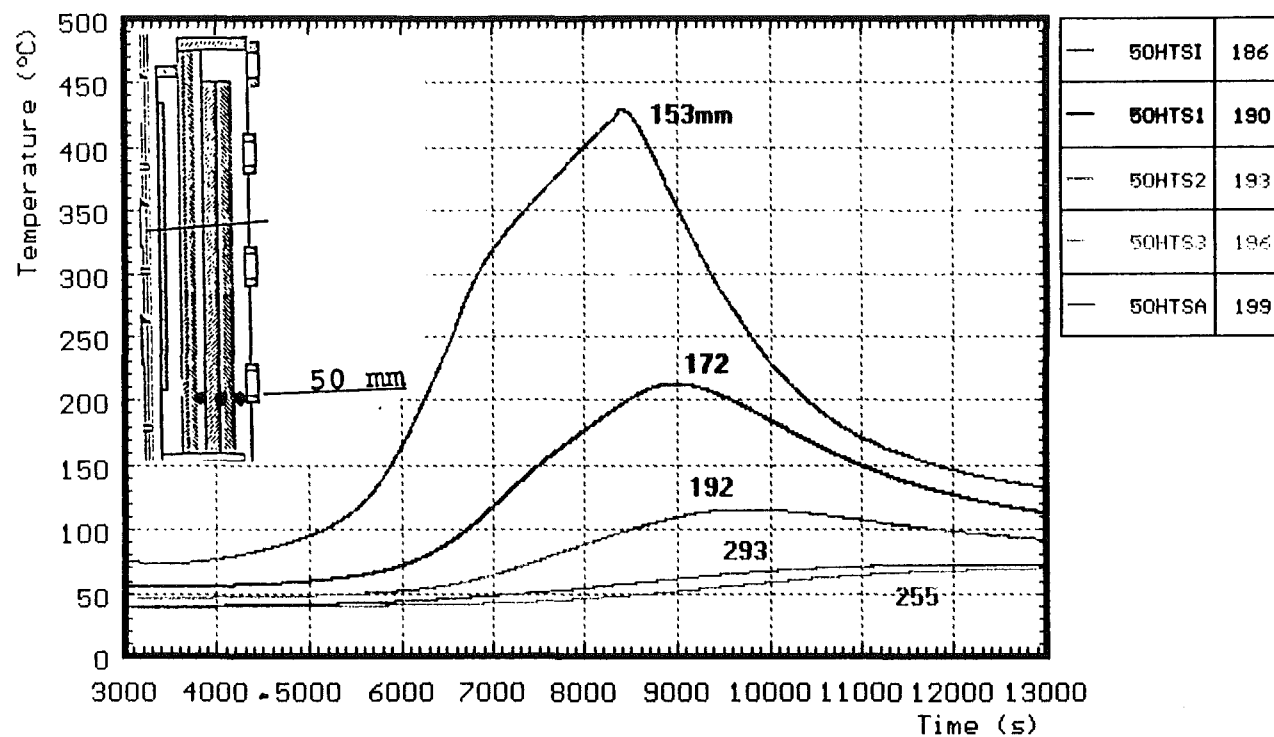


Fig. 62: Radial dependence at 50 mm elevation

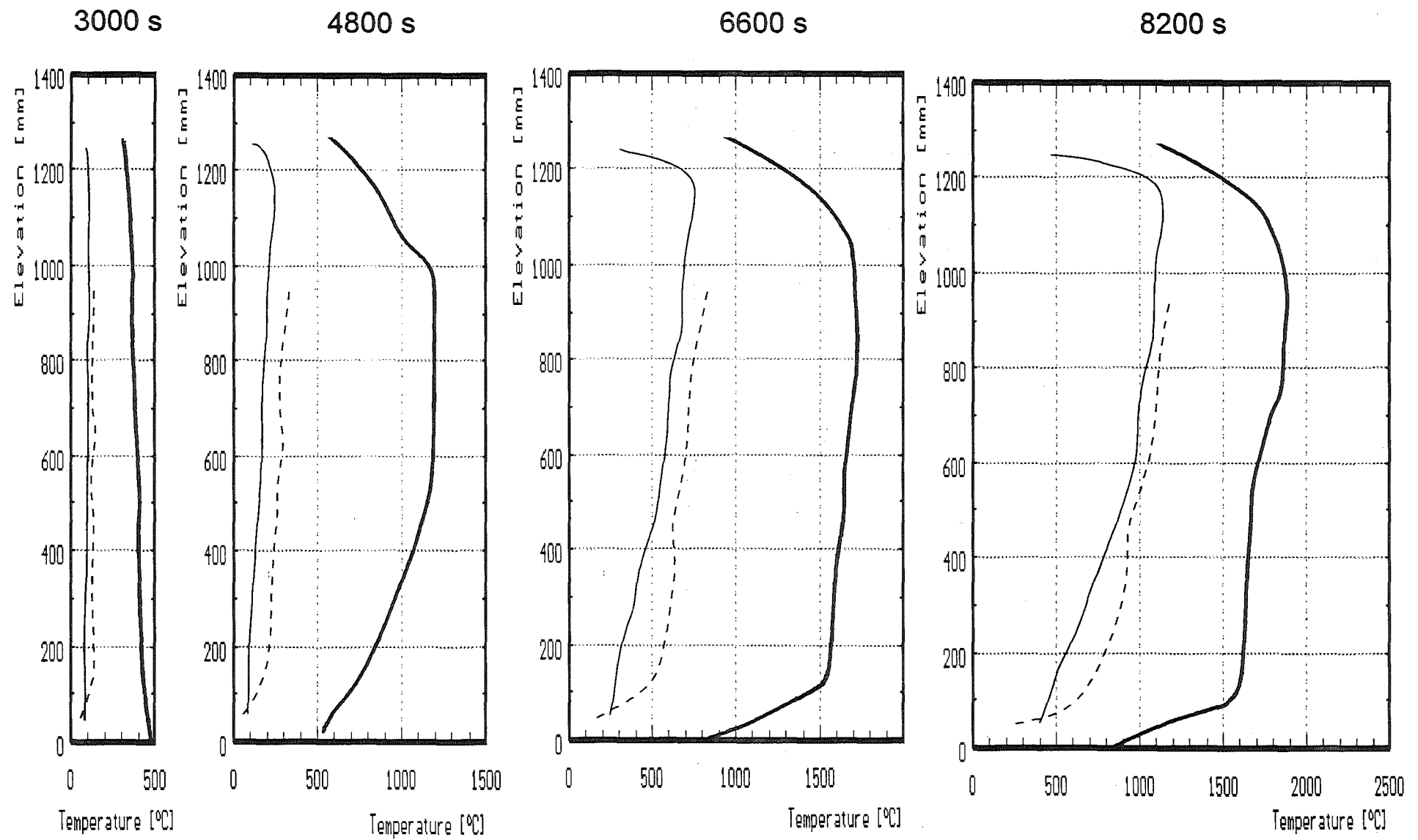


Fig. 63: Axial temperature distribution of bundle(—), on shroudinsulation(—) and on inner side of HTS(---)

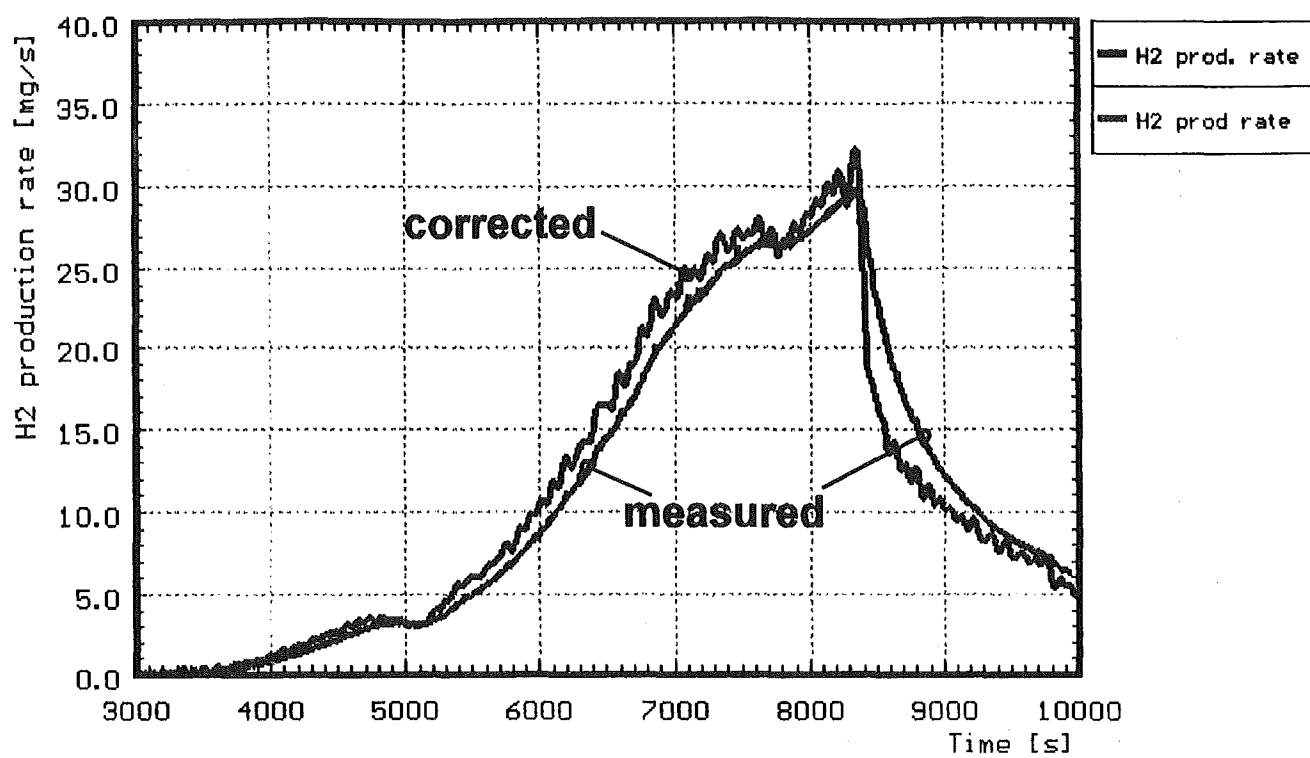


Fig. 64a: CORA-33; Hydrogen production rate

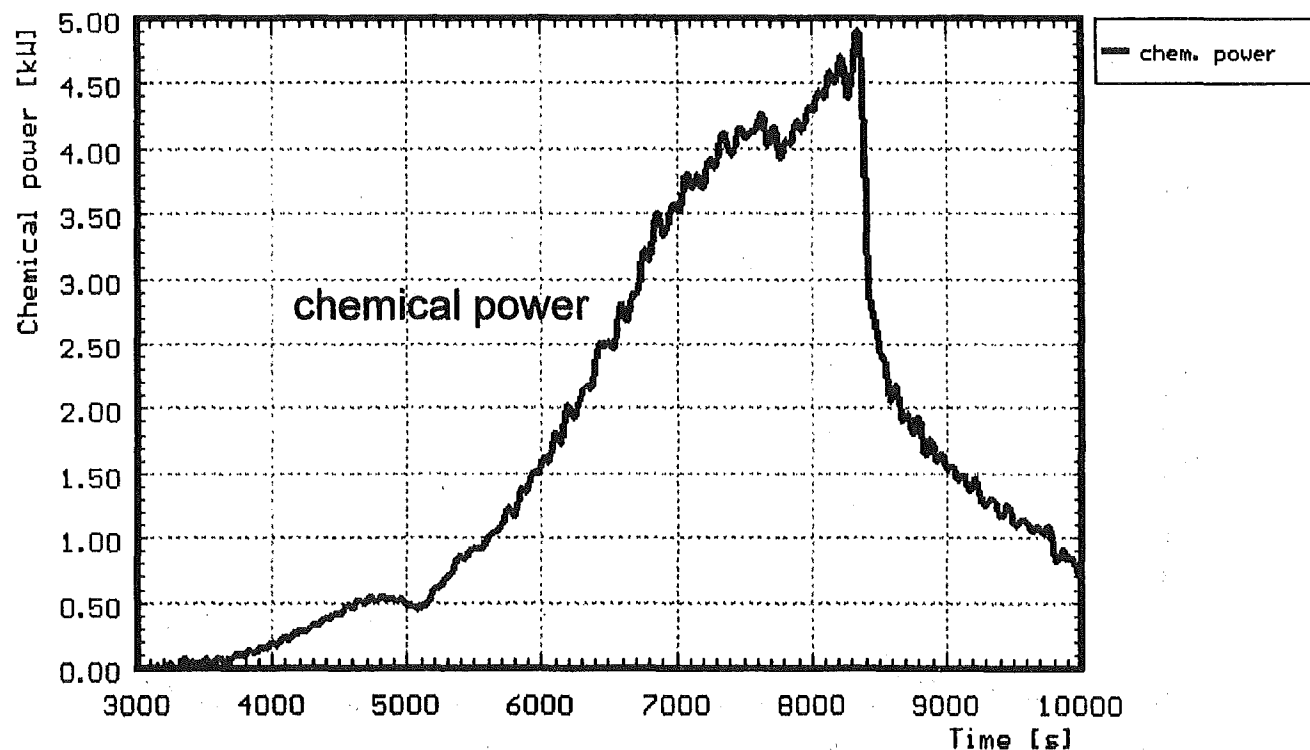


Fig. 64b: CORA-33; Chemical power due to corrected hydrogen measurement

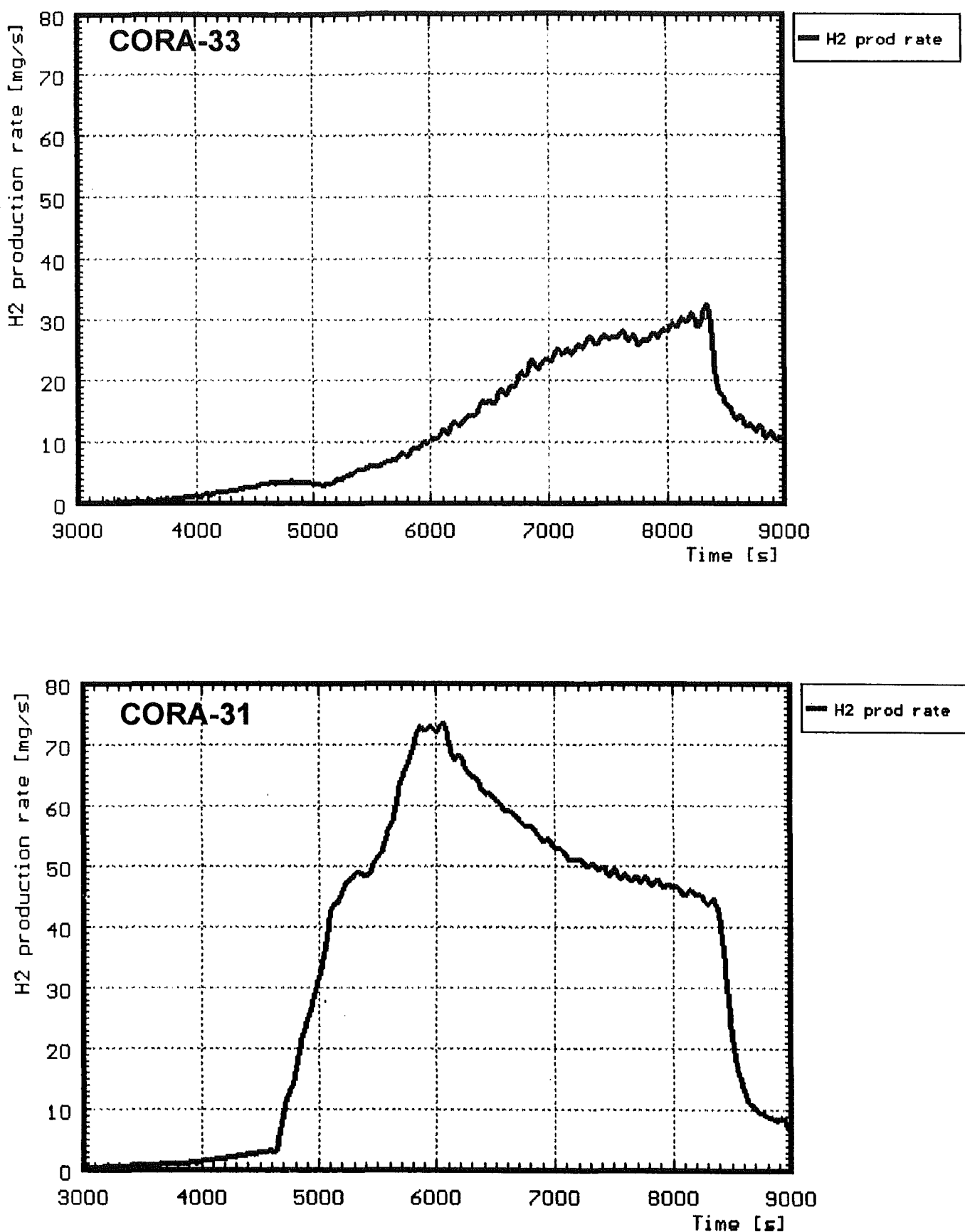


Fig. 65: Comparison of corrected hydrogen production for CORA-33 and CORA-31

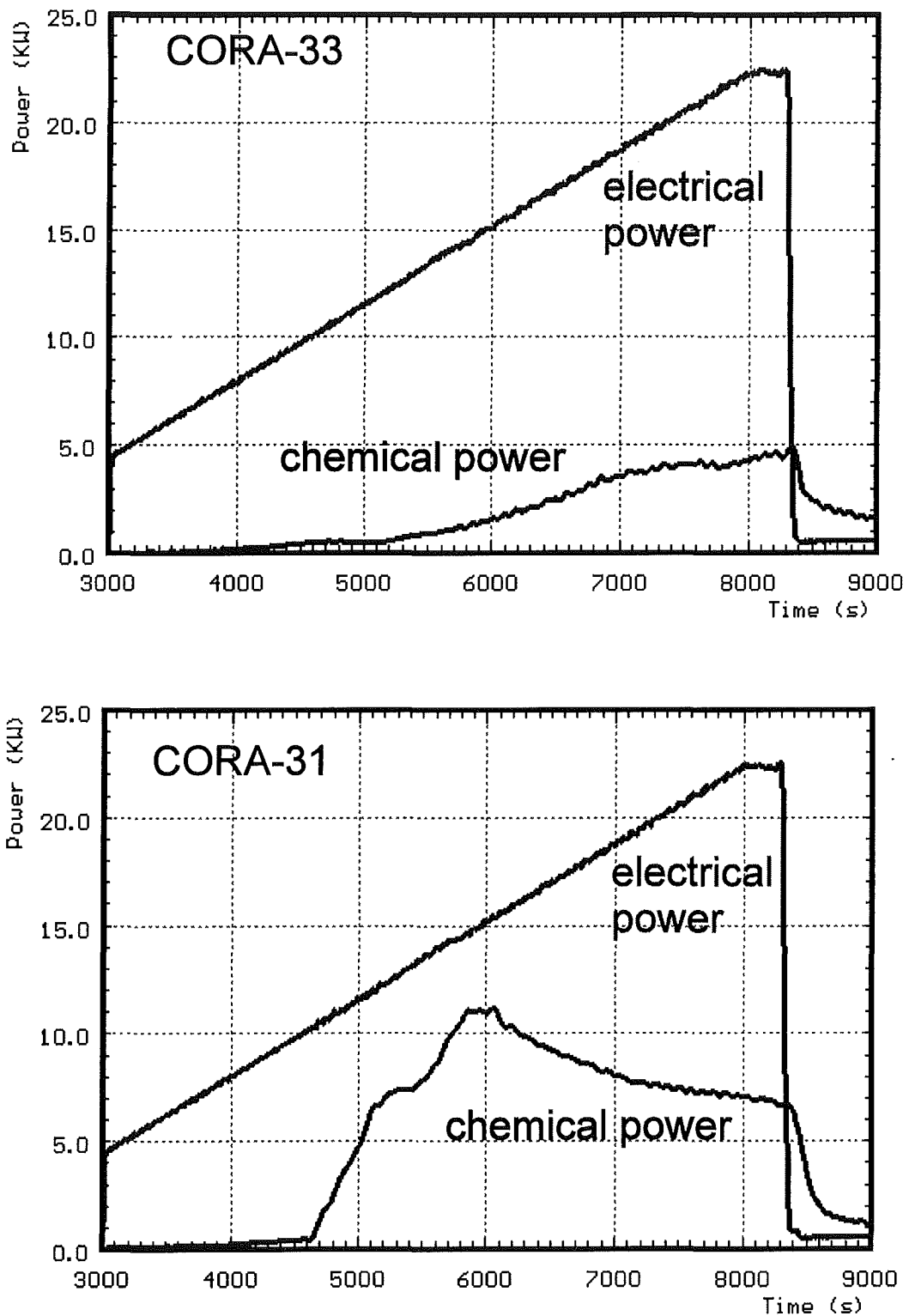


Fig. 66: Comparison of electrical and chemical power, test CORA-33 and CORA-31

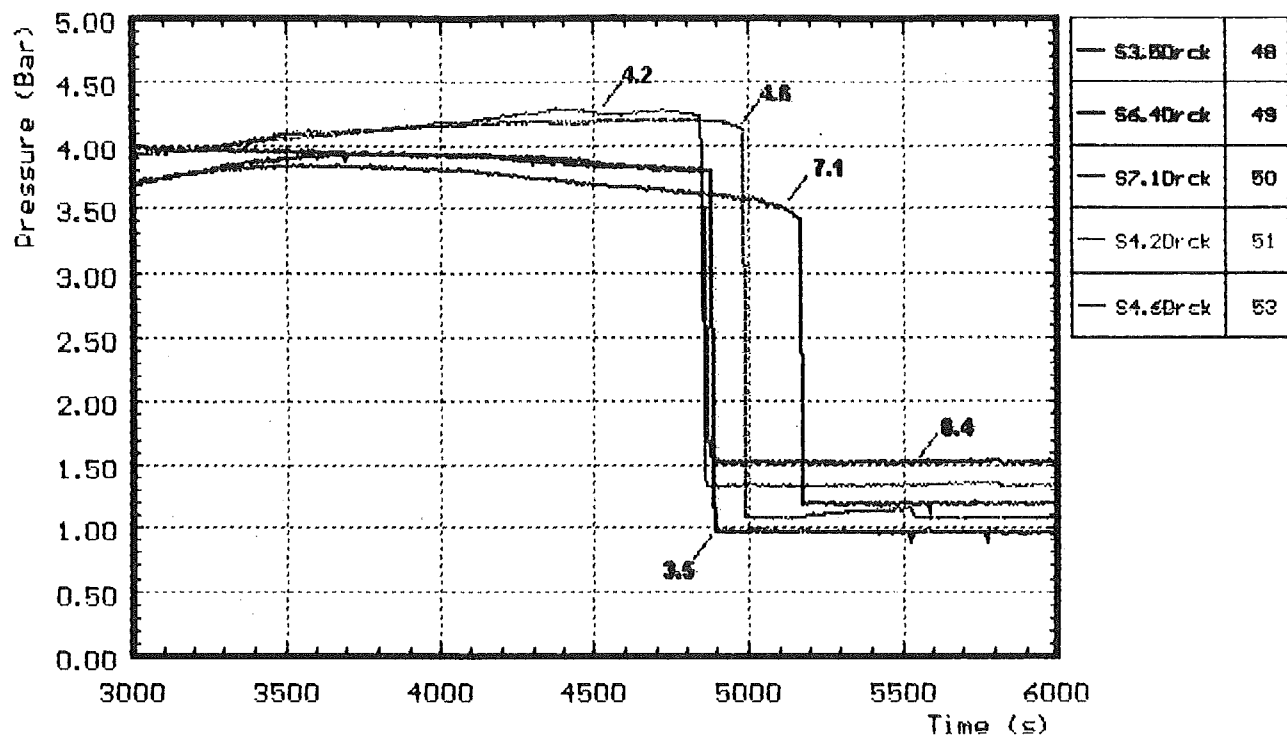


Fig. 67: CORA-33: Internal pressure of fuel rod simulators

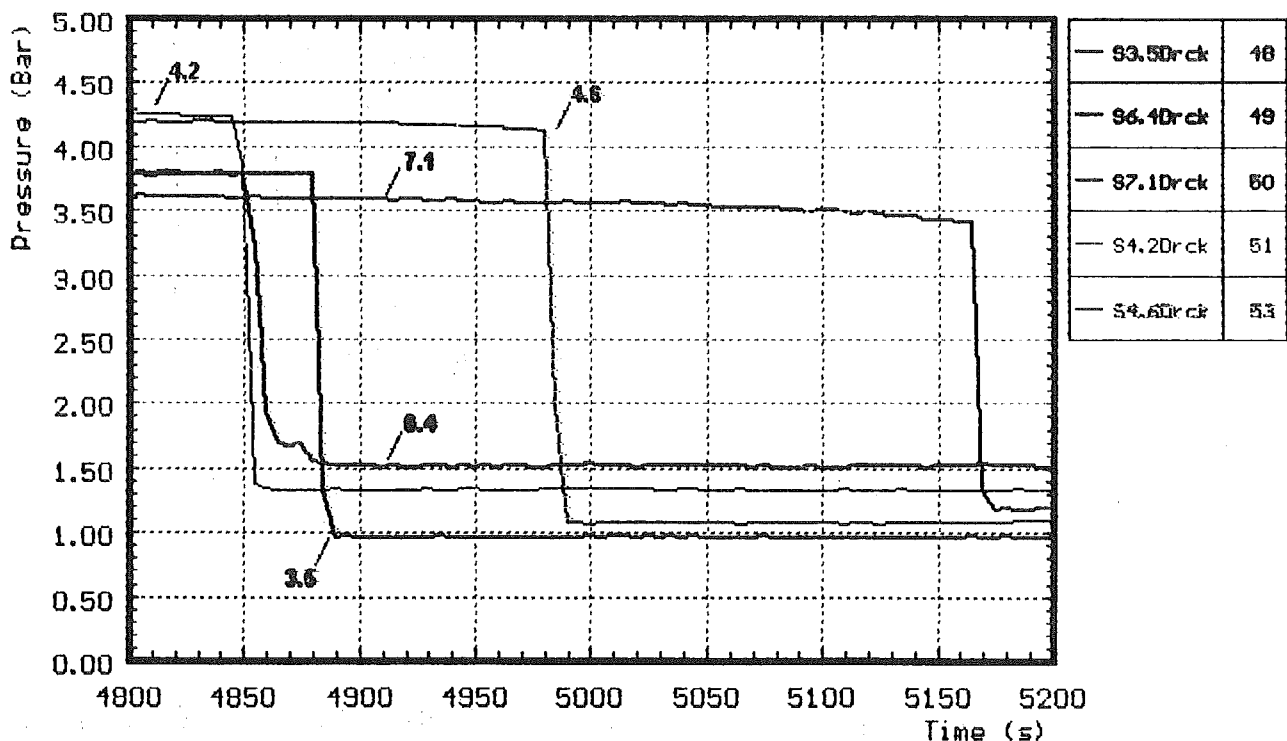


Fig. 68: CORA-33: Determination of failure time by pressure loss measurement

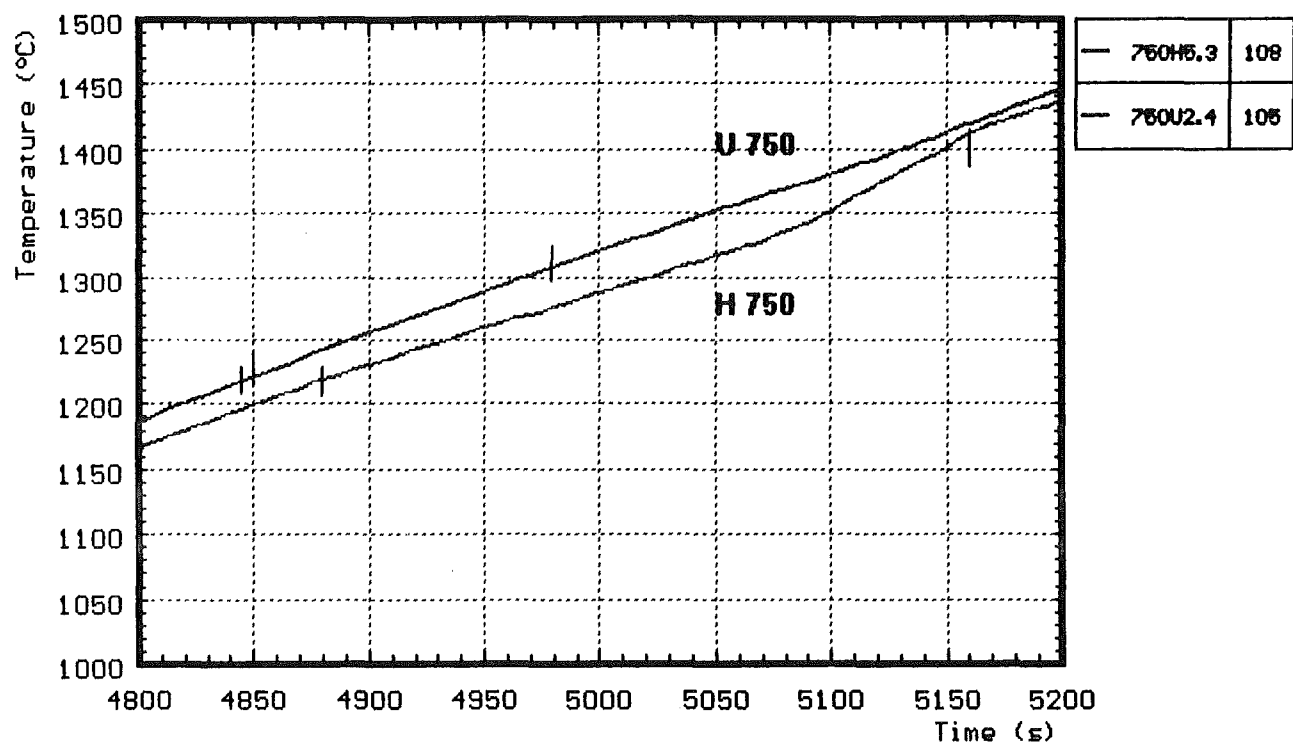


Fig. 69: CORA-33: Temperatures at time of pressure loss

CORA-33: Irregularities in the absorberblade temperatures used for estimation of absorber failure

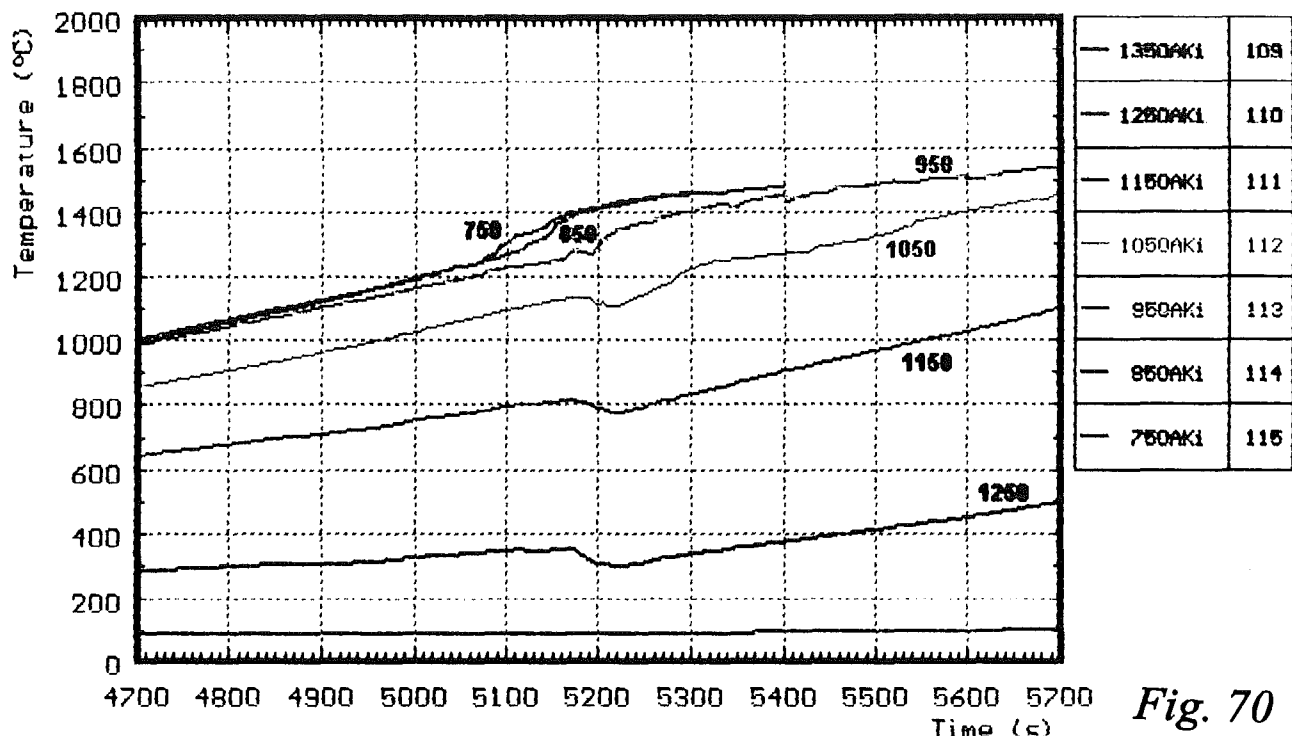


Fig. 70

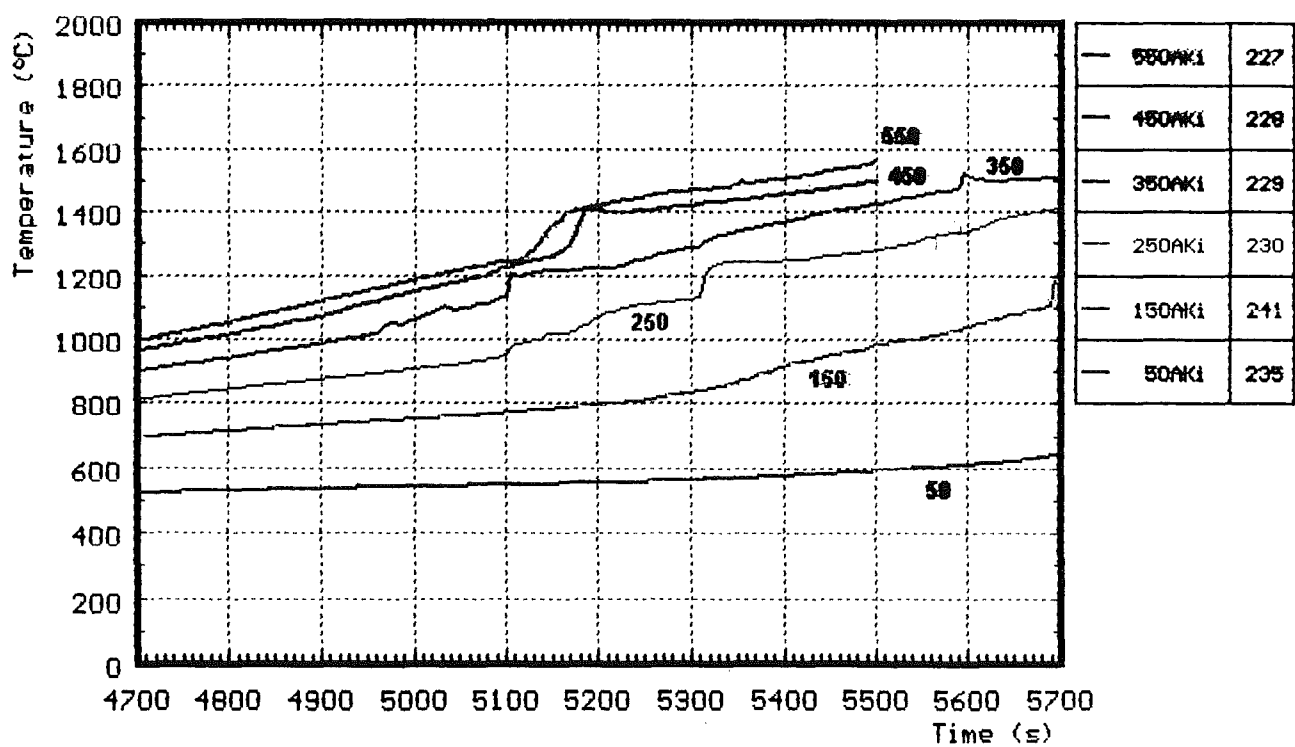


Fig. 71

CORA-33: Irregularities in the absorberblade temperatures used for estimation of absorber failure

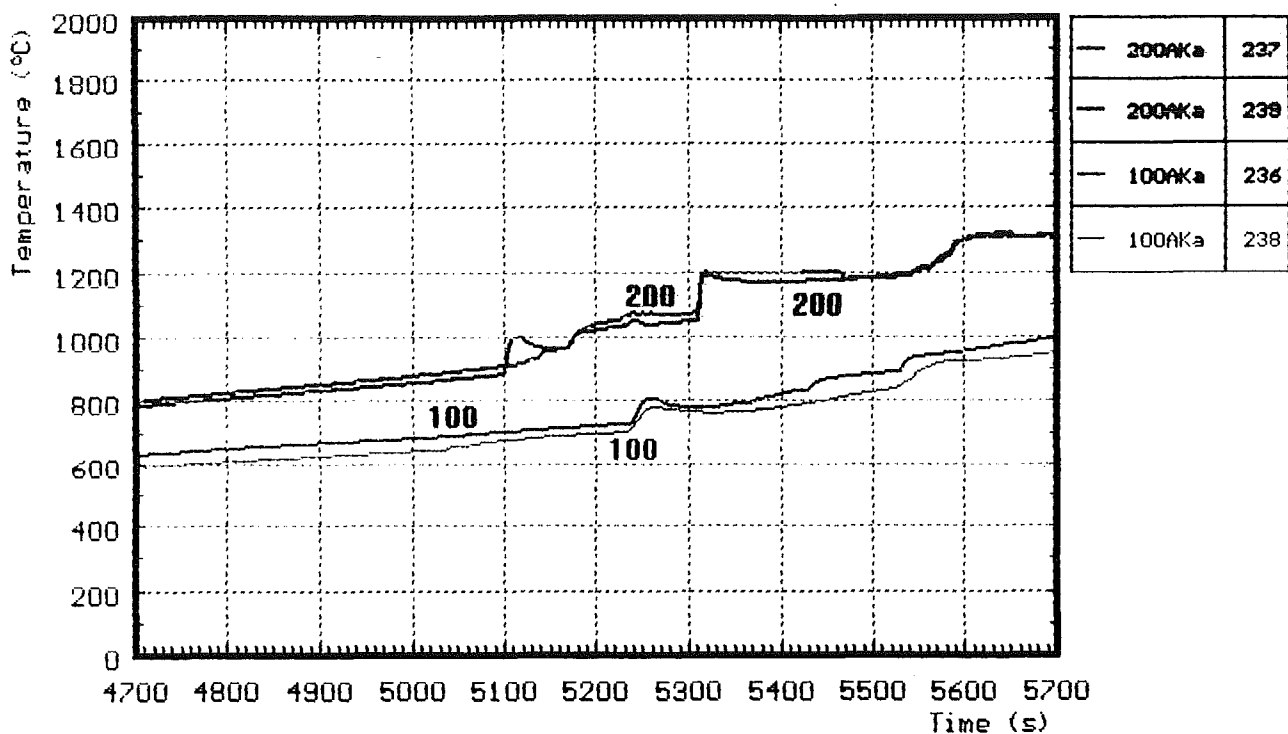


Fig. 71a

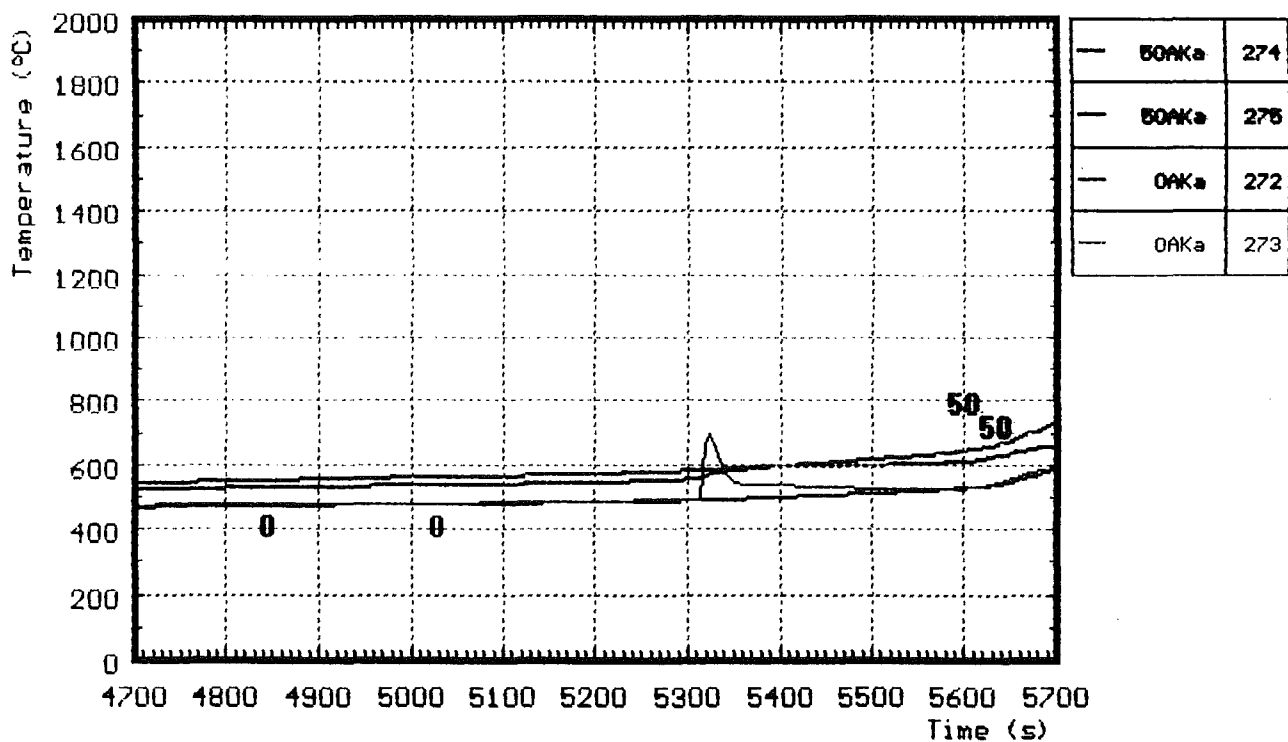


Fig. 71b

CORA-33: Irregularities in the absorberblade temperature (detection of further melt relocation)

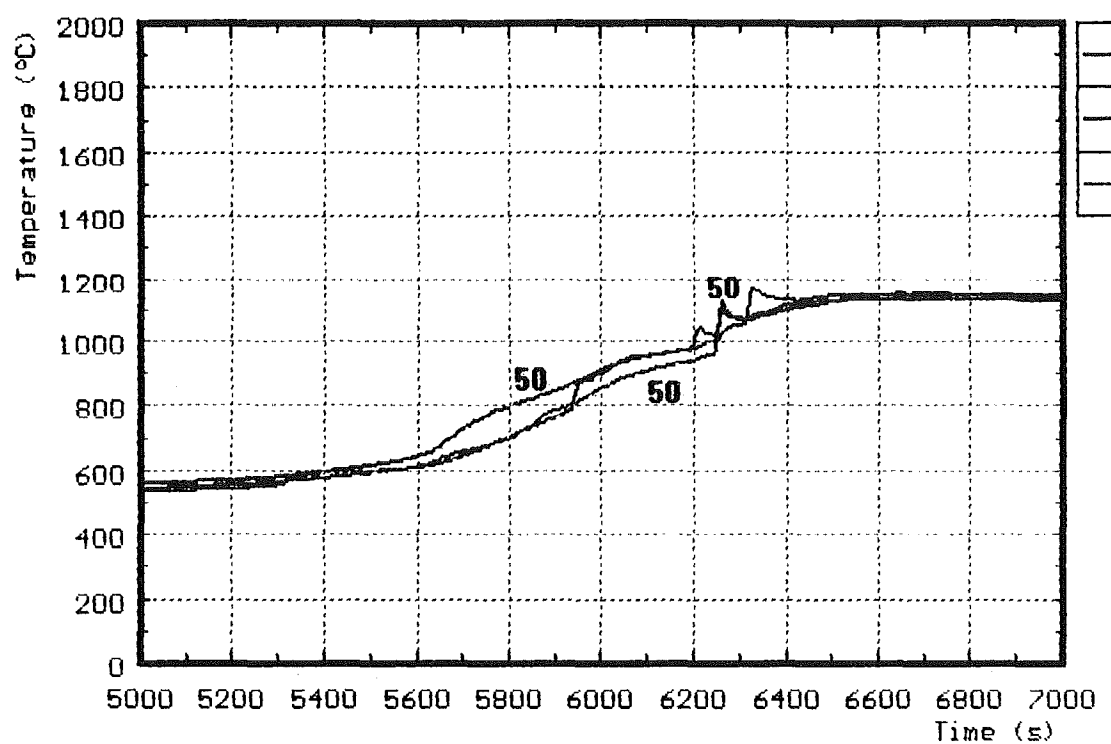


Fig. 71c

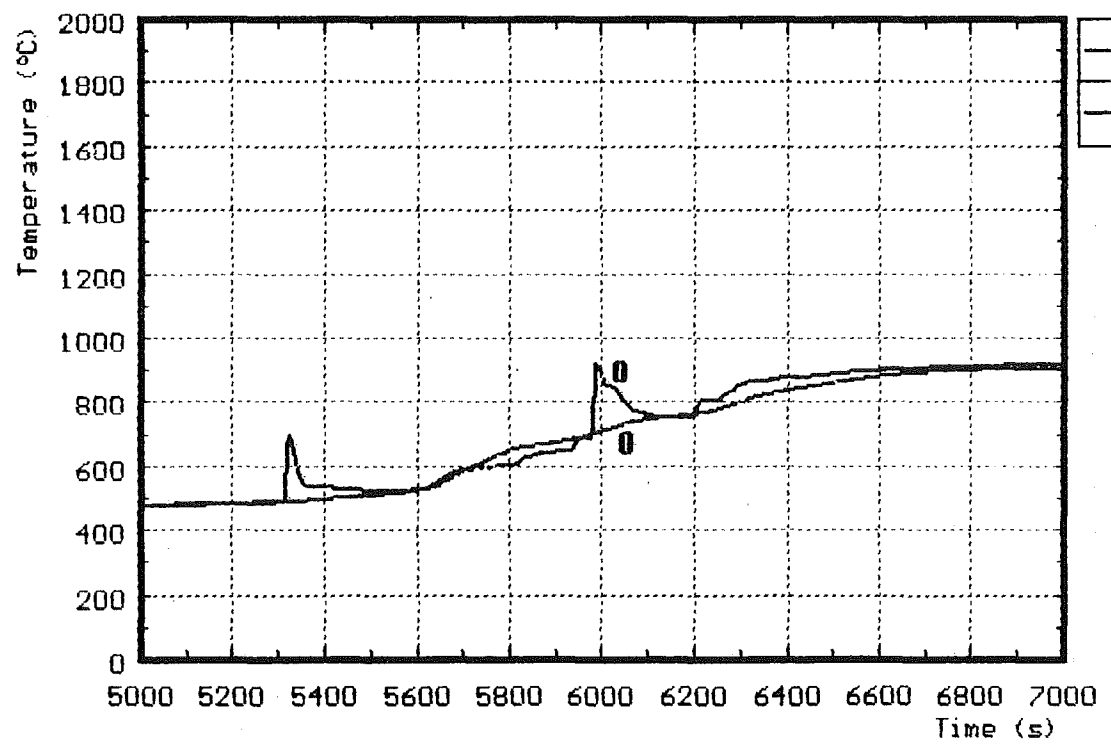


Fig. 71d

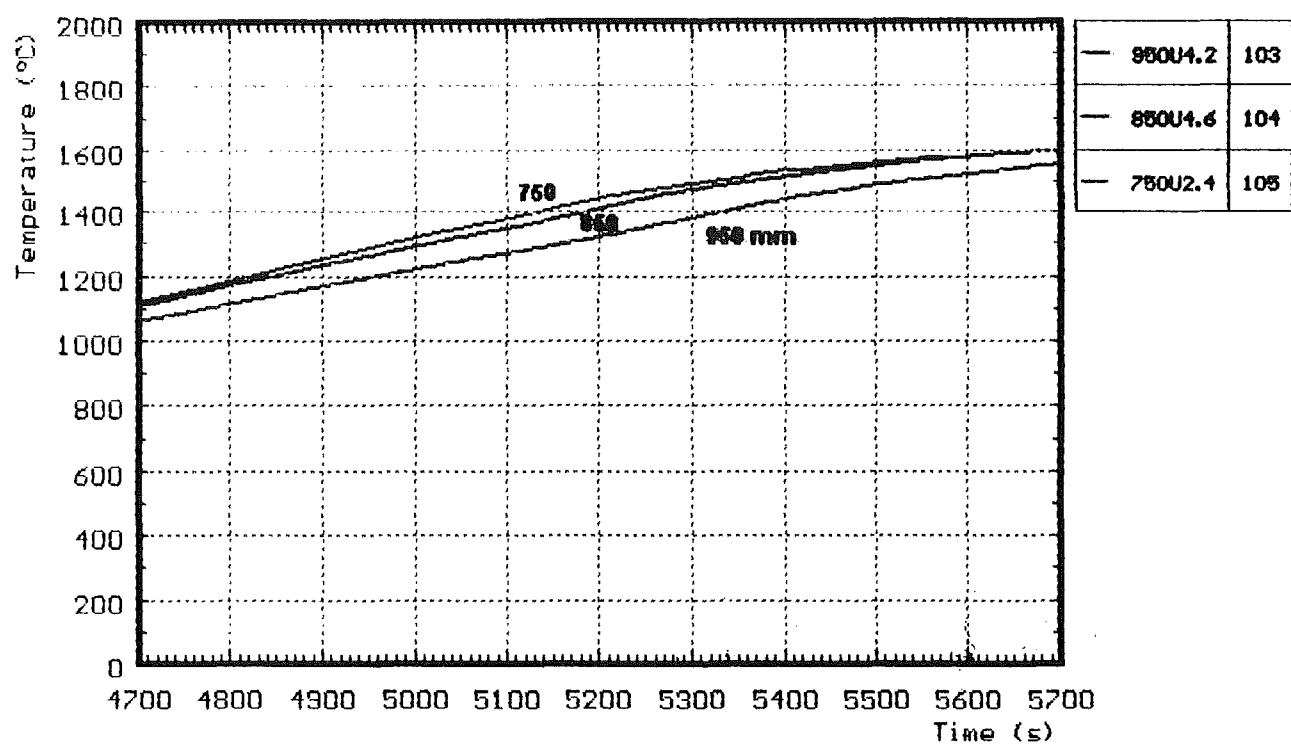


Fig. 72: CORA-33: Smooth temperature increase in unheated rods for comparison to irregularities in temperatures of the absorber blade (see Fig. 70, 71)

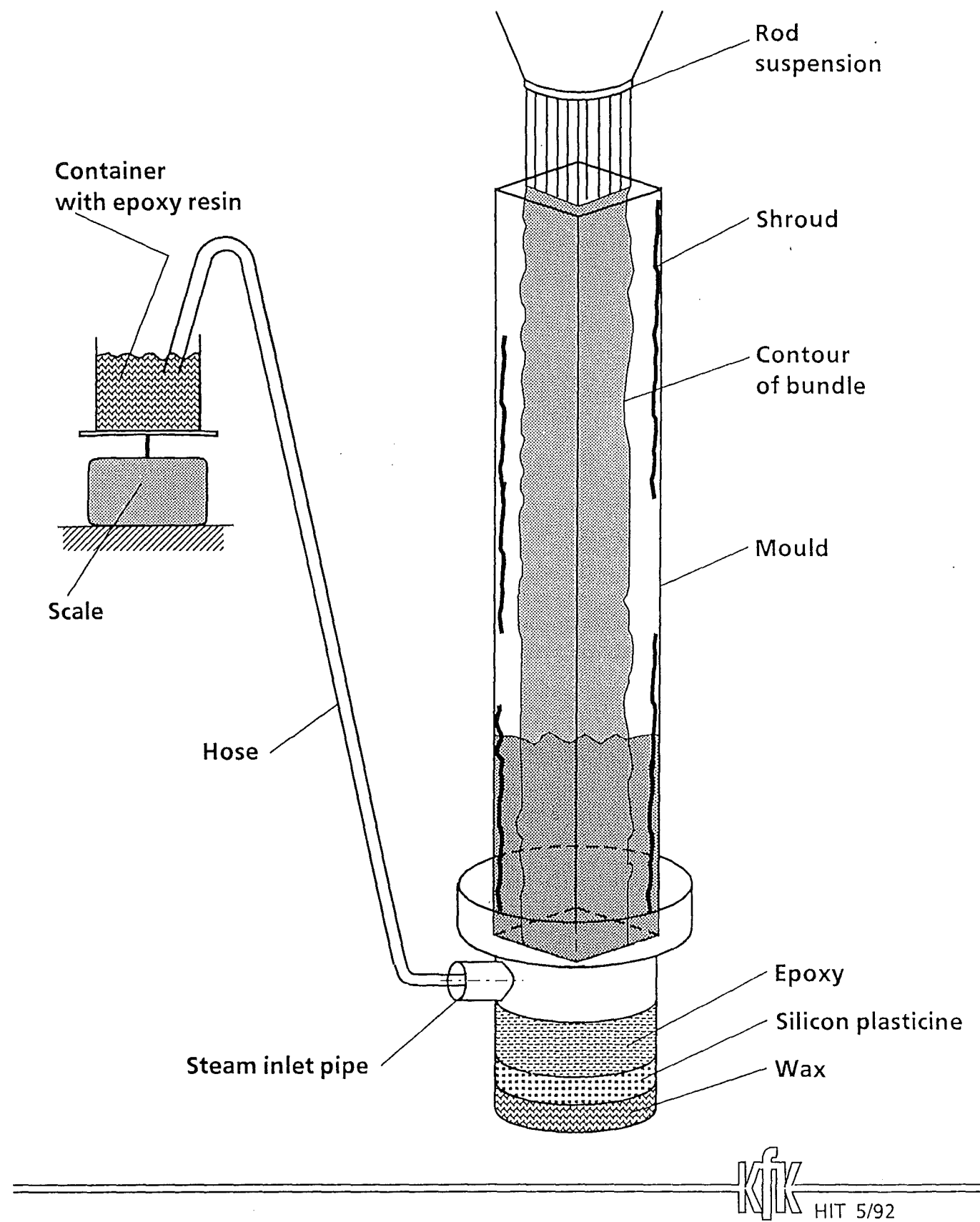
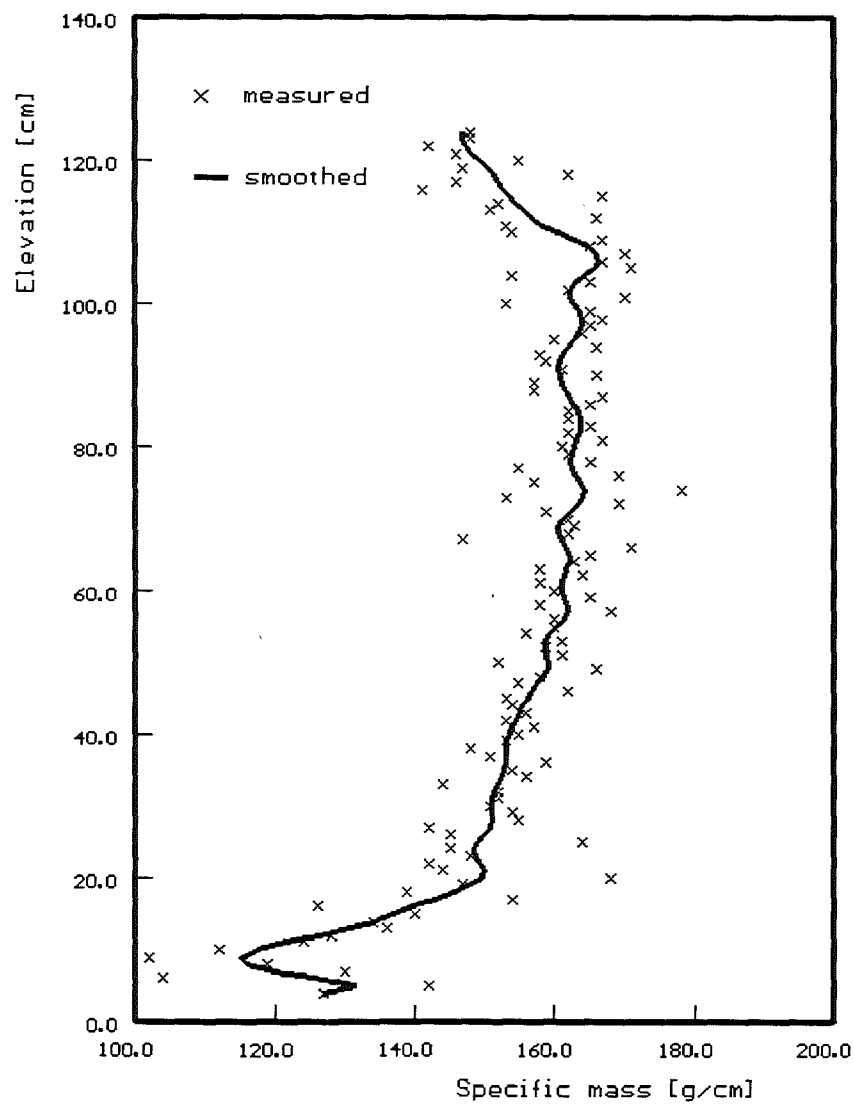


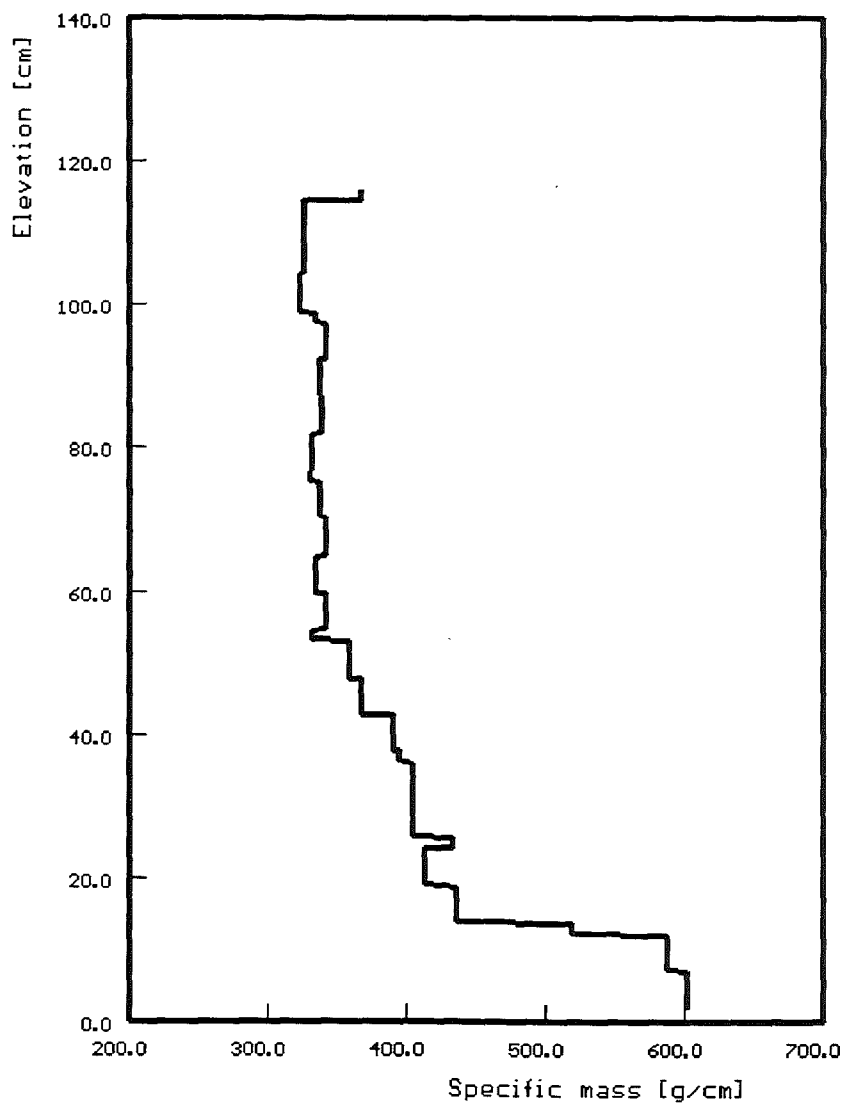
Fig. 73: Epoxying process of the tested bundle

Fig. 74:



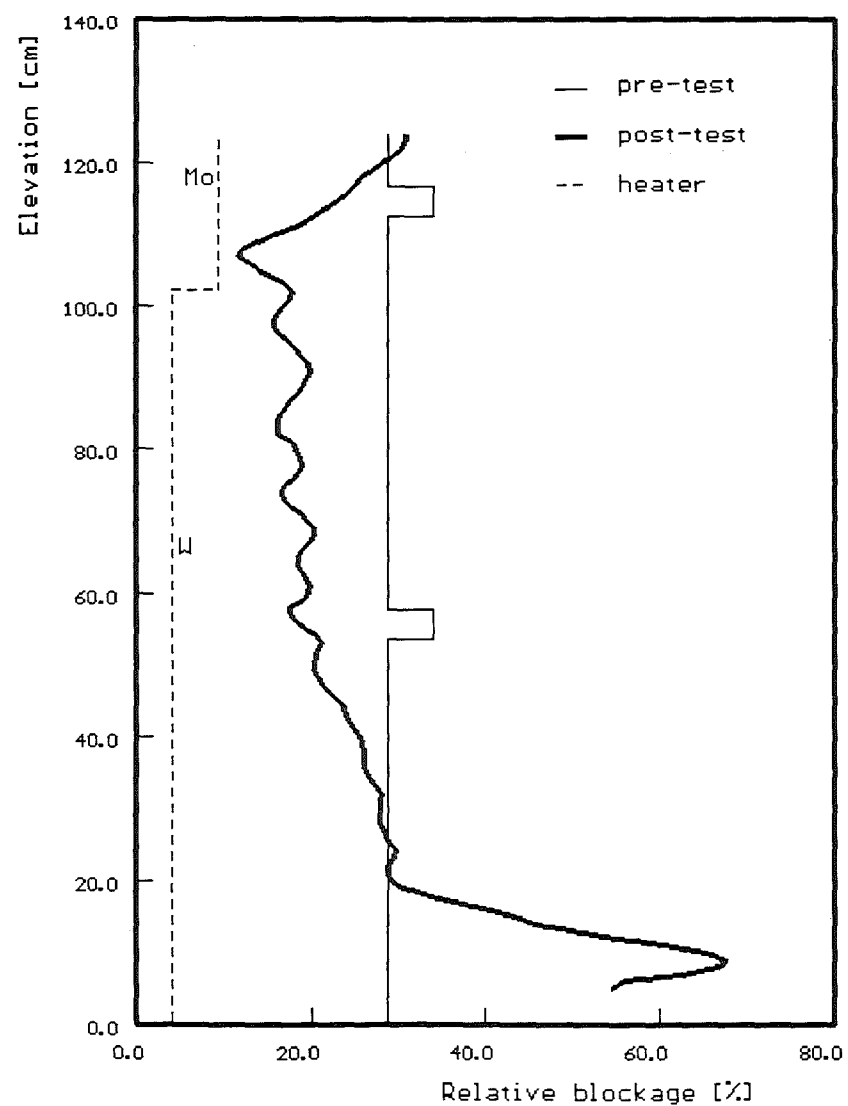
CORA-33: Axial distribution of epoxy bundle fill-up

Fig. 75:



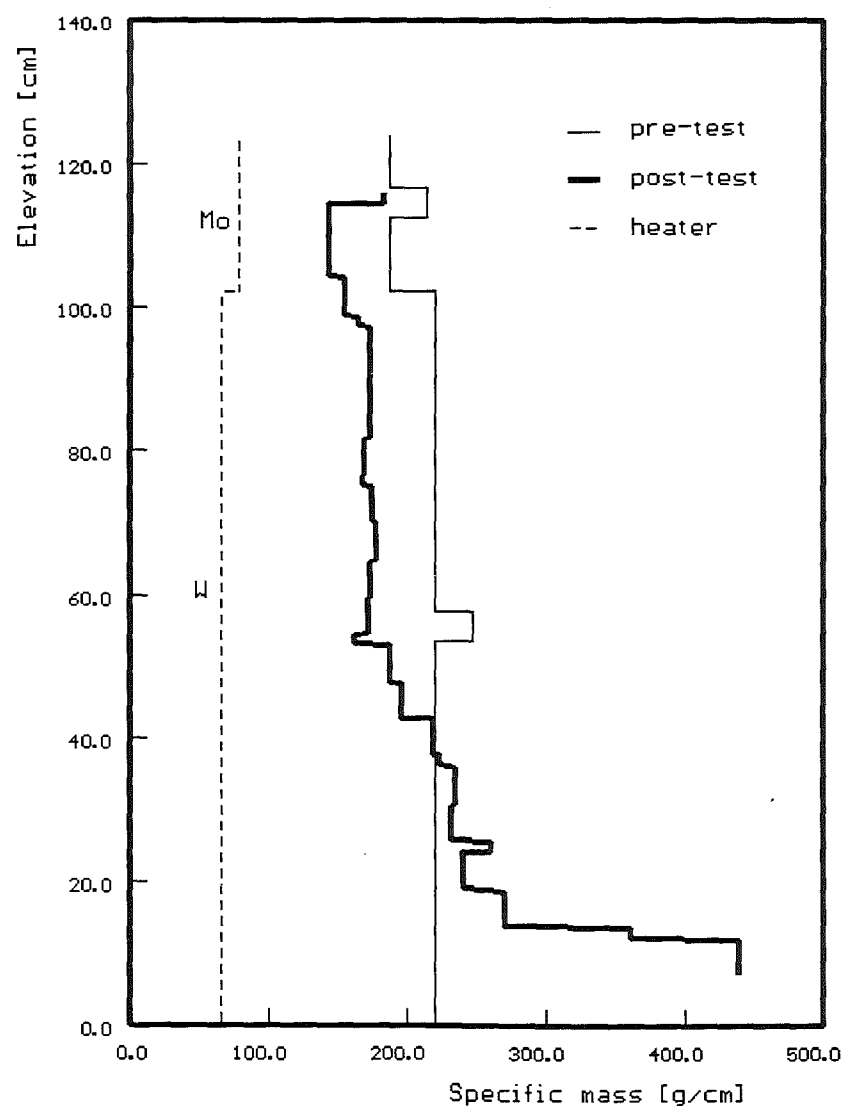
CORA-33: Axial distribution of bundle segments filled with epoxyx

Fig. 76:



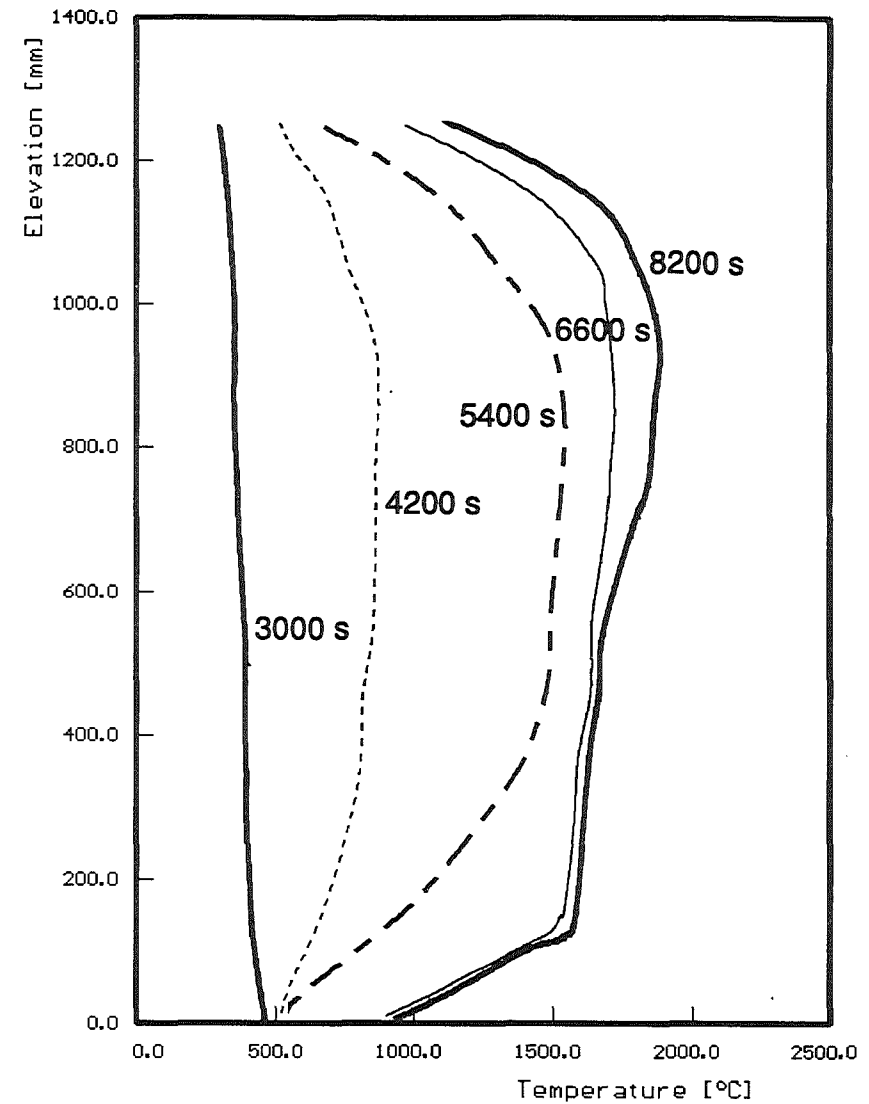
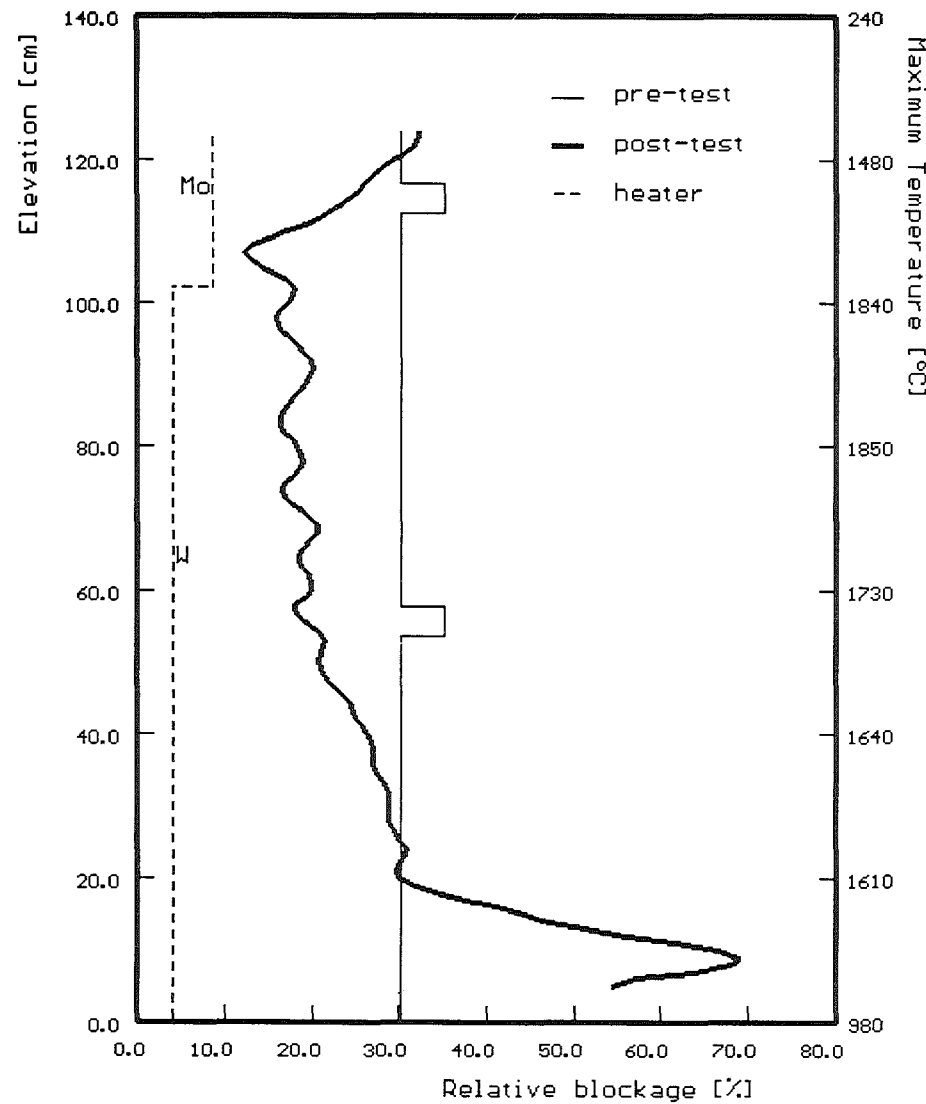
CORA-33: Axial distribution of blocked area inside the shroud

Fig. 77:



CORA-33: Axial mass distribution

CORA 33: Axial volume distribution after the test and axial temperature distribution during the test



CORA 33: Axial mass distribution after the test and axial temperature distribution during the test

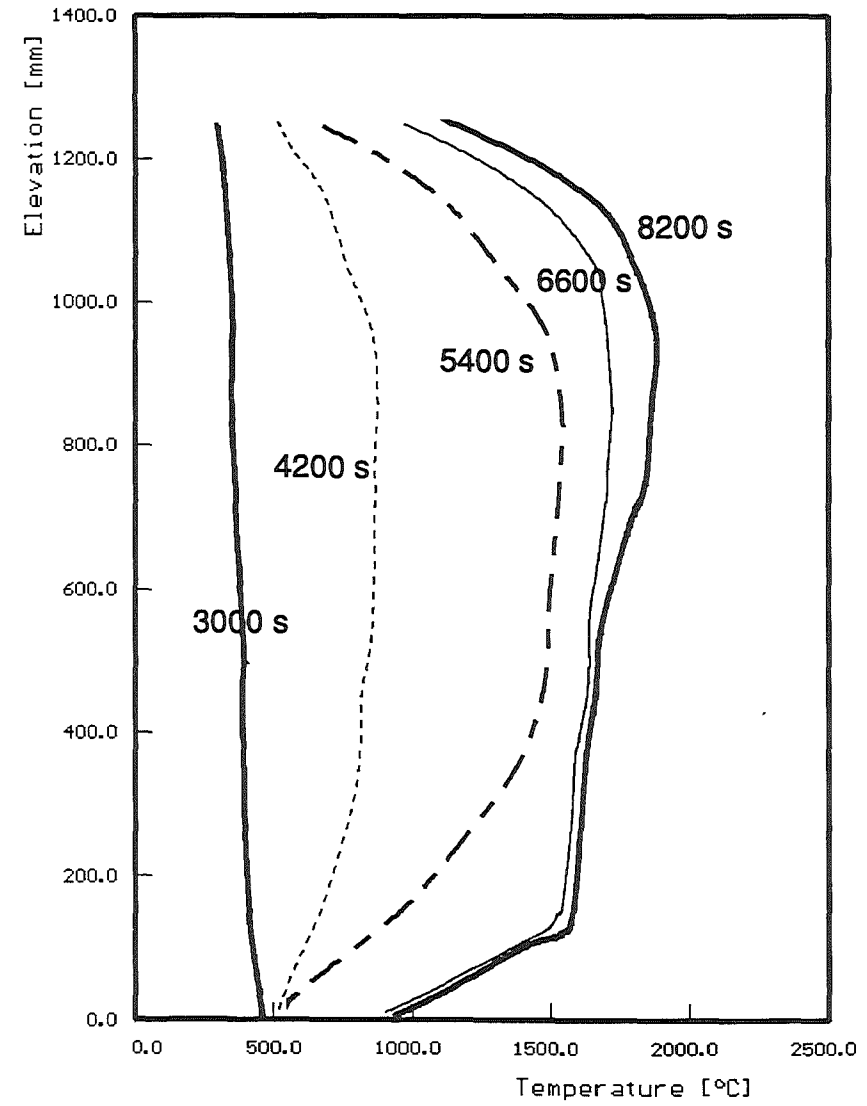
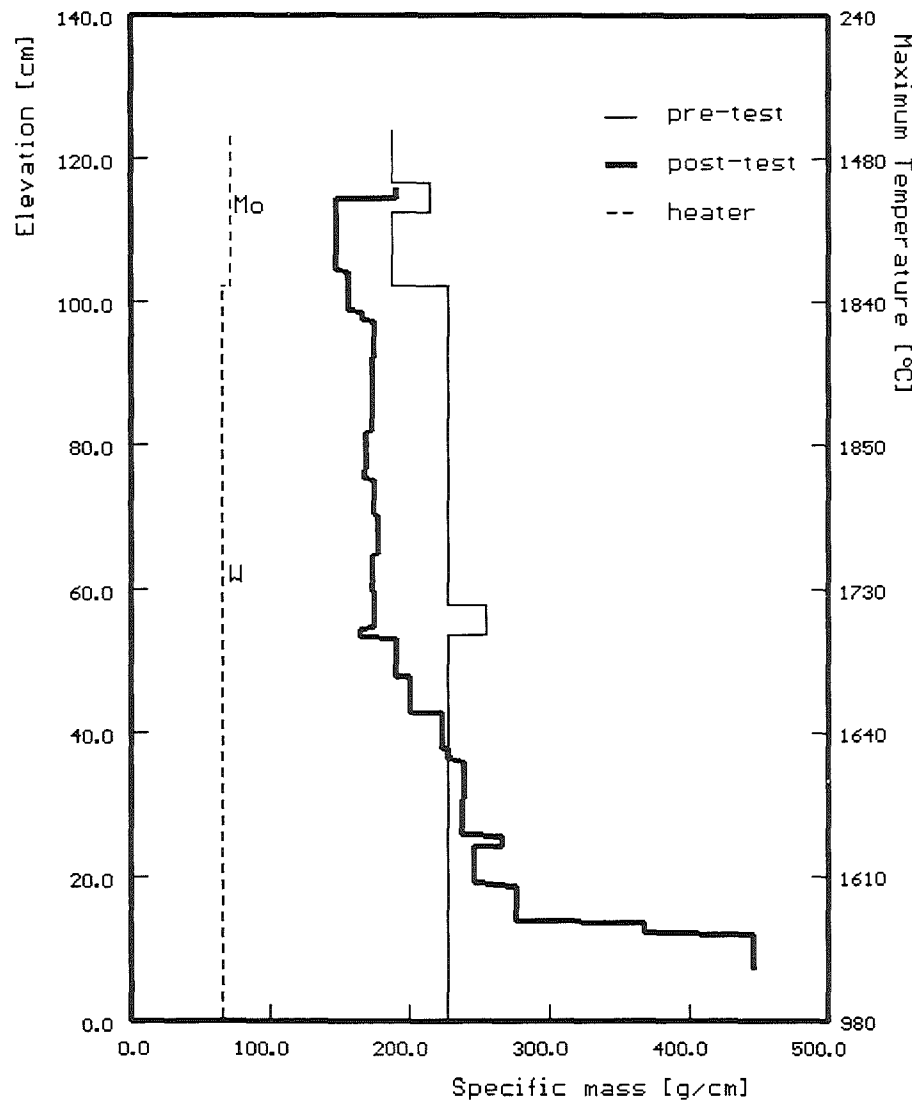
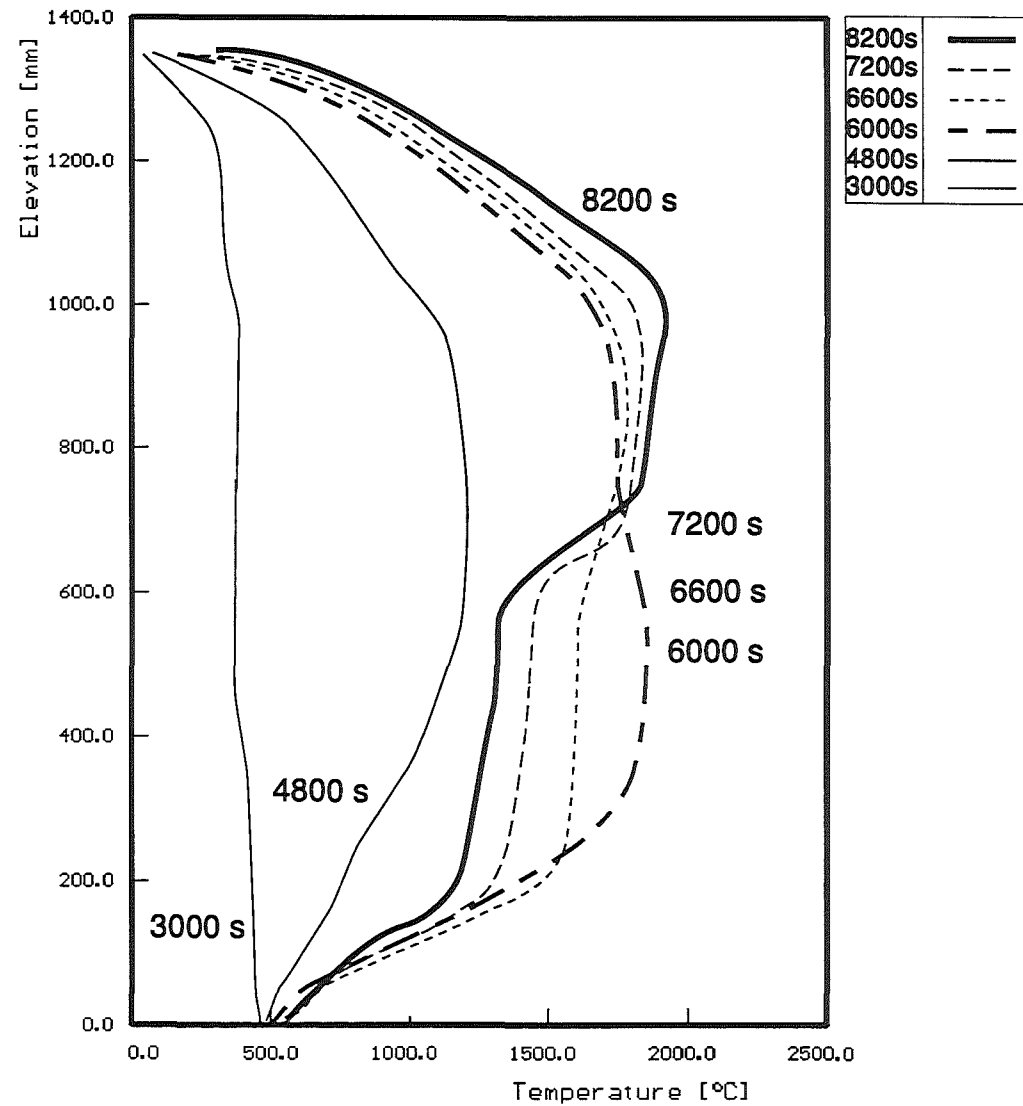
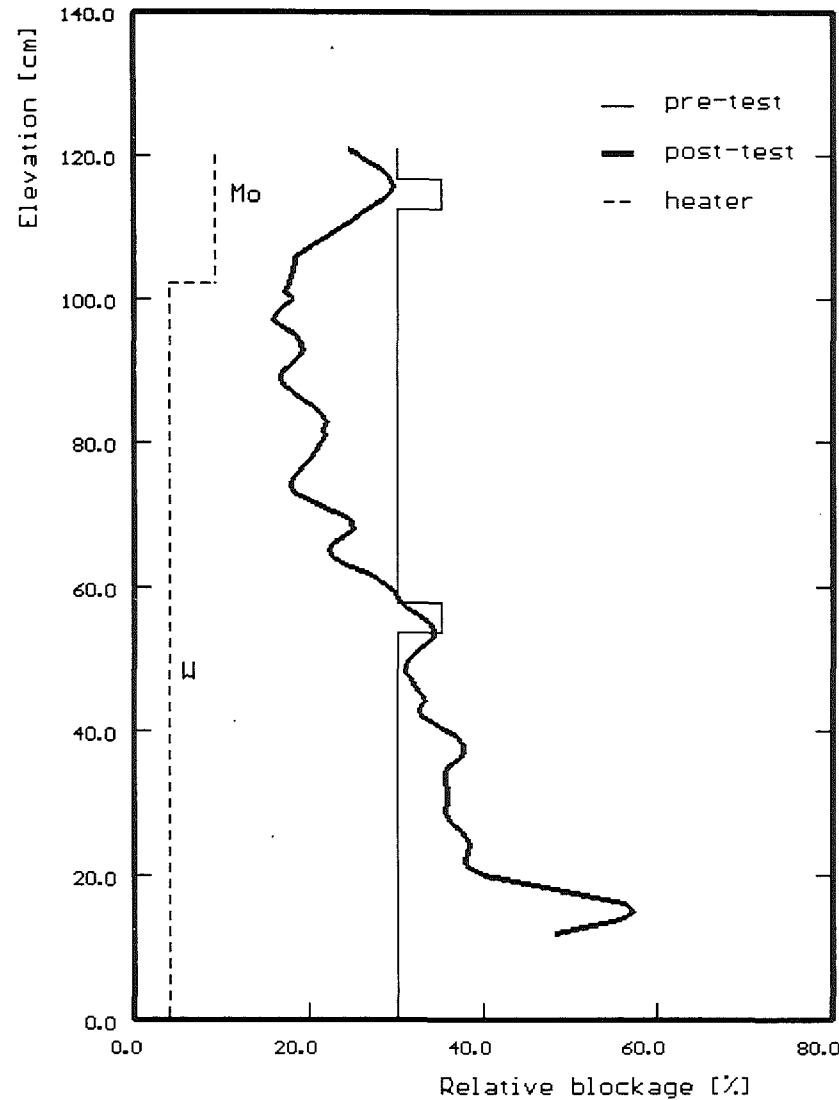


Fig. 79

CORA 31: Axial volume distribution after the test and axial temperature distribution during the test

Fig. 80



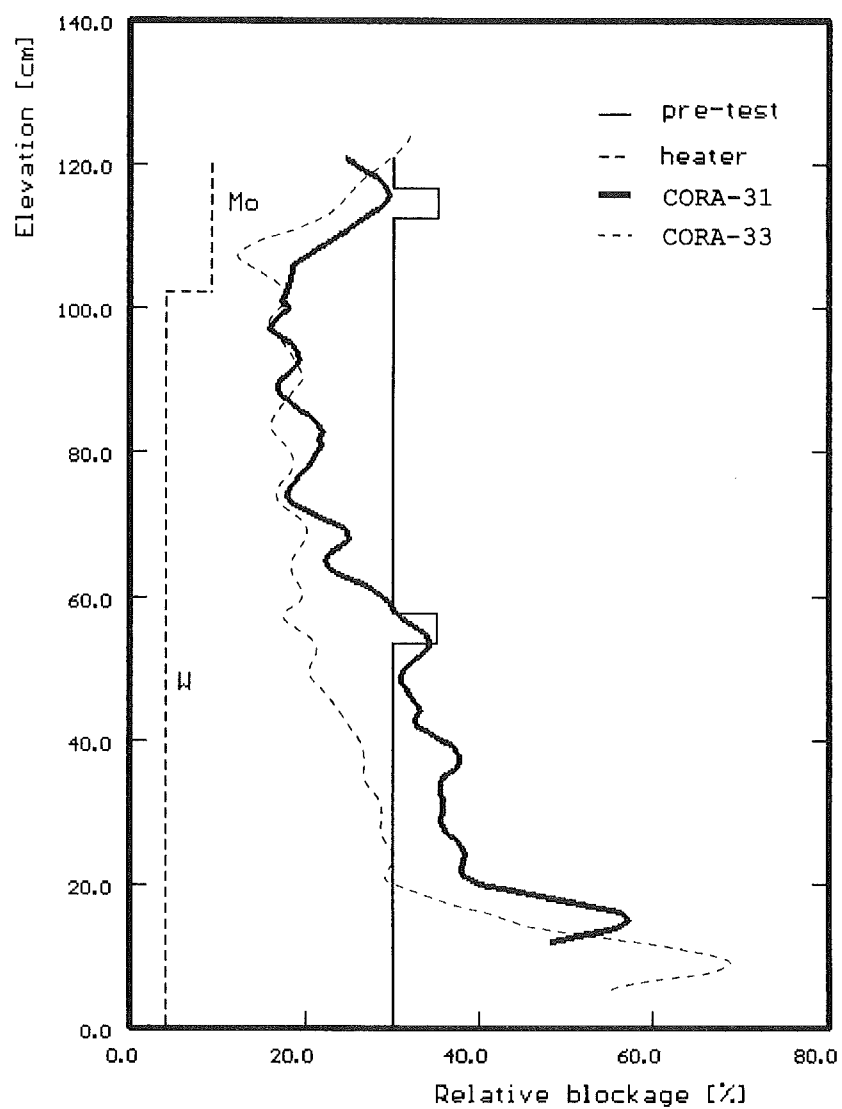
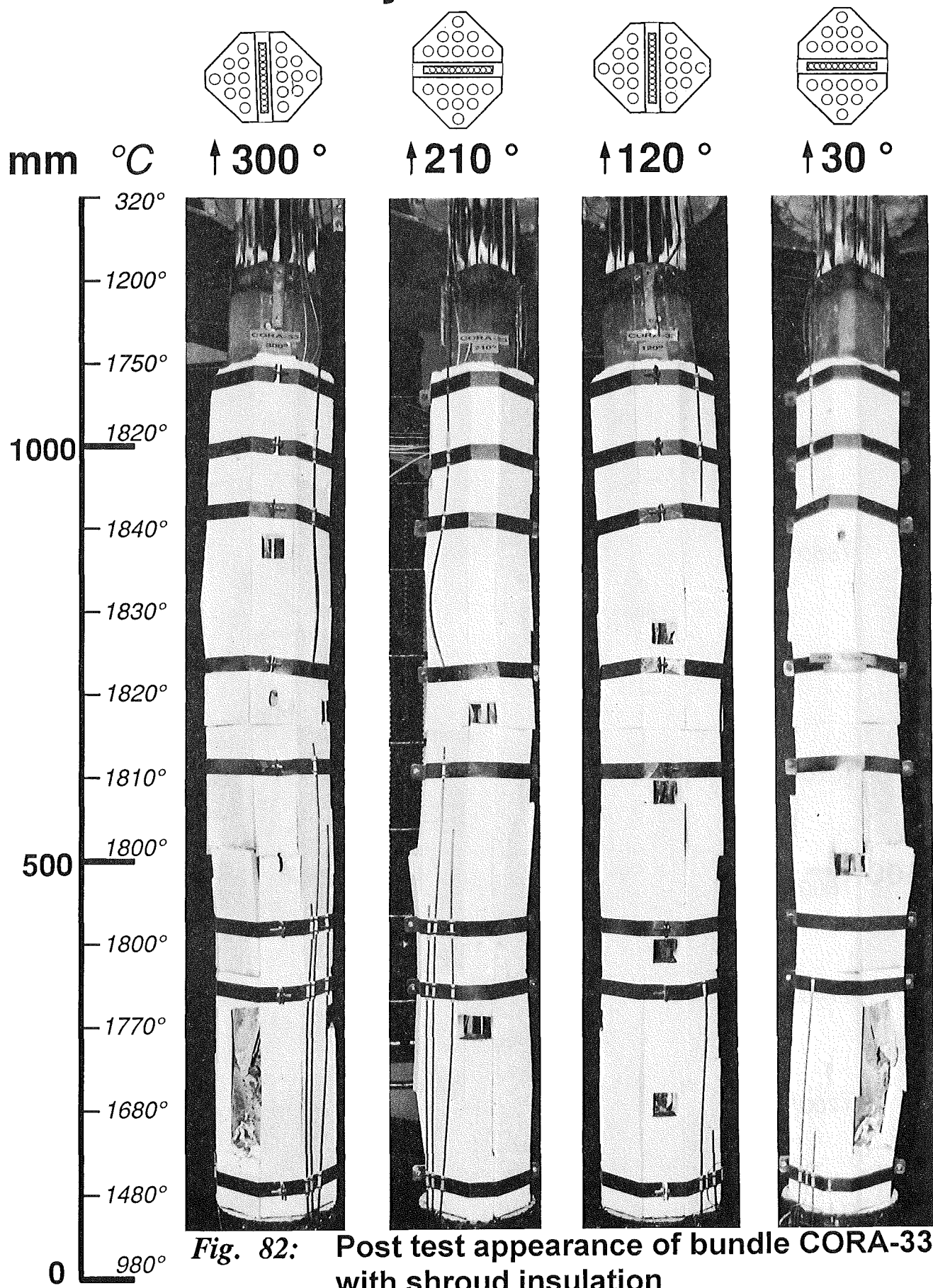


Fig. 81: Comparison of axial volume distribution for test CORA-31 and CORA-33

CORA-33: Dry BWR



CORA-33: DRY BWR

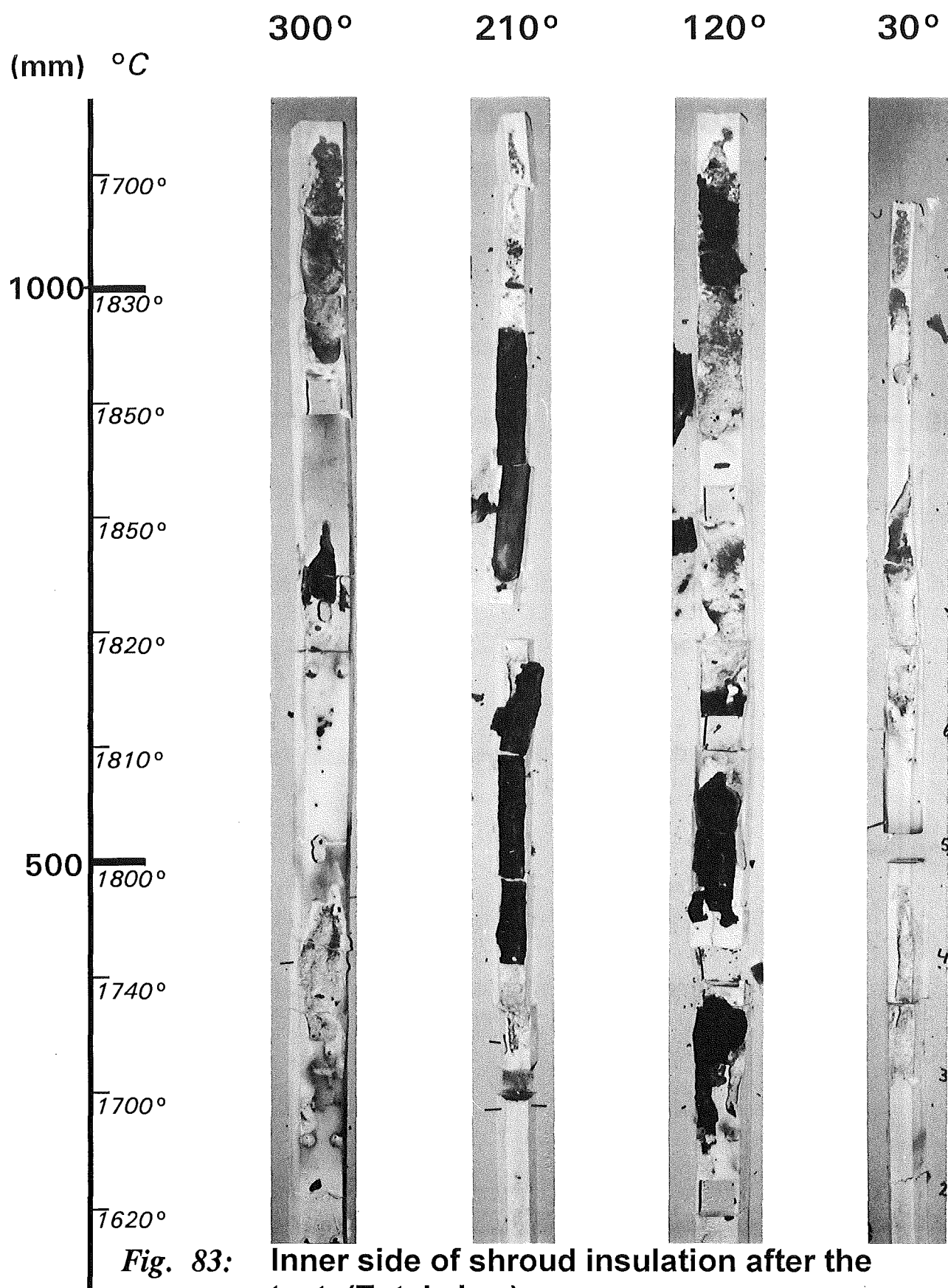


Fig. 83: Inner side of shroud insulation after the test (Total view)

CORA-33: DRY BWR

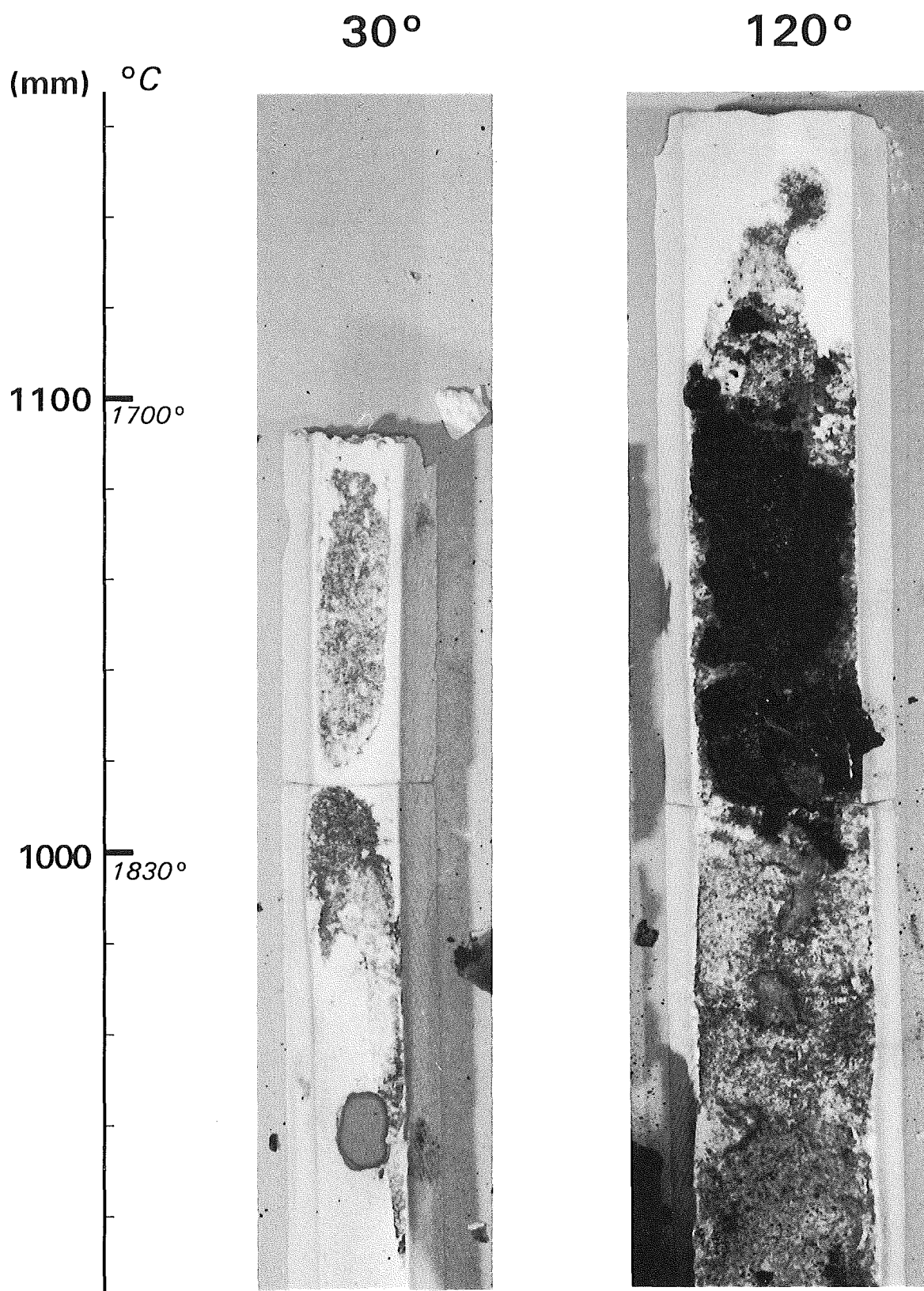


Fig. 84: Inner side of shroud insulation 30° and 120°; 1160-900 mm, partial view

CORA-33: DRY BWR

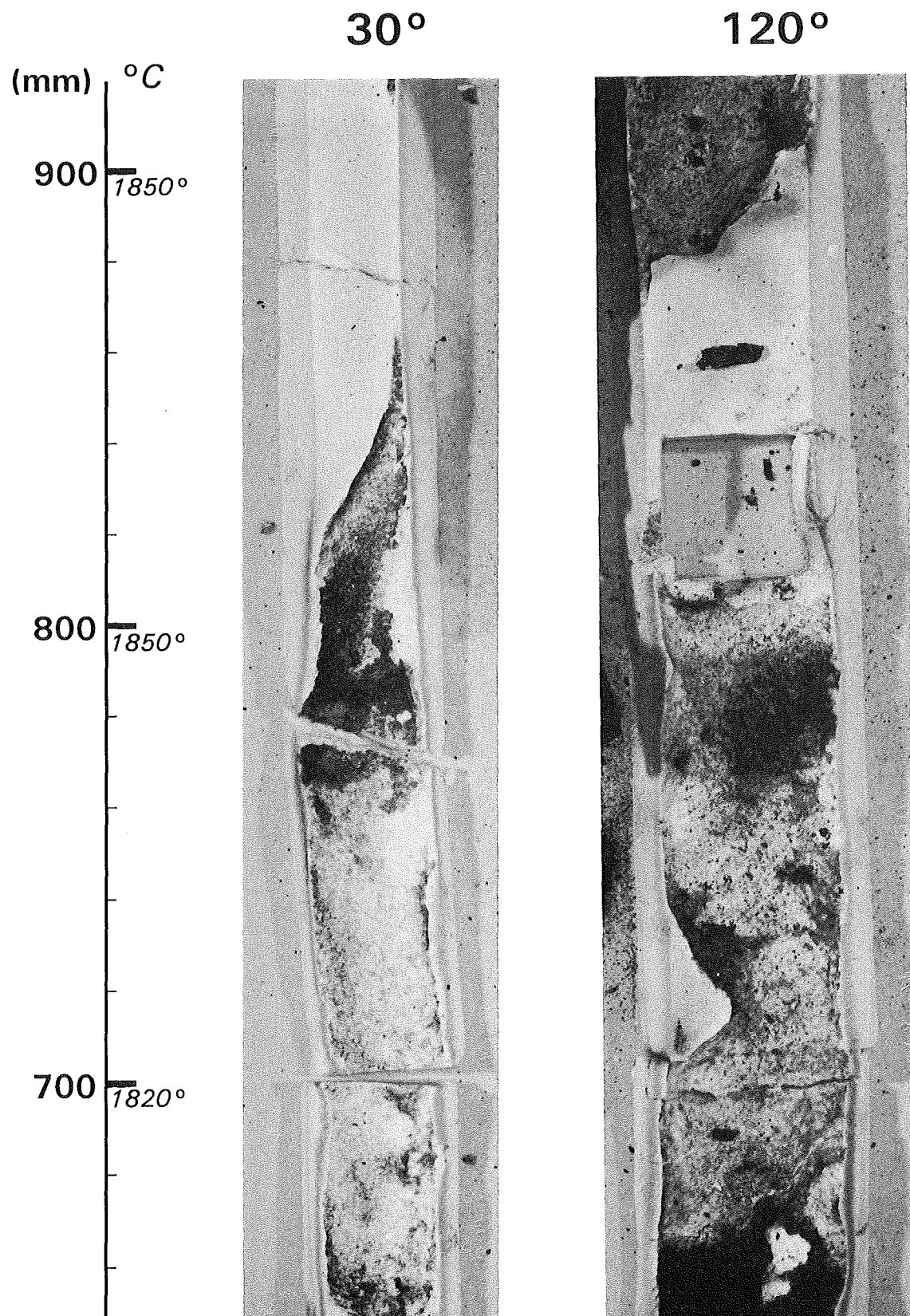


Fig. 85: Inner side of shroud insulation 30° and 120° ; 900-640 mm, partial view

CORA-33: DRY BWR

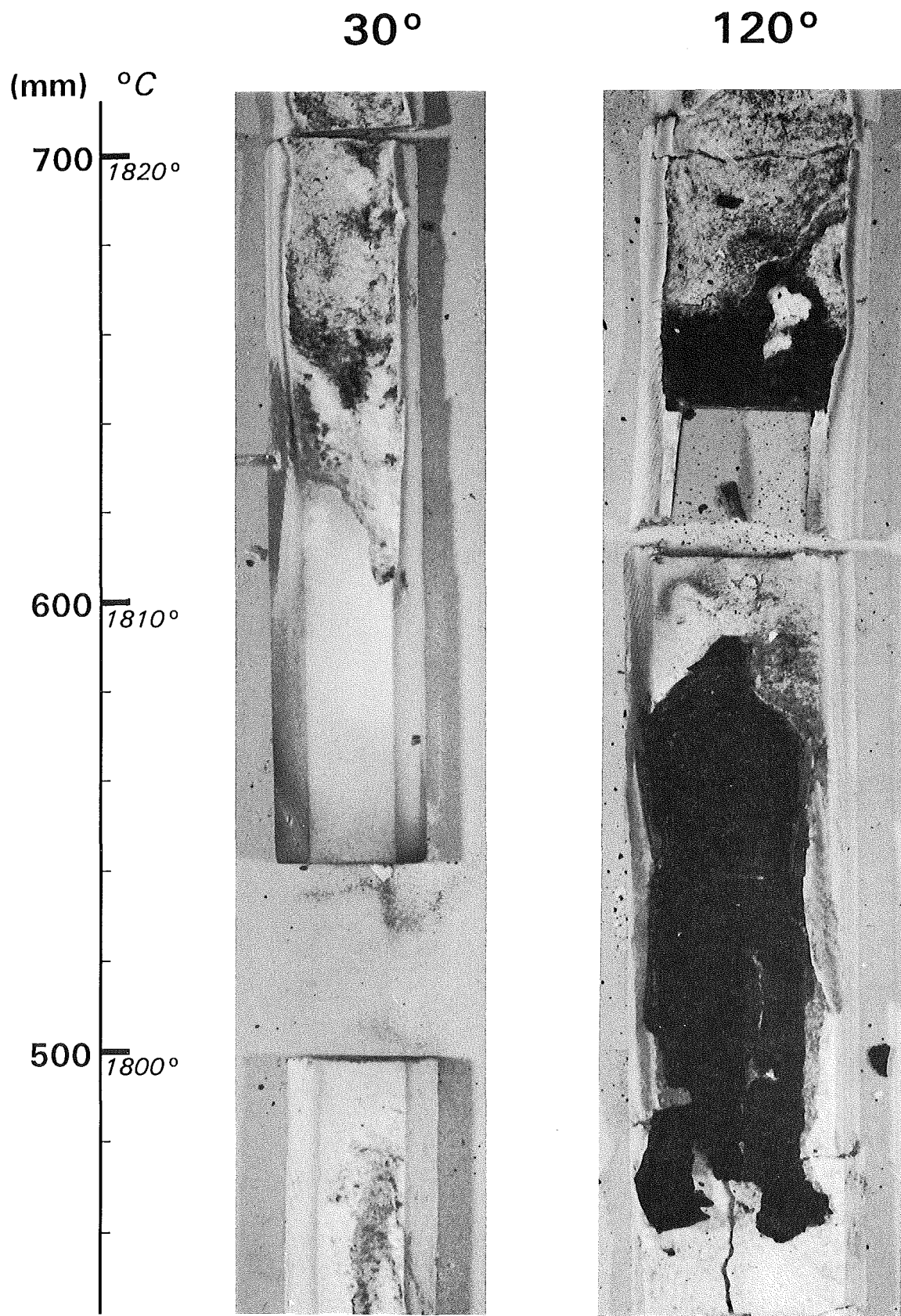


Fig. 86: Inner side of shroud insulation 30° and 120°; 700-440 mm, partial view

CORA-33: DRY BWR

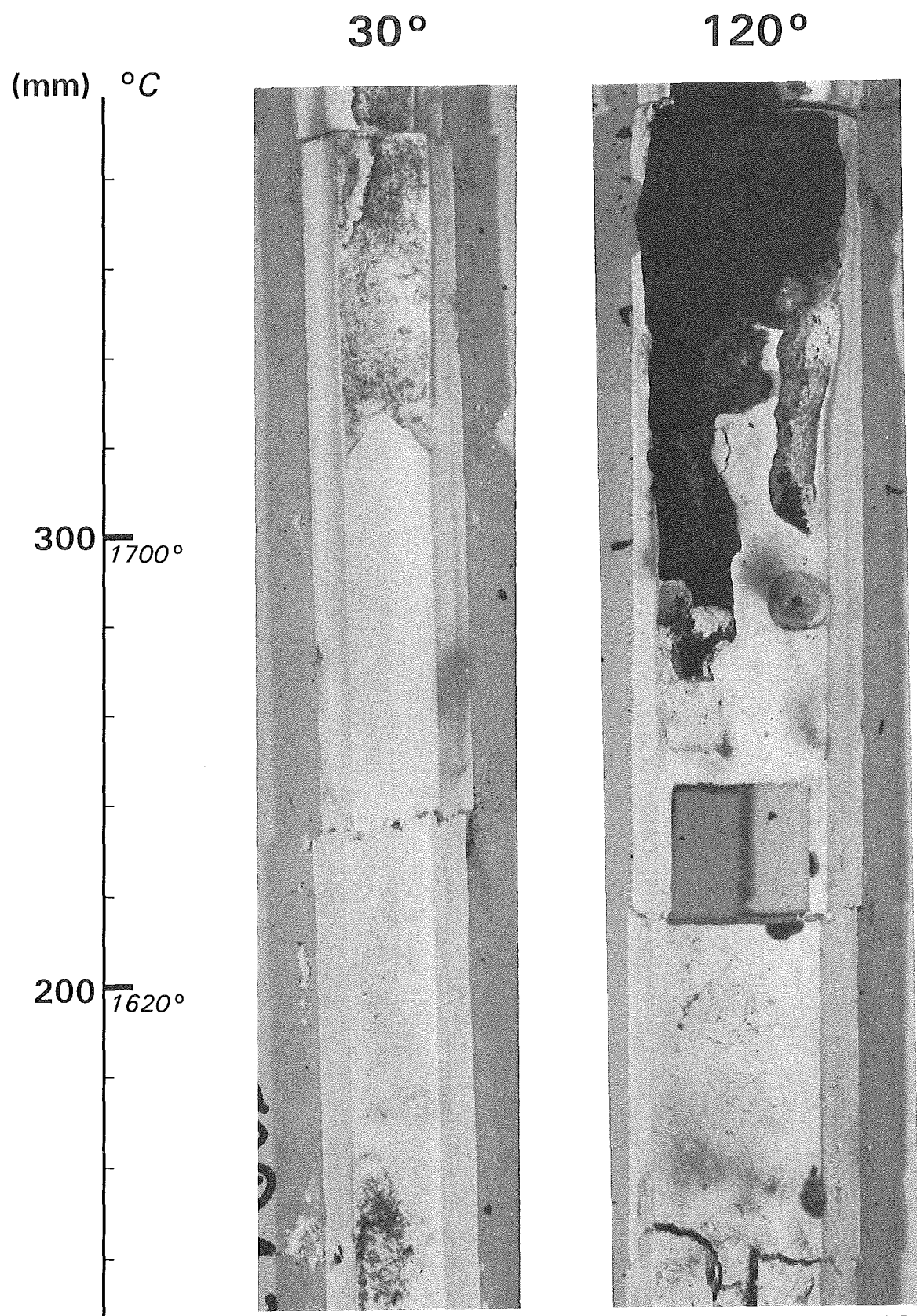


Fig. 87: Inner side of shroud insulation, 30° and 120°;
400-140 mm, partial view

CORA-33: DRY BWR

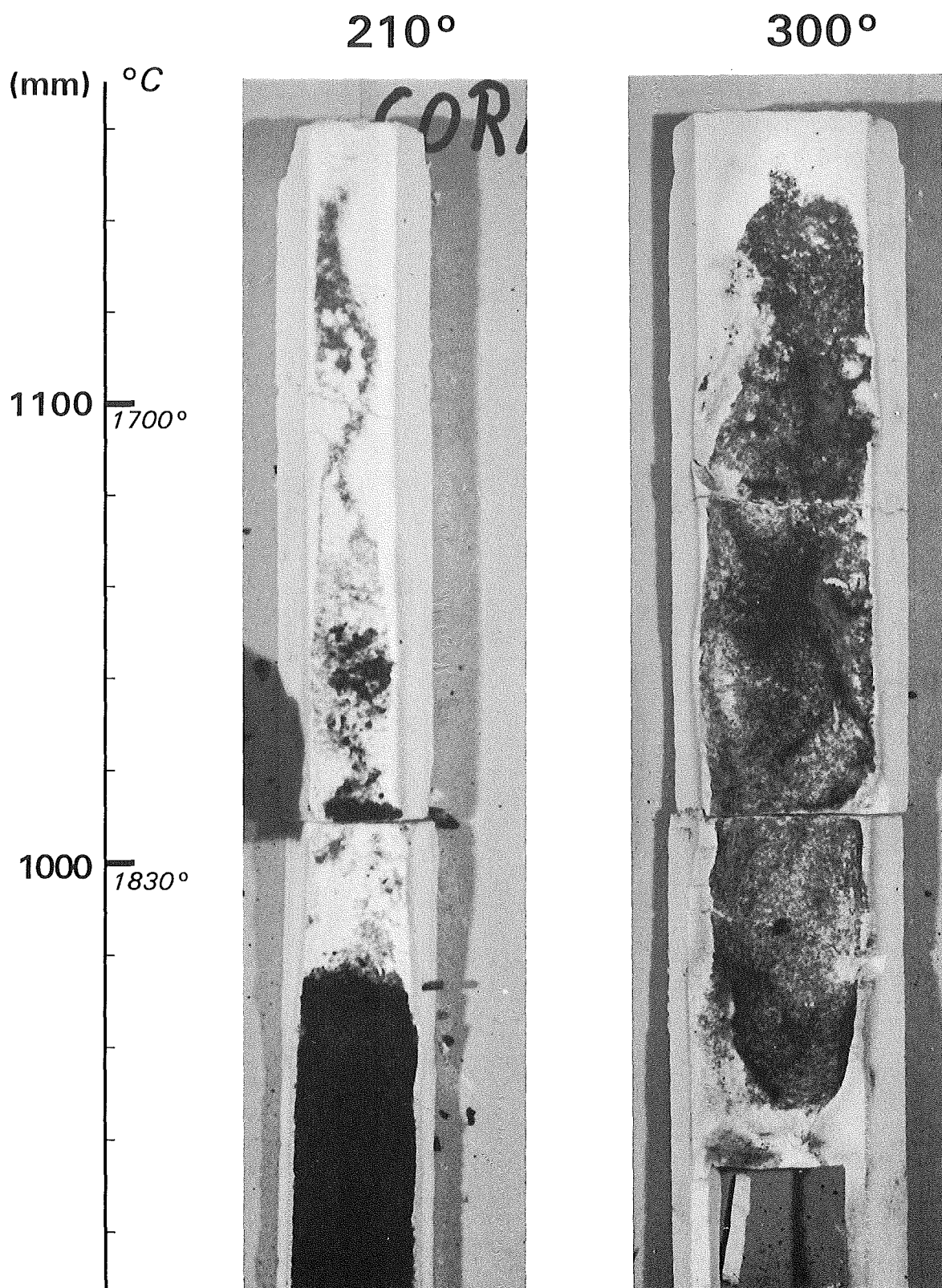


Fig. 88: Inner side of shroud insulation 210° and 300°; 1200-900 mm, partial view

CORA-33: DRY BWR

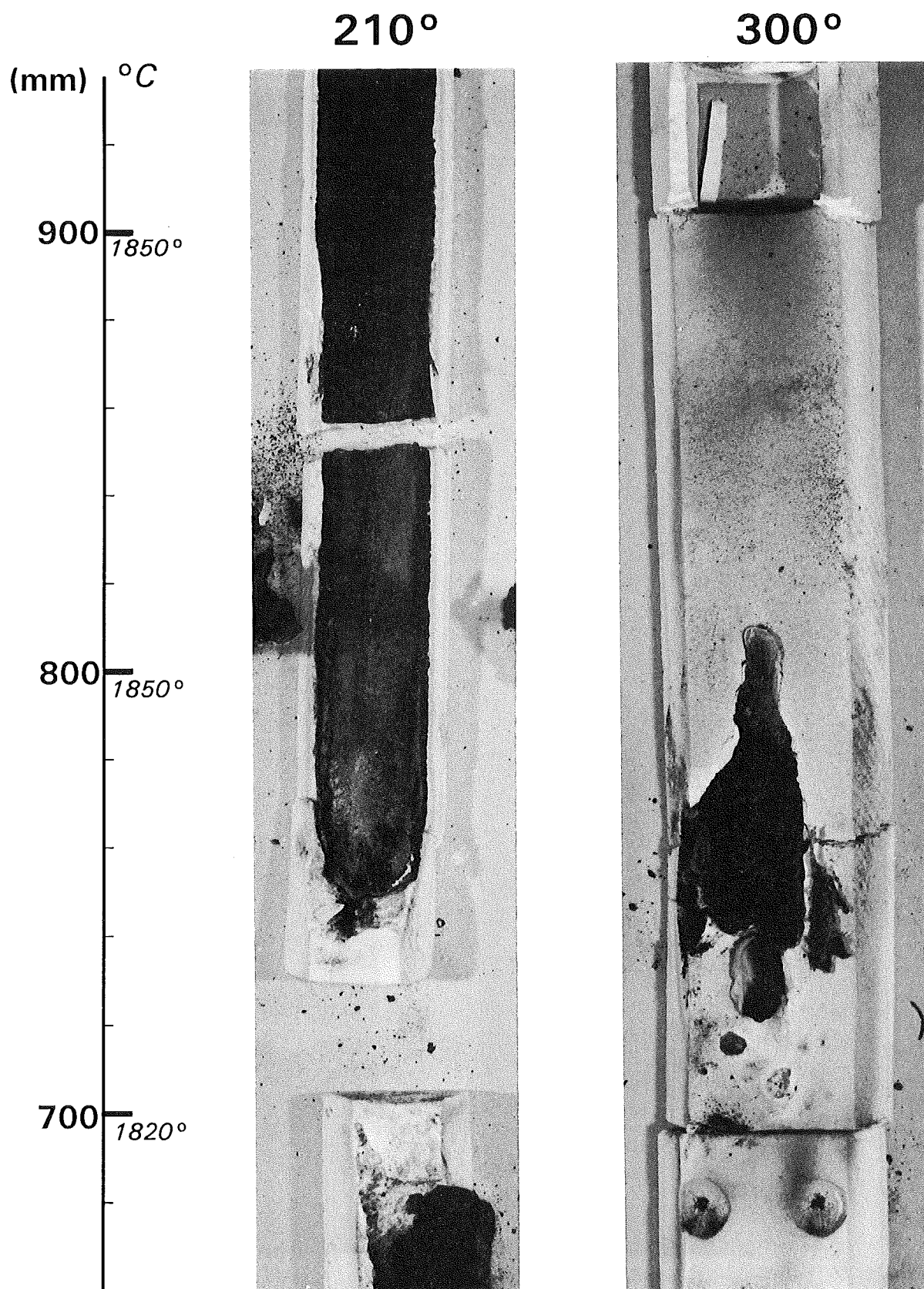


Fig. 89: Inner side of shroud insulation 210° and 300°; 920-660 mm, partial view

CORA-33: DRY BWR

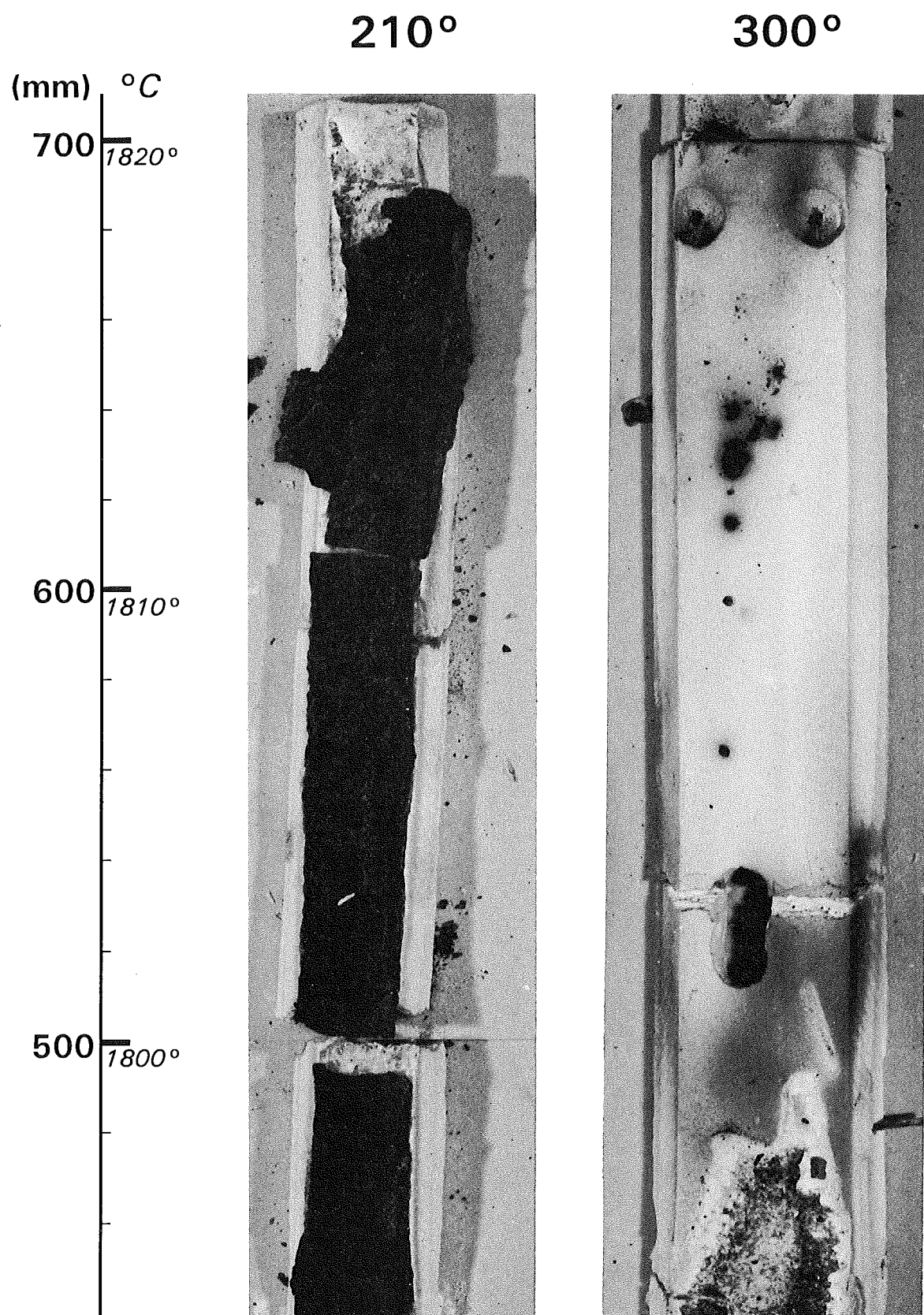


Fig. 90: Inner side of shroud insulation 210° and 300°; 700-440 mm, partial view

CORA-33: DRY BWR

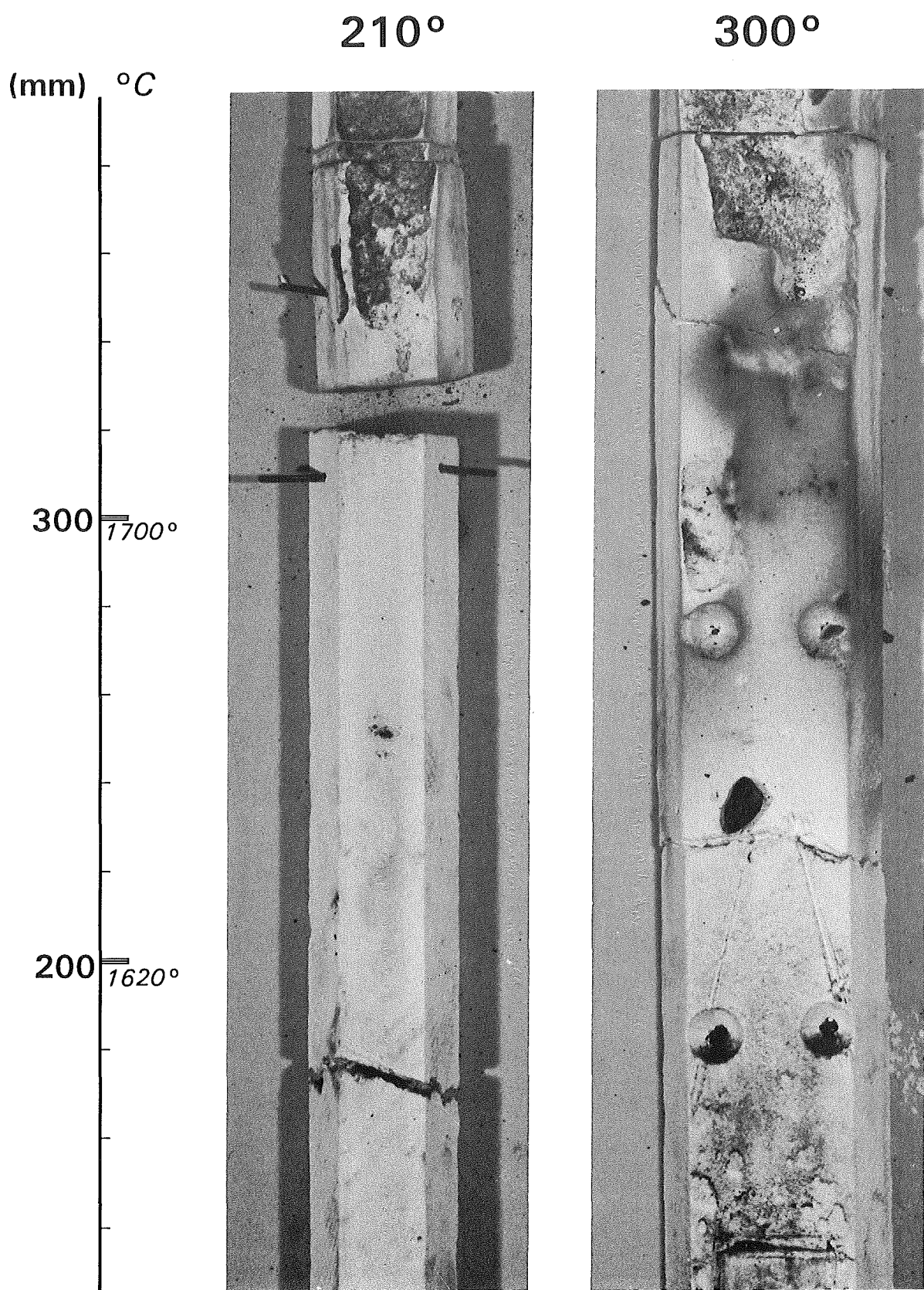


Fig. 91: Inner side of shroud insulation 210° and 300°; 400-120 mm, partial view

CORA-33: DRY BWR

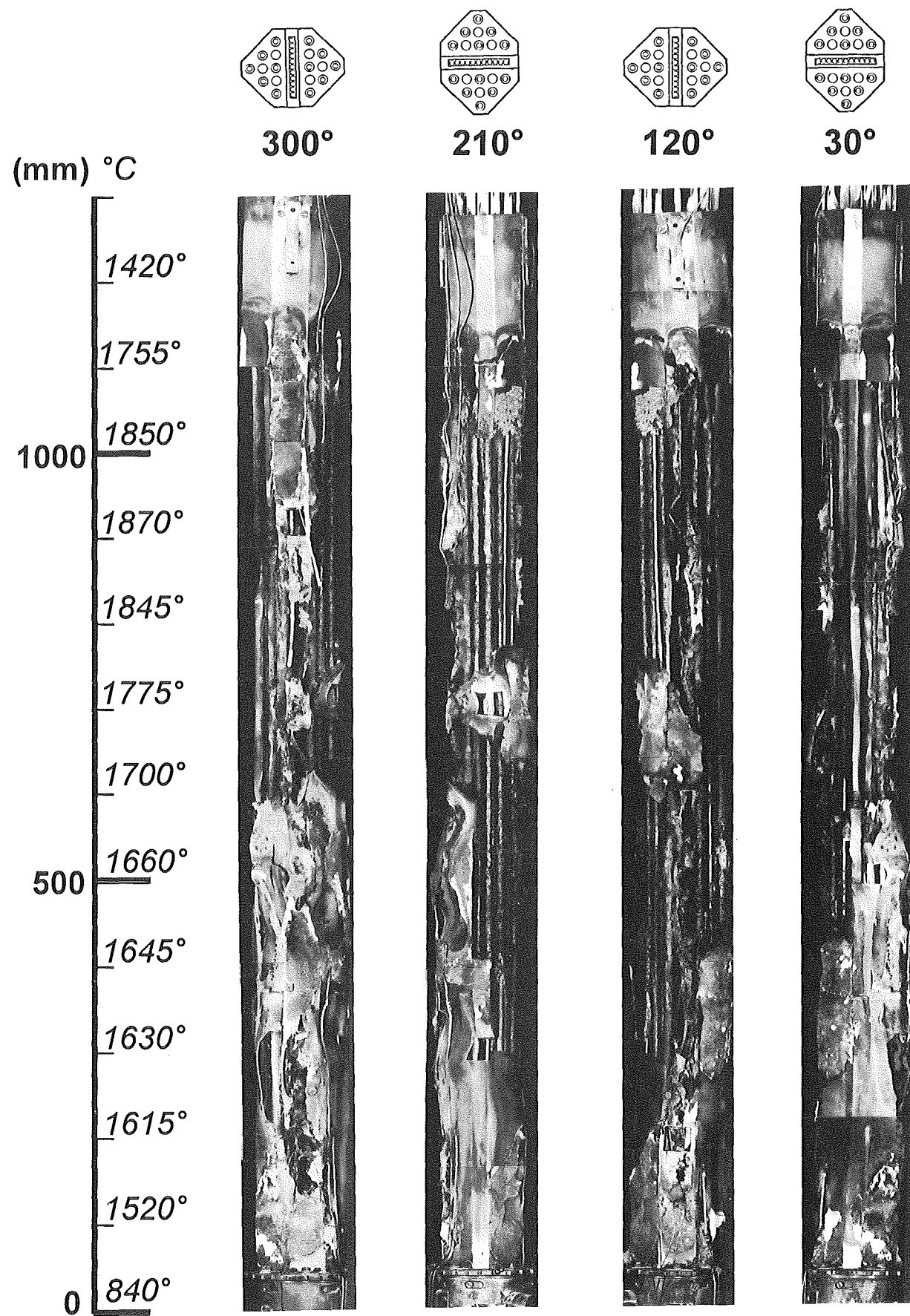
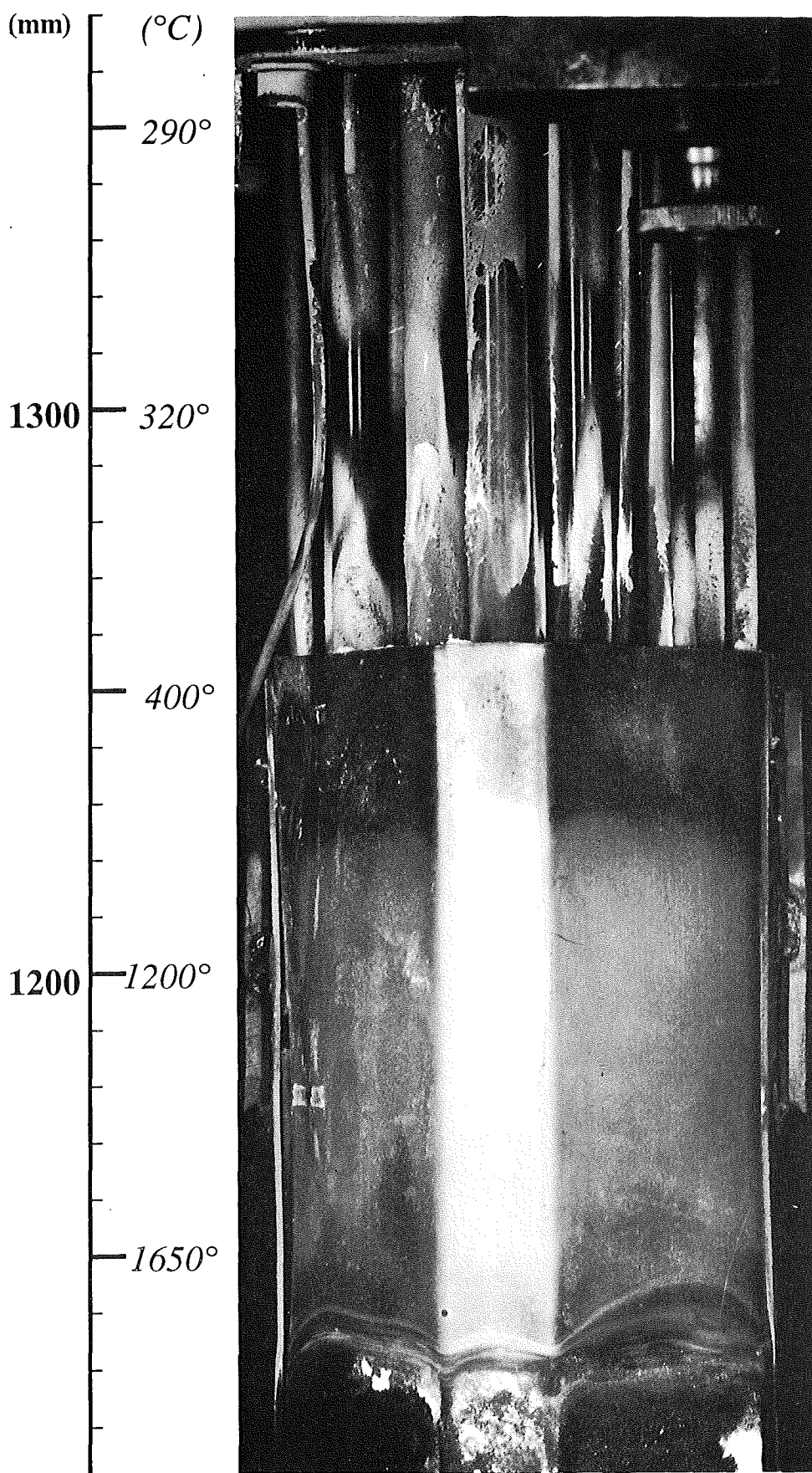
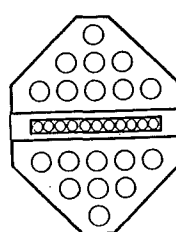


Fig. 92: Post test view of bundle CORA-33 after partial removal of shroud (Total view)

CORA-33

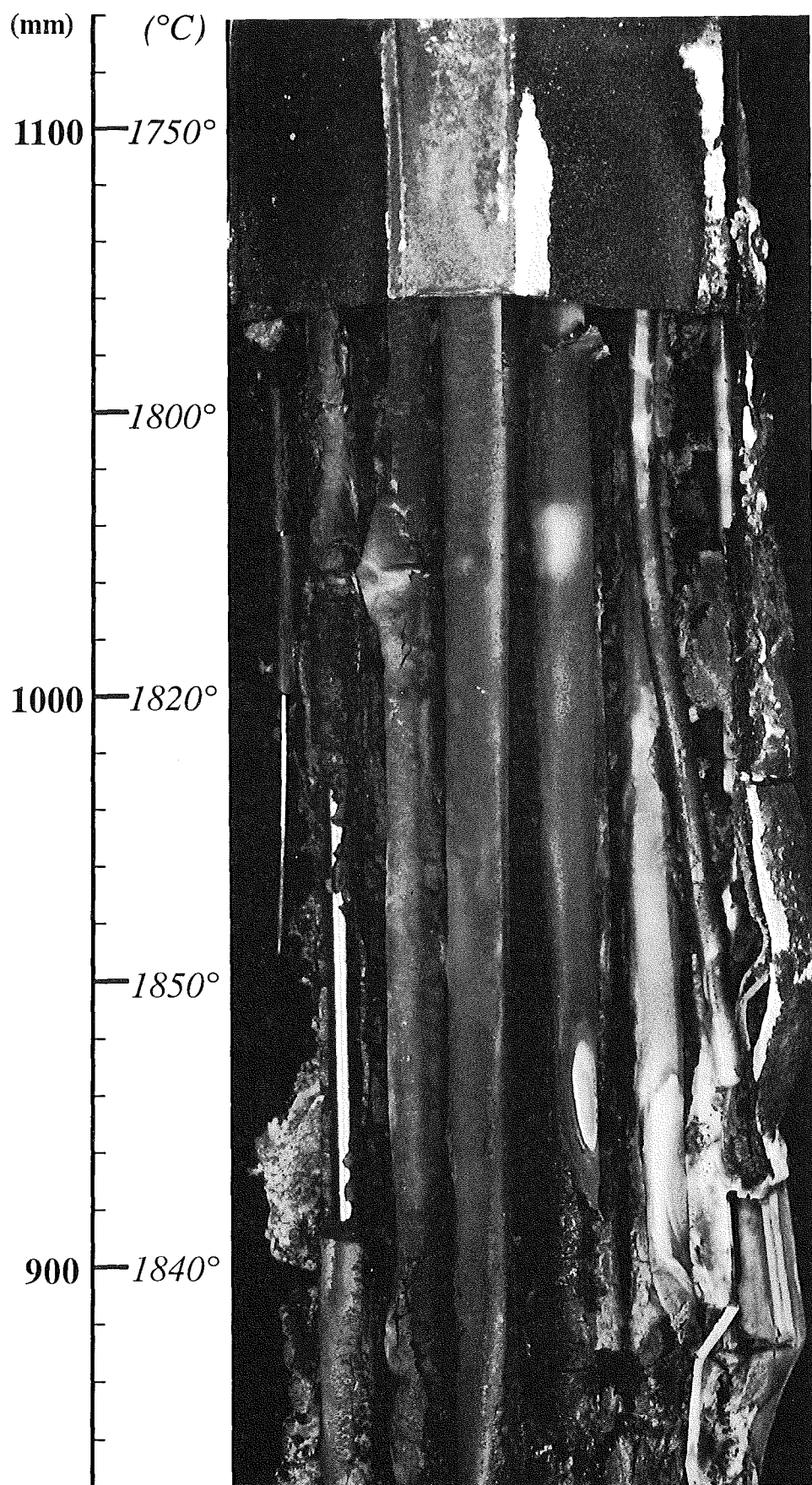


DRY BWR



*Fig. 93: Post test view of bundle, 30°, partial view,
1370-1110 mm*

CORA-33



DRY BWR

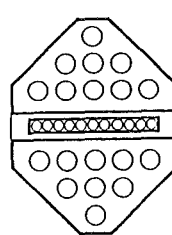
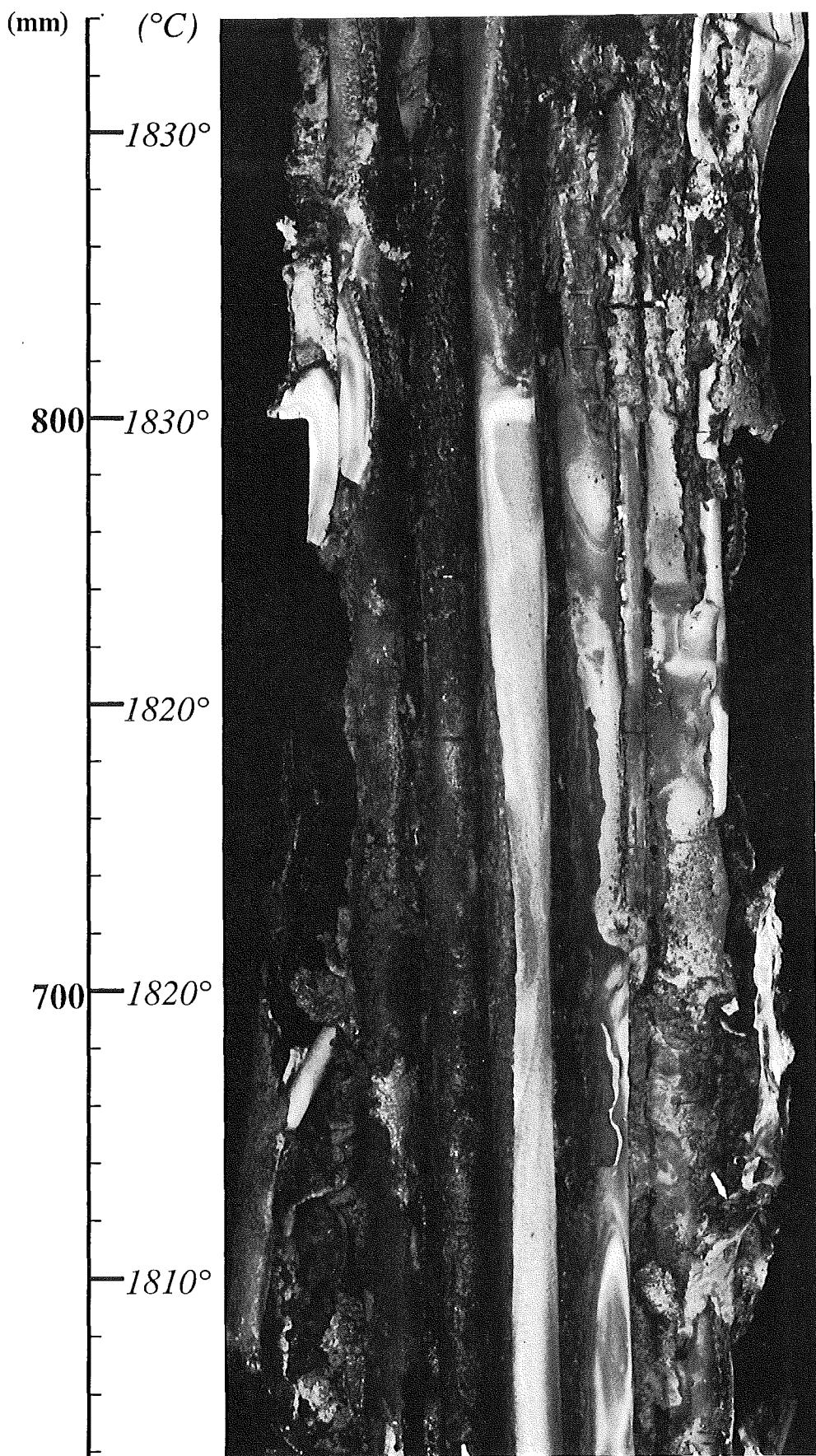
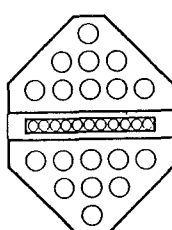


Fig. 94: Post test view of bundle, 30°, partial view,
1120-860 mm

CORA-33



DRY BWR



*Fig. 95: Post test view of bundle, 30°, partial view,
870-620 mm*

CORA-33

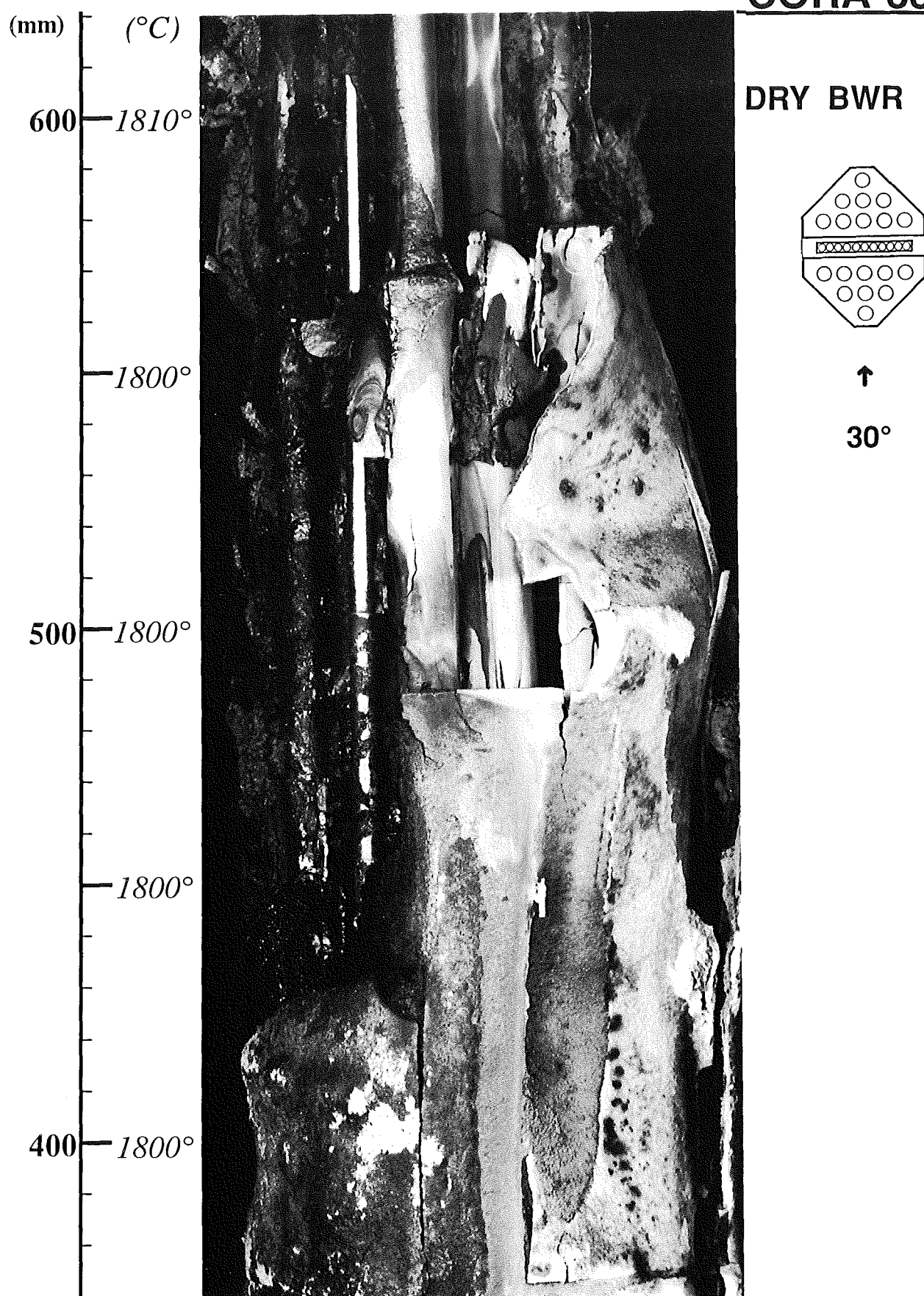


Fig. 96: Post test view of bundle, 30°, partial view,
620-370 mm

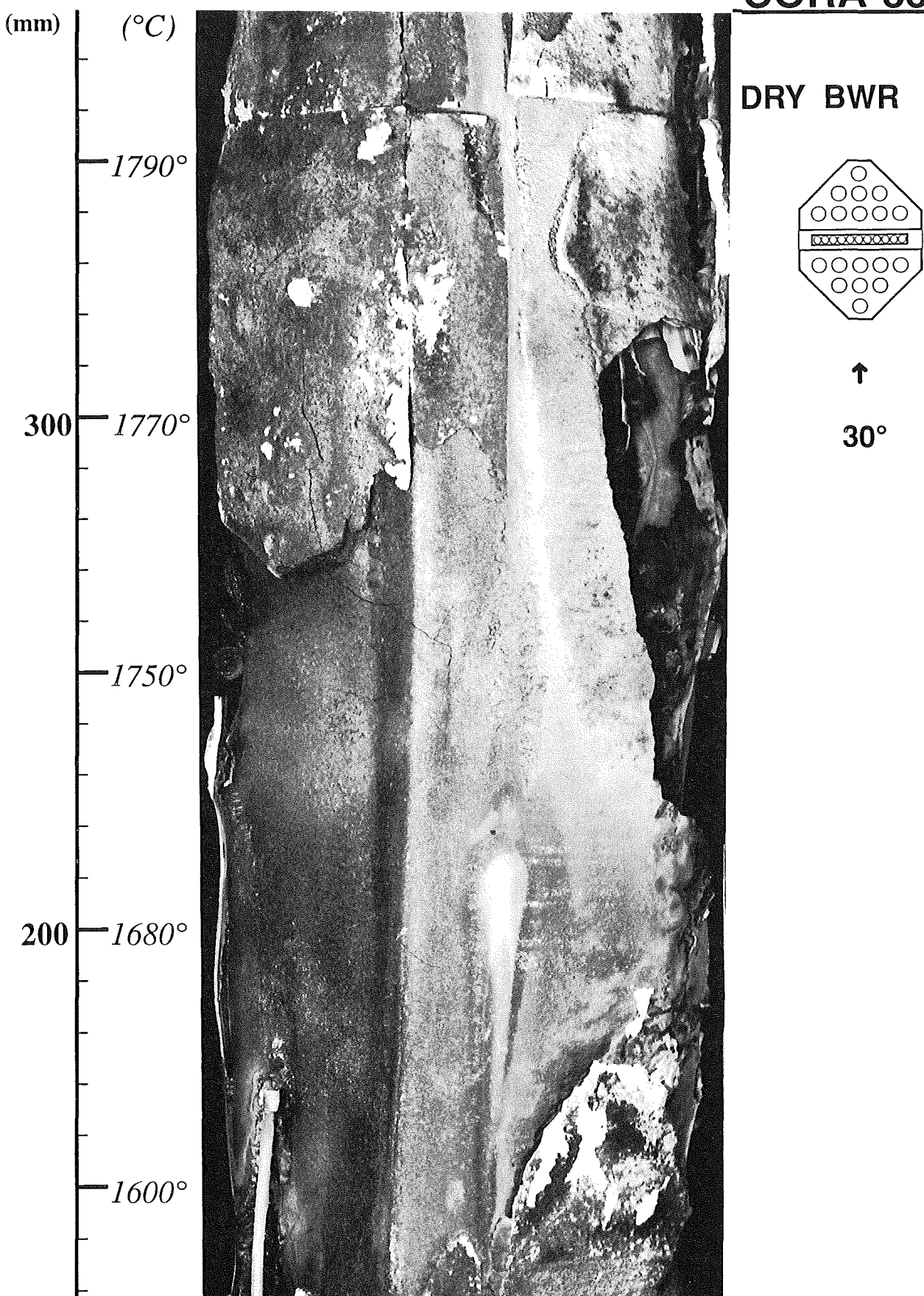
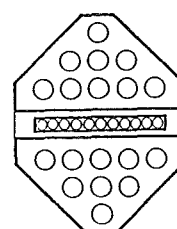


Fig. 97: Post test view of bundle, 30°, partial view,
380-130 mm

CORA-33

DRY BWR



↑

30°

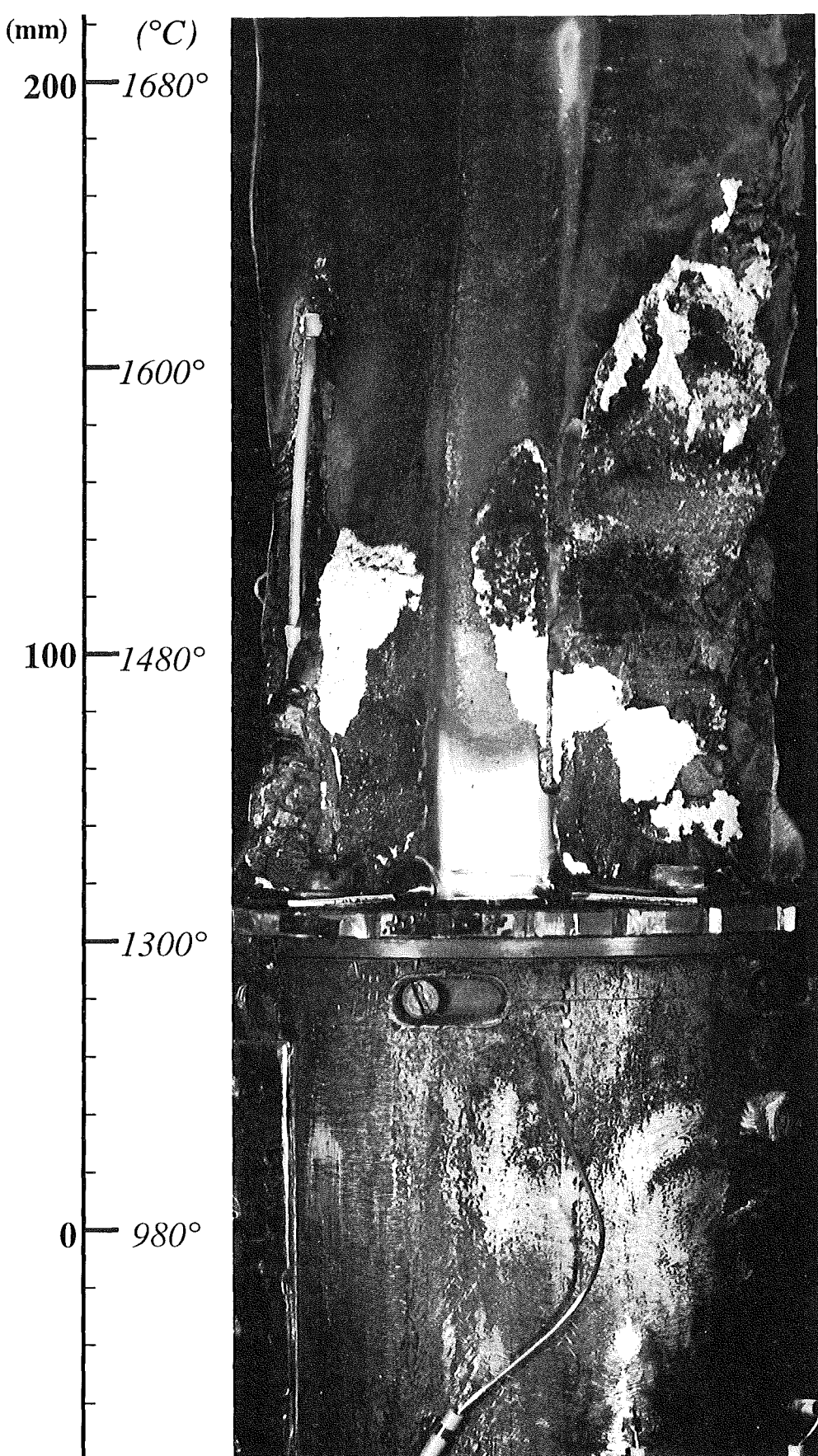
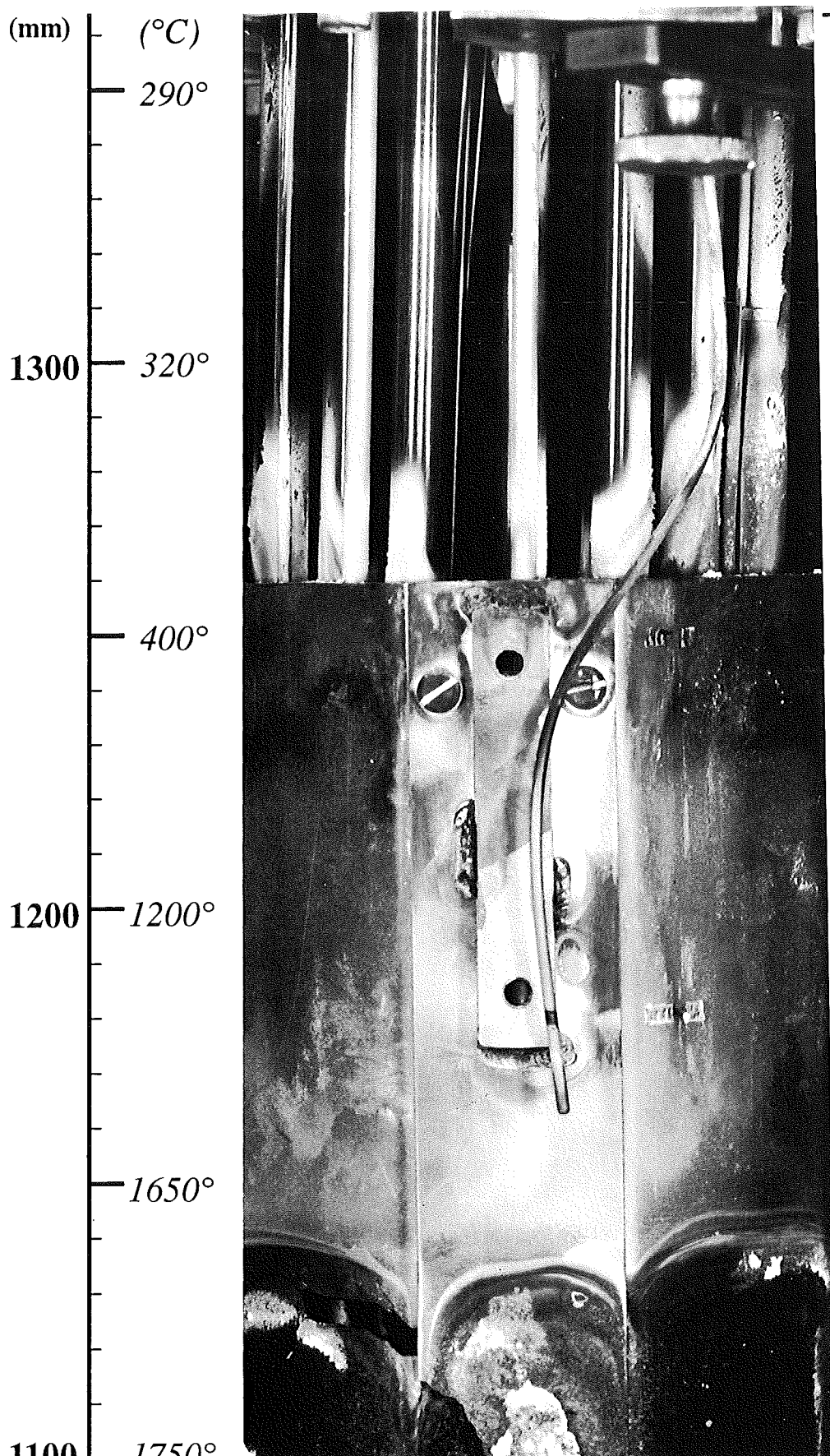


**Fig. 98: Post test view of bundle, 30°, partial view,
210 to -40 mm**



DRY BWR

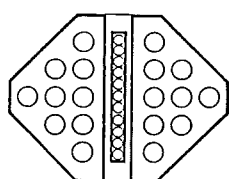
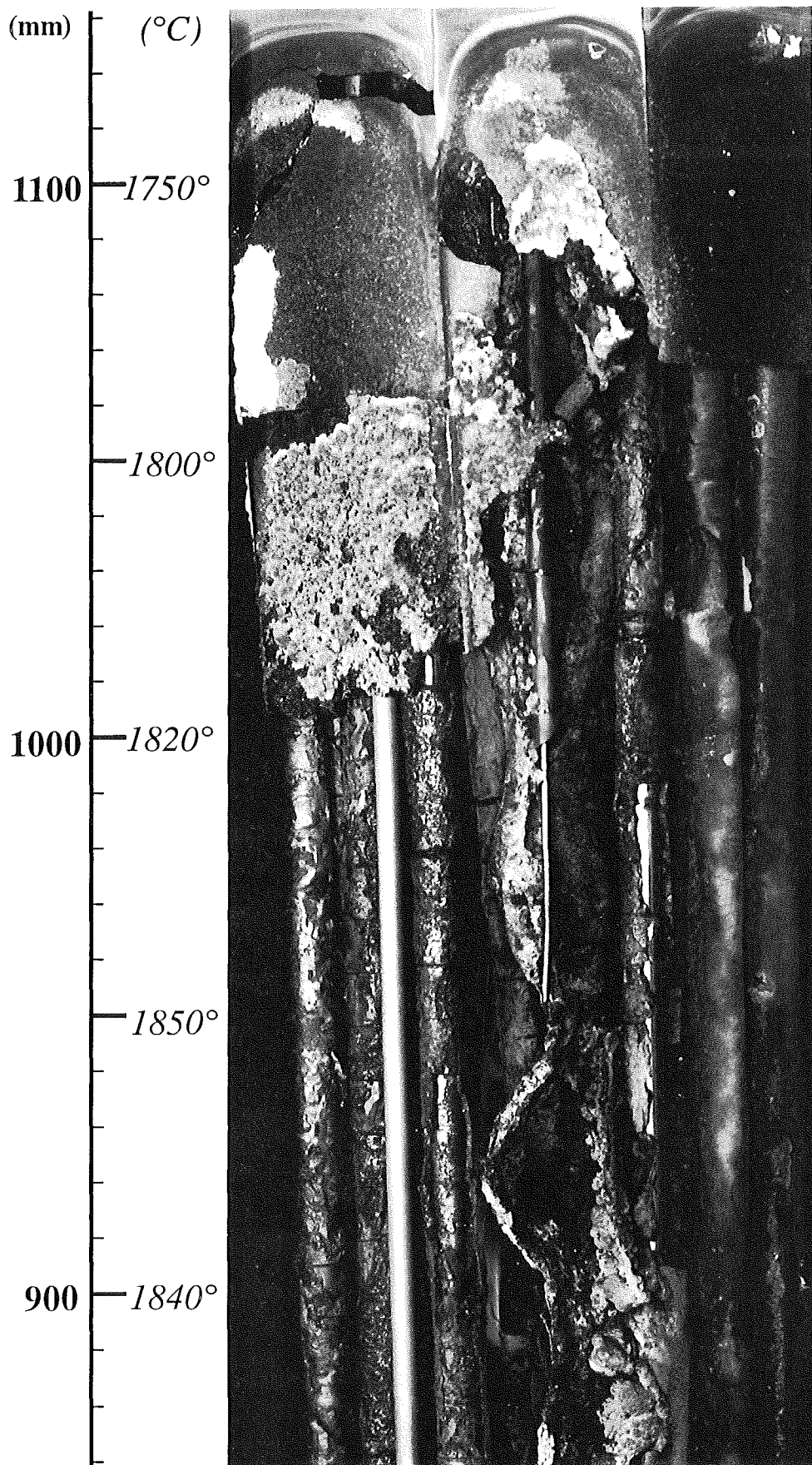
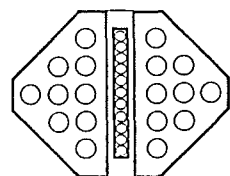


Fig. 99: Post test view of bundle, 120° partial view,
1360-1100 mm

CORA-33



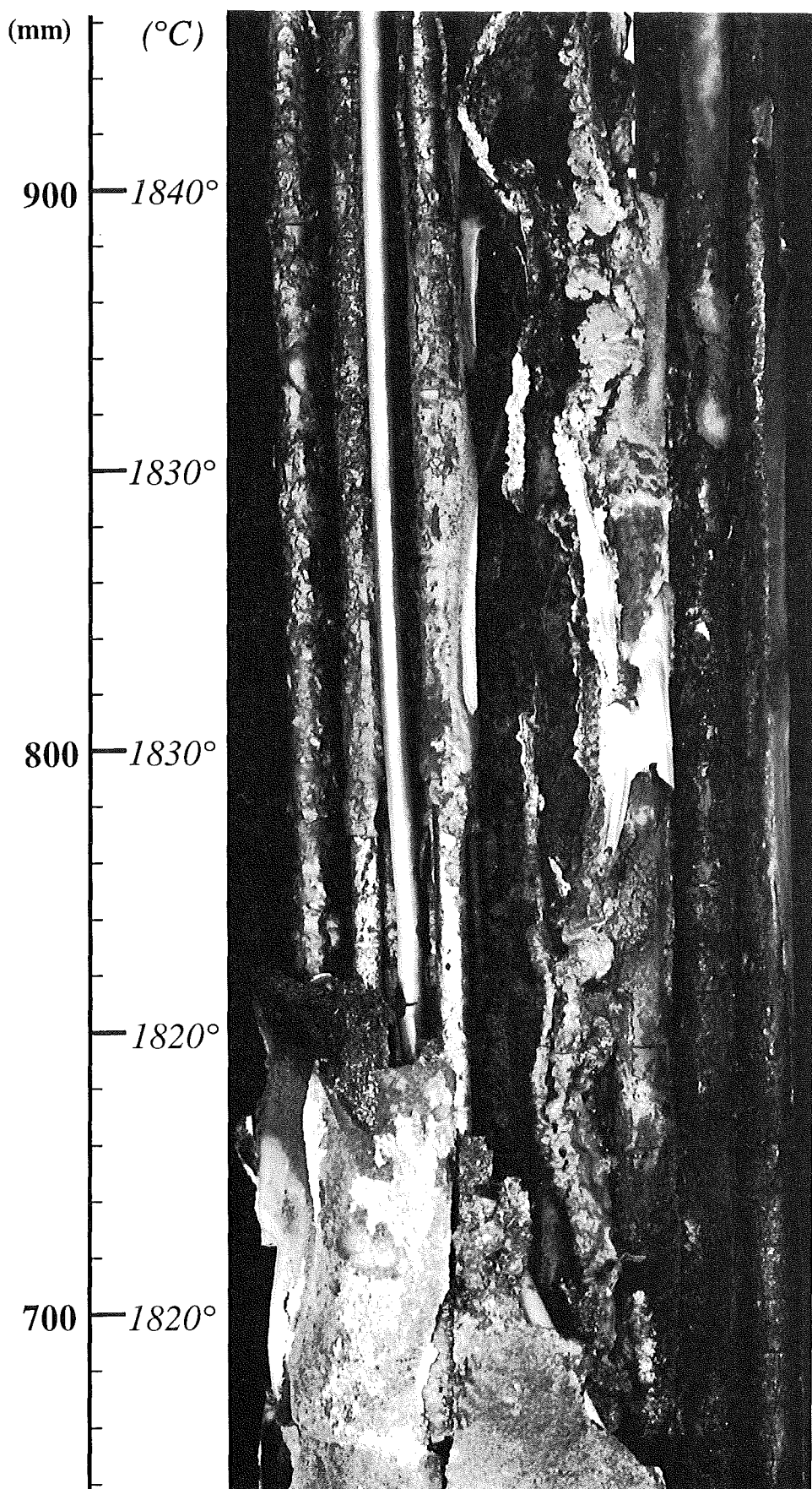
DRY BWR



↑
120°

**Fig. 100: Post test view of bundle, 120° partial view,
1130-870 mm**

CORA-33



DRY BWR

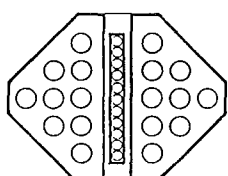
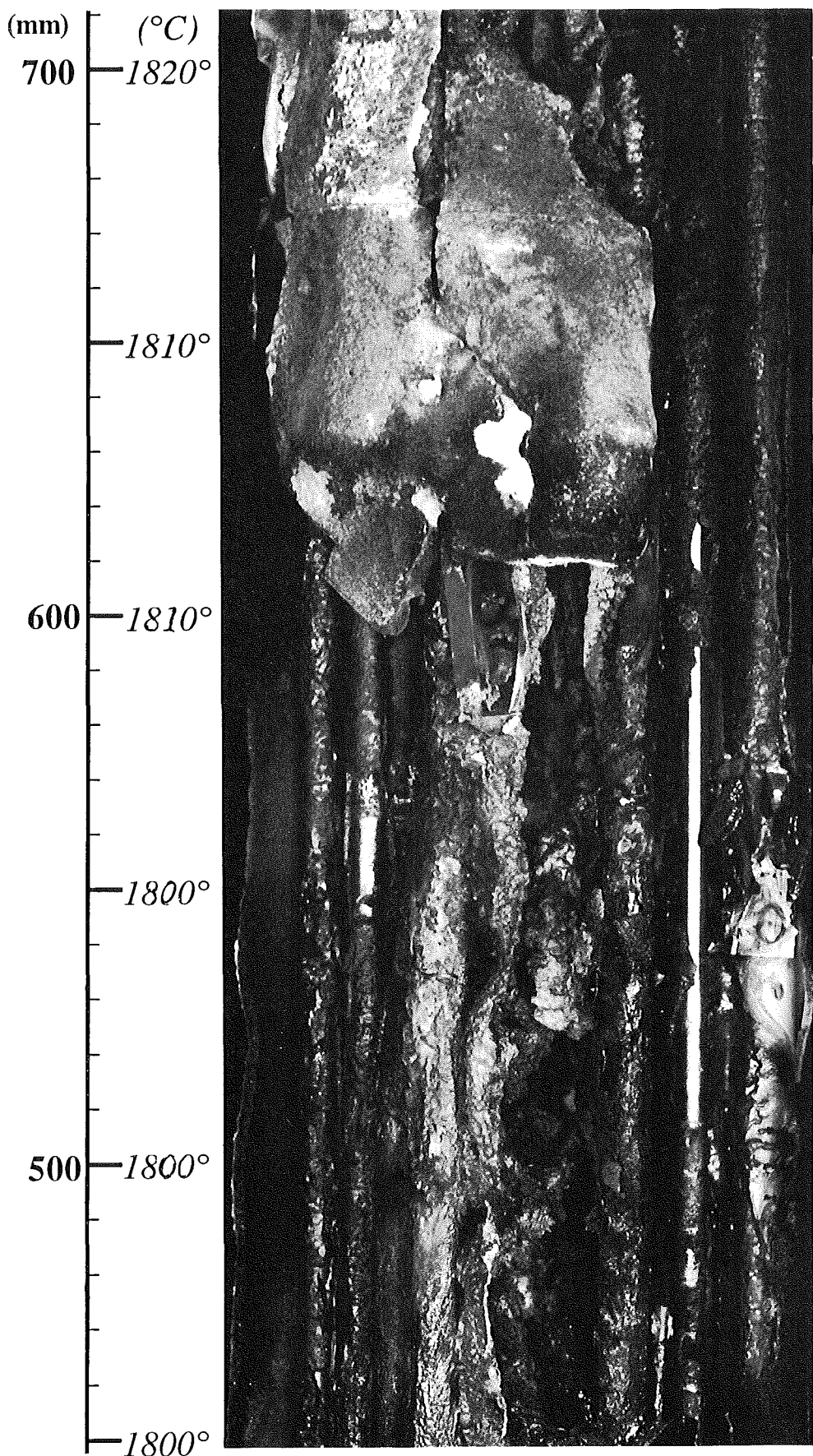


**Fig. 101: Post test view of bundle, 120° partial view,
930-670 mm**

CORA-33



DRY BWR

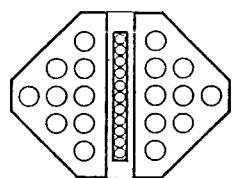


*Fig. 102: Post test view of bundle, 120° partial view,
700-450 mm*

CORA-33

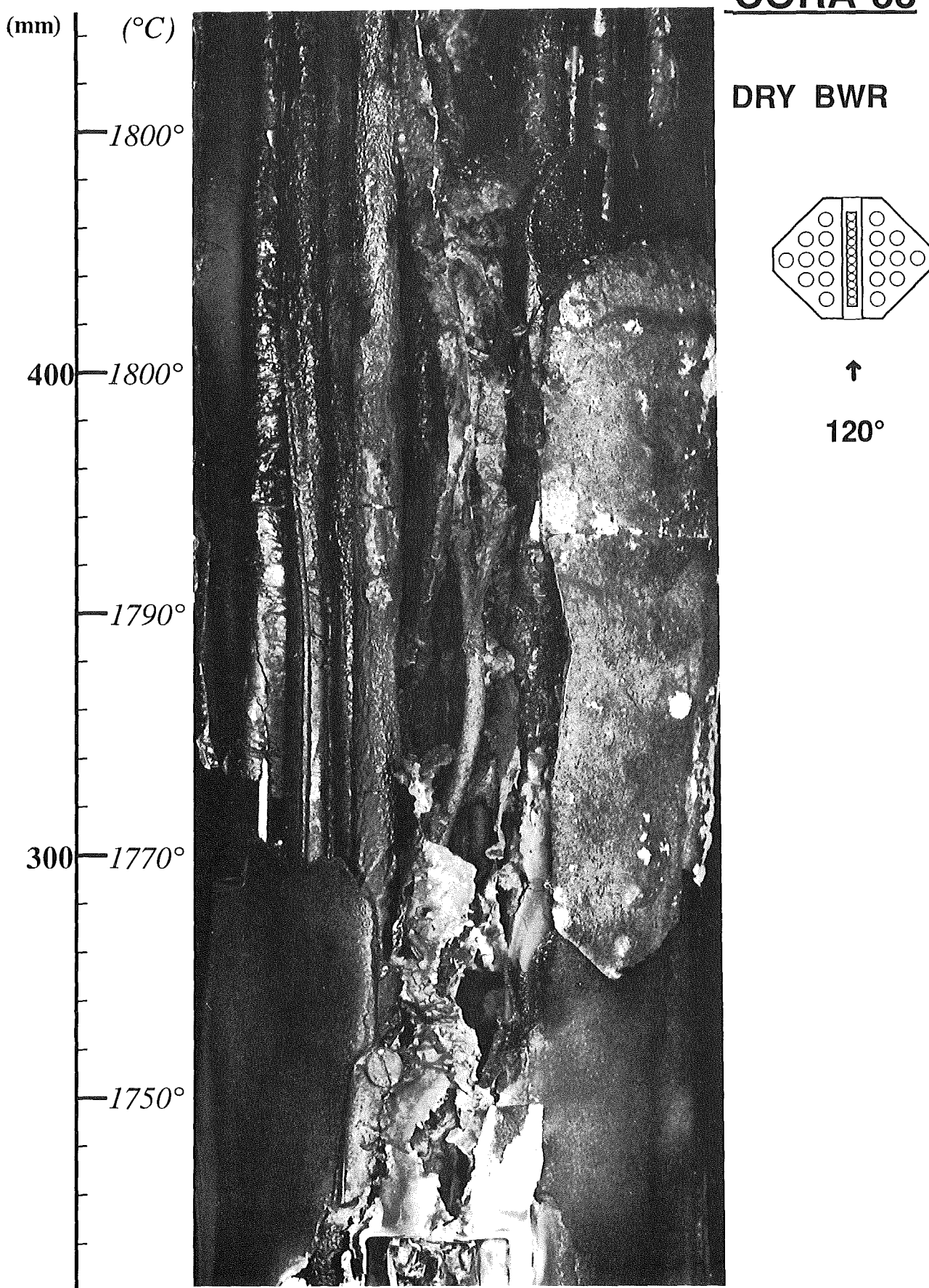
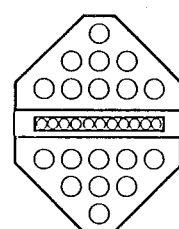


*Fig. 103: Post test view of bundle, 120° partial view,
470-210 mm*

CORA-33

DRY BWR



210°

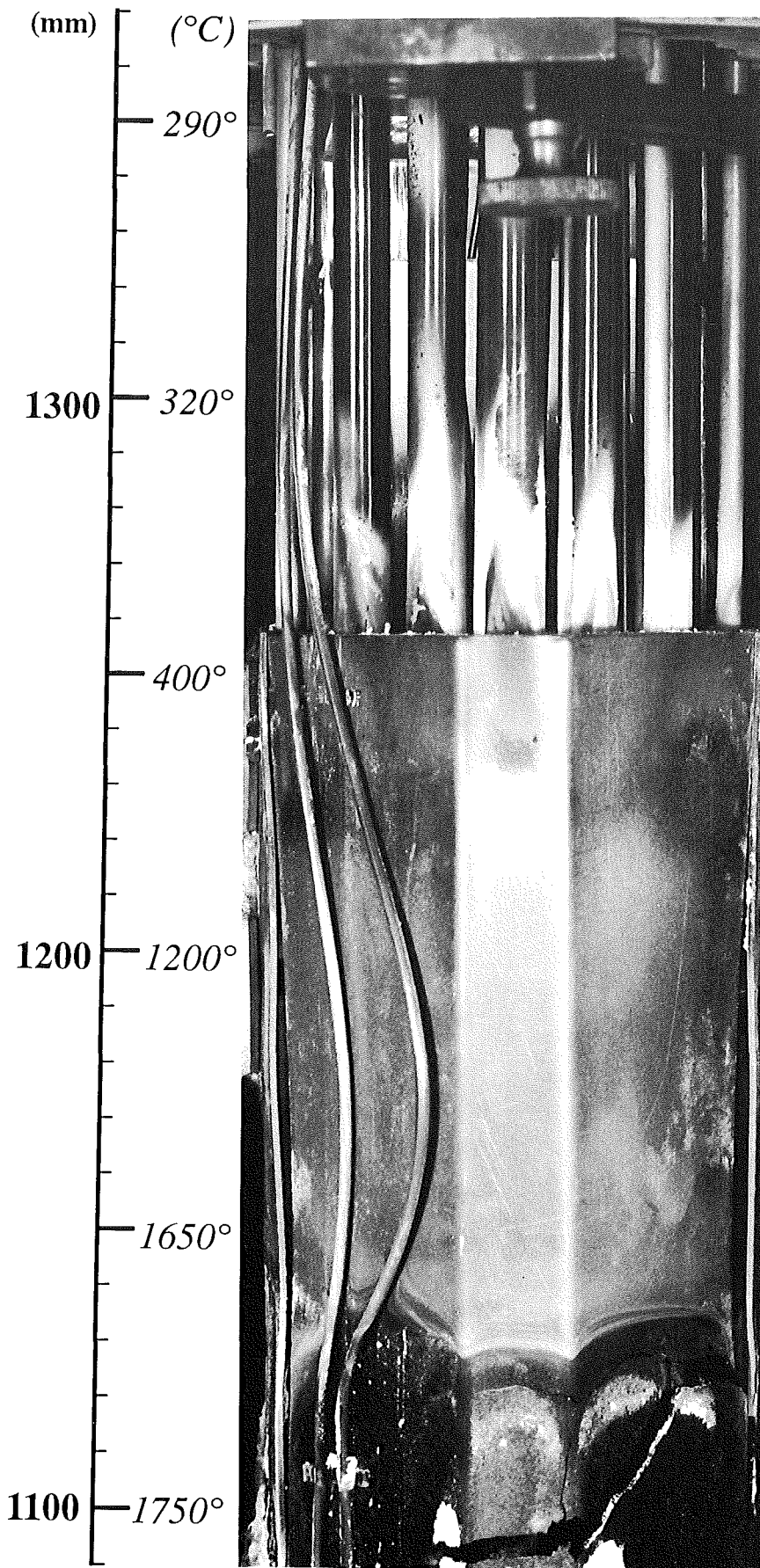
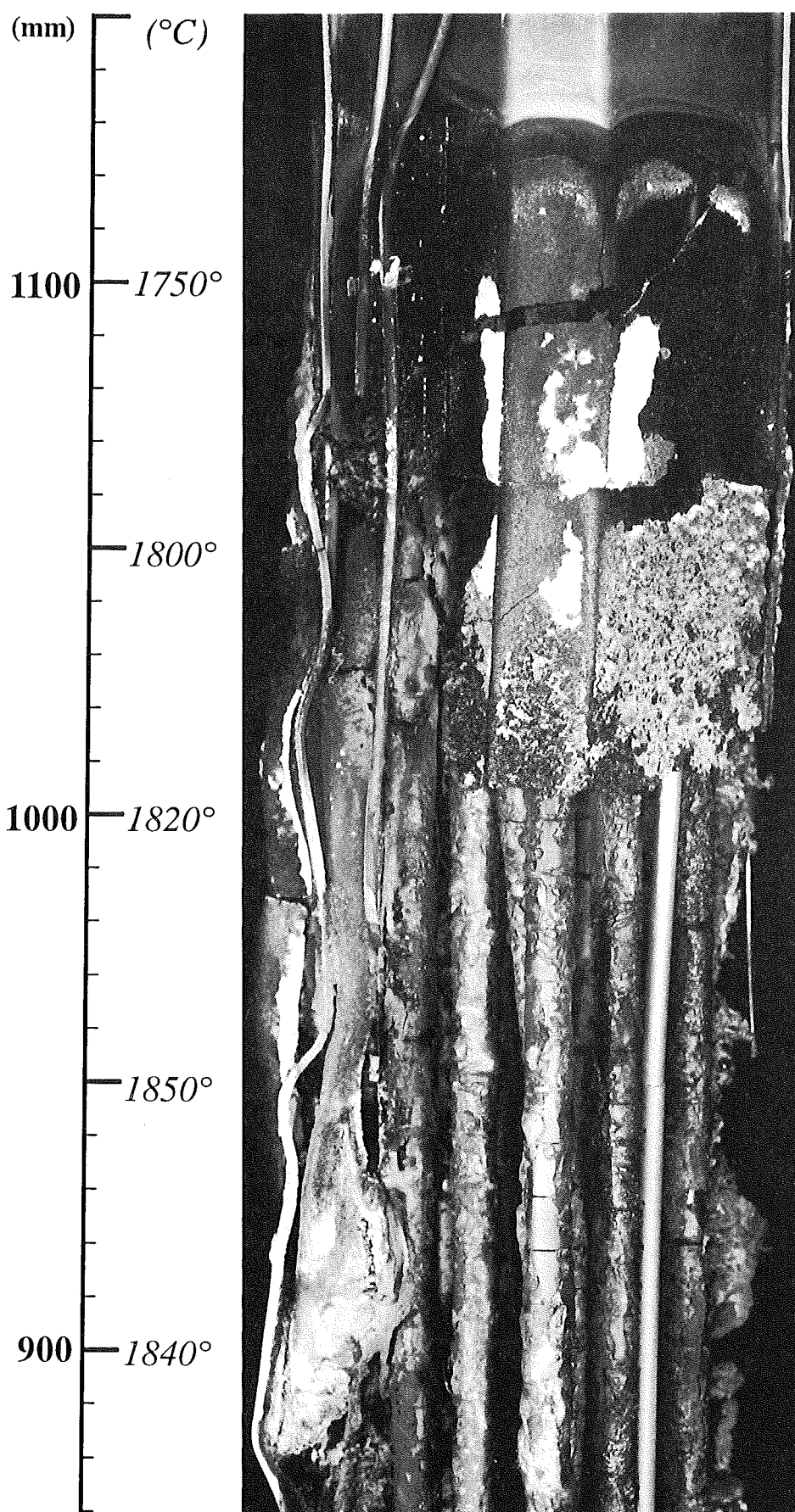
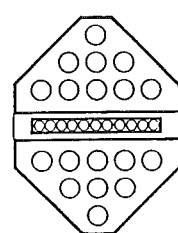


Fig. 104: Post test view of bundle, 210° partial view,
1370-1090mm



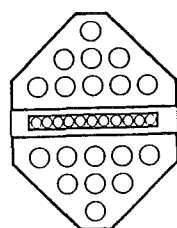
DRY BWR



*Fig. 105: Post test view of bundle, 210° partial view,
1150-870 mm*

CORA-33

DRY BWR



210°

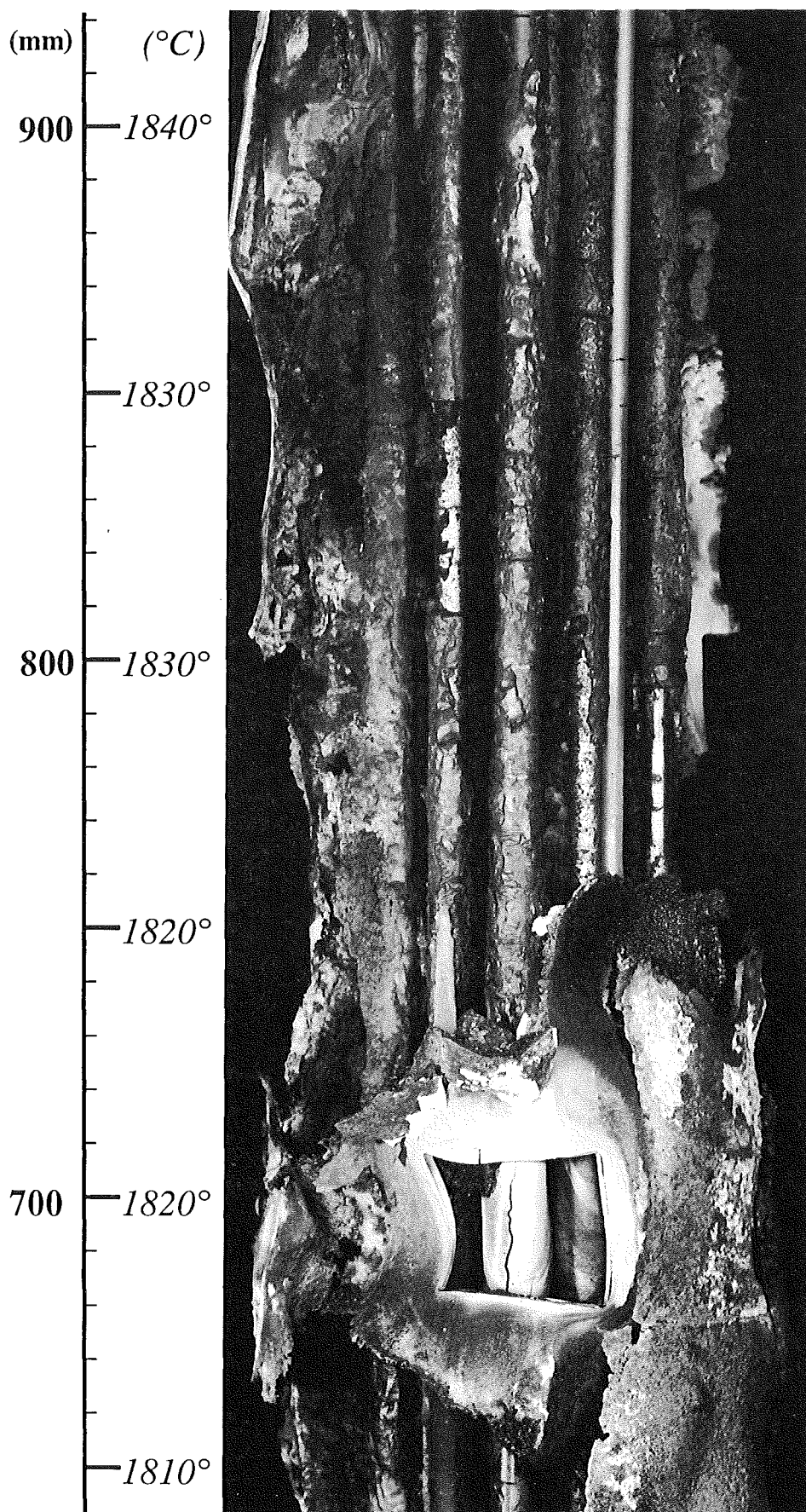
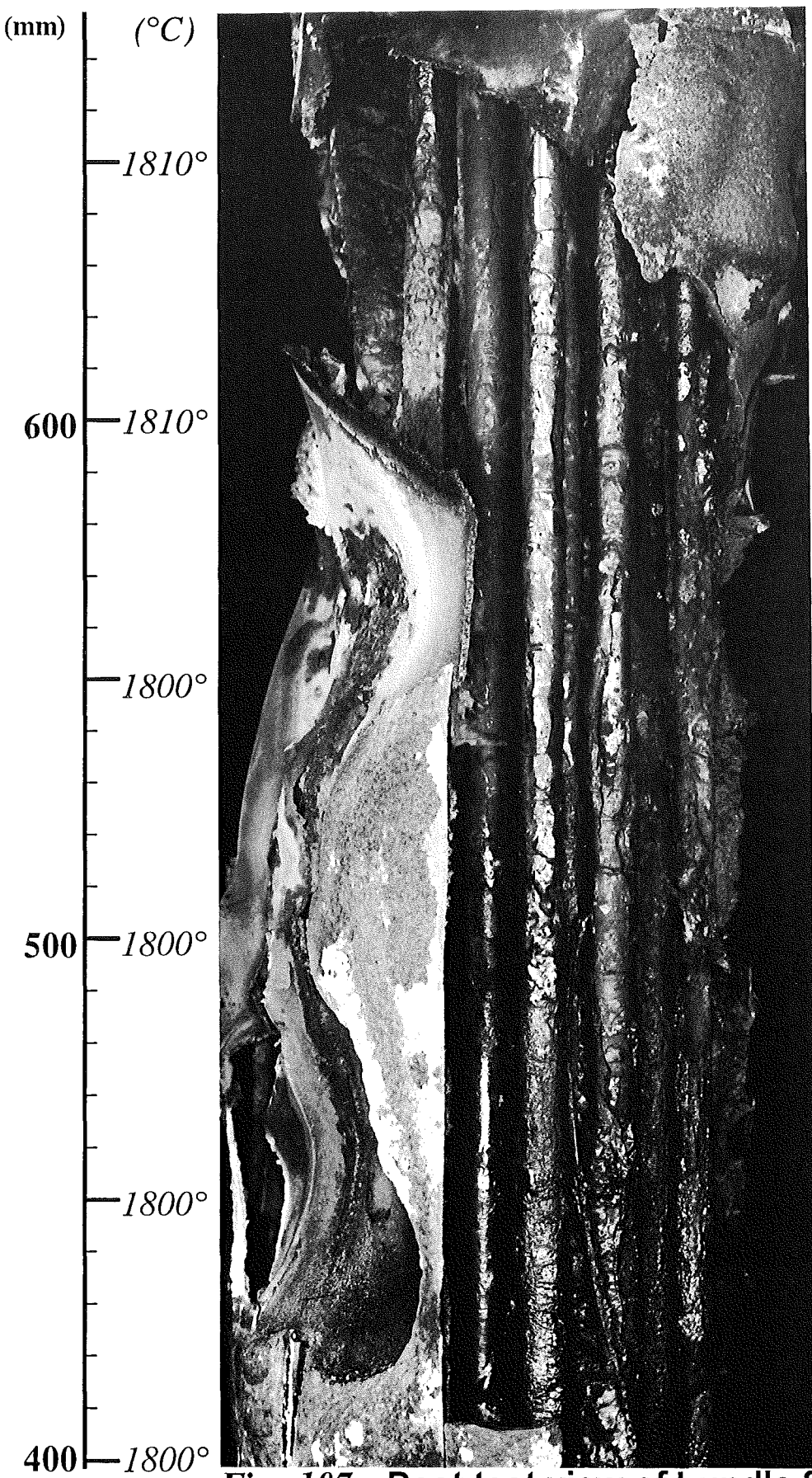
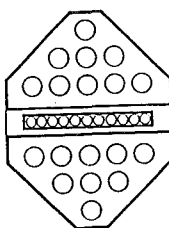


Fig. 106: Post test view of bundle, 210° partial view,
920-650 mm

CORA-33



DRY BWR

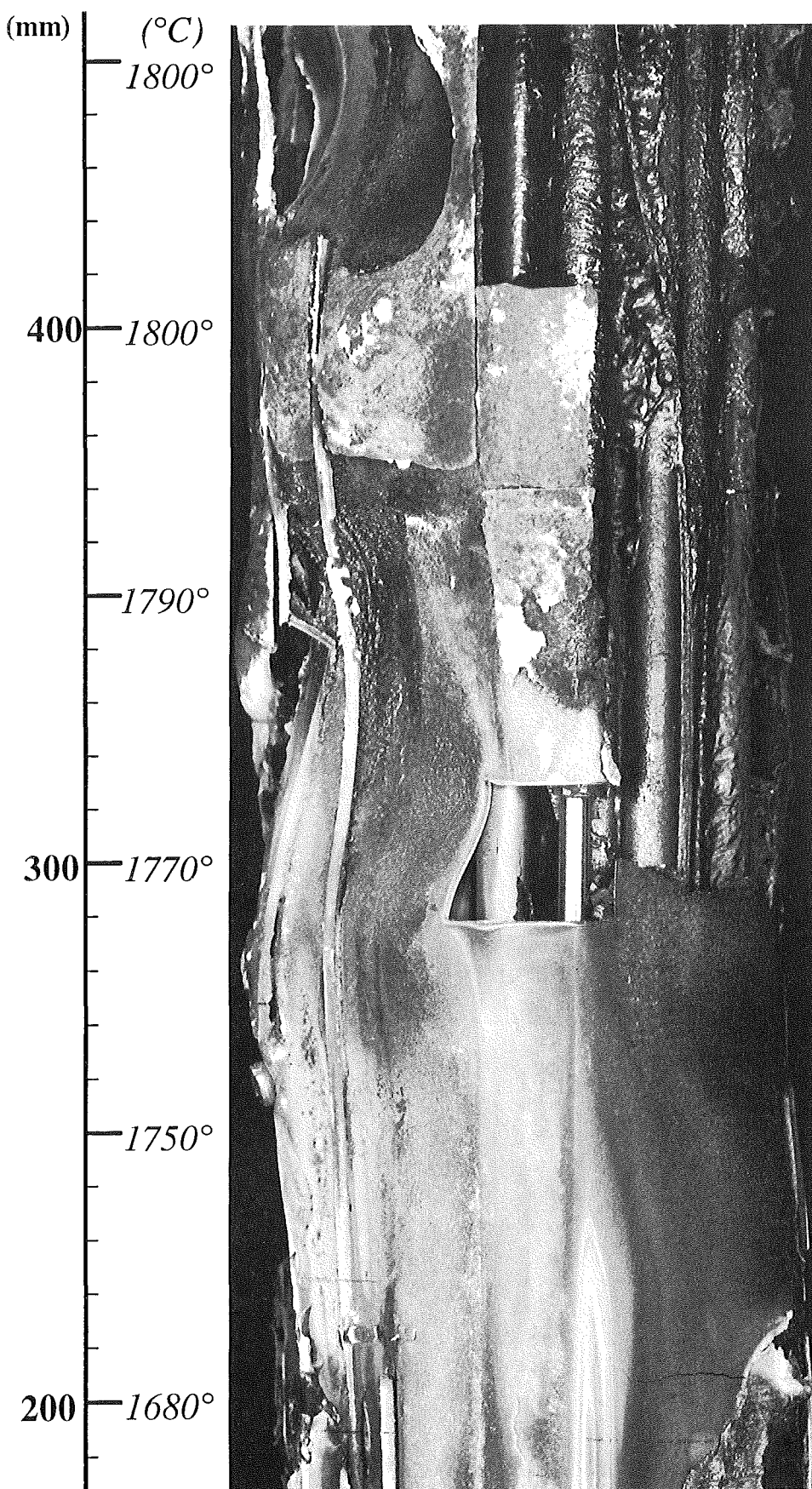


↑

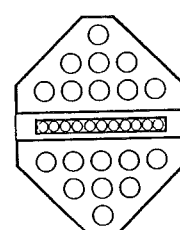
210°

Fig. 107: Post test view of bundle 210° partial view, 680-400 mm

CORA-33



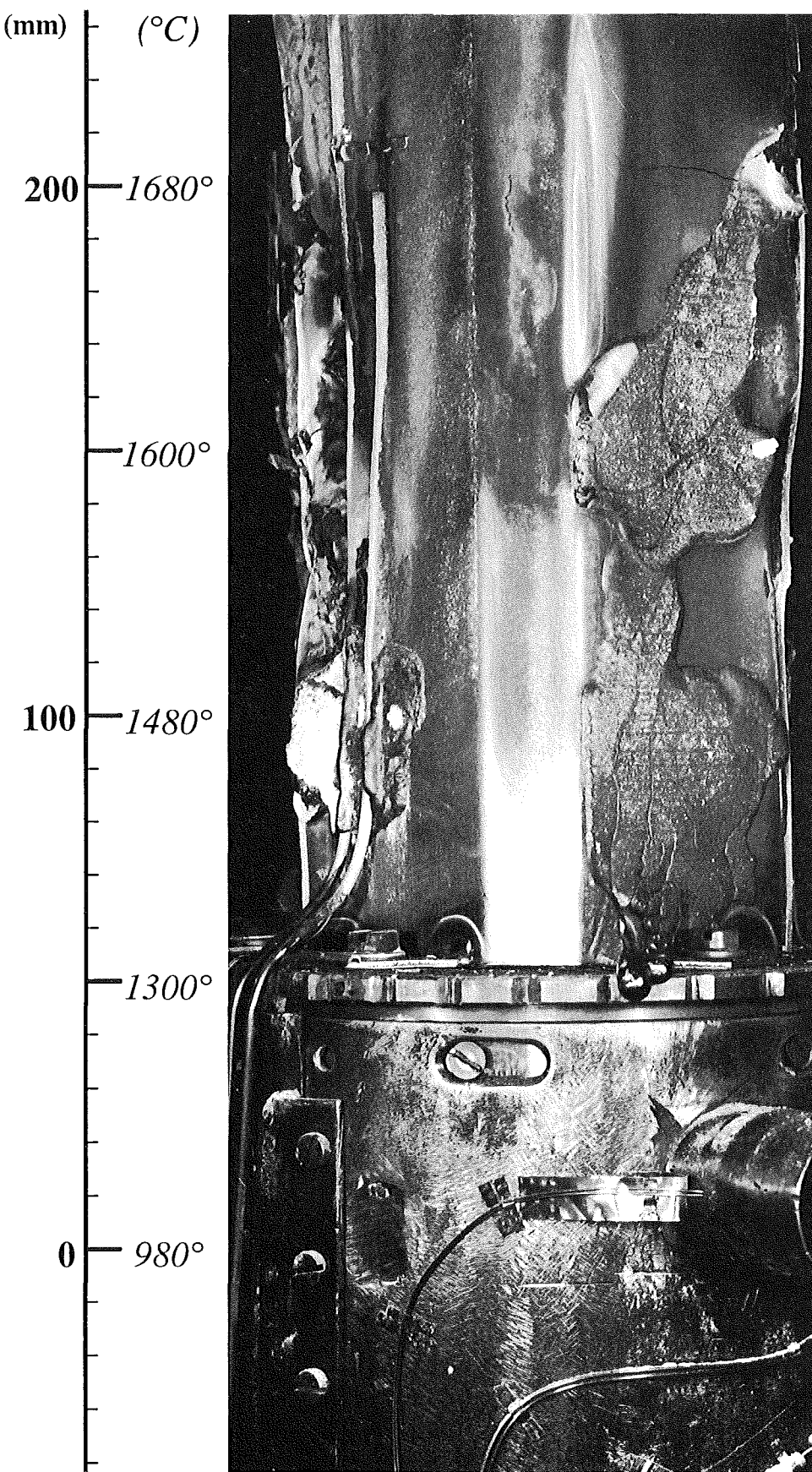
DRY BWR



↑
210°

**Fig. 108: Post test view of bundle 210° partial view,
450-180 mm**

CORA-33



DRY BWR

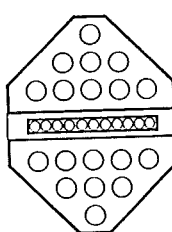
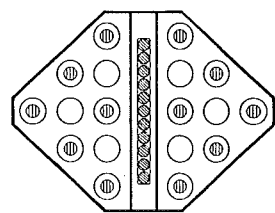


Fig. 109: Post test view of bundle 210° partial view,
230 to -50 mm



CORA-33: Dry BWR

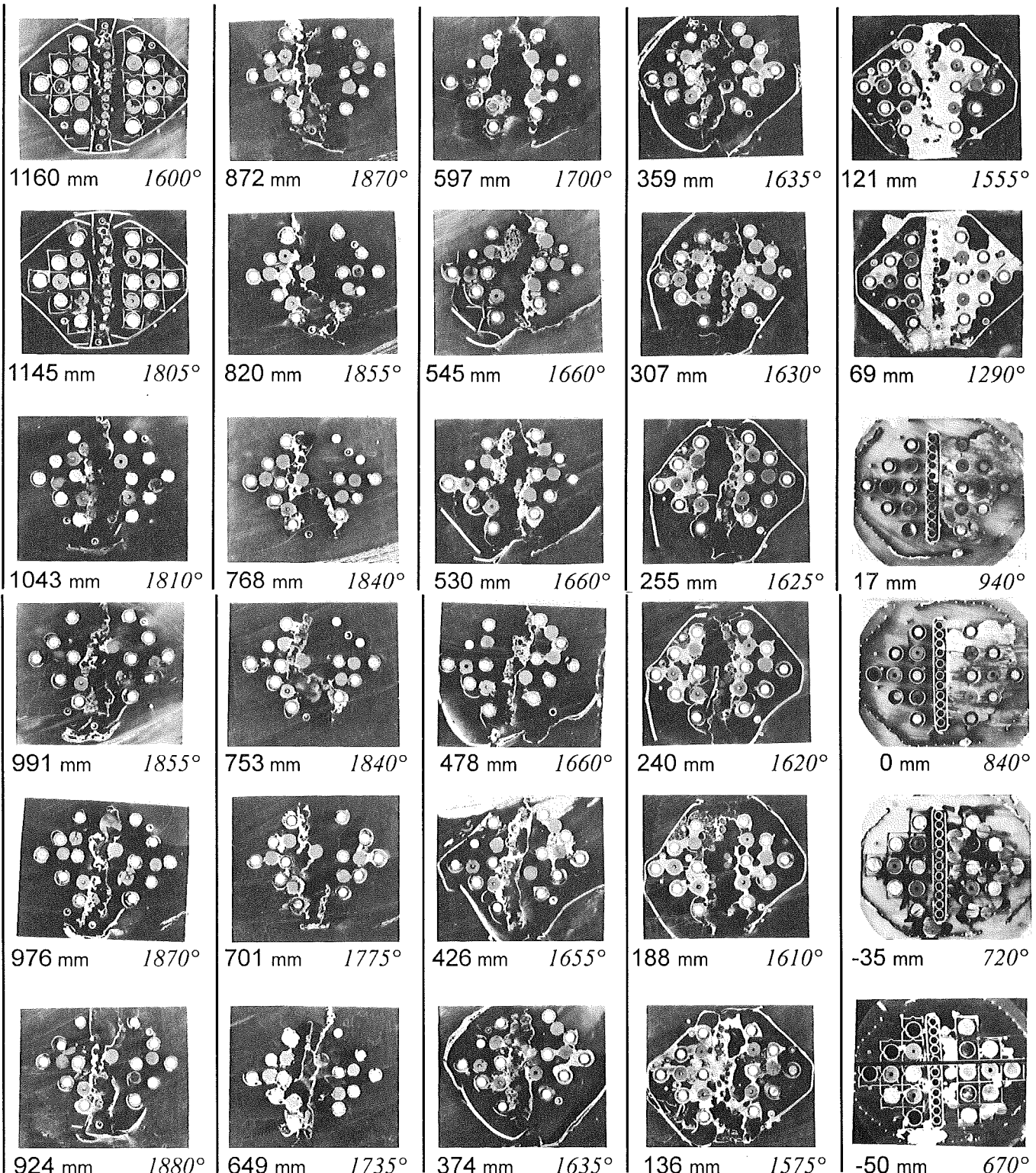
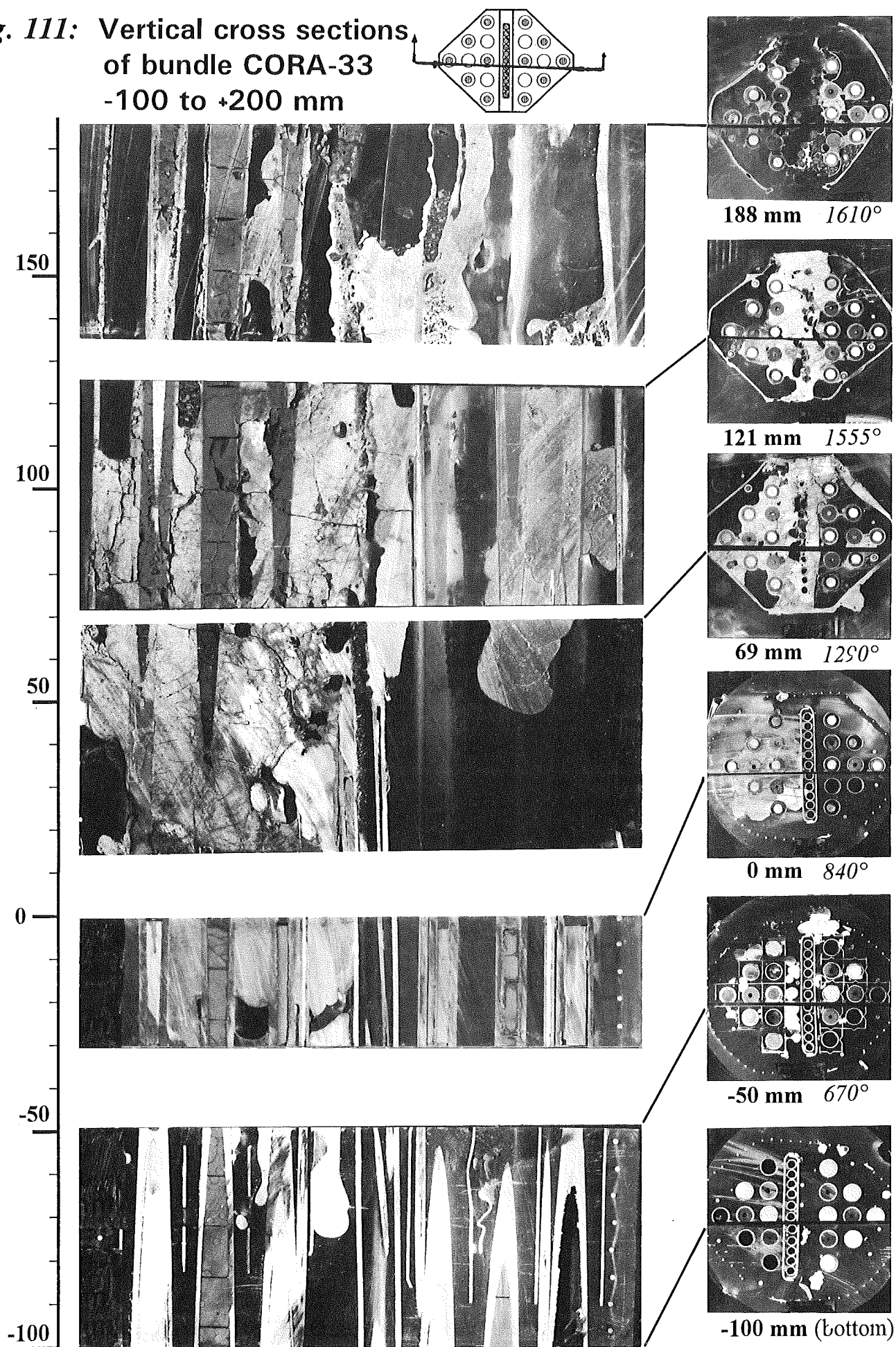


Fig. 110: Horizontal cross sections of bundle
CORA-33, top view

Fig. 111: Vertical cross sections
of bundle CORA-33
-100 to +200 mm



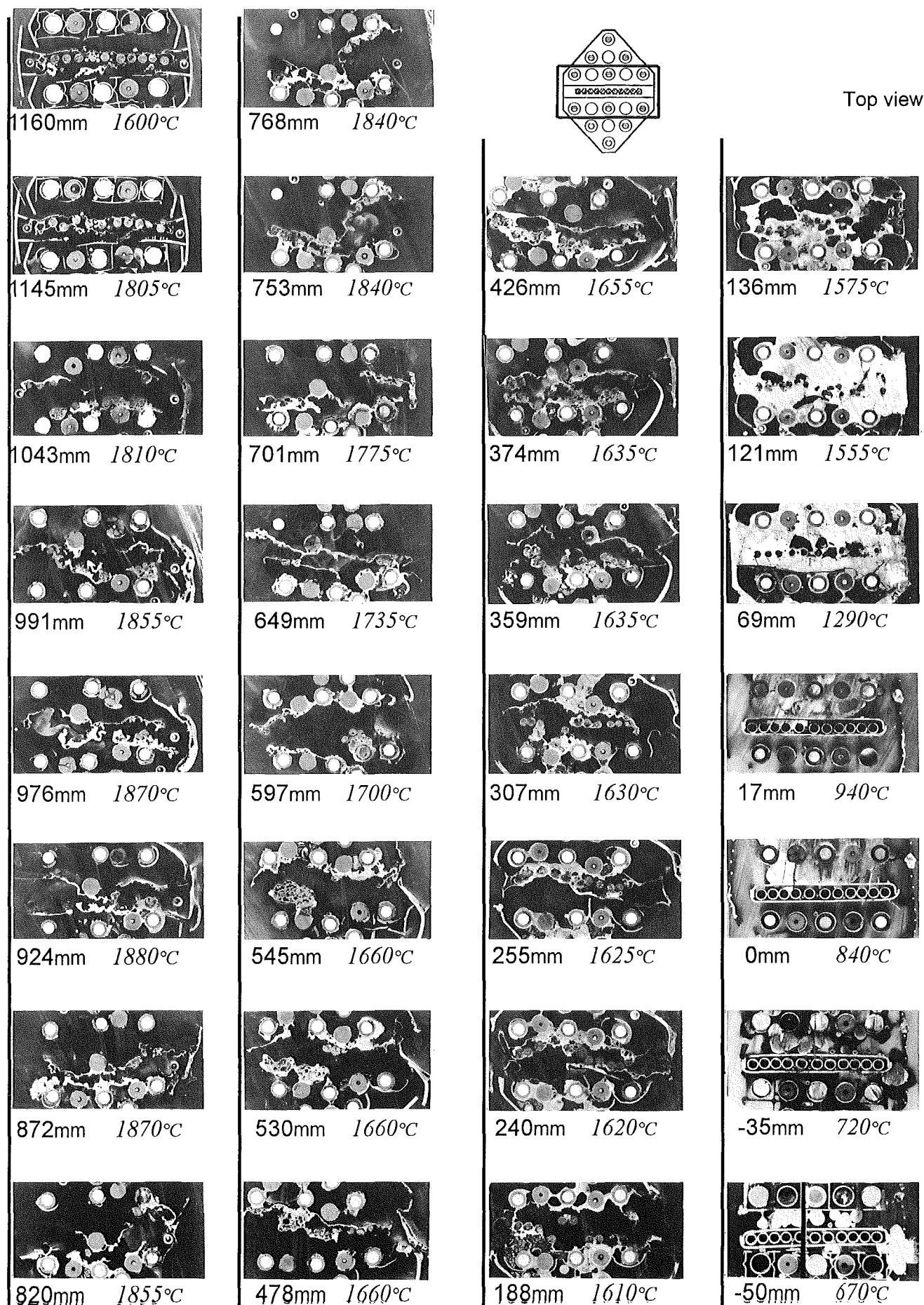


Fig. 112: Horizontal cross sections of the absorber region of bundle CORA-33

Appendix A

**Data on the pre-transient phase
of test CORA-33**

CORA-33:

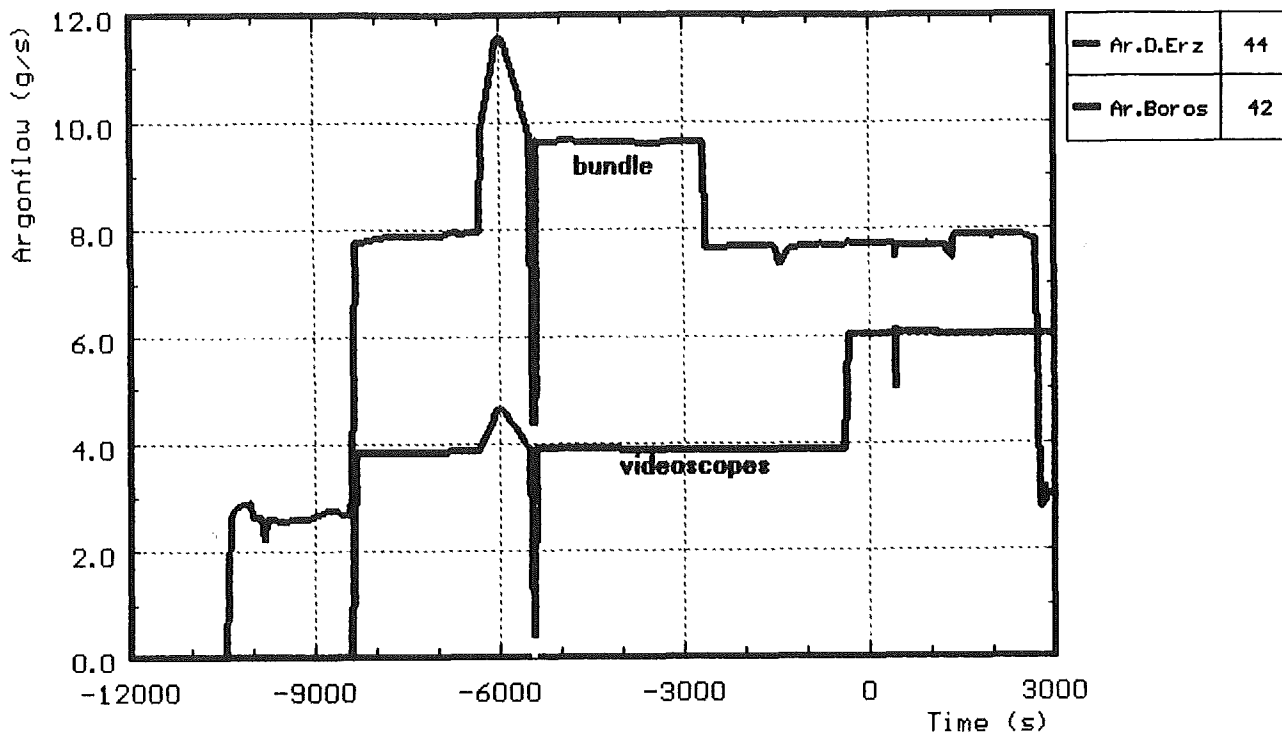


Fig. A1: CORA-33: Argon input prior to test
CORA-33

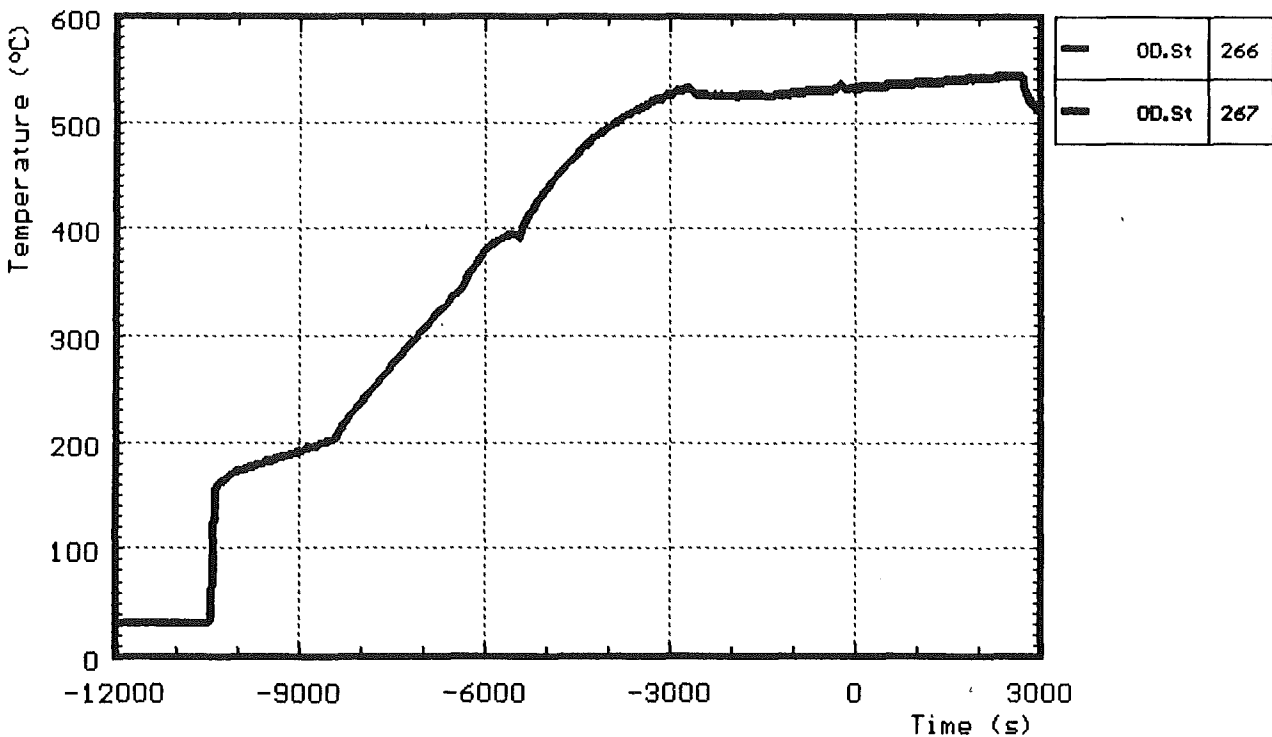


Fig. A2: CORA-33: Temperature at the entrance of
the bundle prior to test

CORA-33:

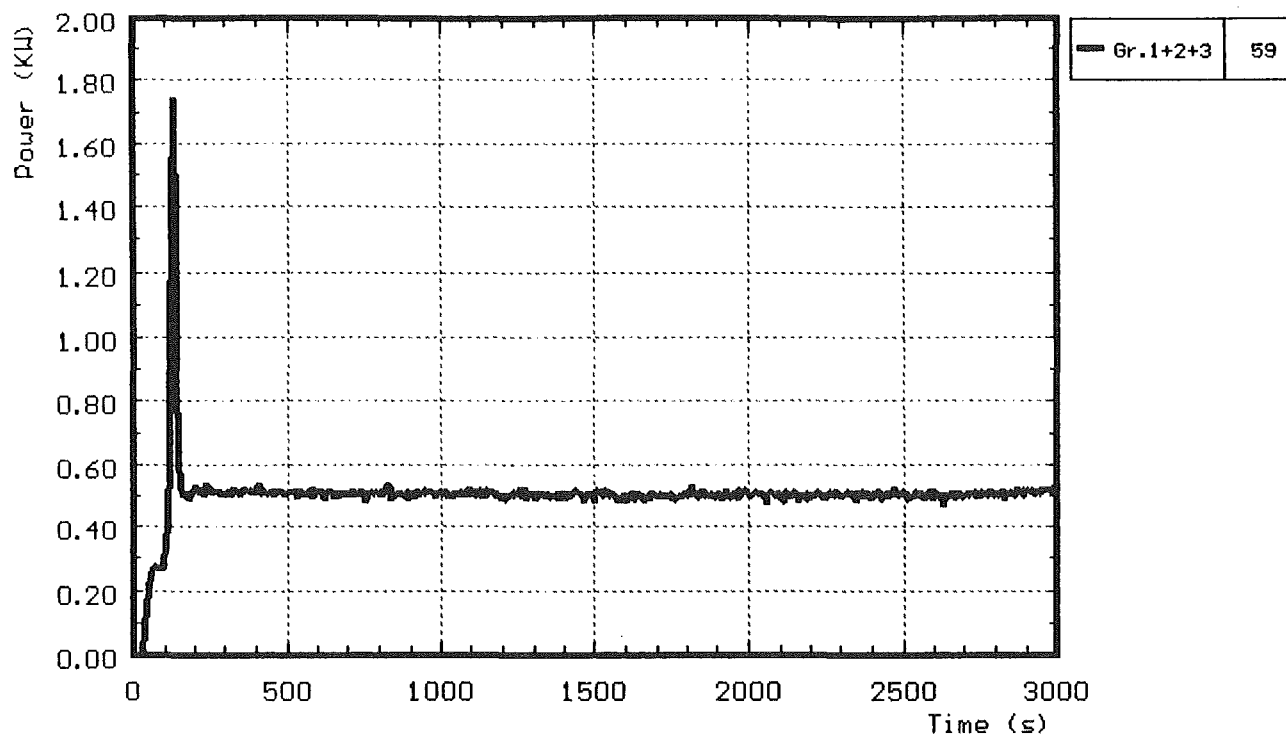


Fig. A3: CORA-33: Power input during the pre-heat phase

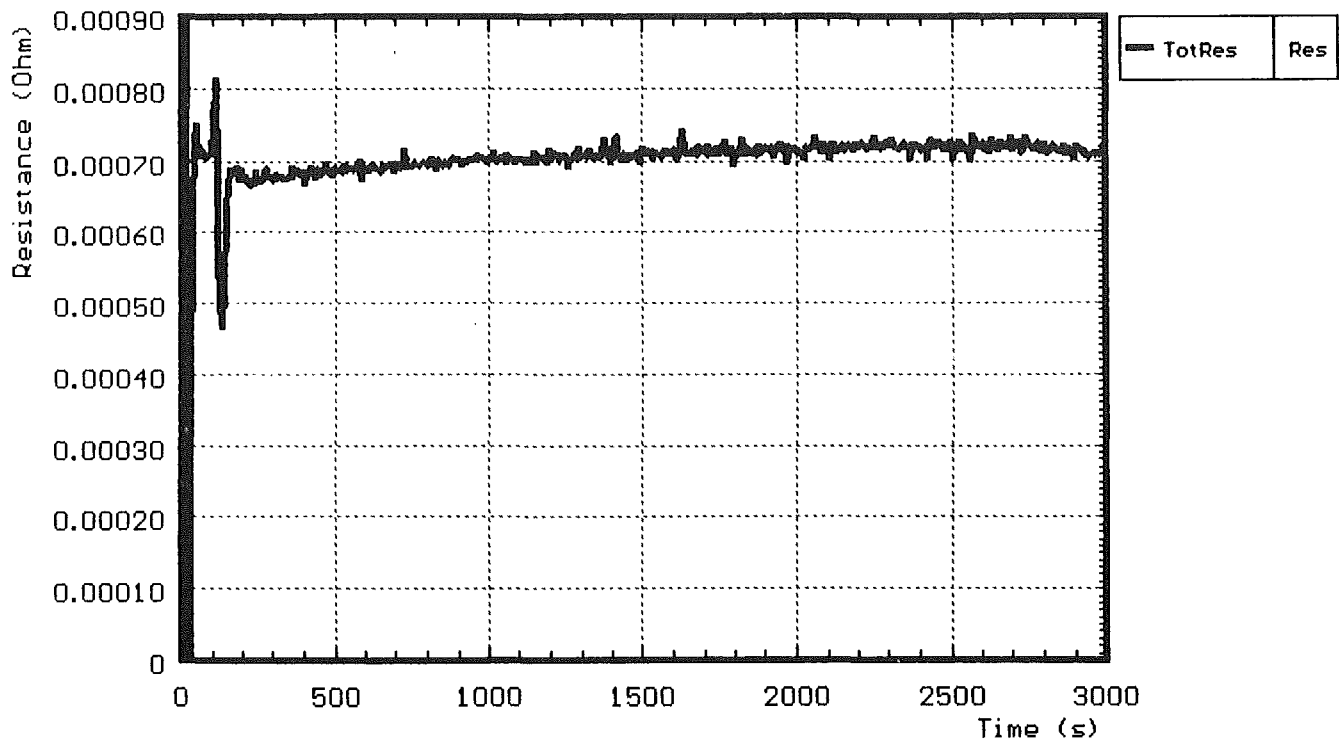


Fig. A4: CORA-33: Resistance during the pre-heat phase

CORA-33: Temperatures on heated rods; pre-heat phase

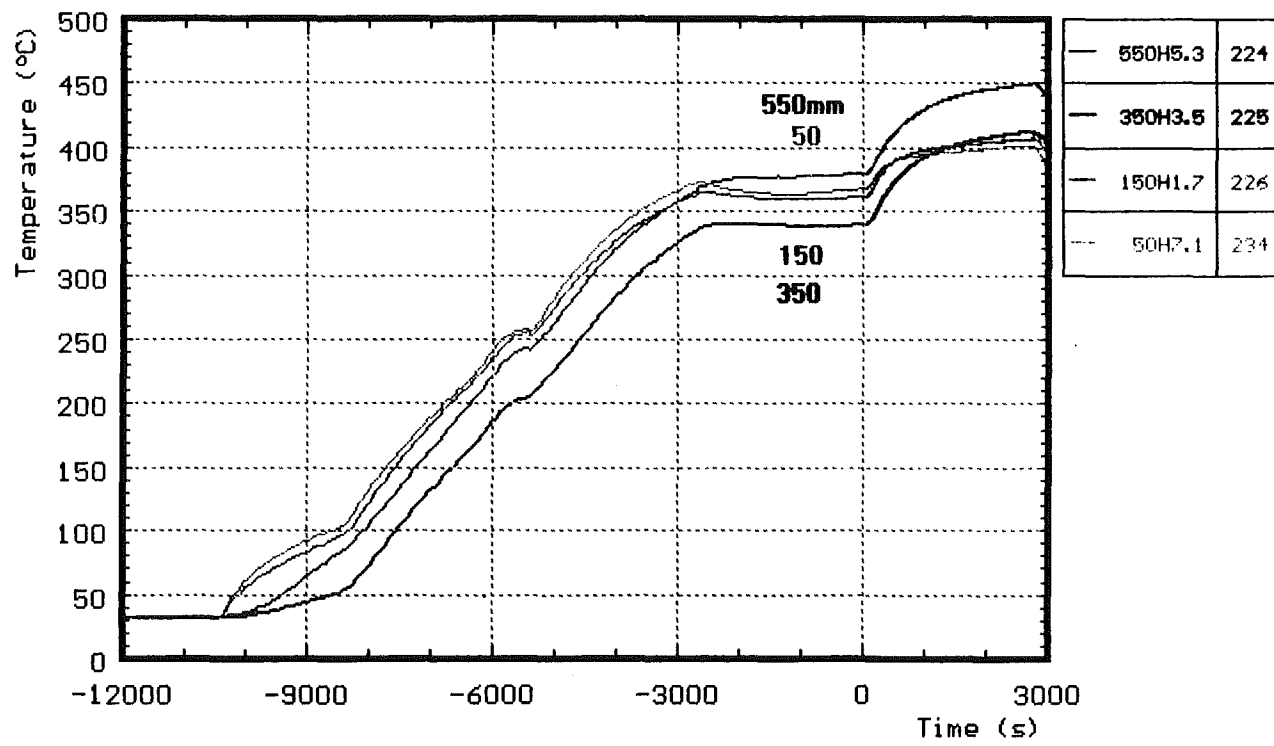
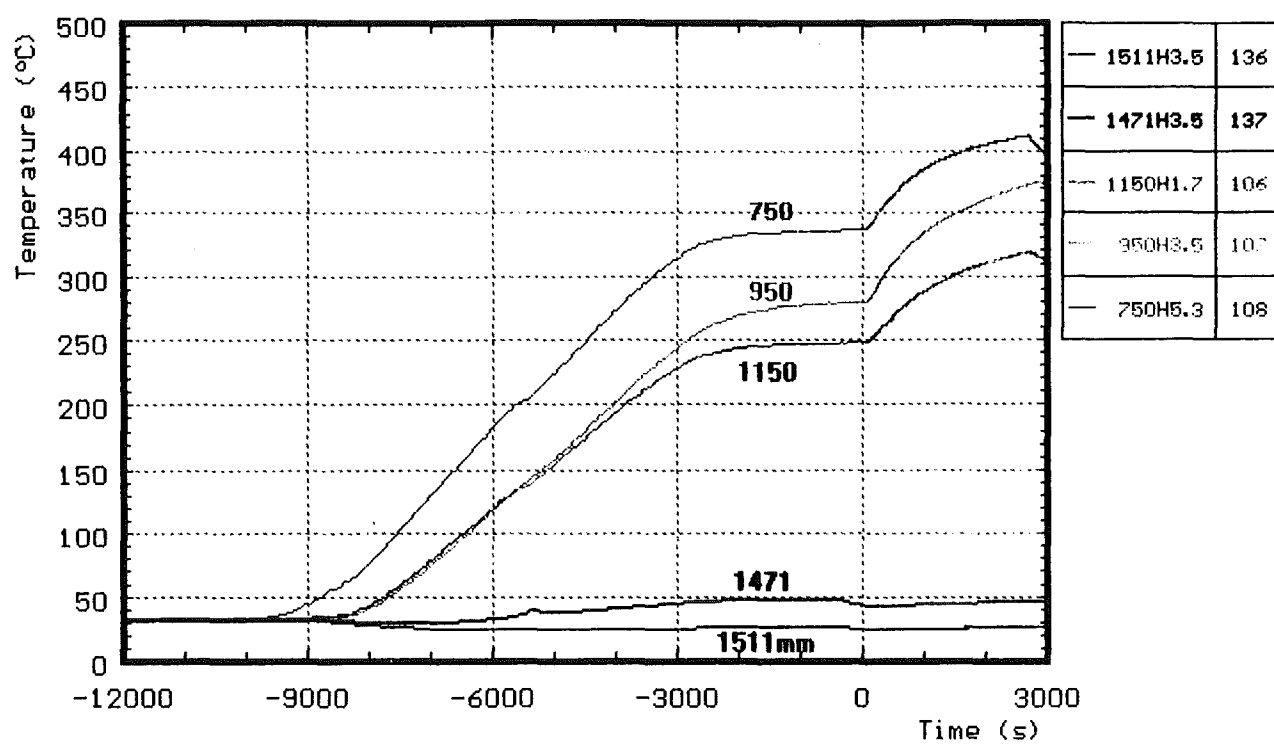


Fig. A5

CORA-33: Temperatures in unheated rods pre-heat phase

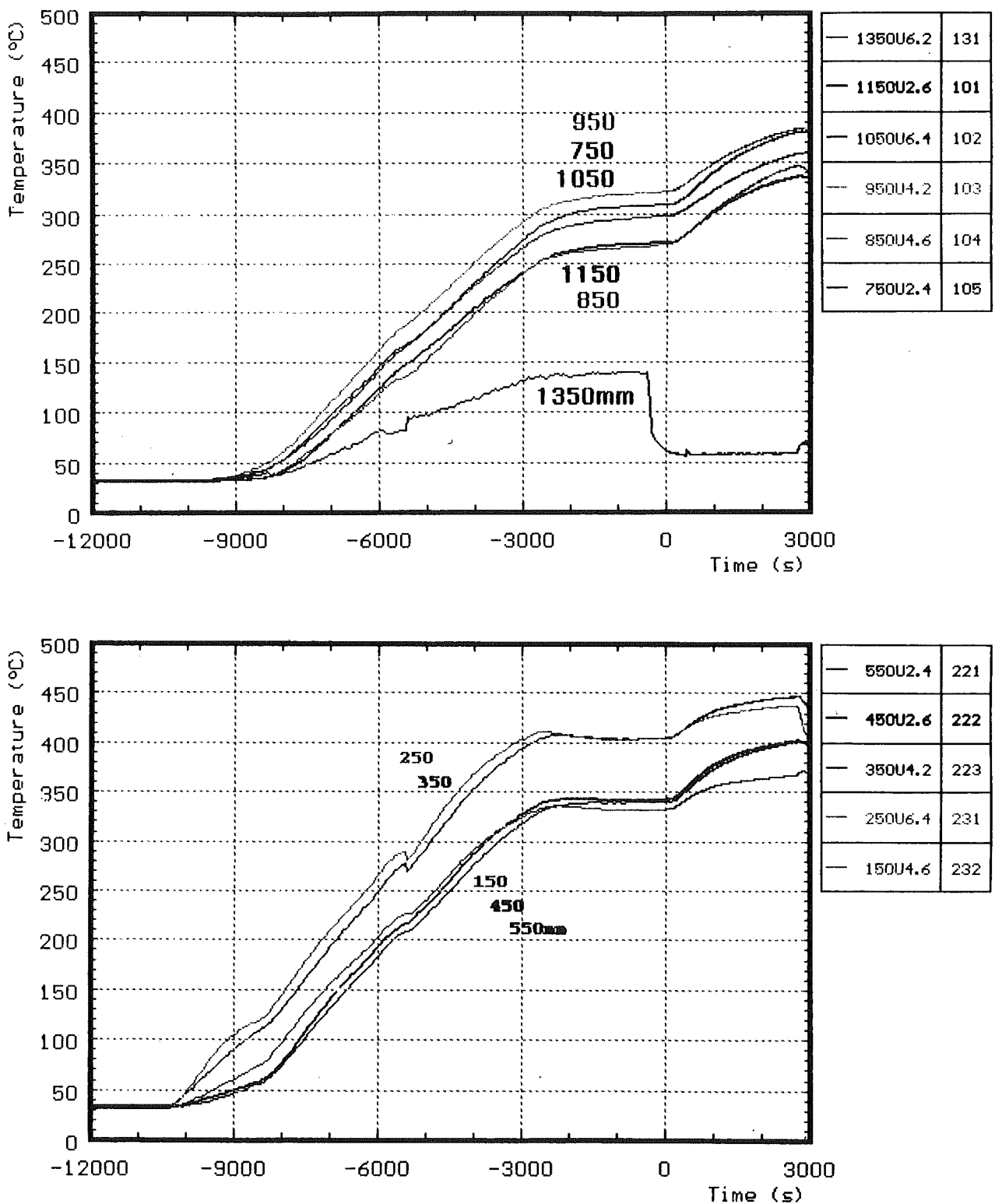


Fig. A6

CORA-33: Temperatures on the channel box walls; pre-heat phase

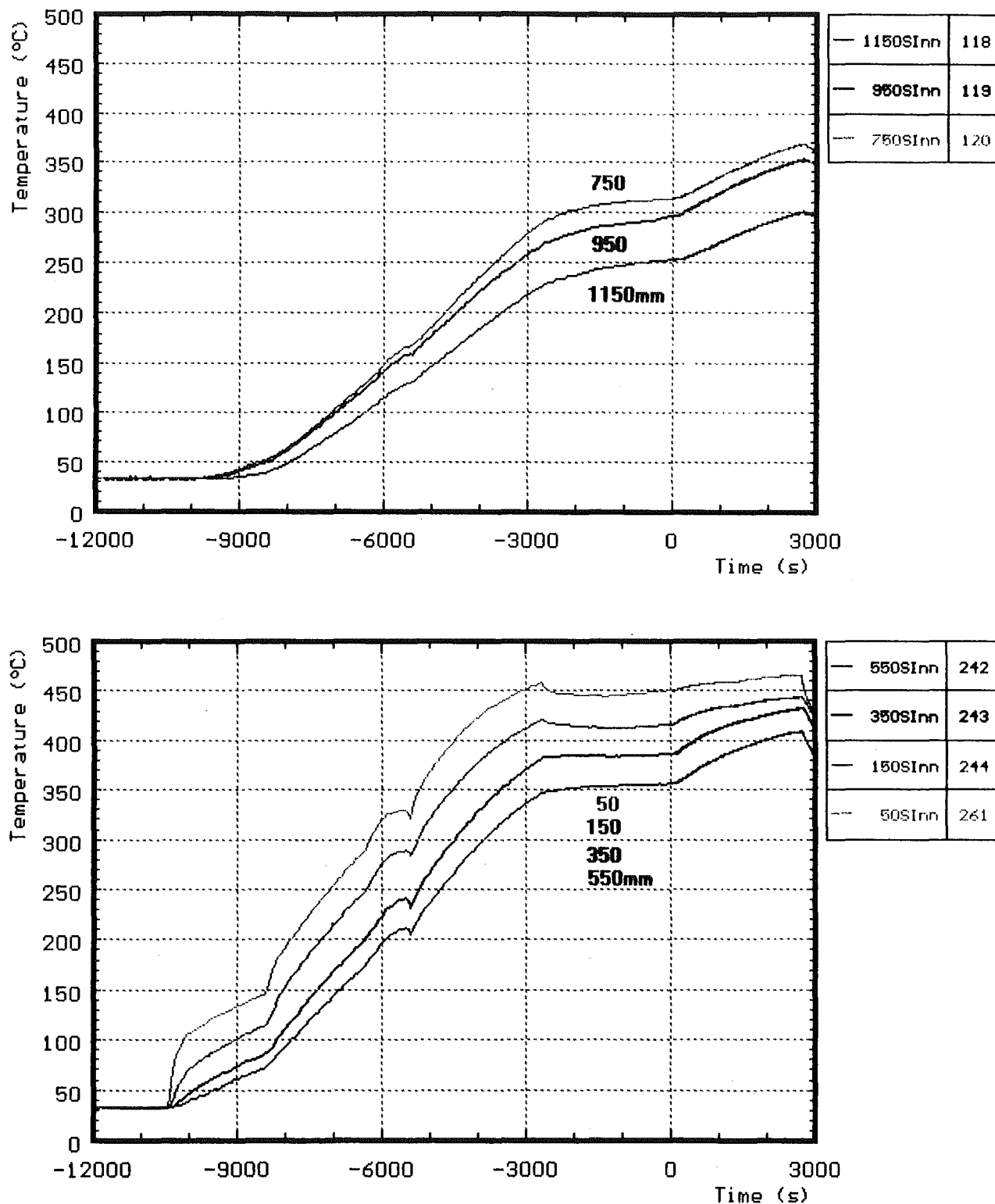


Fig. A7

CORA-33: pre-heat phase Temperatures in the absorberblade

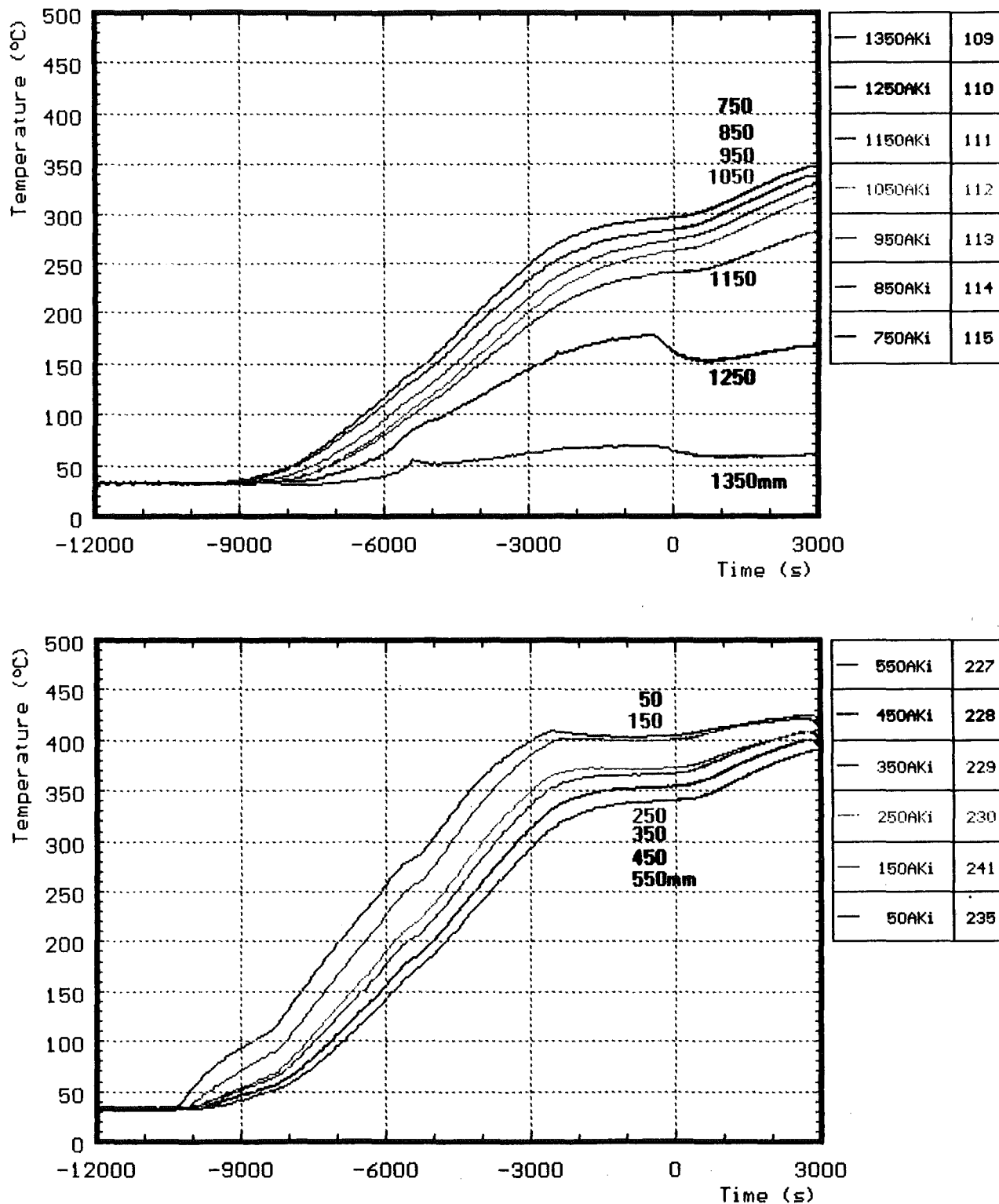


Fig. A8

CORA-33:

Temperatures measured with ceramic protected TCs; pre-heat phase

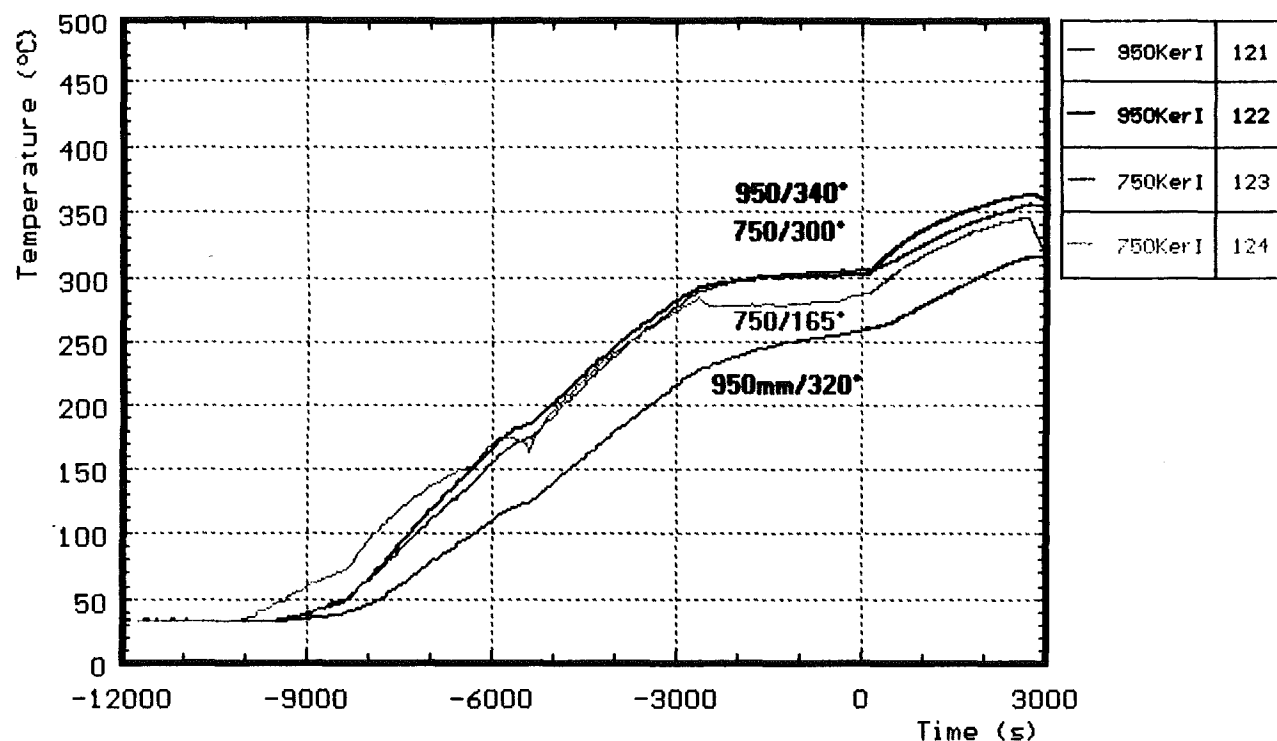


Fig. A9

CORA-33: Temperatures on the spacers; pre-heat phase

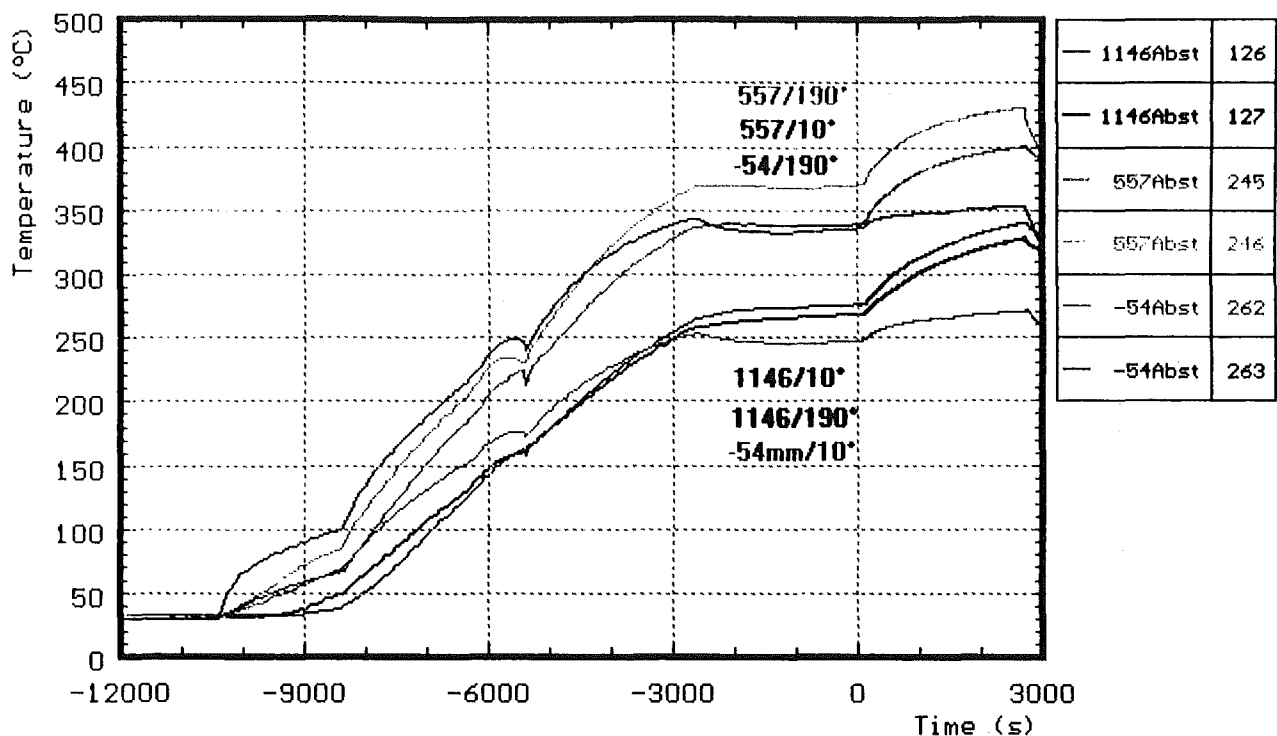


Fig. A10

CORA - 33: Temperatures on the inner side of shroud; pre-heat phase

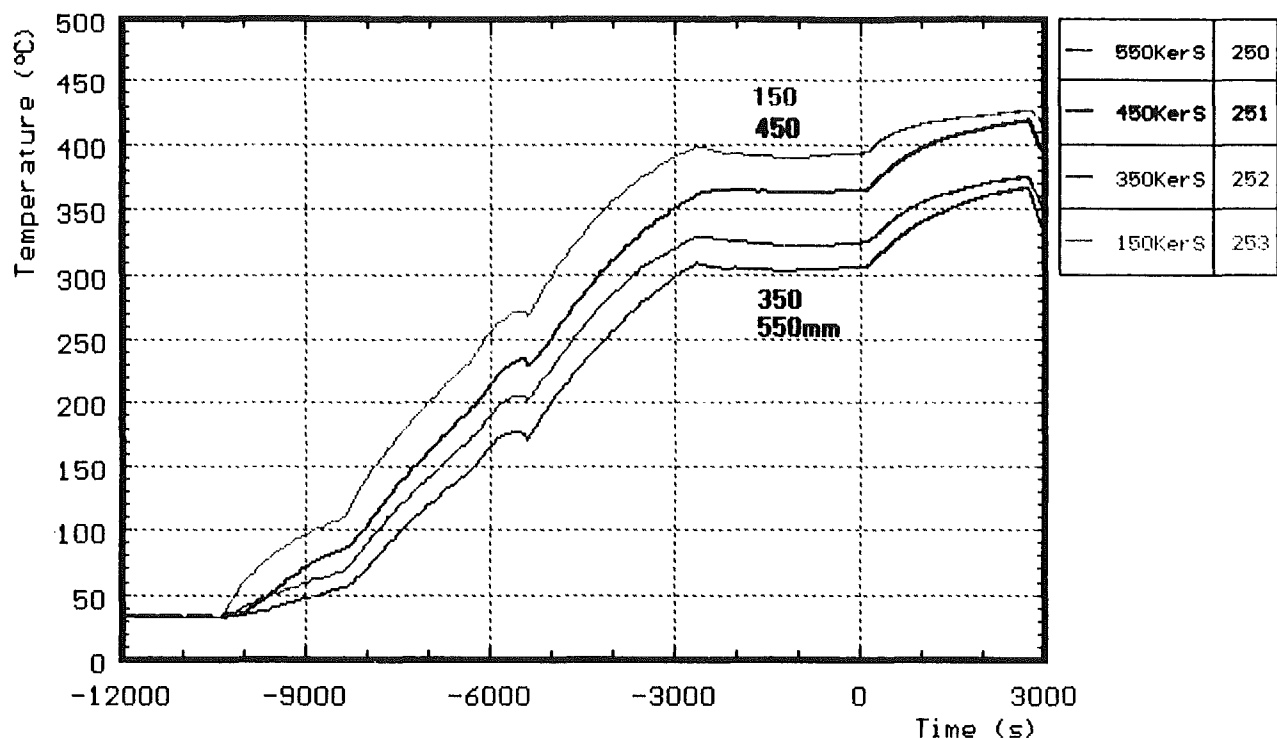


Fig. A11

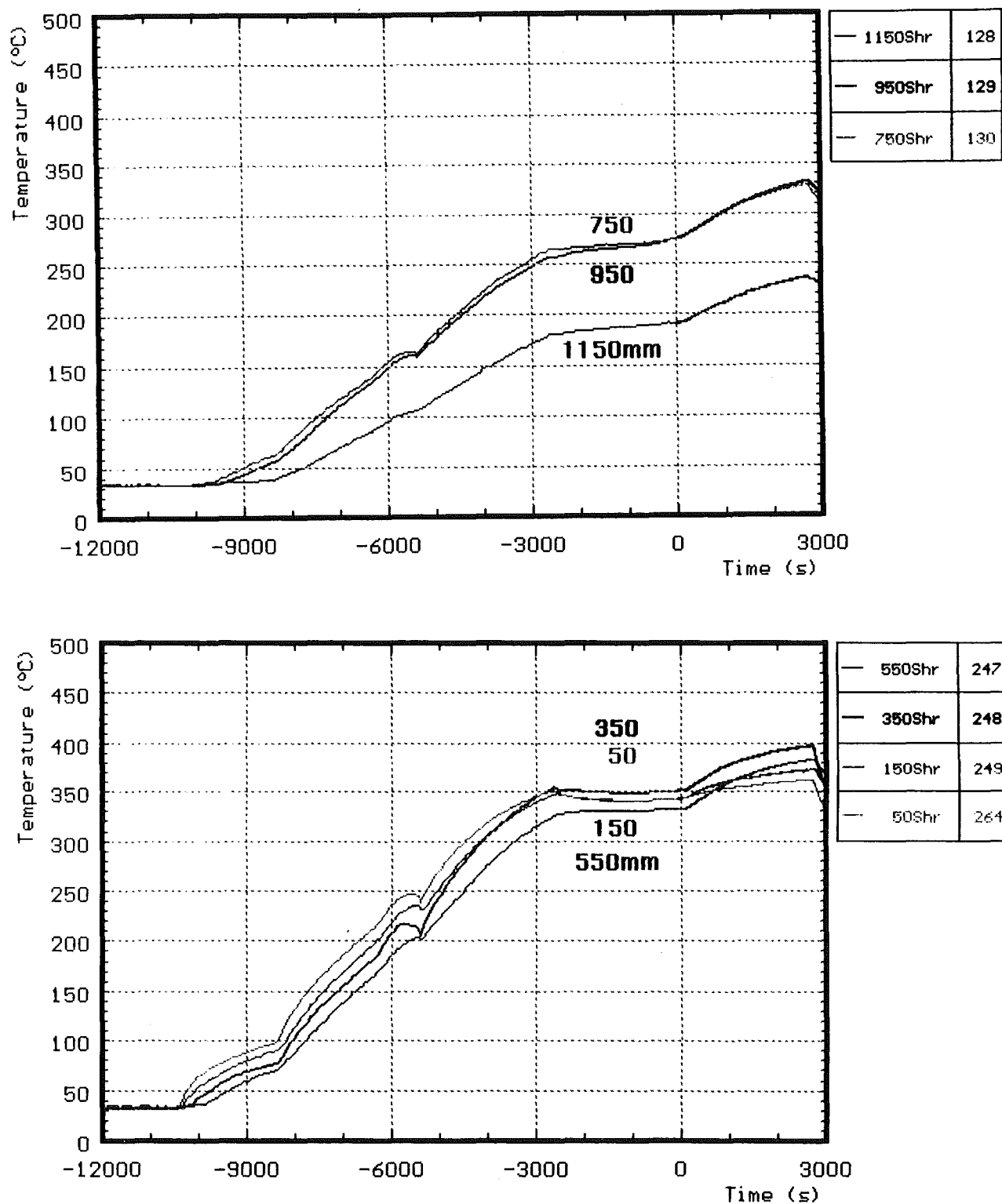


Fig. A12: CORA-33: Temperatures on outer side of shroud, pre-heat phase

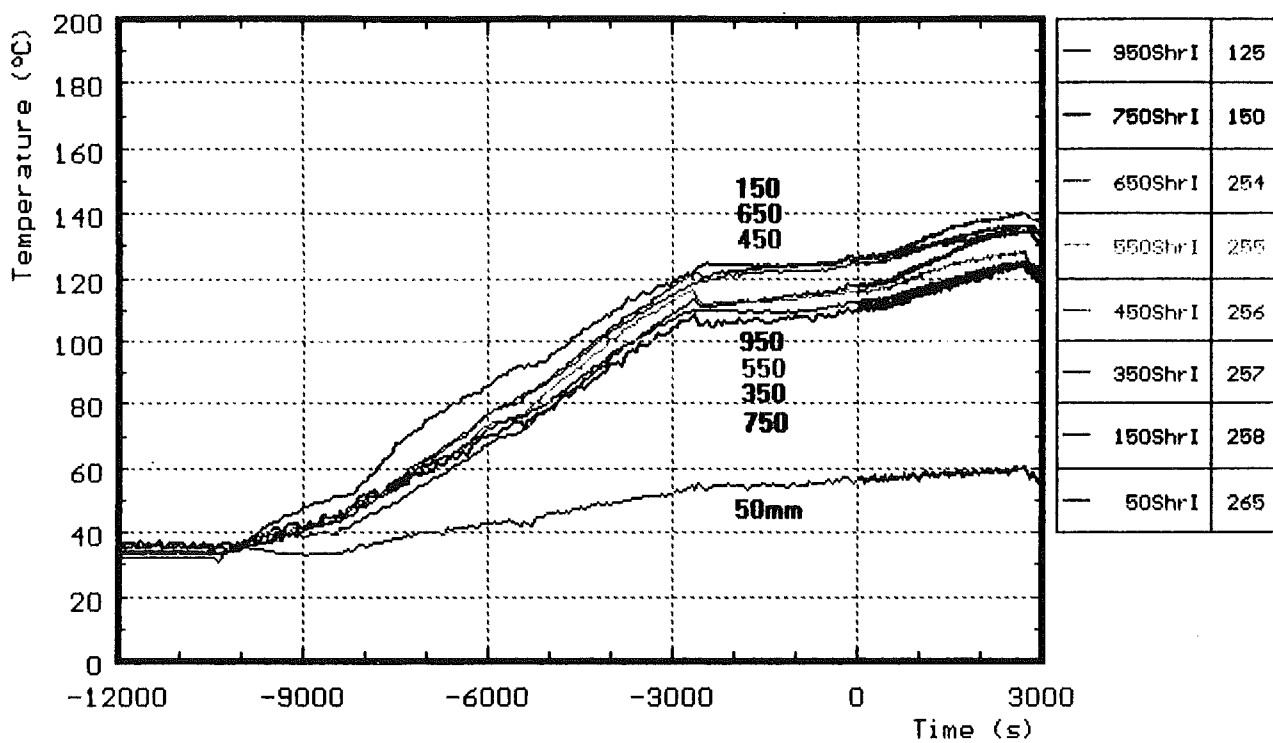


Fig. A13: CORA-33: Temperatures on shroud insulation, pre-heat phase

CORA-33: Gastemperatures in the upper part of the bundle; pre-heat phase

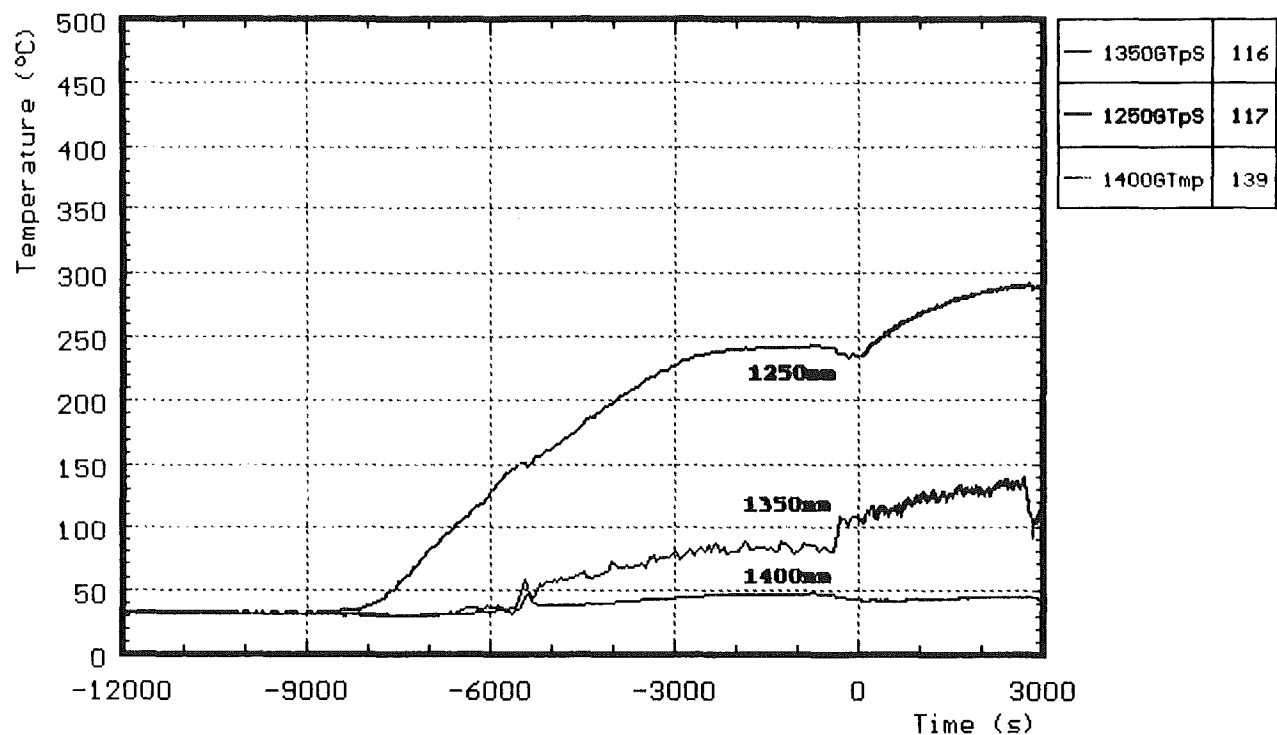


Fig. A14

CORA-33: Temperatures at the bundle head plate; pre-heat phase

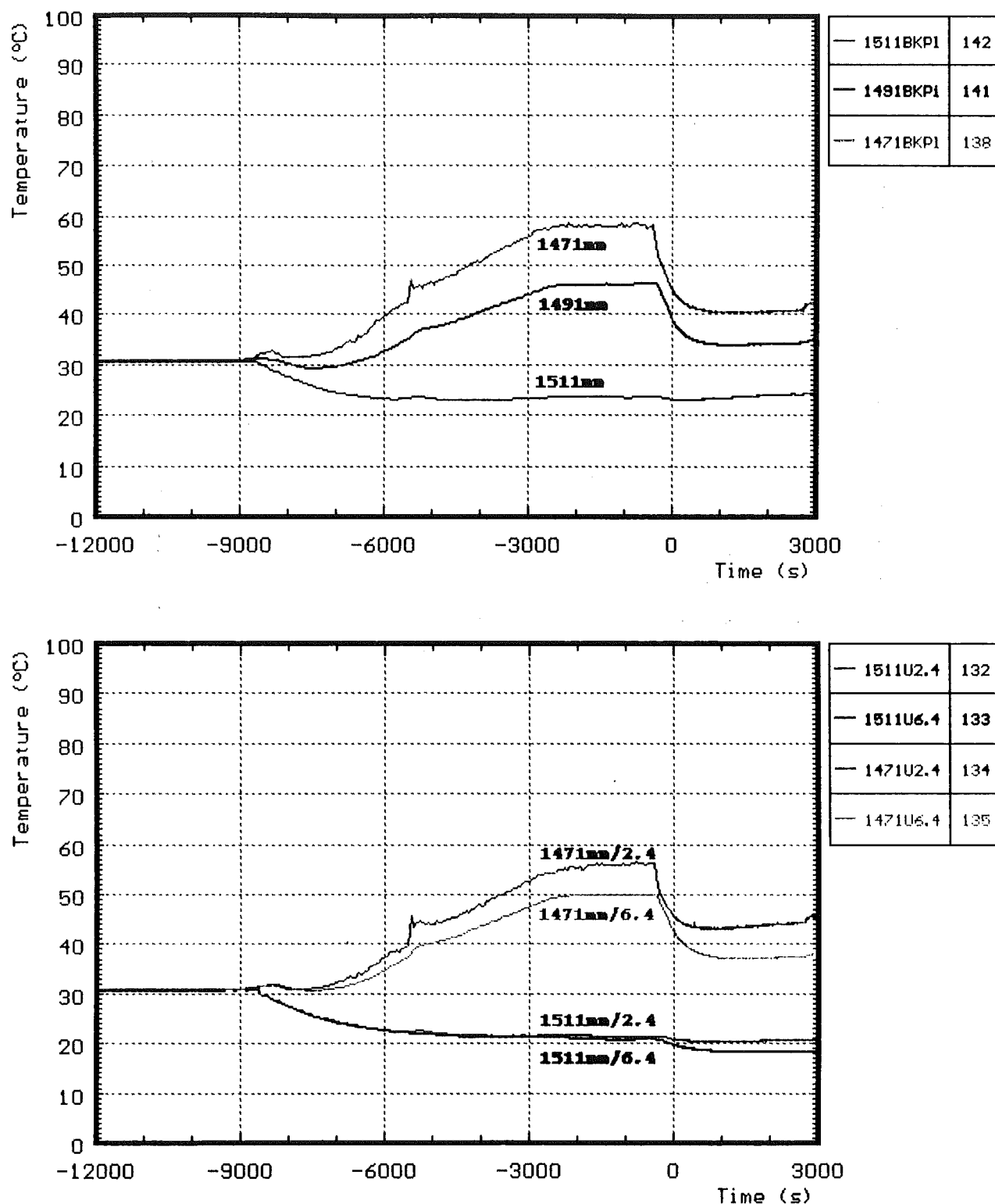
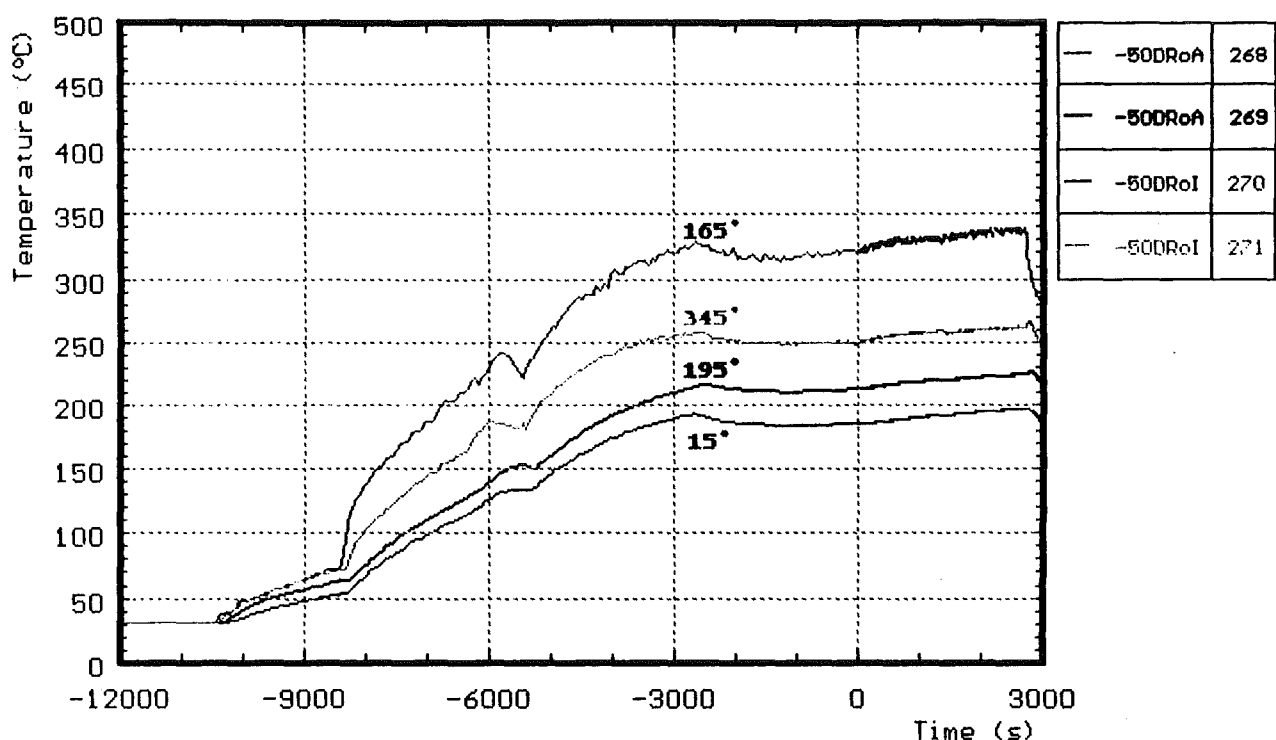


Fig. A15

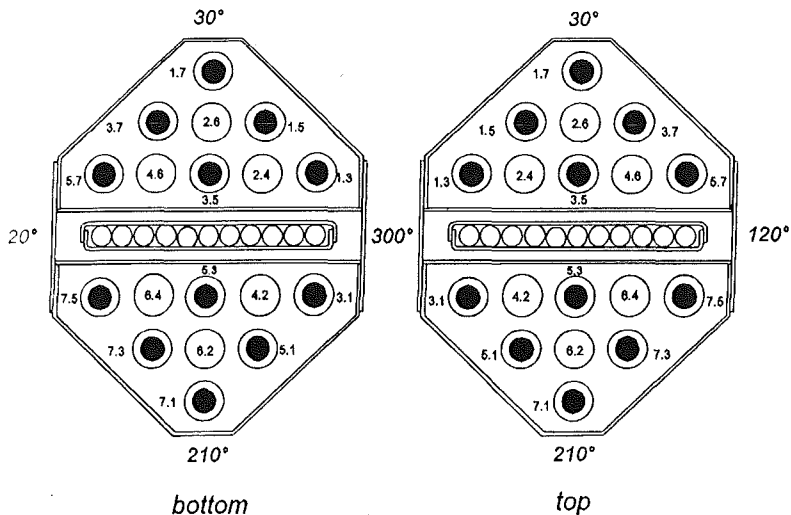


**Fig. A16: CORA-33:Temperatures in the steam tube
at - 50 mm elevation; pre-heat phase**

Appendix B

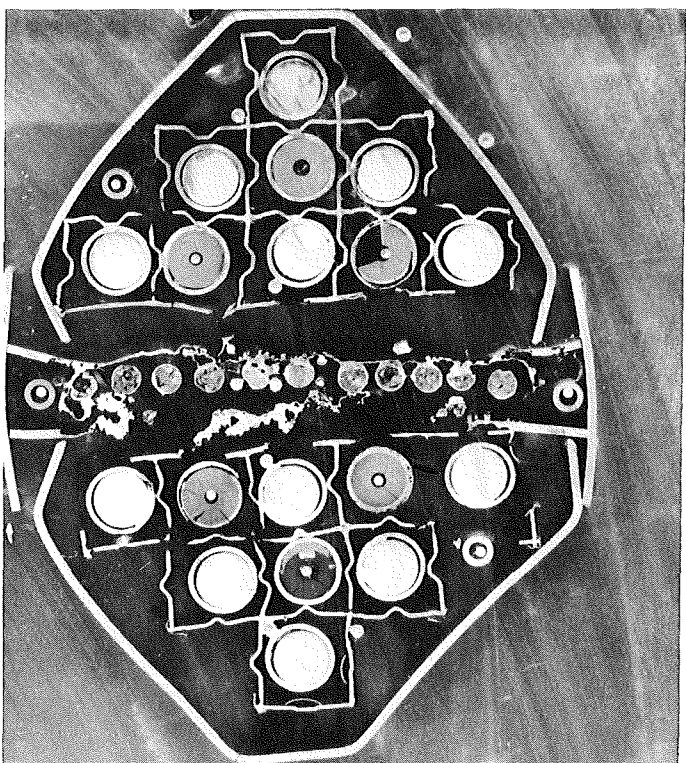
Complete set of cross sections

CORA-33: Dry-BWR



1600° C

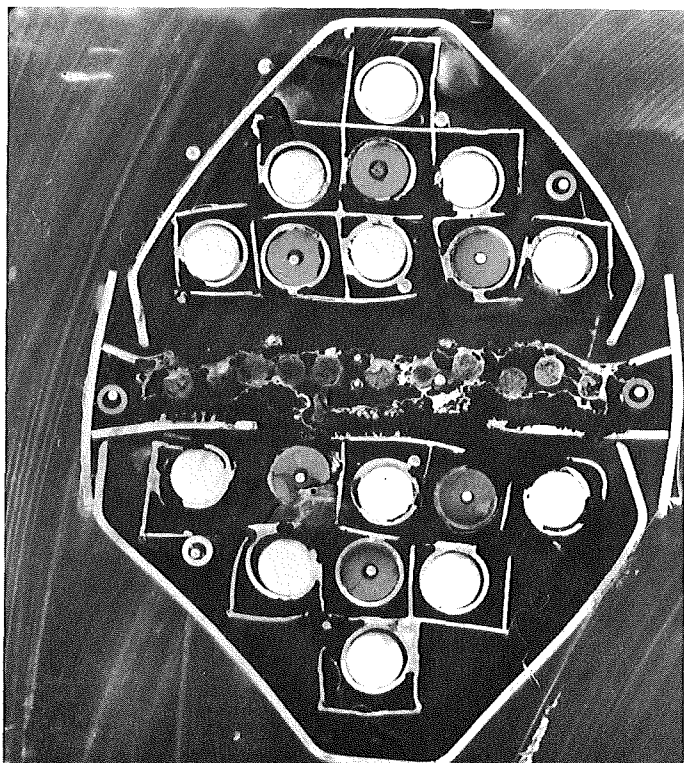
1160 mm



Top

1600° C

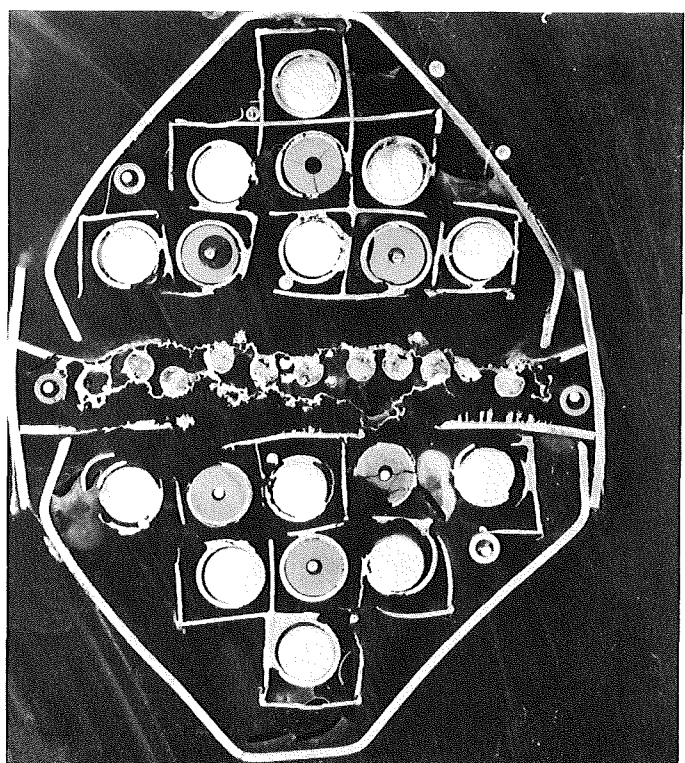
1147 mm



Bottom

1600° C

1145 mm



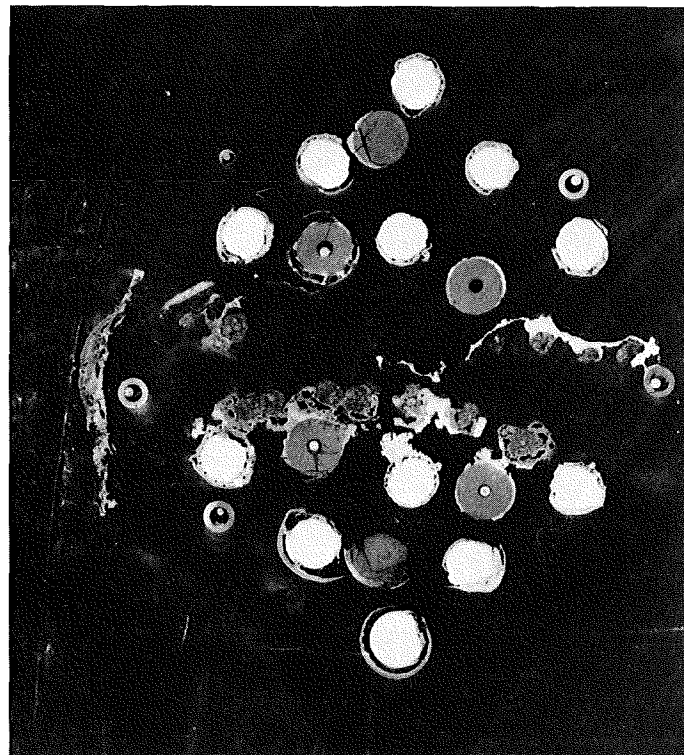
Top

Fig. B1: Horizontal cross sections of bundle
CORA-33; 1160, 1147, 1145 mm

CORA-33: Dry-BWR

1800° C

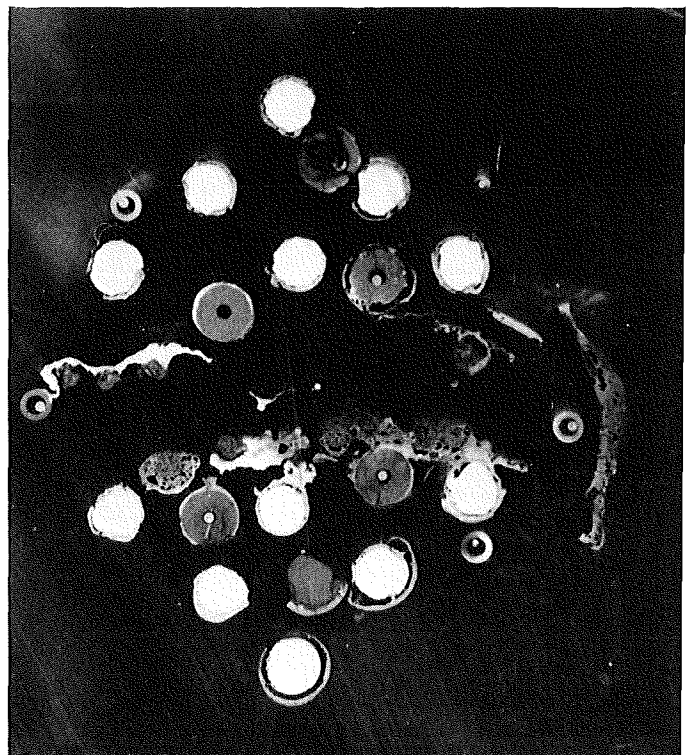
1045 mm



Bottom

1800° C

1043 mm



Top

1830° C

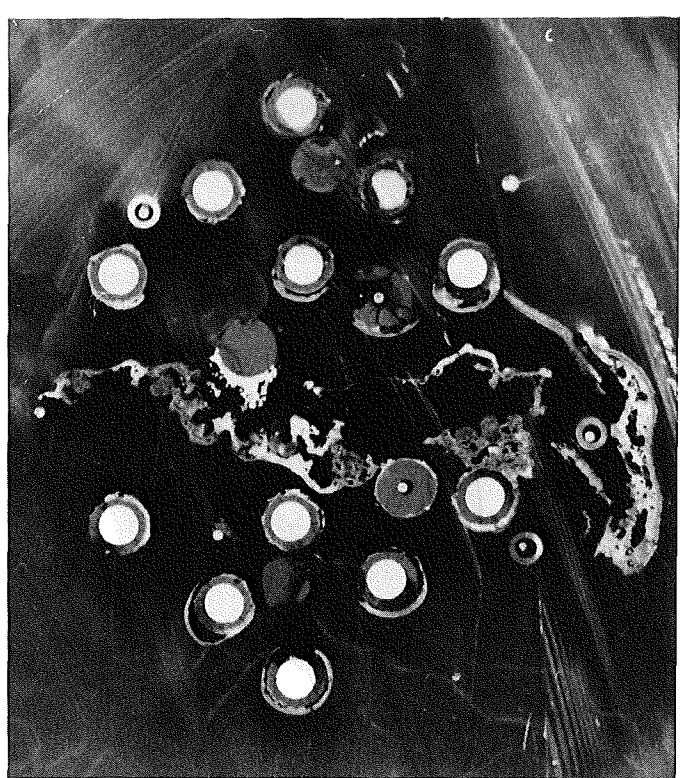
993 mm



Bottom

1830° C

991 mm



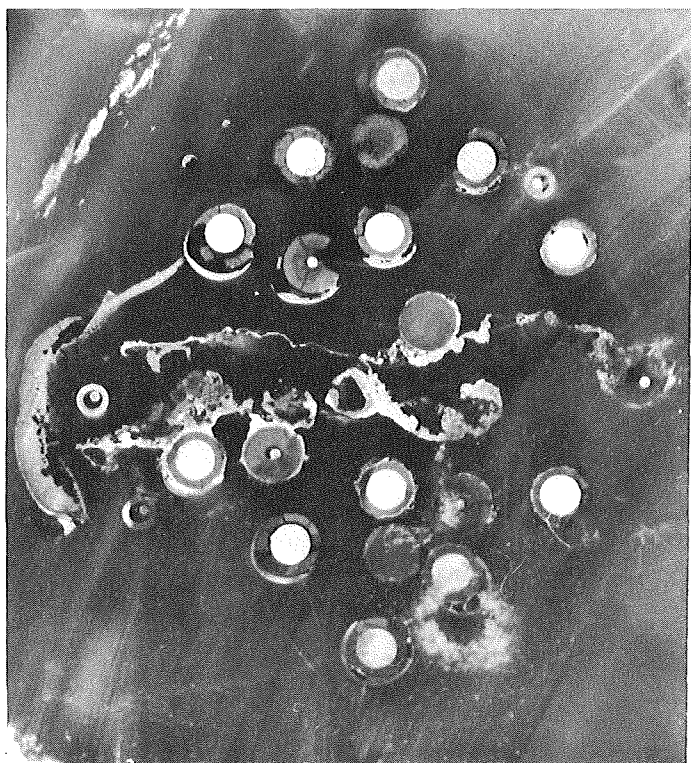
Top

Fig. B2: Horizontal cross sections of bundle CORA-33; 1045, 1043, 993, 991 mm

CORA-33: Dry-BWR

1830° C

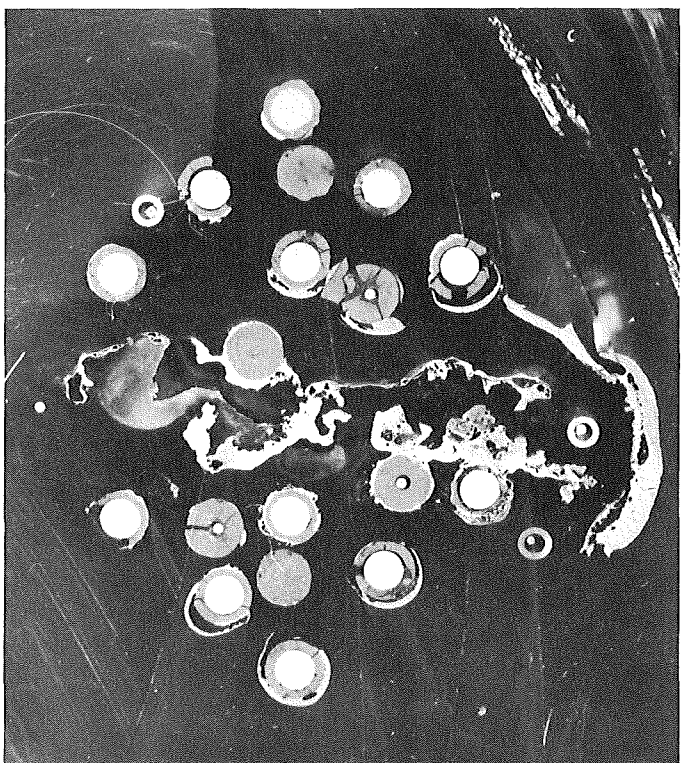
978 mm



Bottom

1830° C

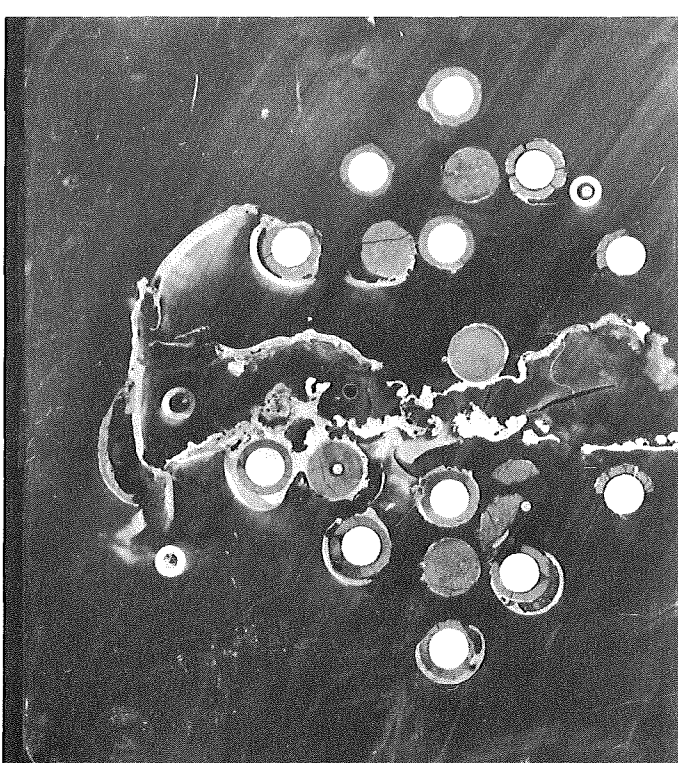
976 mm



Top

1850° C

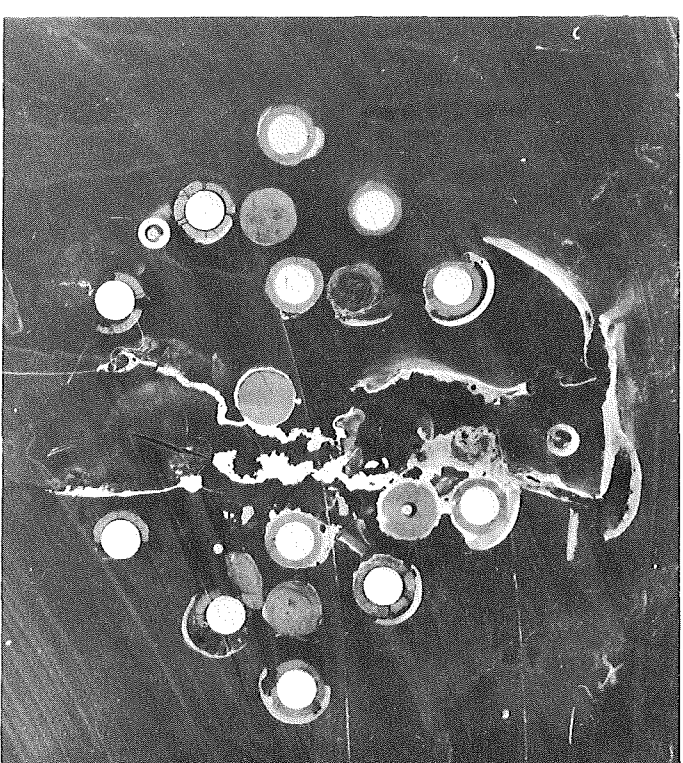
926 mm



Bottom

1850° C

924 mm



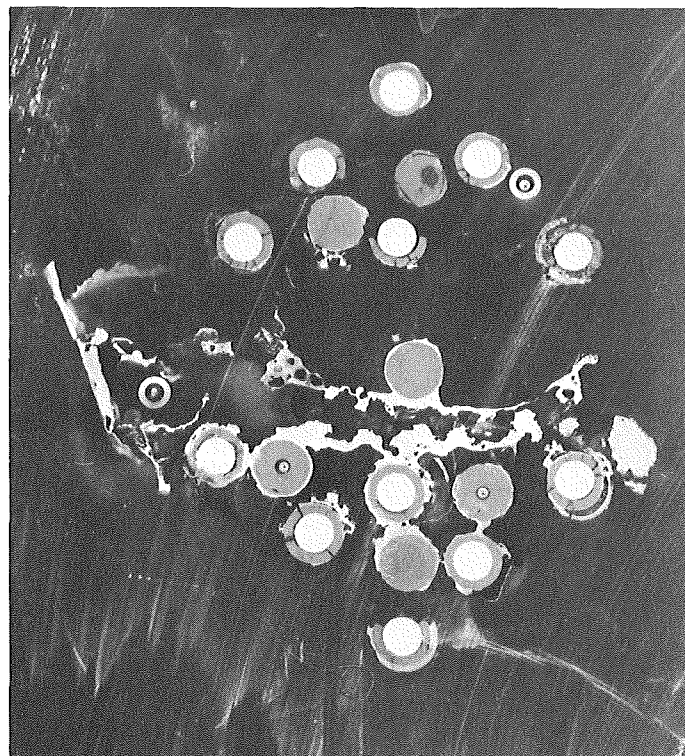
Top

Fig. B3: Horizontal cross sections of bundle CORA-33; 978, 976, 926, 924 mm

CORA-33: Dry-BWR

1850° C

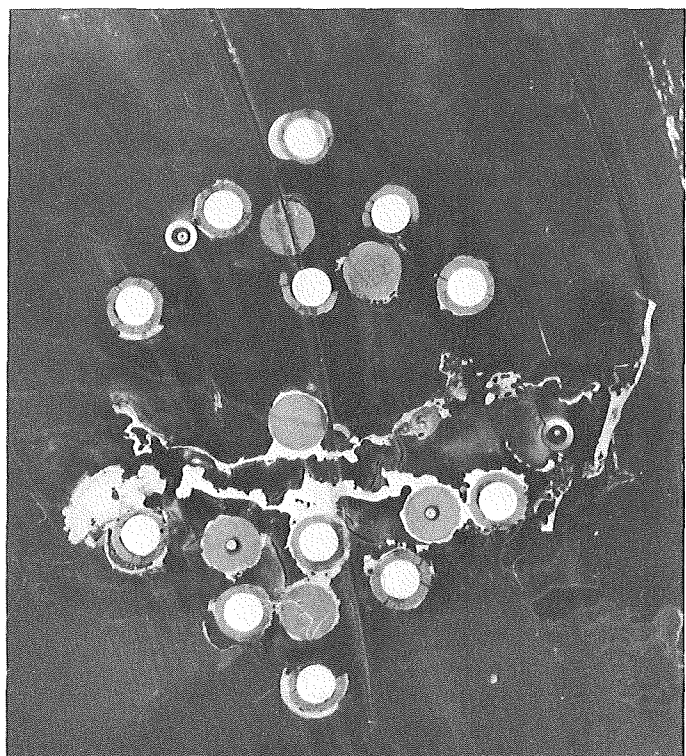
874 mm



Bottom

1850° C

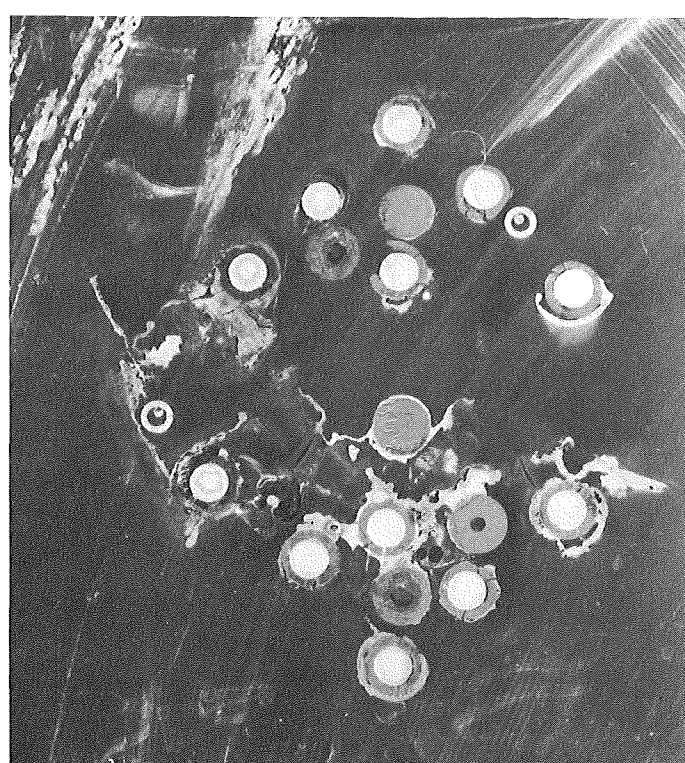
872 mm



Top

1830° C

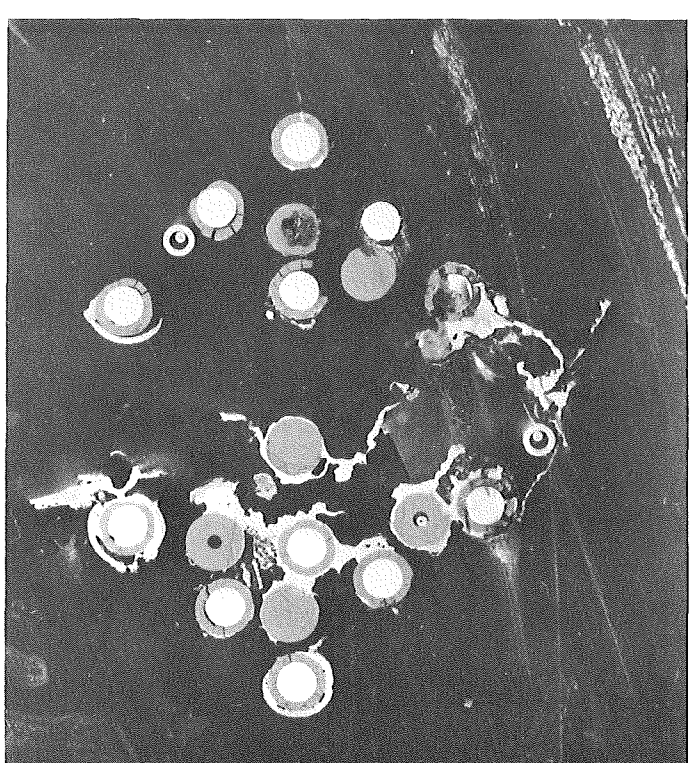
822 mm



Bottom

1830° C

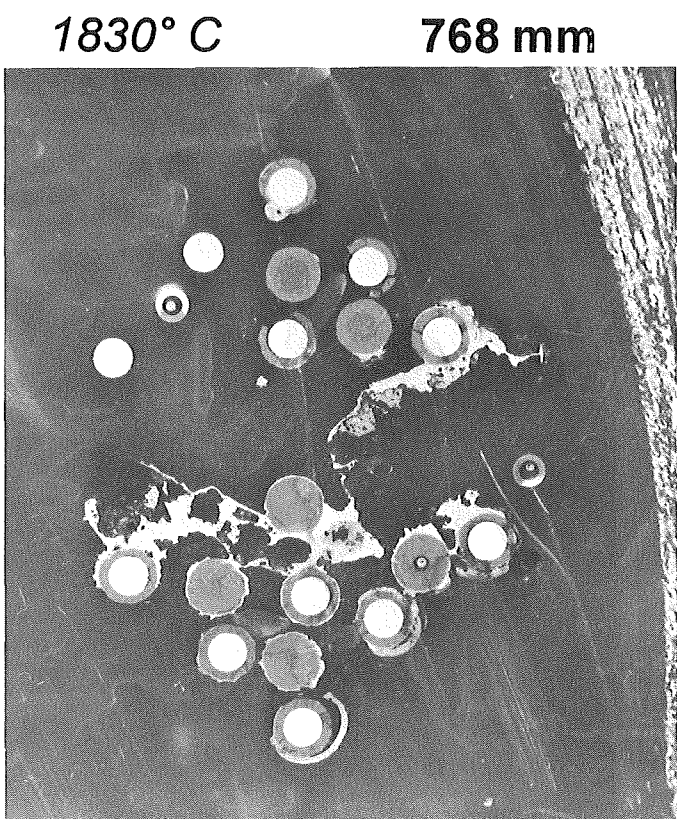
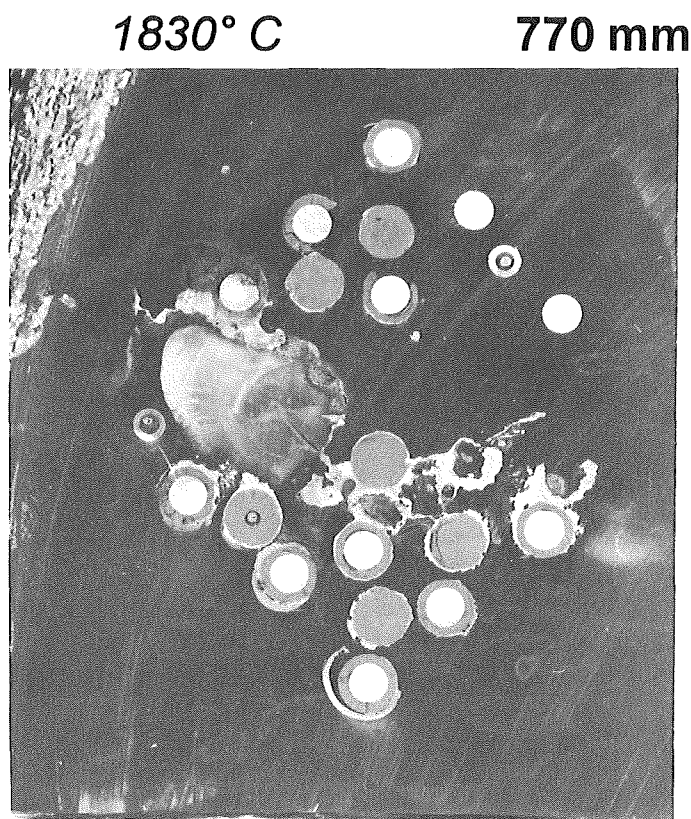
820 mm



Top

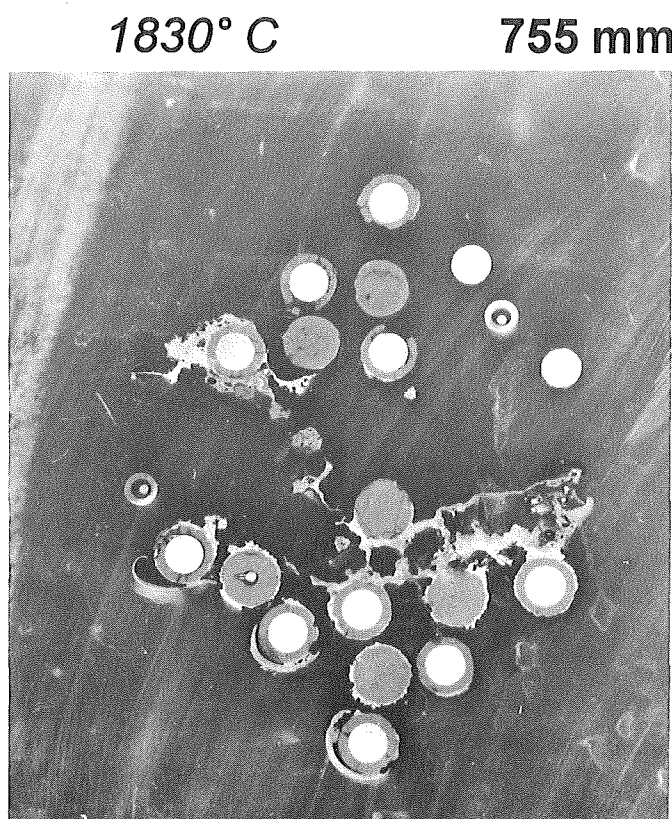
Fig. B4: Horizontal cross sections of bundle CORA-33; 874, 872, 822, 820 mm

CORA-33: Dry-BWR

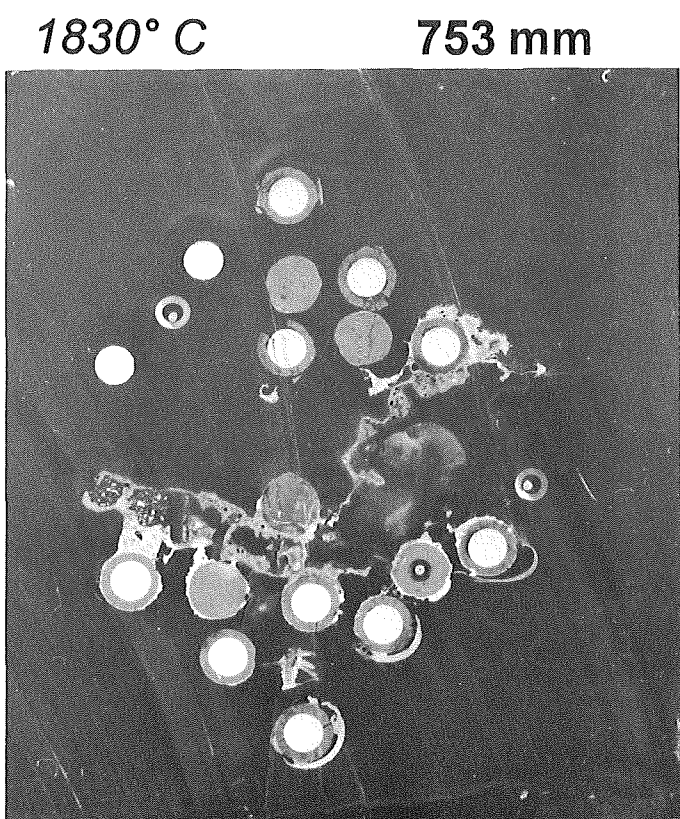


Bottom

Top



Bottom



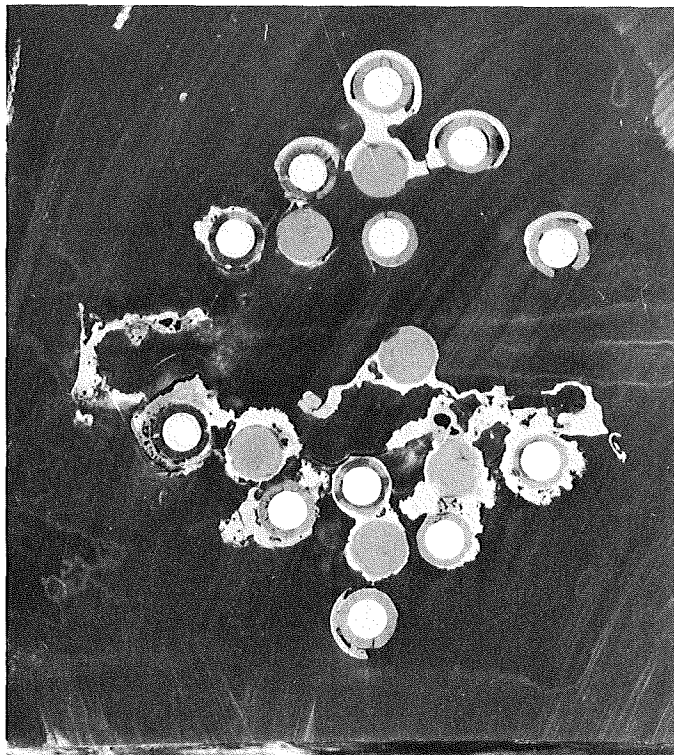
Top

Fig. B5: Horizontal cross sections of bundle
CORA-33; 770, 768, 755, 753 mm

CORA-33: Dry-BWR

1820° C

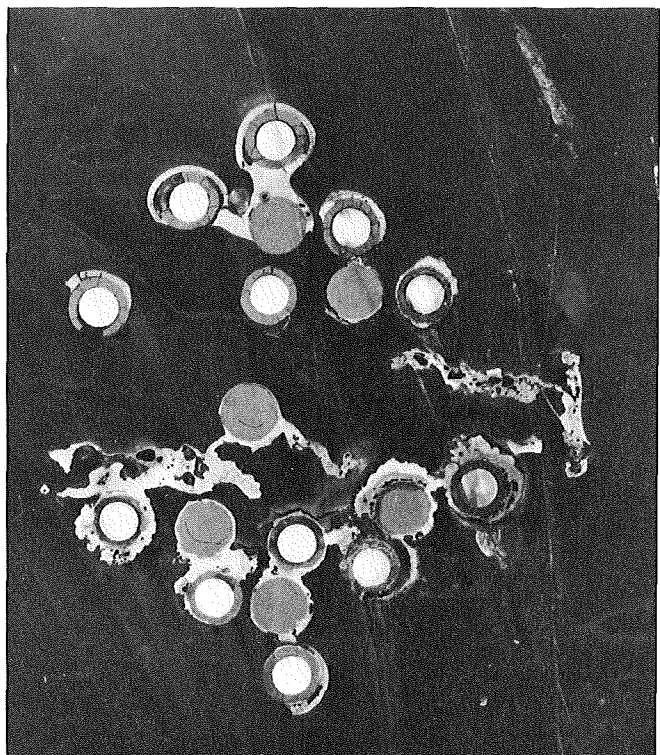
703 mm



Bottom

1820° C

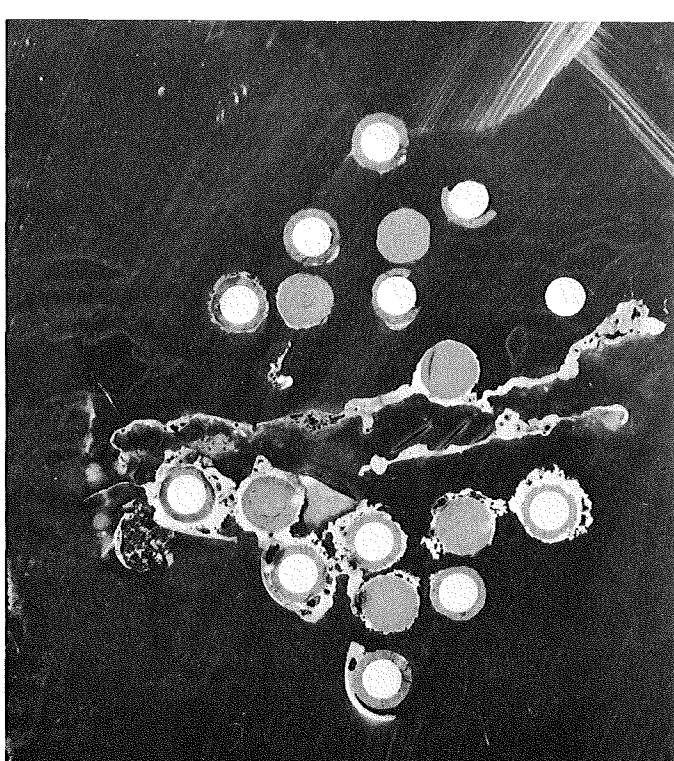
701 mm



Top

1820° C

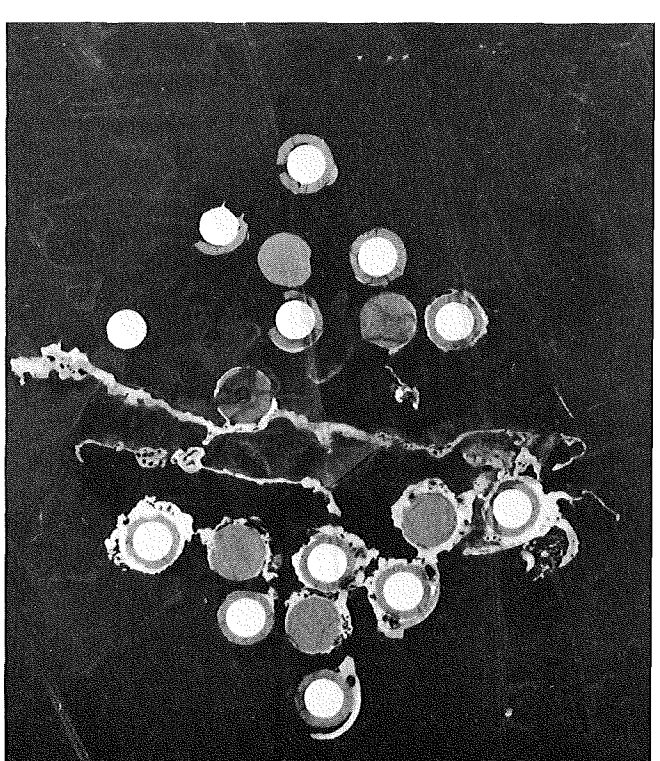
651 mm



Bottom

1820° C

649 mm



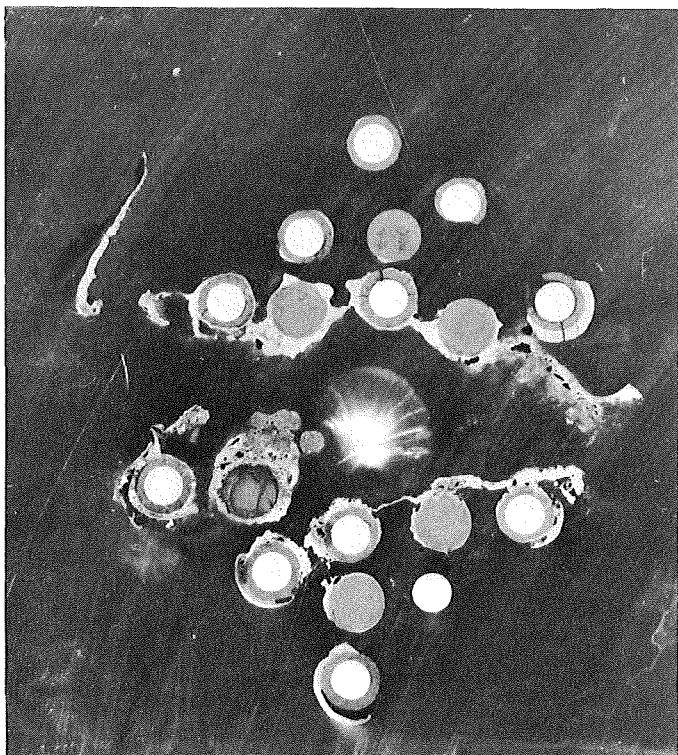
Top

Fig. B6: Horizontal cross sections of bundle CORA-33; 703, 701, 651, 649 mm

CORA-33: Dry-BWR

1810° C

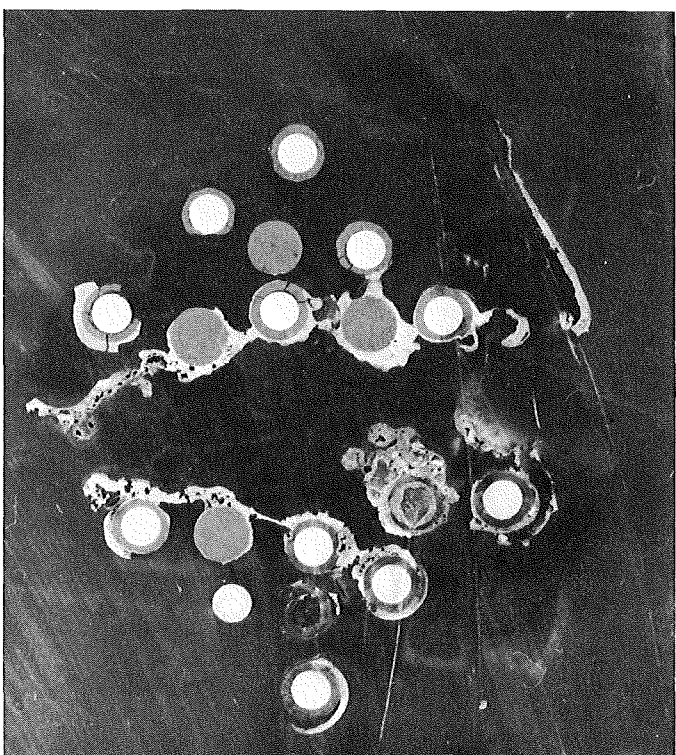
599 mm



Bottom

1810° C

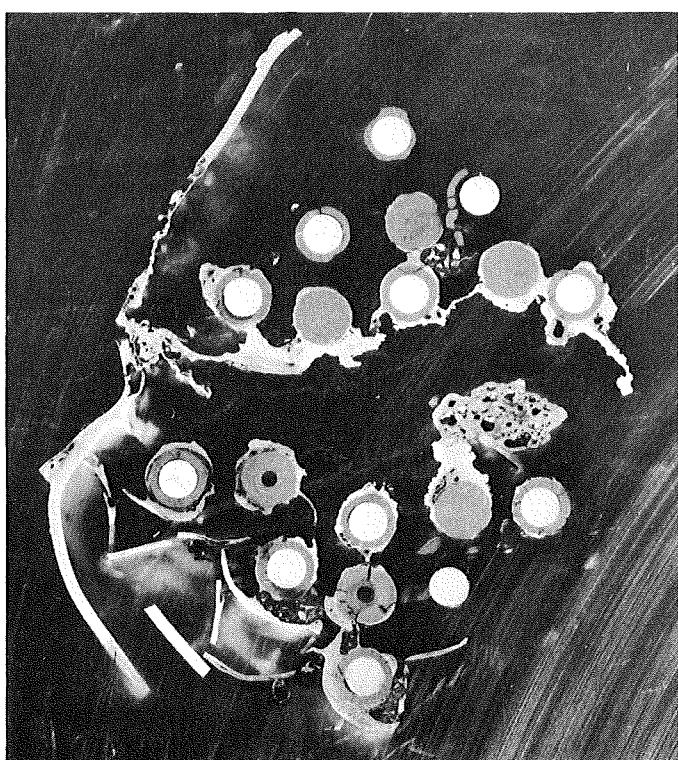
597 mm



Top

1800° C

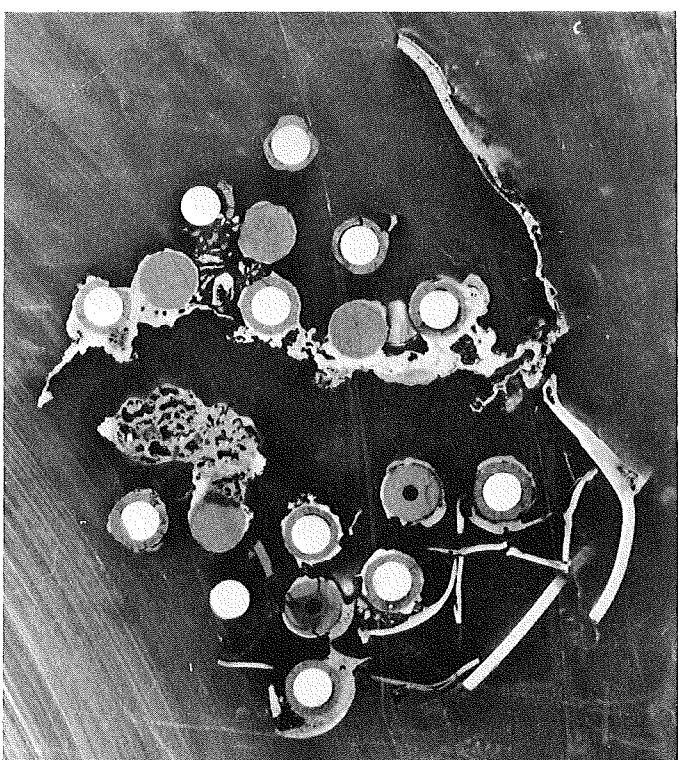
547 mm



Bottom

1800° C

545 mm



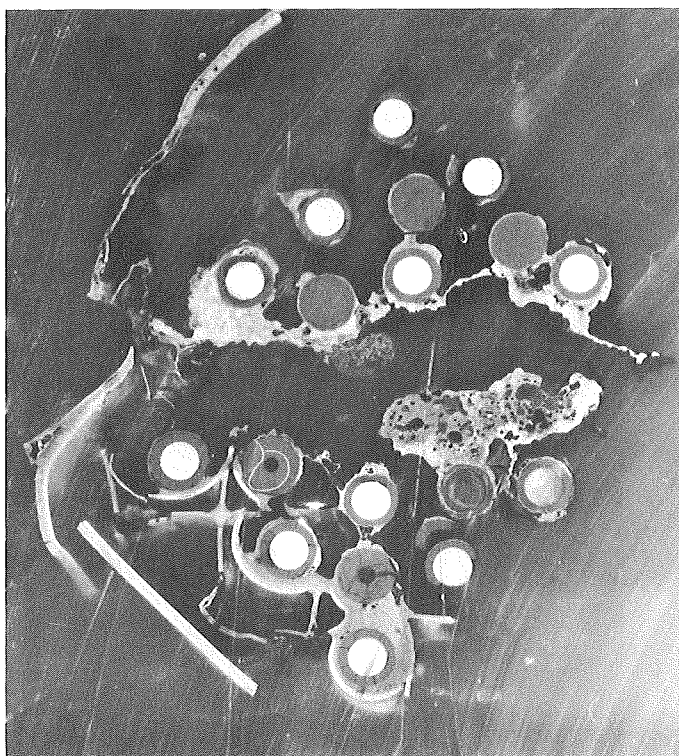
Top

Fig. B7: Horizontal cross sections of bundle CORA-33; 599, 597, 547, 545 mm

CORA-33: Dry-BWR

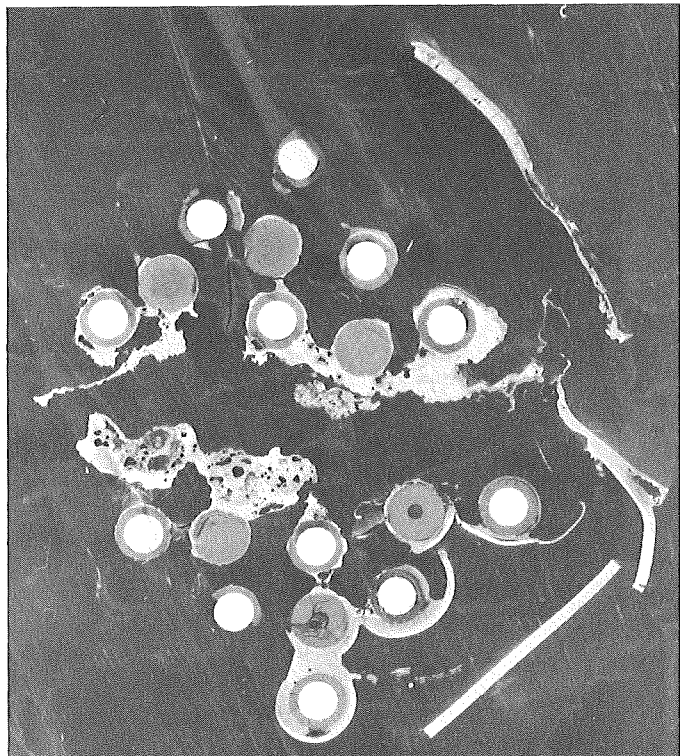
1800° C

532 mm



1800° C

530 mm

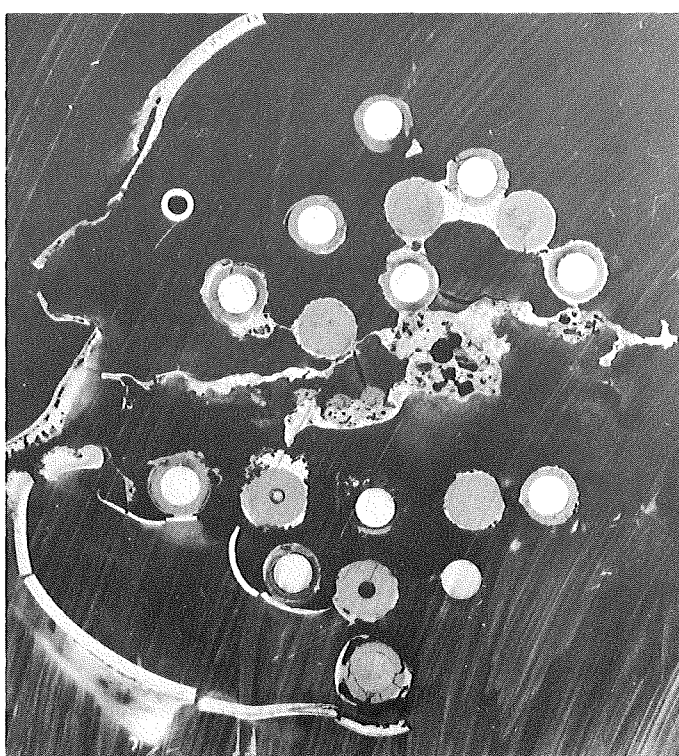


Bottom

Top

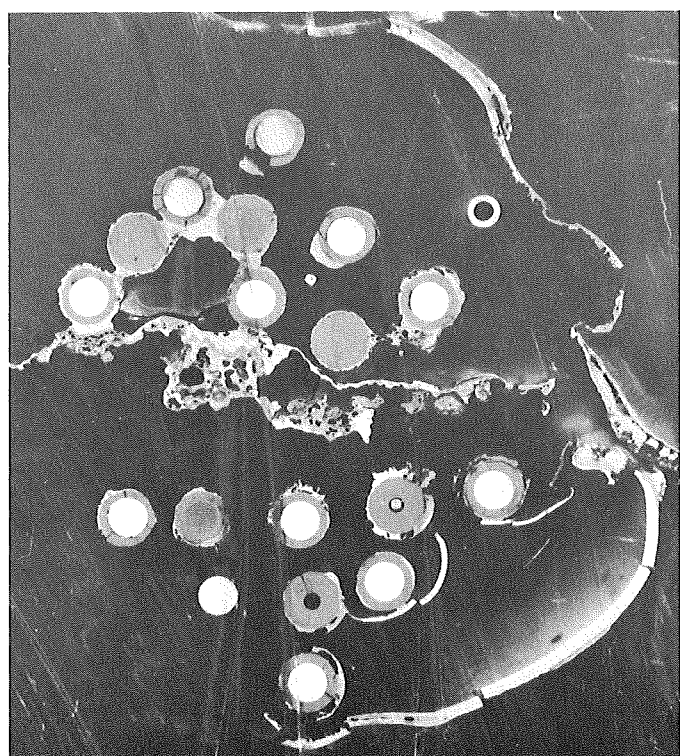
1800° C

480 mm



1800° C

478 mm



Bottom

Top

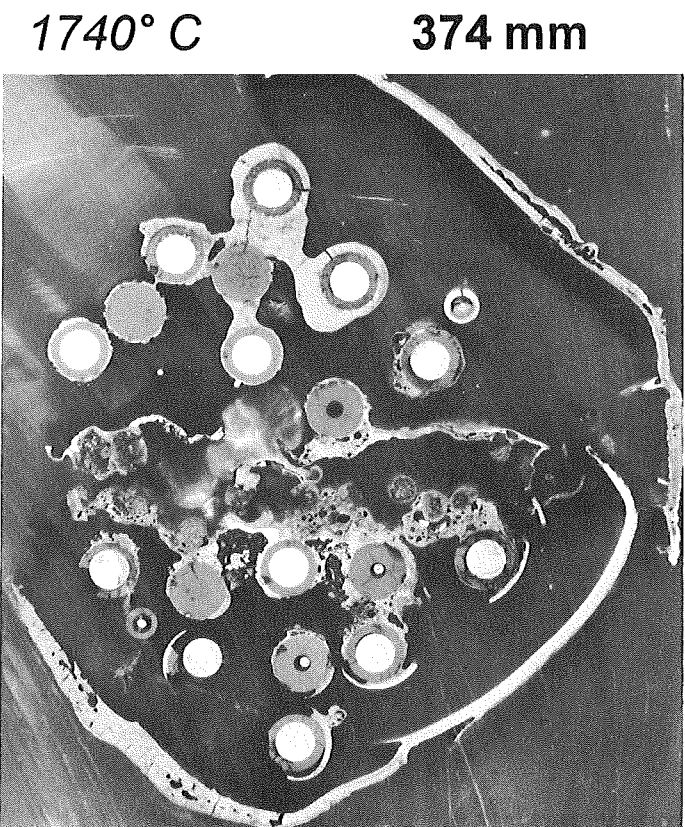
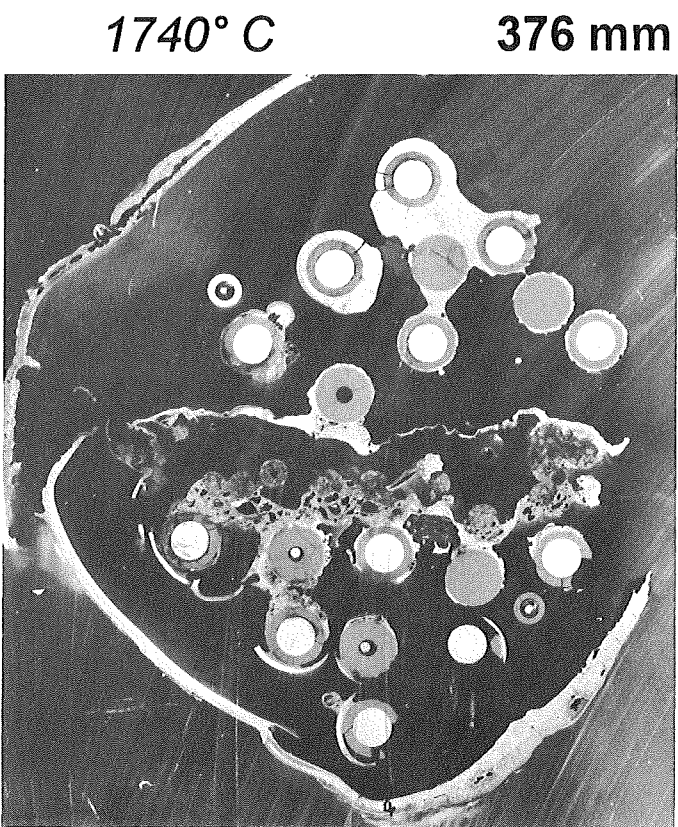
Fig. B8: Horizontal cross sections of bundle CORA-33; 532, 530, 480, 478 mm

CORA-33: Dry-BWR



Bottom

Top



Bottom

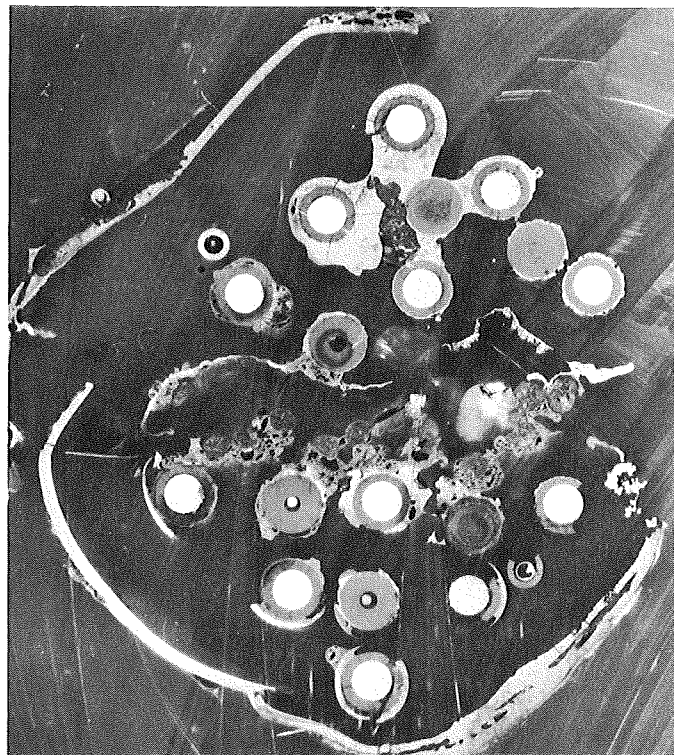
Top

Fig. B9: Horizontal cross sections of bundle
CORA-33; 428, 426, 376, 374 mm

CORA-33: Dry-BWR

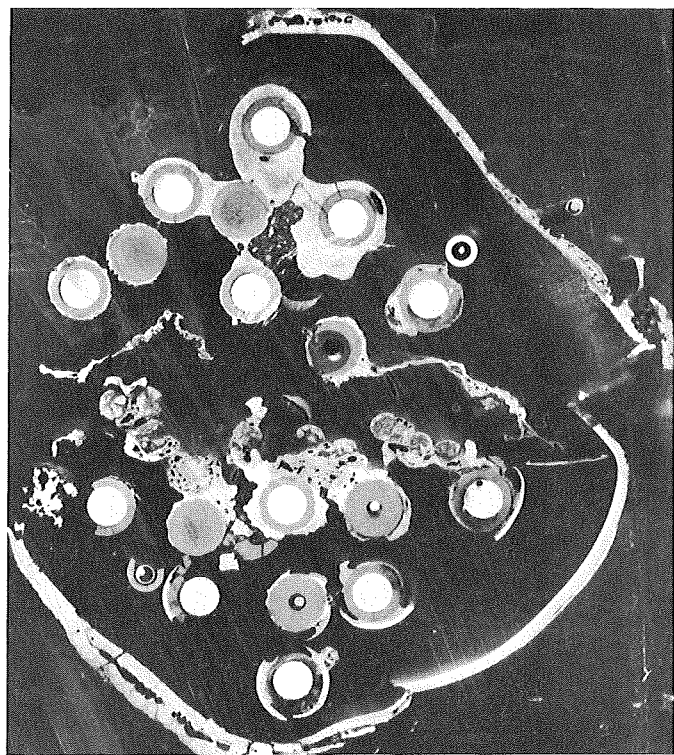
1750° C

361 mm



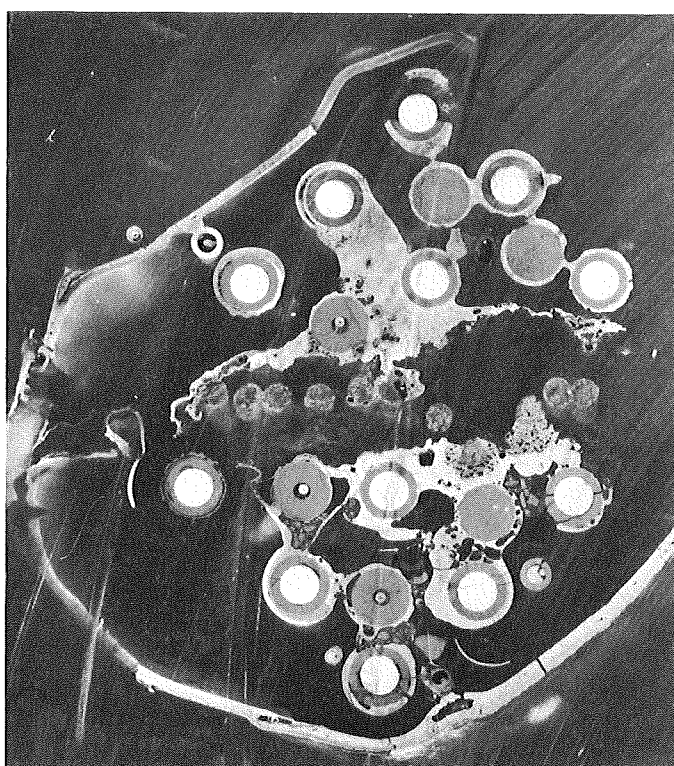
1750° C

359 mm



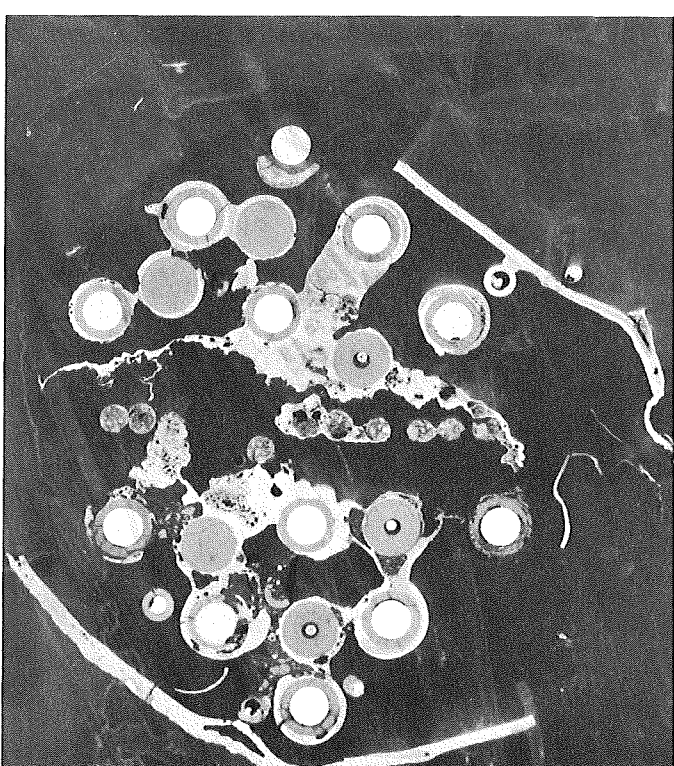
1700° C

309 mm



1700° C

307 mm

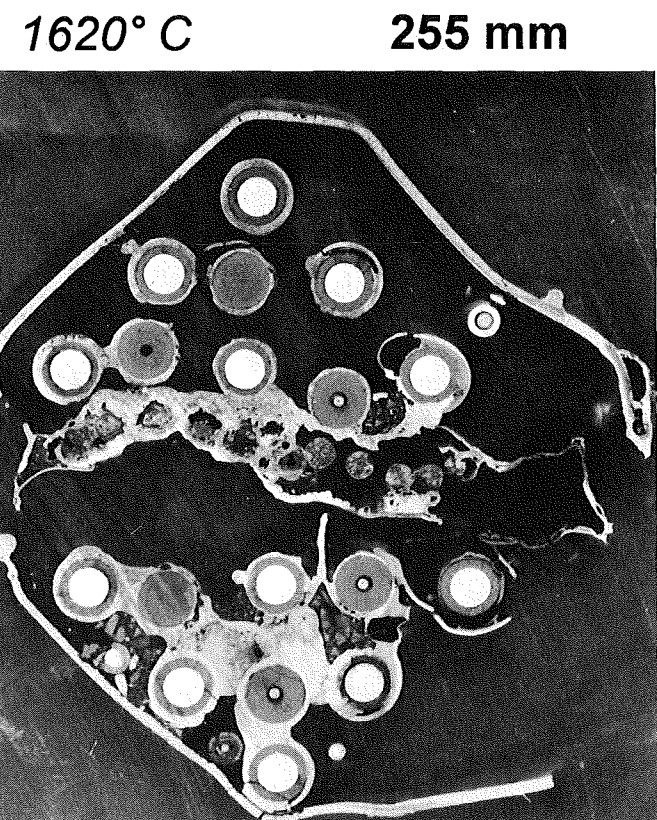
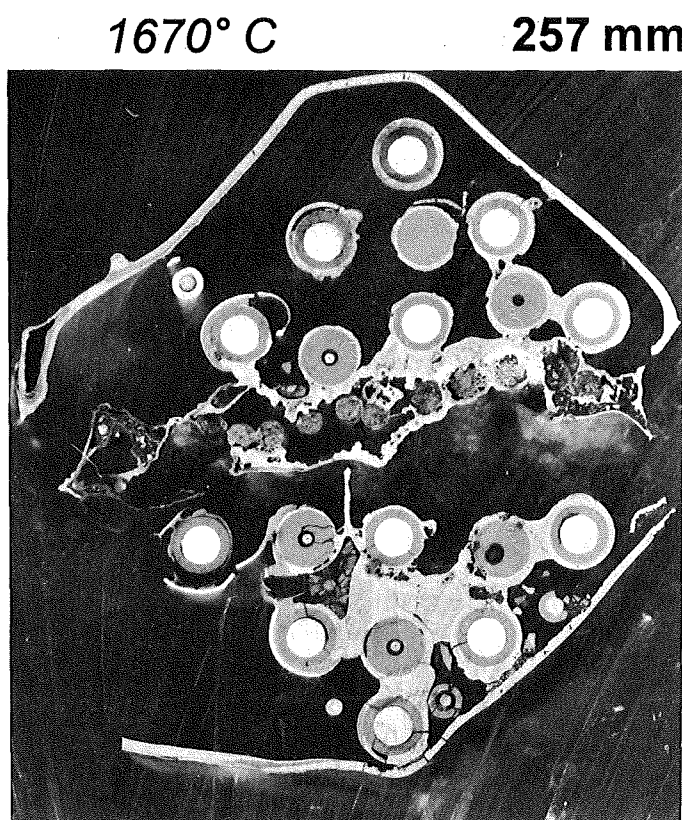


Bottom

Top

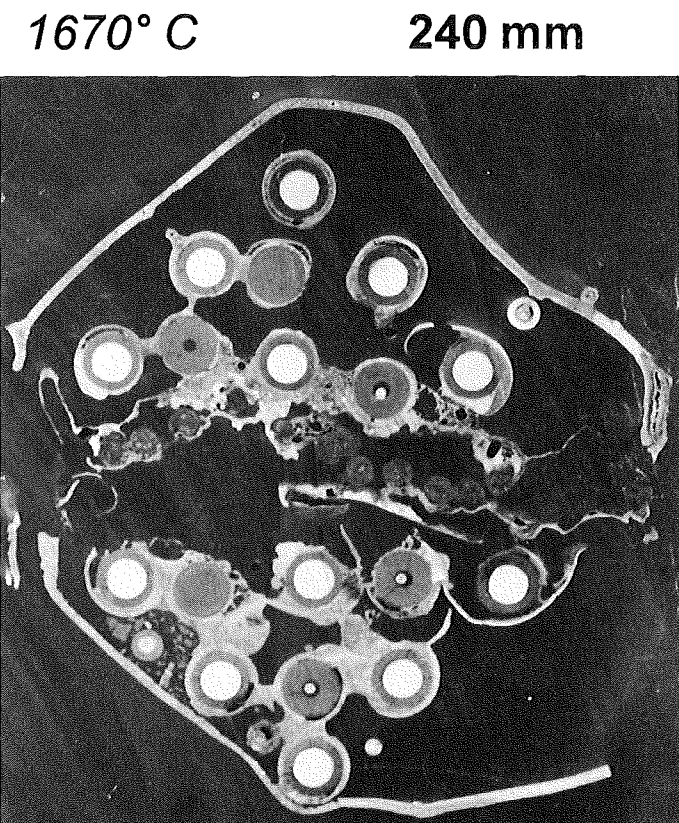
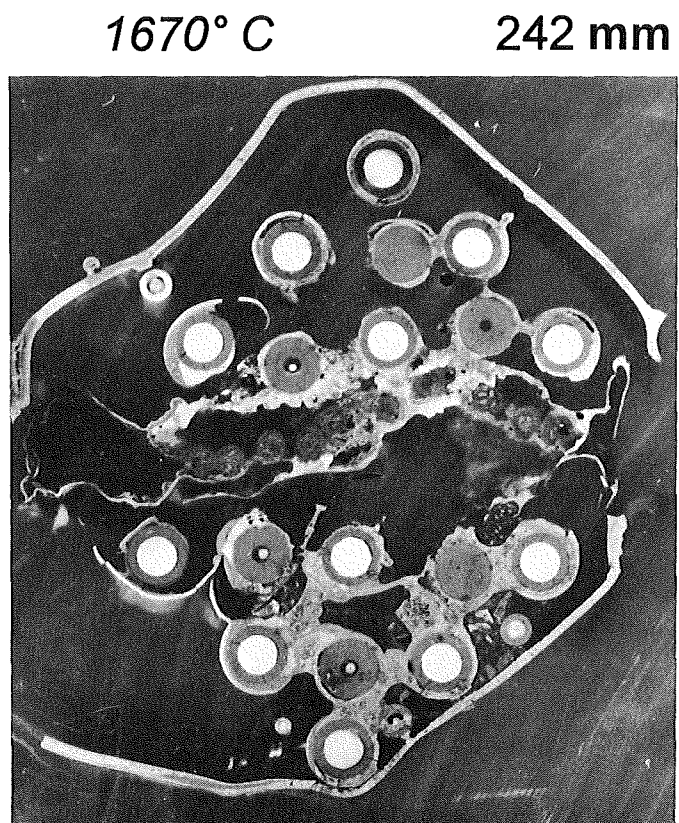
Fig. B10: Horizontal cross sections of bundle CORA-33; 361, 359, 309, 307 mm

CORA-33: Dry-BWR



Bottom

Top



Bottom

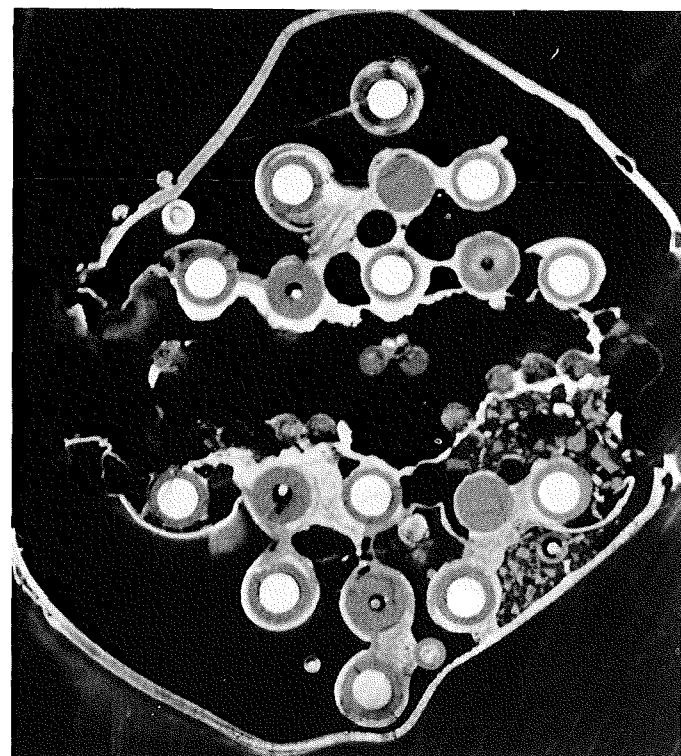
Top

**Fig. B11: Horizontal cross sections of bundle
CORA-33; 257, 255, 242, 240 mm**

CORA-33: Dry-BWR

1620° C

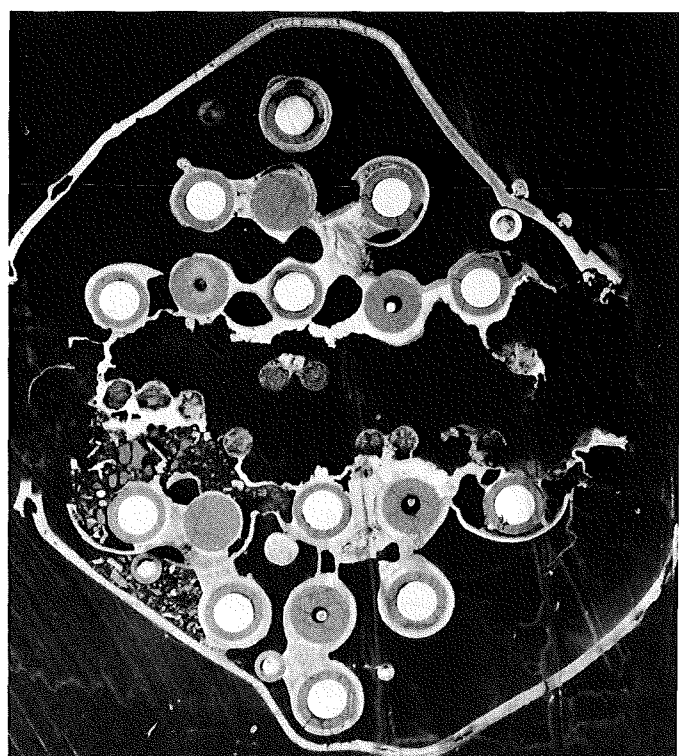
190 mm



Bottom

1620° C

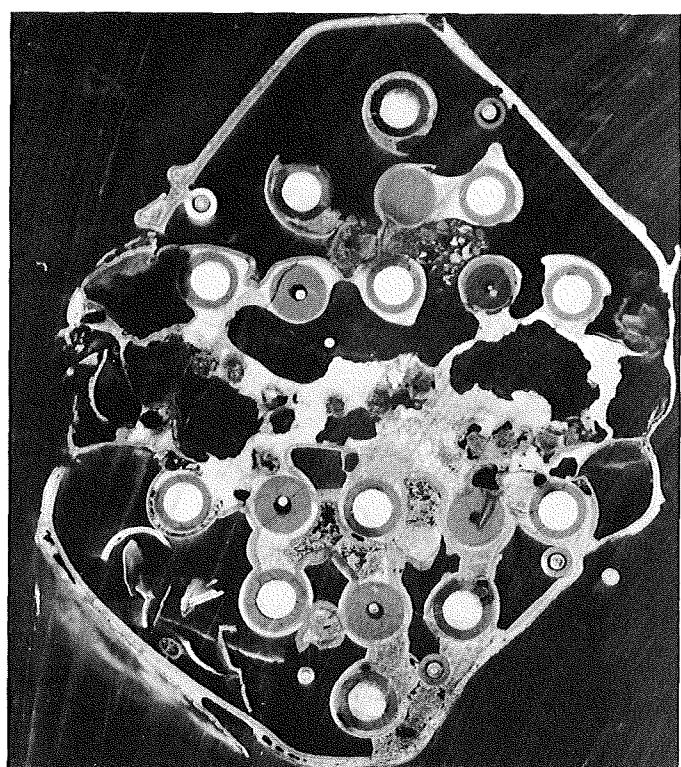
188 mm



Top

1590° C

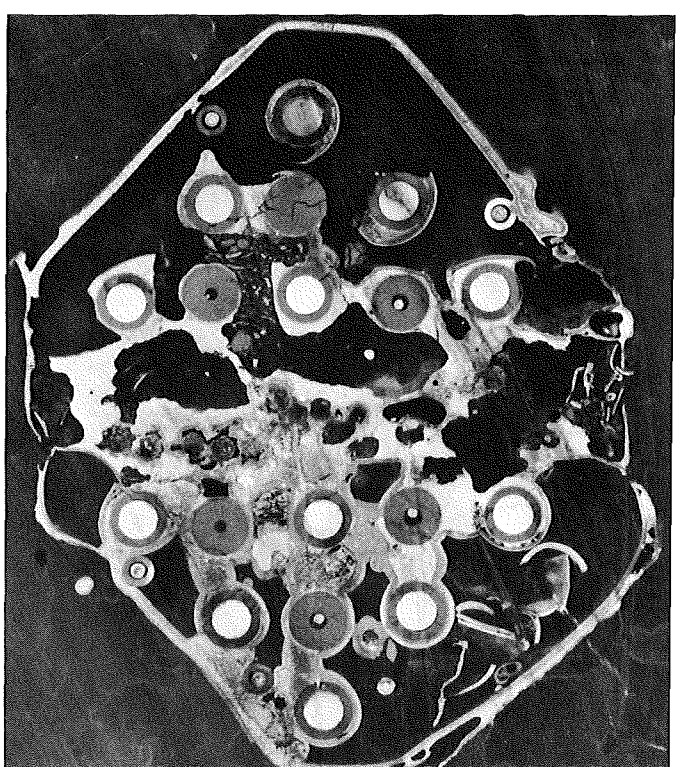
138 mm



Bottom

1590° C

136 mm



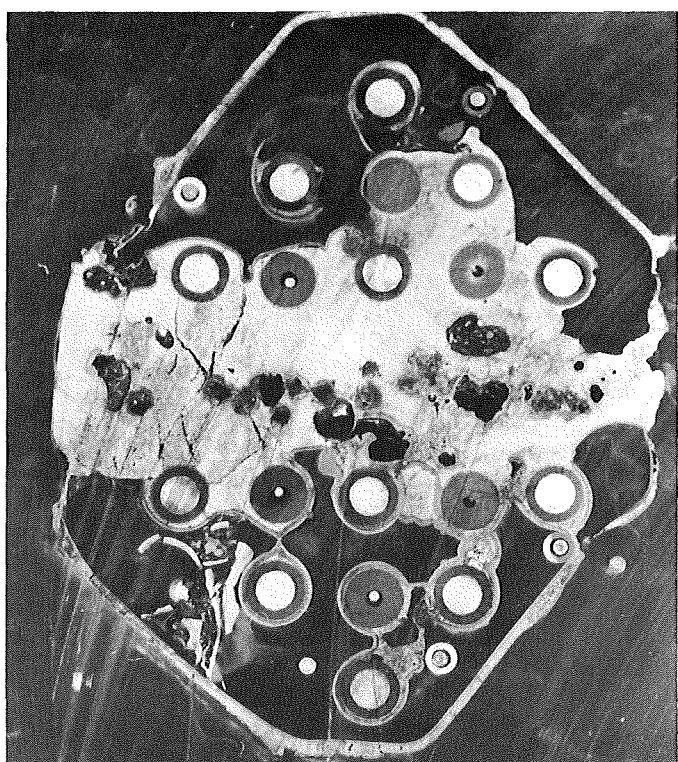
Top

Fig. B12: Horizontal cross sections of bundle
CORA-33; 190, 188, 138, 136 mm

CORA-33: Dry-BWR

1390° C

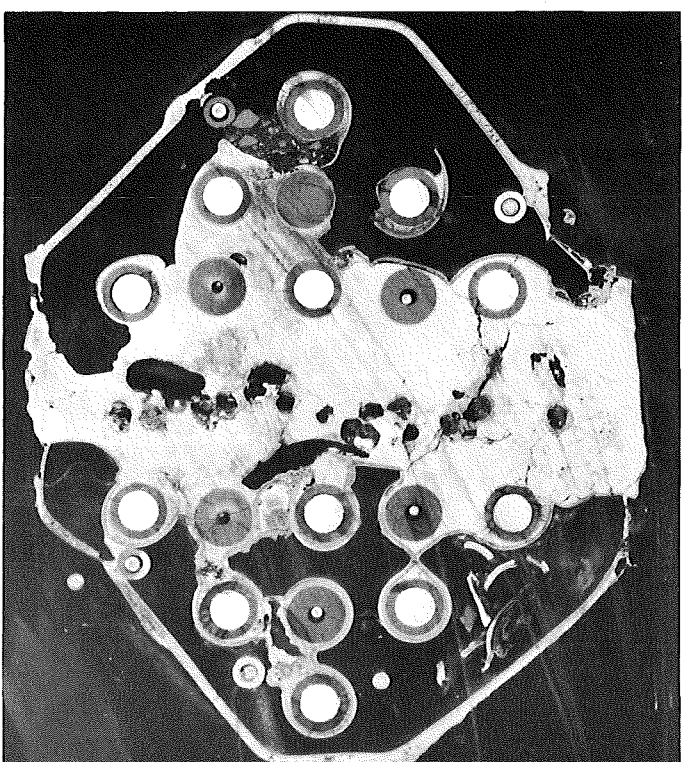
123 mm



Bottom

1390° C

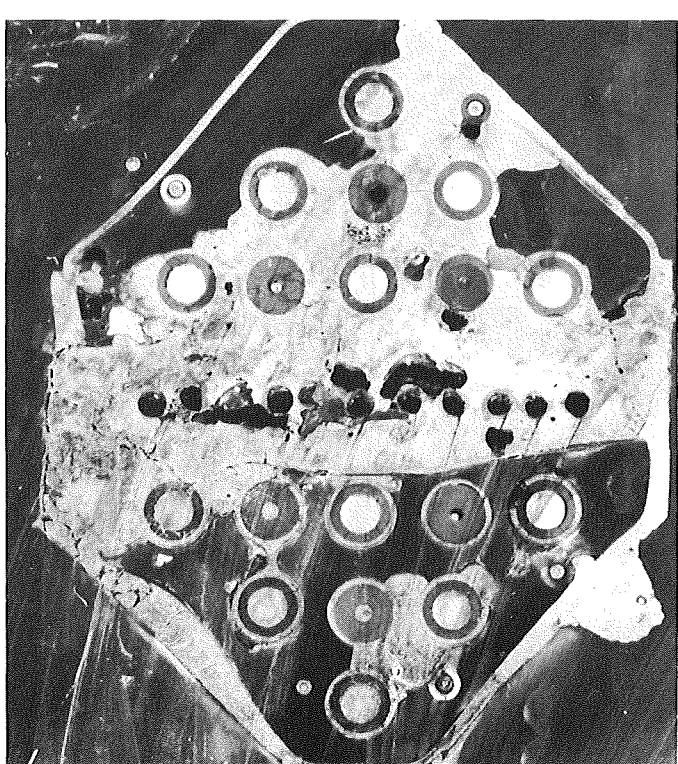
121 mm



Top

1100° C

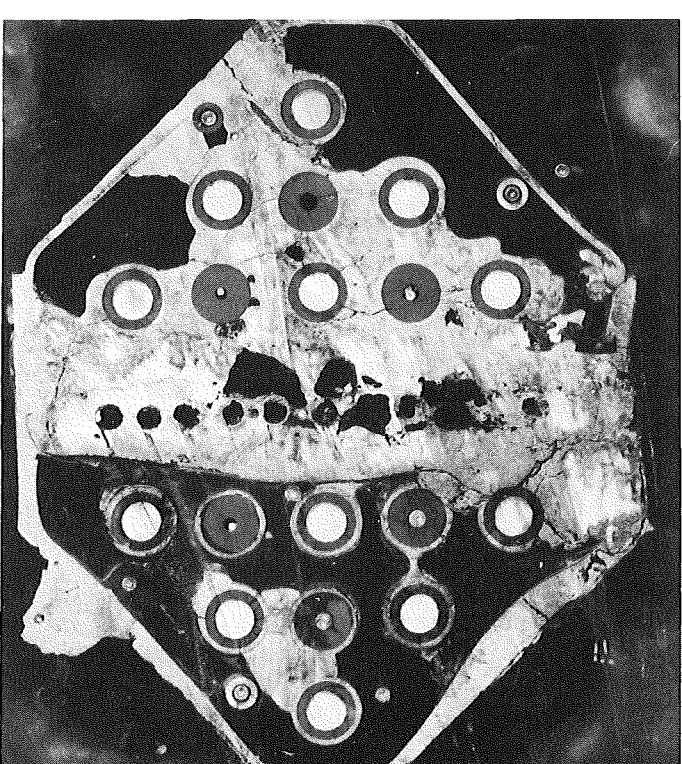
71 mm



Bottom

1100° C

69 mm



Top

*Fig. B13: Horizontal cross sections of bundle
CORA-33; 123, 121, 71, 69 mm*

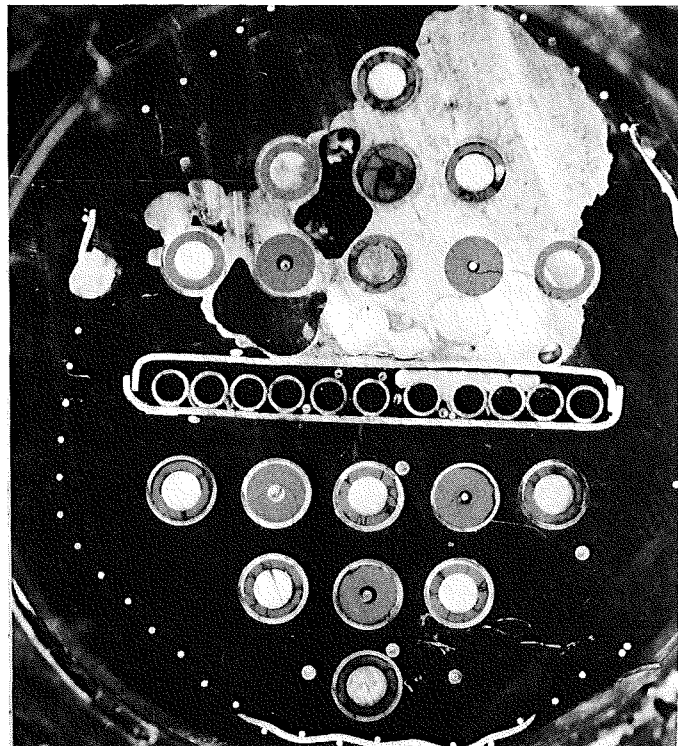
CORA-33: Dry-BWR

980° C

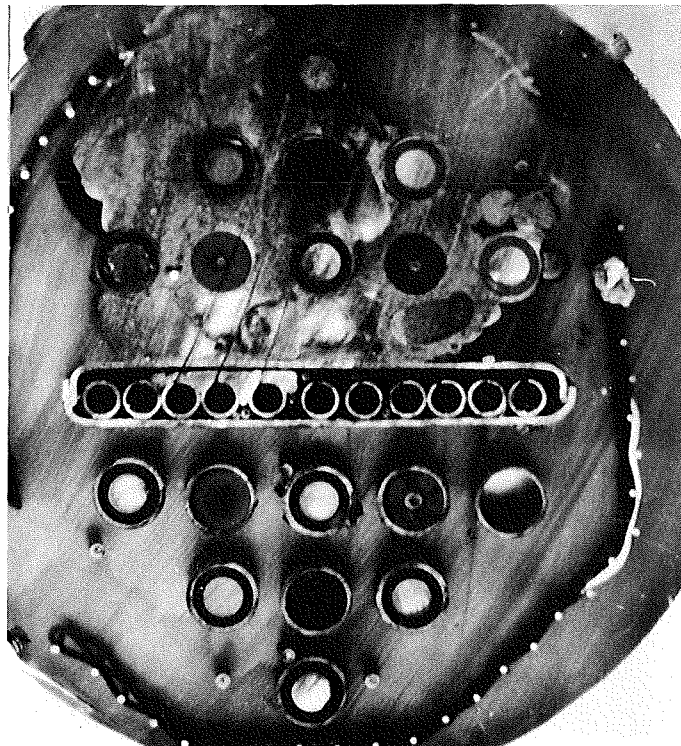
19 mm

980° C

17 mm



Bottom



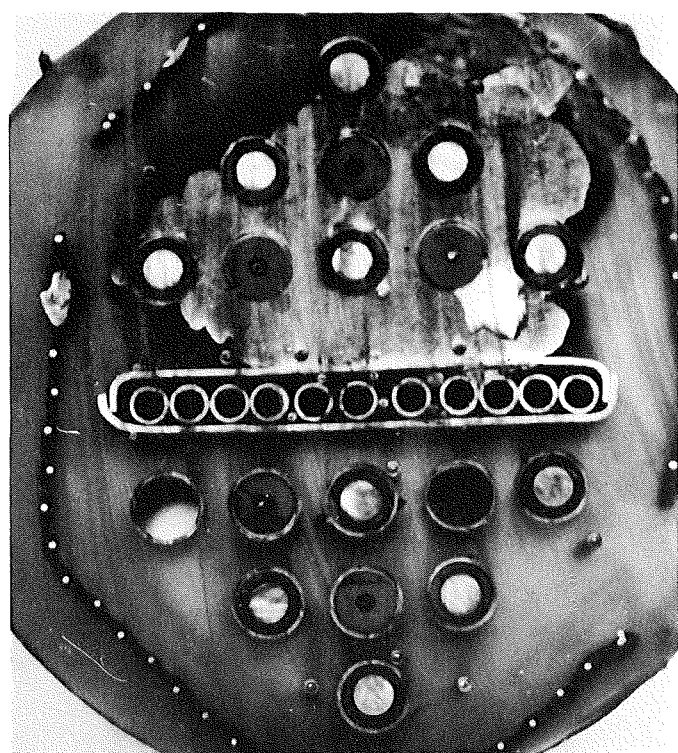
Top

980° C

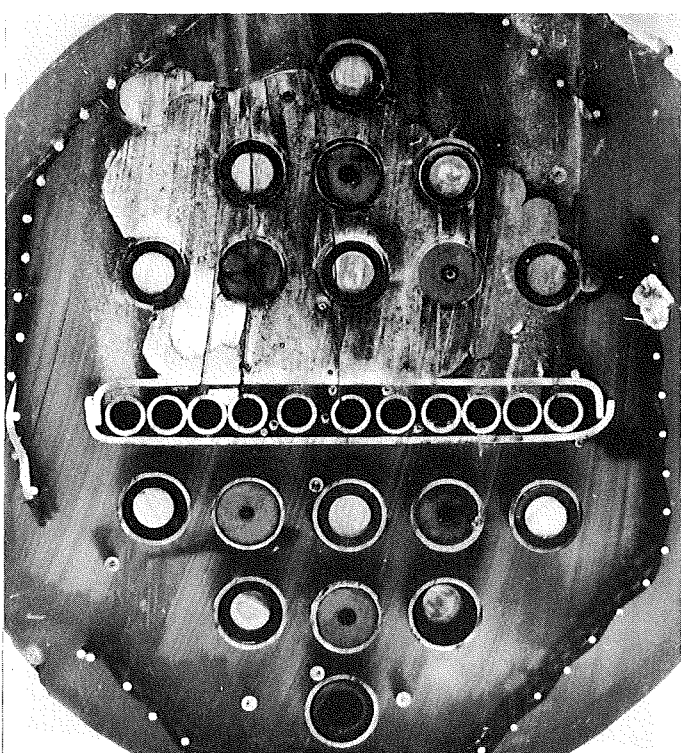
2 mm

980° C

0 mm



Bottom



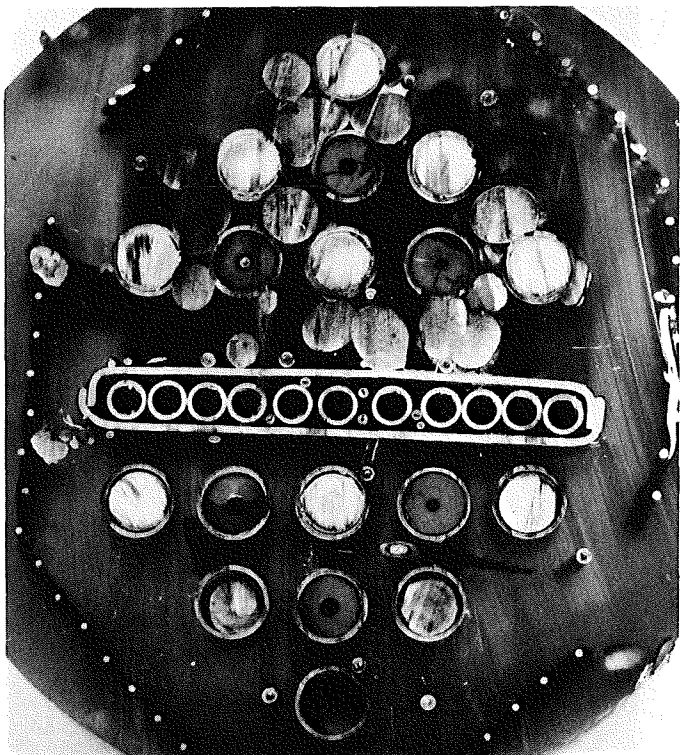
Top

Fig. B14: Horizontal cross sections of bundle CORA-33; 19, 17, 2, 0 mm

CORA-33: Dry-BWR

750° C

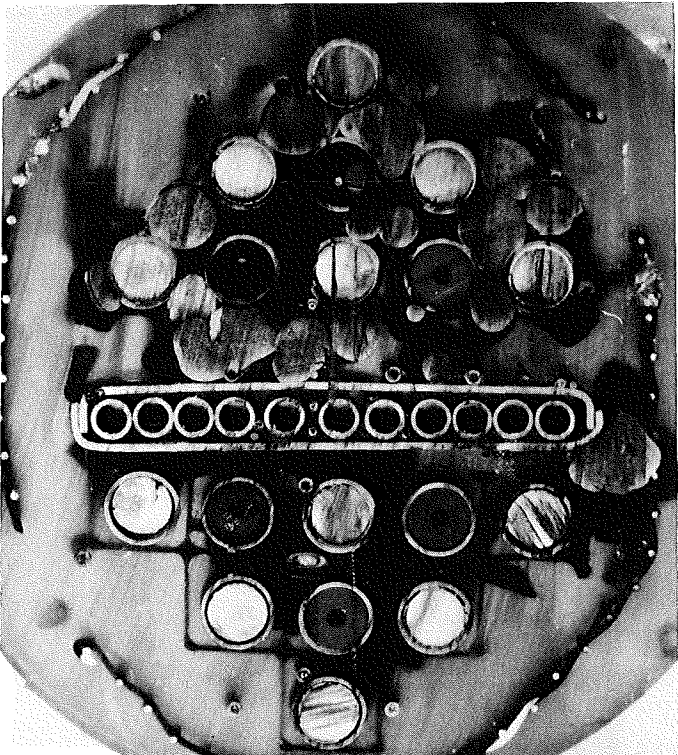
- 33 mm



Bottom

750° C

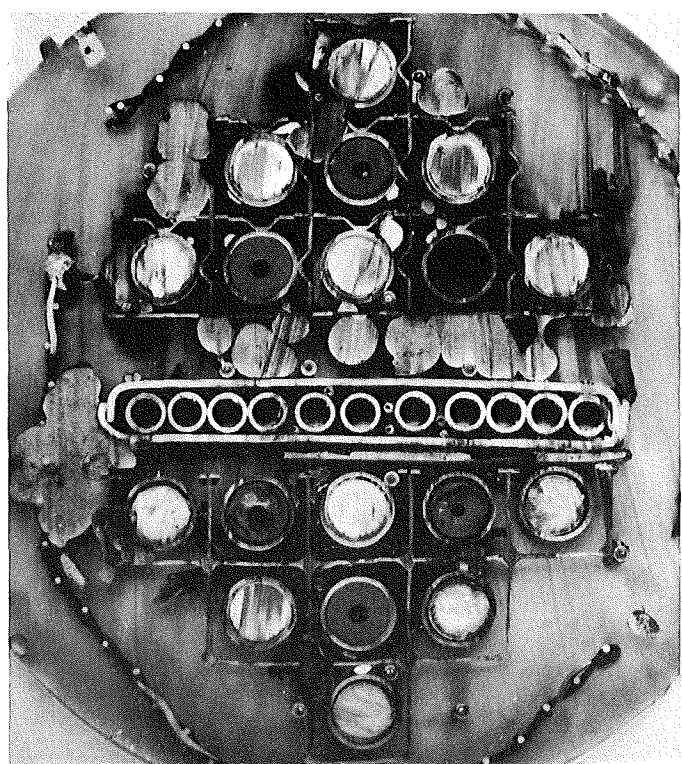
- 35 mm



Top

750° C

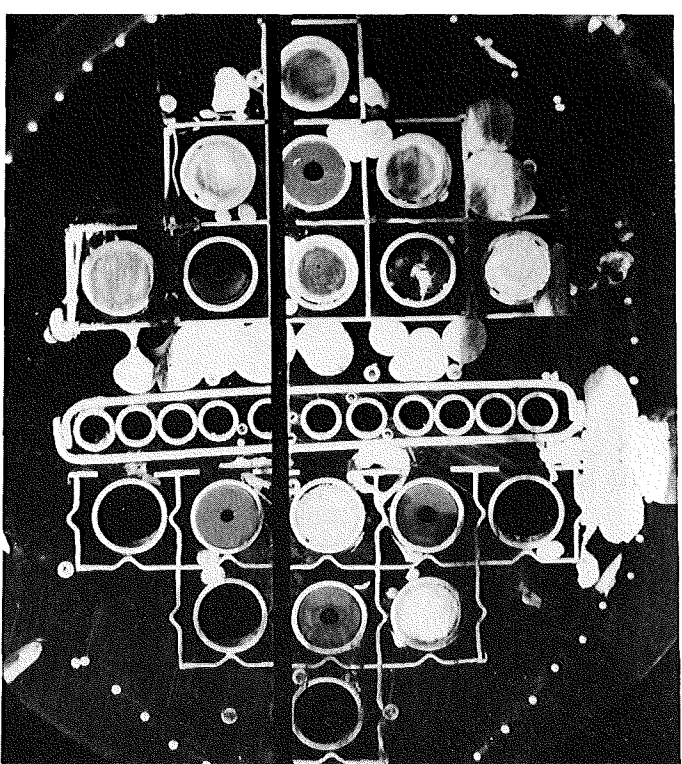
- 48 mm



Bottom

750° C

- 50 mm

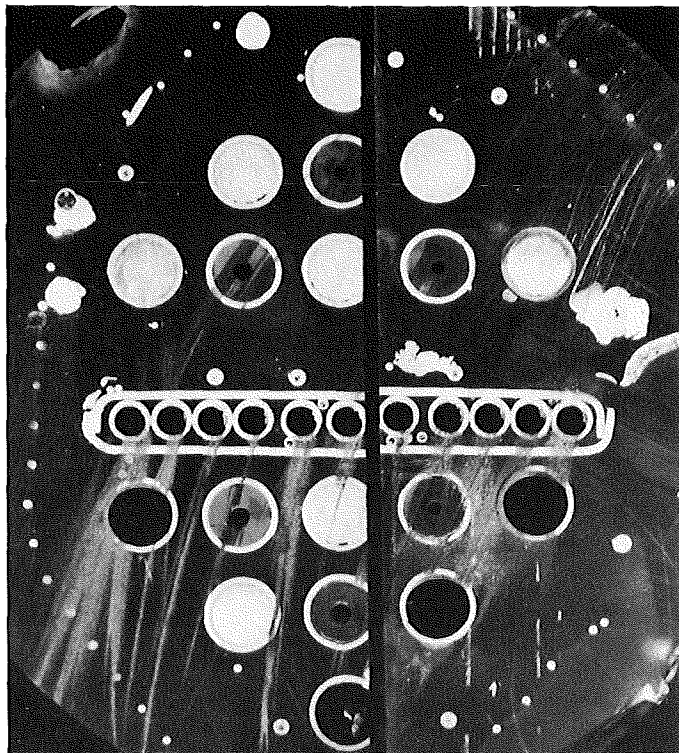


Top

Fig. B15: Horizontal cross sections of bundle
CORA-33; -33, -35, -48, -50 mm

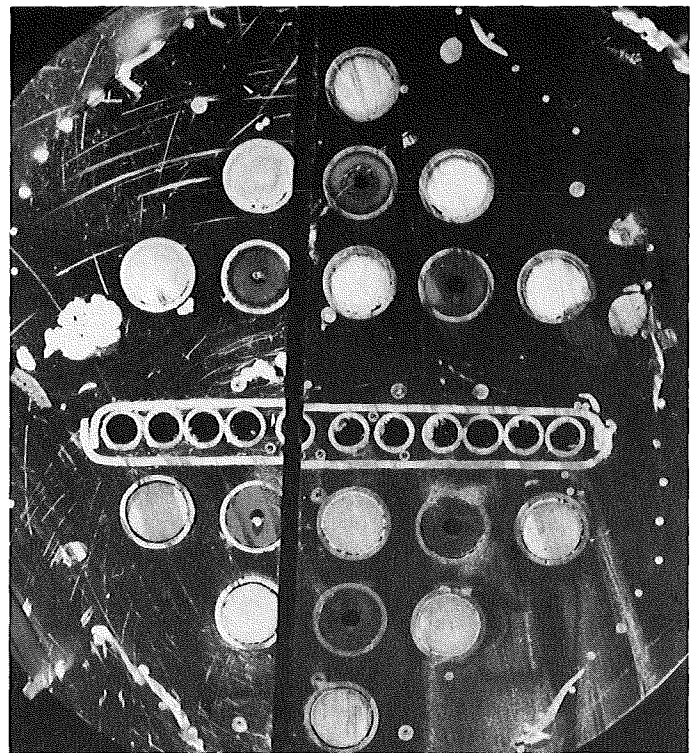
CORA-33: Dry-BWR

- 100 mm



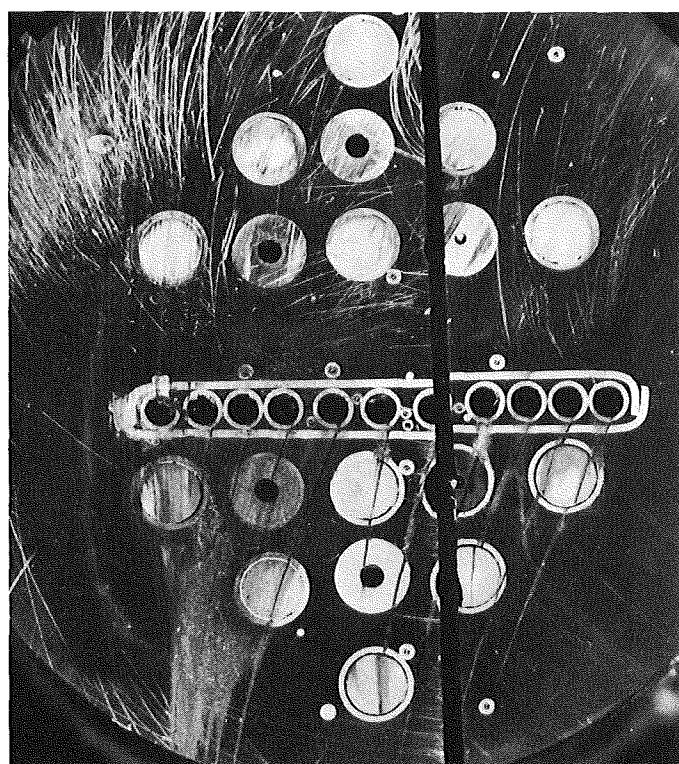
Bottom

- 102 mm



Top

- 212 mm



Bottom

Fig. B16: Horizontal cross sections of bundle CORA-33; -100, -102, -212 mm